

Hierarchical Supramolecular Assemblies Based on  
Host-Guest Chemistry between Cucurbit[ $n$ ]uril  
and Azobenzene Derivatives

*Author:*

Chenyan Liu

*Supervised by:*

Professor Oren A. Scherman

*This dissertation is submitted for the degree of Doctor of Philosophy*  
September 30, 2018

# Abstract

Cucurbit[8]uril (CB[8]) has attracted great interest in the cucurbit[ $n$ ]uril (CB[ $n$ ]) family on account of its capability to simultaneously accommodate two guests inside its cavity, to form strong yet dynamic ternary complexes. Owing to the photo-induced *trans* to *cis* isomerisation property, azobenzene (Azo) derivatives have been widely employed in several host-guest systems, leading to various light-responsive materials. This thesis focuses on CB[8]-based ternary complexes, especially those involving Azo derivatives. These systems can be exploited as a platform to hierarchically fabricate supramolecular constructs, including crystalline structures and composite materials. Specifically, novel morphology-controlled (1D needle-like, 2D sheet-like) crystals have been prepared by adjusting the assembly of Azo-CB[8] complexes, which can be further developed to oriented macroscopic free-standing crystalline pillars grown from a glass surface. Next, a composite micelle-nanoparticle complex has been prepared utilising Azo-CB[8] assemblies, which demonstrates  $\sim 90\%$  efficiency in surfactant recycling. Finally, an organic CB[8]-mediated hydrogel reinforced by inorganic nanowires has been prepared. This hybrid structure shows increased stiffness due to various supramolecular interactions.

Chapter 1 gives a brief introduction to CB[ $n$ ] host-guest chemistry with emphasis on CB[ $n$ ]-based crystalline structures and CB[8] ternary complexes. Recent progress of Azo-based host-guest chemistry is then reviewed. In addition, shape-controlled crystals formed *via* supramolecular interactions are discussed at the end of the chapter.

Chapter 2 focuses on the crystalline structure of the 1:2 homoternary complex formed between CB[8] and a methyl orange (MO) guest, which is the fastest CB[8]-based crystallisation to date. As a commonly used pH indicator, MO possesses an azobenzene moiety with both an electronically positive amino group and an anionic sulfonate group. At

---

low pH values, formation of the homoternary complex 2MO@CB[8] occurs, serving as a ‘tectonic’ building block, which rapidly stacks into a herringbone arrangement. The intermolecular and intercomplex interactions inside 2MO@CB[8] crystals are discussed, whereby the CB[8] macrocycle orients the electrostatic charges on MO guests resulting in the repulsive interactions being shielded; this in turn leads to fast electrostatically-driven crystal growth. The 2MO@CB[8] system provides a promising approach for designing ultrarapid crystallisation systems derived from CB[*n*] host-guest complexes. Moreover, the host-guest chemistry between CB[8] and a variety of Azo derivatives with different functional groups is discussed, demonstrating the influence of guest structures on their crystalline behaviours.

Chapter 3 further explores the mechanism of 2MO@CB[8] crystallisation through a series of experimental and computational methods. Control over the crystal shape, length and growth rate can be achieved in a facile manner whilst maintaining the same (internal) unit cell. Therefore, the properties of the macro-scale crystals can be tuned at the molecular level through adjusting the assembly of 2MO@CB[8] building blocks. For example, tuning the ionic strength of the solution enables a second growth dimension, yielding 2D crystals with sheet-like and more complex morphologies. Furthermore, our understanding of oriented electrostatics provided by the homoternary tecton can then be exploited to prepare oriented macroscopic free-standing crystalline pillars grown from a glass surface at room temperature.

Next, CB[8] ternary complexes have been employed as ‘bridges’ to link (organic) soft and (inorganic) hard materials together, resulting in composite materials. In chapter 4, a micelle-nanoparticle complex (**MNC**) structure has been assembled *via* host-guest interactions between Azo-functionalised, cargo-loaded micelles and magnetic SiO<sub>2</sub> nanoparticles (NPs) functionalised with CB[8] catenanes. Owing to the photo-responsive and magnetic properties, **MNCs** can be exploited to recycle detergents (micelles) from aqueous solution. This is followed by the controlled release of the encapsulated hydrophobic molecules inside the micelle cavity. In this process, both the micelles and NPs can be recycled efficiently. The novel **MNC** structure provides a promising approach to

---

recycle versatile drug carriers through host-guest chemistry.

Chapter 5 introduces a CB[8]-based hydrogel in which inorganic nanowires (NWs) are employed to enhance the gel stiffness. The supramolecular hydrogel is comprised of methylviologen-functionalised poly(vinyl alcohol) (PVA-MV), hydroxyethyl cellulose with naphthyl moieties (HEC-Np) and CB[8]. The gel structure is effectively enhanced by the framework supporting effects of  $\text{CePO}_4$  NWs and additional hydrogen bonding interactions between NWs and PVA-MV/HEC-Np polymers. The high aspect ratio NWs serve as a 'skeleton' for the network, providing extra physical crosslinks. This results in a single continuous phase hybrid supramolecular network with improved strength, showcasing a general approach to reinforce soft materials.

Finally, this thesis closes with a summary and perspective chapter, concluding the present work and highlighting an insight towards future work. Utilising CB[8] ternary complexes, various supramolecular constructs can be prepared through hierarchical self-assemblies, leading to a wide variety of composite systems and functional materials in the future.

# Contents

<b>1</b>	<b>Introduction</b>	<b>1</b>
1.1	Recent progress in cucurbit[ <i>n</i> ]uril host-guest chemistry . . . . .	1
1.1.1	CB[ <i>n</i> ] host-guest complexation . . . . .	2
1.1.2	CB[ <i>n</i> ]-based crystals . . . . .	5
1.1.3	Supramolecular ‘hand-cuff’ based on CB[8] . . . . .	9
1.2	Azobenzene in host-guest chemistry . . . . .	13
1.2.1	Photo-responsive host-guest complexes . . . . .	14
1.2.2	Azobenzene-CB[ <i>n</i> ] complexation . . . . .	16
1.3	Shape-controlled crystals . . . . .	19
1.4	Project aim and thesis overview . . . . .	23
<b>2</b>	<b>Complexation between CB[8] and methyl orange derivatives</b>	<b>26</b>
2.1	Introduction . . . . .	27
2.2	Structural characterisation of the 2MO@CB[8] complex . . . . .	29
2.2.1	Characterisation of the 2MO@CB[8] solution . . . . .	30
2.2.2	Characterisation of the 2MO@CB[8] crystal . . . . .	32
2.3	Host-guest chemistry between CB[8] and methyl orange derivatives . . . . .	35
2.4	Conclusions . . . . .	38
2.5	Experimental . . . . .	38
2.5.1	Theoretical calculation . . . . .	38
2.5.2	Materials and general methods . . . . .	39
2.5.3	Preparation and characterisation of the 2MO@CB[8] complex . . . . .	40
2.5.4	Characterisation of complexes between CB[8] and MO derivatives . . . . .	46

---

<b>3 Formation of shape-controlled crystals through rapid assembly of host-guest tectons</b>	<b>47</b>
3.1 Introduction . . . . .	48
3.2 Shape-controlled 2MO@CB[8] crystals . . . . .	51
3.2.1 Computational results . . . . .	51
3.2.2 Shape-controlled crystallisation mechanism . . . . .	52
3.2.3 Preparation of shape-controlled crystals . . . . .	53
3.3 Influencing factors of 2MO@CB[8] crystal growth . . . . .	55
3.3.1 Ionic strength effect . . . . .	56
3.3.2 pH effect . . . . .	57
3.3.3 Competitive guests effect . . . . .	58
3.4 Oriented organic crystals . . . . .	59
3.5 Conclusions . . . . .	60
3.6 Experimental . . . . .	60
3.6.1 Theoretical calculation . . . . .	60
3.6.2 Materials and general methods . . . . .	64
3.6.3 Preparation and characterisation of shape-controlled 2MO@CB[8] crystals . . . . .	65
3.6.4 Preparation and characterisation of oriented 2MO@CB[8] crystals . . . . .	65
<b>4 Conjugation of micelles and nanoparticles via CB[8] host-guest chemistry</b>	<b>68</b>
4.1 Introduction . . . . .	69
4.2 Azo-functionalised micelles . . . . .	72
4.3 Self-assembly of Azo-functionalised micelles and silica nanoparticles . . . . .	76
4.4 Applications of micelle-nanoparticle complexes . . . . .	79
4.5 Conclusions . . . . .	81
4.6 Experimental . . . . .	82
4.6.1 Materials and general methods . . . . .	82
4.6.2 Preparation and characterisation of Azo-functionalised micelles . . . . .	83
4.6.3 Preparation of micelle-nanoparticle complexes . . . . .	89

---

<b>5 Hybrid organic-inorganic supramolecular hydrogel reinforced with CePO<sub>4</sub> nanowires</b>	<b>93</b>
5.1 Introduction . . . . .	94
5.2 Design and preparation of nanowire-reinforced hydrogels . . . . .	98
5.3 Characterisation of nanowire-reinforced hydrogels . . . . .	102
5.4 Conclusions . . . . .	109
5.5 Experimental . . . . .	110
5.5.1 Materials and general methods . . . . .	110
5.5.2 General procedure for hydrogel preparation . . . . .	111
5.5.3 Hydrogel characterisation . . . . .	113
<b>6 Summary and outlook</b>	<b>115</b>
<b>Bibliography</b>	<b>119</b>

# List of Abbreviations and Common Units

- ACVA - 4,4'-azobis(4-cyanopentanoic acid)
- ADA - 1-adamantylamine
- AIBN - azodiisobutyronitrile
- APTES - (3-aminopropyl)triethoxysilane
- ATRP - atom transfer radical polymerisation
- Azo - azobenzene
- BFDH - Bravais-Friedel-Donnay-Harker
- CB[n] - cucurbit[n]uril
- CBC - CB[8] catenane
- CCDC - Cambridge crystallographic data centre
- CD - cyclodextrin
- CIE - crystallisation-induced effect
- CMC - critical micelle concentration
- COSY - correlation spectroscopy
- CTA - chain transfer agent
- DCM - dichloromethane
- DFT - density functional theory



- DLS - dynamic light scattering
- DI - deionised water
- DMAEMA - *N,N*-dimethylaminoethyl methacrylate
- DMF - dimethylformamide
- DMSO - dimethyl sulfoxide
- Dp - degree of polymerisation
- EDX - energy-dispersive X-ray spectroscopy
- FT-IR - fourier transform infrared spectroscopy
- GPC - gel permeation chromatography
- HEC - hydroxyethyl cellulose
- HEAA - *N*-hydroxyethyl acrylamide
- HEMA - 2-hydroxyethyl methacrylate
- HMBC - heteronuclear multiple bond correlation
- HMTETA - 1,1,4,7,10,10-hexamethyltriethylenetetramine
- HRC - hybrid raspberry-like colloid
- HSQC - heteronuclear single quantum coherence
- JCPDS - joint committed on powder diffraction standards
- LCST - lower critical solution temperature
- MC - sodium (E)-4-((4-(dimethylamino)phenyl)diazenyl)benzoate
- MD - (E)-4-((4-aminophenyl)diazenyl)-*N,N*-dimethylaniline
- ME - sodium (E)-4-((4-(diethylamino) phenyl)diazenyl)benzenesulfonate

- 
- MH - (E)-4-(phenyldiazenyl)aniline
  - MI - (E)-4-((4-nitrophenyl)diazenyl)aniline
  - MMA - methyl methacrylate
  - MN - sodium (E)-4-((4-aminophenyl)diazenyl)benzenesulfonate
  - MNC - micelle-nanoparticle complex
  - MO - methyl orange
  - MP - sodium (E)-4-((4-(phenylamino)phenyl)diazenyl)benzenesulfonate
  - MS - mass spectrometry
  - MV - methyl viologen
  - MVHex-NCO - 1-(2-(((6-isocyanatohexyl)carbonyl)oxy)ethyl)-1'-methyl-[4,4'-bipyridine]-1,1'-dium
  - MV-silane - 1-(4,4-diethoxy-9-oxo-3,10-dioxo-8-aza-4-siladodecan-12-yl)-1'-methyl-[4,4'-bipyridine]-1,1'-dium chloride
  - NMP - N-methyl-2-pyrrolidone
  - NMR - nuclear magnetic resonance
  - Np - 2-naphthol
  - NP - nanoparticle
  - NW - nanowire
  - PDI - polydispersity index
  - PDMAEMA - poly [2-(*N,N*-dimethyl amino) ethyl methacrylate]
  - PMDETA - *N,N,N',N'',N''*-pentamethyldiethylenetriamine
  - PMMA - poly(methyl methacrylate)

- PNIPAM - poly(*N*-isopropyl acrylamide)
- PS - polystyrene
- PVA - poly(vinyl alcohol)
- PVT - physical vapor transport
- QEq - charge equilibration
- RAFT - reversible addition fragmentation transfer
- SEC - size-exclusion chromatography
- SEM - scanning electron microscopy
- St - styrene
- TBACl - tetrabutylammonium chloride
- TDL - dibutyltin dilaurate
- TEM - transmission electron microscope
- TEOS - tetraethyl orthosilicate
- TGA - thermal gravimetric analysis
- THF - tetrahydrofuran
- vdW - van der Waals
- XRD - X-ray diffraction

# Declaration

This report is submitted in the fulfilment for the PhD Study in Chemistry. Except where indicated to the contrary, either directly or by reference, the work described in this dissertation is solely the work of the author. This work by no means surpasses the word limit of 60000.

Signed,

Chenyan Liu,  
University of Cambridge

# Acknowledgements

First of all, I would like to thank my supervisor, Professor Oren A. Scherman, for giving me the opportunity to work with so many brilliant researchers in one of the world's best universities, and for his extensive guidance during my PhD study. I still remember four years ago, I first met Oren in Beijing. We did a unique interview in the Forbidden City, after which I got the chance to study in Cambridge. I believe this would be one of the best memories in my life.

Next, I would like to acknowledge my colleagues in the Melville Laboratory during the past four years in Cambridge. I want to thank Dr. Ji Liu, who is the first person I have met in the Scherman's group. He trained me how to do research with a good habit, from making records on laboratory notebooks to carrying out experiments and characterisations. Secondly, Yuchao Wu, now Dr. Wu, is one of my best colleagues and friends in the lab. As a senior, he helped me a lot in/outside the lab. I really enjoy the brainstorming we made in front of our fume cupboards. We felt really proud of making these ideas to real projects. Also, he is always the first person to proof-read my manuscripts. He gave me many helpful suggestions about my research and future plan. Now he has become a scientist in BASF. Wish him all the best in his future career. Next, Dr. Guolei Xiang, who is the co-author of my first publication. He is a very hard working person, and now has started his own research group in China. Hope one day in the future, his dream of publishing a 'Science' paper will come true. Fourth, Hongbin Liu, is a PhD candidate majoring in computational chemistry in the University of Washington. We did our undergraduate together in Fudan University in Shanghai. I am really grateful of having the opportunity to continue work with him during my PhD. Fifth, I want to thank Xiaohe for the research we have done and the great trip we had in Morocco. Hope

you get well soon from the injured leg. Then I want to thank Dr. Guanglu Wu for teaching me how to use Latex, Yang (now Dr. Lan) for treating me my first meal in Cambridge, Chi (now Dr. Hu) for letting me familiar with Illustrator, Chris for encouraging me to do my first poster presentation, Dr. Kamil for my first time of ‘working at midnight’ in the lab, Dr. David for the help on peptide synthesis, Dr. Vijay, Dr. Stefan and Dr. Steven for proof-reading my manuscripts.

Next, I want to thank the supporting staffs in the Melville Lab, especially for our lab manager Dr. Elisabetta. I was really touched for the food she treated me when I was in an extremely hard financial situation. Also, I want to say thanks to the three secretaries (Glenda, Ishita and Alex) and two lab technicians (Athen and Matt) for their efforts to make us work in a safe and productive lab. Additionally, I really appreciate the two examiners of my CPGS viva, Prof. Stuart Clarke and Dr. Silvia Vignolini, for providing me the opportunity to continue my study after the first year assessment.

Finally, I would like to thank my parents as always, for their unlimited understanding and support far away from China. Thank you for taking care of me when I was seriously sick in the hospital. Wish you all good health and good fortune. Thanks for the financial support from China Scholarship Council, the Cambridge Commonwealth, European and International Trust and Jesus College (Cambridge).

# List of Publications

## Publications

Liu, C.<sup>‡</sup>; Ren, X.<sup>‡</sup>; Wu, Y.; Scherman, O. A. 'A novel surfactant recycling system based on cucurbit[8]uril-mediated host-guest chemistry'. (submitted)

Liu, C.<sup>‡</sup>; Liu, H.; Wu, Y.; Wu, G.; Horton, P. N.; Xiang, G.; Matak-Vinkovic, D.; Li, X.; Scherman, O. A. 'Formation of shape-controlled crystals through rapid assembly of host-guest tectons'. (submitted)

Wu, Y.<sup>‡</sup>; Shah, D. U.<sup>‡</sup>; Liu, C.; Yu, Z.; Liu, J.; Ren, X.; Rowland, M. J.; Abell, C.; Ramage, M. H.; Scherman, O. A. 'Bioinspired supramolecular fibers drawn from a multi-phase self-assembled hydrogel', *Proc. Natl. Acad. Sci. U. S. A.* **2017**, *114*, 8163–8168.

Liu, C.<sup>‡</sup>; Xiang, G.<sup>‡</sup>; Wu, Y.; Barrow, S. J.; Rowland, M. J.; Clarke, D. E.; Wu, G.; Scherman, O. A. 'Hybrid organic–inorganic supramolecular hydrogel reinforced with CePO<sub>4</sub> nanowires', *Polym. Chem.* **2016**, *7*, 6485–6489.

# Chapter 1

## Introduction

### 1.1 Recent progress in cucurbit[*n*]uril host-guest chemistry

Traditional chemistry is based on covalent bonds between atoms, which leads to the formation of molecules, while supramolecular chemistry focuses on weaker and reversible (non-covalent) interactions between molecules, such as van der Waals forces, hydrogen bonding,  $\pi$ - $\pi$  interactions, hydrophobic forces and metal coordinations.<sup>1</sup> Based on the lock-and-key principle (Emil Fischer, 1873)<sup>2</sup> and hydrogen bonding theory (Linus Pauling, 1939),<sup>3</sup> Lehn (Nobel laureate in 1987) defined supramolecular chemistry as 'chemistry beyond the molecule',<sup>1</sup> which has since made remarkable contributions in the fields of materials science,<sup>4-7</sup> medical chemistry<sup>8,8,9</sup> and catalysis.<sup>1,10</sup>

Macrocyclic host-guest chemistry is a typical form of molecular self-assembly, where the guest molecules and macrocyclic hosts bind selectively through various supramolecular interactions. The macrocycles are able to form inclusion complexes where the guests are encapsulated within the cavity of the macrocyclic host on account of either energy favourable environments or a specific shape compatibility. Over the past several decades, a wide variety of macrocycles have been synthesised, including cucurbit[*n*]urils,<sup>11</sup> cyclodextrins<sup>12</sup> and calixarenes,<sup>13</sup> which have been and are being broadly studied in materials science.<sup>12</sup>

In 1905, the most prominent member of the cucurbit[*n*]uril family, cucurbit[6]uril was successfully synthesised by Behrend.<sup>14</sup> However, although the host-guest chemistry of



other macrocycles (such as cyclodextrin) developed steadily over the past century, only a small number of reports of CB[ $n$ ] supramolecular chemistry were published prior to the new millennium, where the CB[ $n$ ] family began to increase dramatically, owing to the discovery of CB[5], CB[7], CB[8] and CB[5]@CB[10].<sup>15,16</sup> Among CB[ $n$ ] homologues, CB[8] has attracted much attention on account of its capability to simultaneously encapsulate two guests. A wide variety of functional materials have been developed based on CB[8] host-guest chemistry, such as hydrogels,<sup>17,18</sup> polymeric networks,<sup>19,20</sup> microcapsules<sup>21,22</sup> and colloids.<sup>23,24</sup> Therefore, CB[8] can be employed as a supramolecular ‘hand-cuff’ to coordinate different components together, building complicated architectures.

### 1.1.1 CB[ $n$ ] host-guest complexation

A class of macrocyclic host molecules made by glycoluril monomers are named as cucurbit[ $n$ ]uril (CB[ $n$ ]) (Figure 1.1) due to their shape resemblance of pumpkins, where  $n$  represents the number of glycoluril units in the host molecule. Cucurbit[6]uril (CB[6]) was first synthesised in 1905 by Behrend through the condensation of glycoluril.<sup>14</sup> However, its structure has not been completely investigated until 1981, when Mock and co-workers reported that CB[6] was composed of 6 glycolurils and 12 methylene bridges.<sup>25</sup> CB[5], CB[7] and CB[8] were discovered and isolated by Kim and Day in 2000.<sup>15,16</sup> Then a new homologue, CB[10], was isolated by Isaacs after five years.<sup>11</sup> The structural dimension of CB[ $n$ ], including portal diameter, outer cavity diameter, height of torus and volume of cavity have already been investigated and shown in Figure 1.2 and Table 1.1.<sup>26,27</sup>

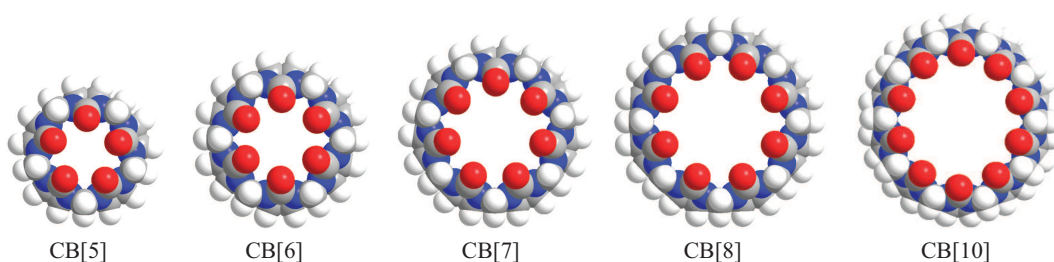


Figure 1.1: Molecular structure of CB[ $n$ ] homologues CB[5]-CB[8].<sup>11</sup>

All CB[ $n$ ] homologues have the common depth of 9.1 Å, as the height of the single glycoluril is fixed. From CB[5] to CB[10], the increases of portal size (from 2.4 to 11.0 Å)

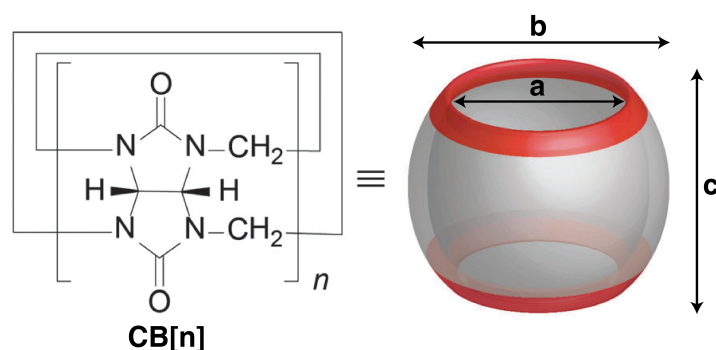


Figure 1.2: Chemical framework (left) and dimensional structure (right) of CB[n].<sup>27</sup>

Table 1.1: Dimensions and solubility of CB[n] homologues.<sup>26</sup>

CB[n]	a [Å]	b [Å]	c [Å]	V [Å <sup>3</sup> ]	S <sub>H<sub>2</sub>O</sub> [mM]	pK <sub>a</sub>
CB[5]	2.4	4.4	9.1	82	20-30	-
CB[6]	3.9	5.8	9.1	164	0.018	3.02
CB[7]	5.4	7.3	9.1	279	20-30	-
CB[8]	6.9	8.8	9.1	479	<0.01	-
CB[10]	9.0-11.0	10.7-12.6	9.1	870	-	-

a: portal diameter; b: outer cavity diameter;  
c: height of torus; V: volume of cavity; S<sub>H<sub>2</sub>O</sub>: solubility in water.

and cavity diameter (from 4.4 to 12.6 Å) lead to a cavity volume expansion from 82 to 870 Å<sup>3</sup>, resulting in the discernible host-guest features of different CB[n] homologues. Interestingly, the water solubility of CB[n] displays an odd–even pattern (Table 1.1), presumably on account of the stronger intermolecular interactions in the solid state of CB[6] and CB[8] than CB[5] and CB[7].<sup>28</sup> Therefore, CB[5] and CB[7] have relatively high solubility in water (20-30 mM), whereas CB[6] and CB[8] show much lower solubility of less than 0.02 mM.<sup>26</sup> In addition, as CB[n]s are insoluble (less than 10<sup>-5</sup> M) in organic solvents, most investigations of CB[n] complexes in the literature to date are carried out in the aqueous media.

The host-guest binding principle of CB[n] has already been extensively studied.<sup>29-31</sup> As shown in Figure 1.3, the ion-dipole and hydrophobic interactions are the two major driving forces for the binding activity of CB[n] host-guest chemistry. More recently, a ‘high-energy water’ theory has been proposed to explain the favourable binding event from an energy perspective.<sup>27,32-34</sup> Water molecules inside the CB[n] cavity are of high

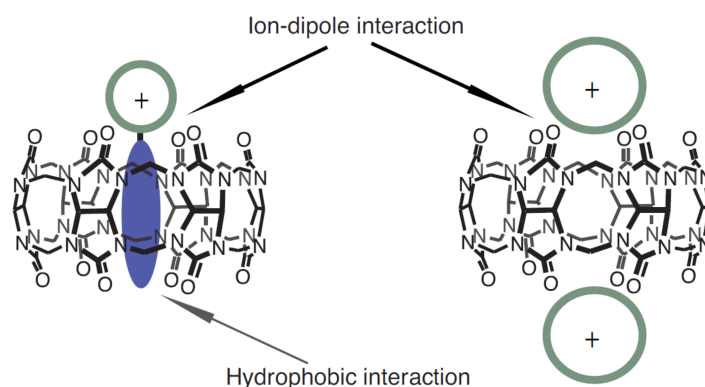


Figure 1.3: Two major types of supramolecular interactions between CB[ $n$ ] and guest molecules.<sup>29,30</sup>

energy due to their greatly limited hydrogen bonding. As shown in Figure 1.4, in the event of a guest molecule entering CB[ $n$ ] cavity, high-energy water molecules are liberated from the cavity. As a result, reconstruction of the natural hydrogen bonding network around formerly trapped water molecules occurs. This release exhibits a negative enthalpy and simultaneously increases the entropy of the system, promoting its overall stability.

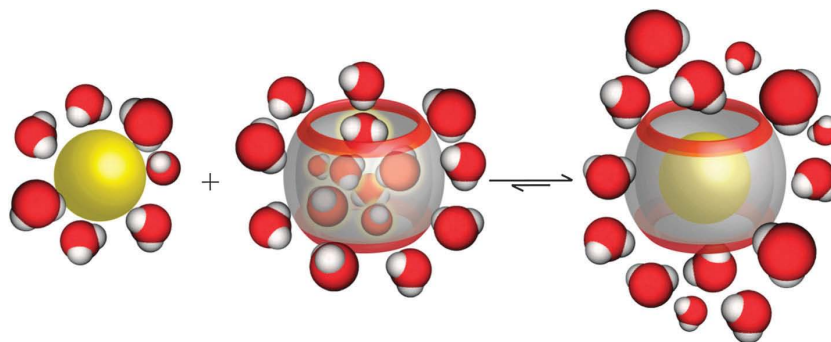


Figure 1.4: Schematic illustration of the release of high-energy water molecules from the CB[7] cavity upon binding of a hydrophobic guest.<sup>27</sup>

As mentioned above, CB[ $n$ ] has guest selectivity that varies with the cavity size.<sup>27,28,35</sup> Smaller homologues of the cucurbit[ $n$ ]uril family (CB[5], CB[6] and CB[7]) are able to bind with single guests. As the smallest analogue in CB[ $n$ ] family, CB[5] only binds with small guests such as protons, gas molecules (Ar, Kr, Xe, N<sub>2</sub>, O<sub>2</sub>, CO, CO<sub>2</sub>) and solvent molecules.<sup>28,36</sup> CB[6], with a larger cavity volume, is able to bind with aliphatic compounds.<sup>37,38</sup> CB[7] is capable to encapsulate a range of positively charged guests, such as

bicyclooctane and adamantane amine.<sup>39,40</sup> Particularly, CB[8], with a further increase in cavity volume, is able to accommodate two guests simultaneously.<sup>41</sup> CB[8] can first complex with an electron-deficient guest such as a viologen derivative (MV) and then with an electron-rich second guest such as a naphthalene derivative (Np), forming a stable 1:1:1 heteroternary complex (Figure 1.5a). However, the formation of this complex is reversible. For example, if a competitive guest like 1-adamantane amine (ADA) is introduced, CB[8] would prefer to bind with ADA and therefore dissociate from the first and second guest (Figure 1.5b).

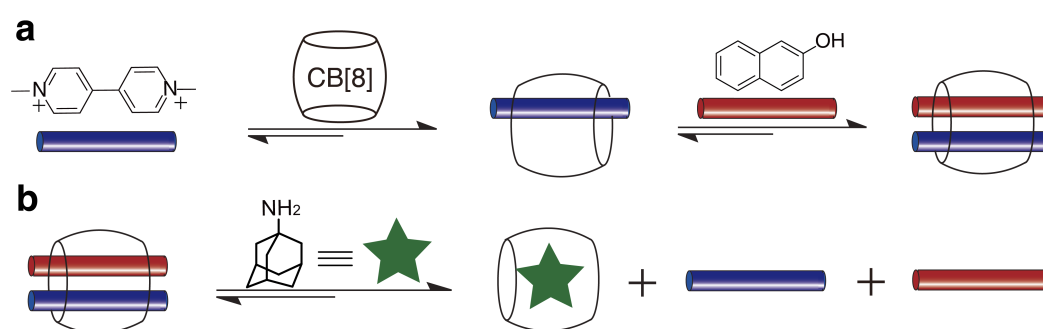


Figure 1.5: Schematic illustration of **a**, CB[8] binding with MV and Np, **b**, Disassembly of the ternary complex by addition of adamantane amine.<sup>42</sup>

### 1.1.2 CB[*n*]-based crystals

Between 2000 and 2002, a variety of crystalline structures of cucurbituril macrocycles (CB[5], CB[7], CB[8] and CB[10]) were characterised by Kim<sup>16</sup> and Day.<sup>43–45</sup> Most CB[*n*]-based crystals are prepared through cooling crystallisation or evaporative crystallisation.<sup>46,47</sup> Recently, a variety of functionalised CB[*n*] macrocycles have been studied by X-ray diffraction.<sup>48,49</sup> For instance, crystals of monohydroxy-CB[5], CB[6] and CB[8] have been reported by Ouari and co-workers.<sup>49</sup>

CB[*n*] crystals provide various applications owing to their unique 3D crystalline structures. As shown in Figure 1.6, Kim and co-workers have reported a honeycomb-like CB[6] crystalline structure with 1D channels, exhibiting remarkable acetylene sorption properties with permanent porosity and high thermal stability.<sup>50</sup> Two years later, the remarkable selectivity of CO<sub>2</sub> (over CO)<sup>36</sup> and highly anisotropic proton conductivity of

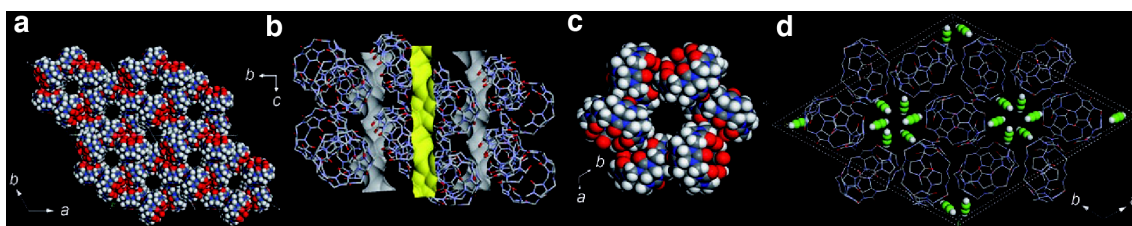


Figure 1.6: **a**, X-ray crystal structure of CB[6], view down the  $c$  axis. **b**, 1D channels in CB[6] with accessible pores emphasised in yellow. **c**, An aperture of the 1D channel formed by a hexagonal arrangement of CB[6]. **d**, X-ray crystal structure showing acetylene molecules adsorbed in the channels.<sup>50</sup>

this interesting crystalline construct has been further studied.<sup>51</sup> More importantly, the investigation of the crystals of CB[ $n$ ] complexes is of great significance in understanding the binding nature and helpful in the rational design of new structures. Therefore, several examples are discussed in this section.

### Crystals of CB[6]-based complexes

In 1984, the first X-ray diffraction crystalline structure of CB[ $n$ ] host-guest complex was reported by Freeman, where a *p*-xylylenediammonium ion was encapsulated in CB[6] (Figure 1.7a).<sup>52</sup> Further investigations by Mock *et al.* have demonstrated that CB[6] host-guest self-assemblies exhibit chain length-dependent selectivity towards alkane diammonium salts.<sup>53,54</sup> As shown in Figure 1.7b and 1.7c, CB[6] binding is significantly stronger to the diammonium ion guests with 5 and 6 methylene groups. This is a result of their optimal cavity filling and maximum ion-dipole interactions. Additionally, in contrast to the traditional understanding of CB[6] binding, crystallographic studies suggest that CB[6] is also capable to form 1:2 host-guest complexes with specific guest molecules.<sup>55,56</sup>

### Crystals of CB[7]-based complexes

CB[7] is capable of binding to a much wider range of guests, such as adamantanes,<sup>57</sup> ferrocenes<sup>39,58,59</sup> and diamantanes,<sup>40,60</sup> forming 1:1 binary complexes. The crystalline constructs of CB[7] complexes are utilised to identify the structural features and design ultratight host-guest binding. As an example, based on the crystals of diamantane diammonium ion@CB[7] complexes, Isaacs *et al.*<sup>40</sup> have reported the strongest guest@CB[7]

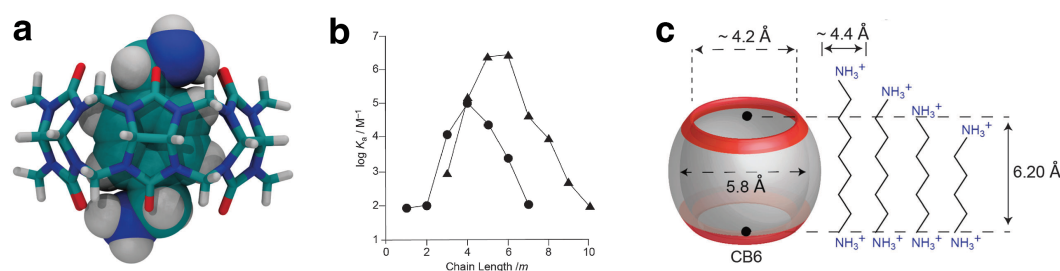


Figure 1.7: **a**, X-ray crystal structure of the p-xylylenediammonium ion encapsulated by CB[6].<sup>52</sup> **b**, Relationship between the binding constant ( $\log K_a$ ) versus chain length  $m$  for  $\text{H}(\text{CH}_2)_m\text{NH}_3^+$  (circle) and  $^+\text{H}_3\text{N}(\text{CH}_2)_m\text{NH}_3^+$  (triangle). **c**, Dimensional comparison between CB[6] and various alkane diammonium ions.<sup>27</sup>

complexation to date, with  $K_a = 7.2 \times 10^{17} \text{ M}^{-1}$  in  $\text{D}_2\text{O}$ . The X-ray crystal structure suggests that the extremely high binding affinity is arising from the van der Waals surface complementarity and the optimal ion-dipole interactions (Figure 1.8).

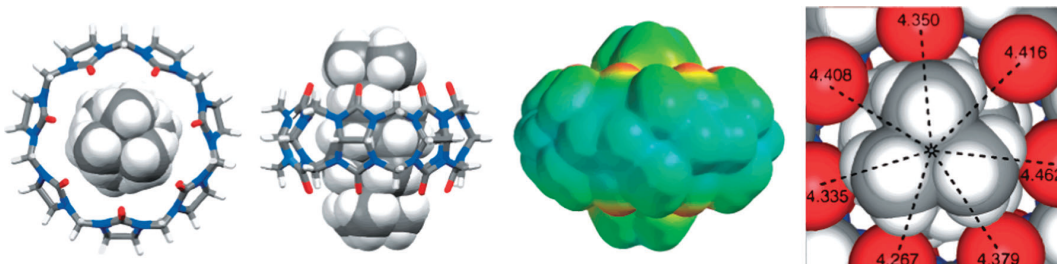


Figure 1.8: Representations of the X-ray crystal structure of the diamantane diammonium@CB[7] complex.<sup>40</sup>

### Crystals of CB[8]-based complexes

A variety of guests@CB[8] ternary complex-based crystals have been studied, such as dicationic,<sup>61</sup> *N*-phenylpiperazine<sup>62</sup> and palladium(II) complexes.<sup>63</sup> The study of these crystals contributes to the discovery of increasingly more fascinating features of CB[8] chemistry among the CB[ $n$ ] family. For instance, while investigating a series of diamantane derivative@CB[8] complex crystals, Isaacs and co-workers have reported that CB[8] was promising to prepare the tightest host-guest complex in CB[ $n$ ] family, with a femtomolar binding affinity.<sup>64</sup> Moreover, CB[8] has been reported for a selective recognition towards aromatic peptides (e.g. Phe-Gly-Gly, Figure 1.9a) by Urbach *et al.*<sup>47</sup> As shown in Figure 1.9b, the crystallographic data suggests that in comparison to most peptides which

formed 1:1 complexes with CB[8], Phe-Gly-Gly is able to bind in a 2:1 stoichiometry. This is on account of the electrostatic interactions between N-terminal ammonium groups from the peptide and the carbonyl oxygens of CB[8] portals (Figure 1.9c). This provides a new approach for peptide separation and has built various dynamic peptide-based constructs through CB[8] host-guest chemistry. However, unfortunately, the time required for crystallisation of CB[8] complexes (typically on the order of months) has limited their further applications.

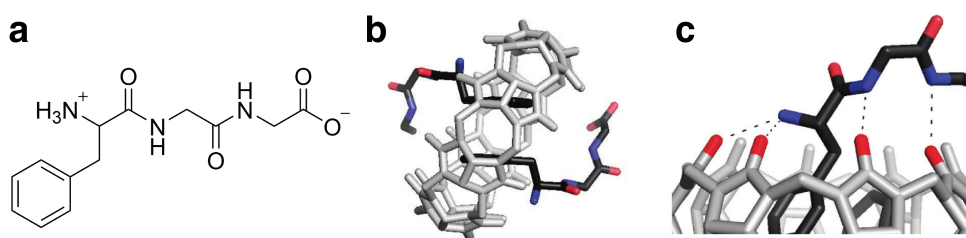


Figure 1.9: The crystal structure of 2(Phe-Gly-Gly)@CB[8]. Hydrogens and solvating water were removed for clarity. **a**, Chemical structure of Phe-Gly-Gly. **b**, Cross-eyed stereoview of the crystalline structure. **c**, The dashed lines indicate key electrostatic interactions.<sup>47</sup>

### Crystals of CB[10]-based complexes

After the first report of CB[5]@CB[10] inclusion complex in 2002 by Day *et al.*,<sup>44</sup> the crystalline structures of various CB[10]-based complexes have been investigated by Isaacs and co-workers,<sup>65–67</sup> leading to a better understanding of CB[10] binding activity. For example, a nor-seco-CB[10] has been isolated by Huang *et al.*, which contains two identical macrocyclic cavities.<sup>68</sup> Its unusual binding profile has been proved through X-ray diffraction, suggesting an unexpected binding affinity towards larger guests. Based on this structural analysis, a homo-ternary complex between nor-seco-CB[10] and viologen guests has been prepared and developed into polymeric nanoparticles, which exhibit metastable properties.<sup>69</sup>

### Other CB[*n*]-based crystals

Utilising the crystallographic studies of CB[*n*] complexes, the packing coefficient (volume of the guest/volume of the host cavity) can be calculated.<sup>30</sup> Rebek has proposed that 55%

is the optimum packing coefficient for CB[n] complexes, and are generally associated with the highest binding affinity.<sup>70</sup> Furthermore, CB[n] macrocycles can also be utilised as building blocks for the assembly of more complicated architectures, including supramolecular crystals<sup>71</sup> and CB[n]-metal frameworks.<sup>72-74</sup>

### 1.1.3 Supramolecular ‘hand-cuff’ based on CB[8]

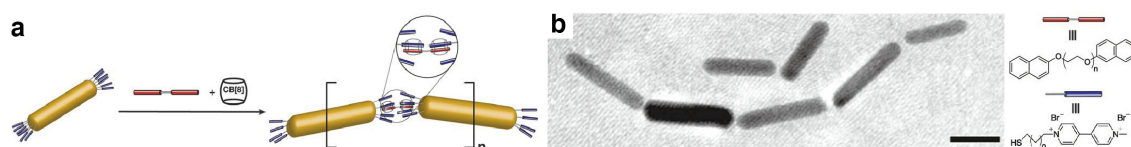


Figure 1.10: **a**, Schematic representation of supramolecular alignment of gold nanorods. **b**, TEM images depicting the alignment of gold nanorods (scale bar: 25 nm).<sup>75</sup>

The fascinating 1:2 binding feature of CB[8] can be exploited as a supramolecular ‘hand-cuff’ to link two synthetically well-designed units together. This provides an outstanding platform for the fabrication of a wide variety of supramolecular materials, such as supramolecular polymers and the related assemblies (hydrogels, micelles, vesicles),<sup>17-21</sup> stimuli-responsive systems (pH, redox and photo responsiveness),<sup>23,76,77</sup> mechanically interlocked molecular systems (rotaxane, catenanes)<sup>24,77,78</sup> and surface-based host-guest assemblies.<sup>75,77,78</sup> For instance, a supramolecular alignment of gold nanorods is shown in Figure 1.10, where CB[8] acts as a ‘hand-cuff’ to link nanorods together *via* host-guest interactions.

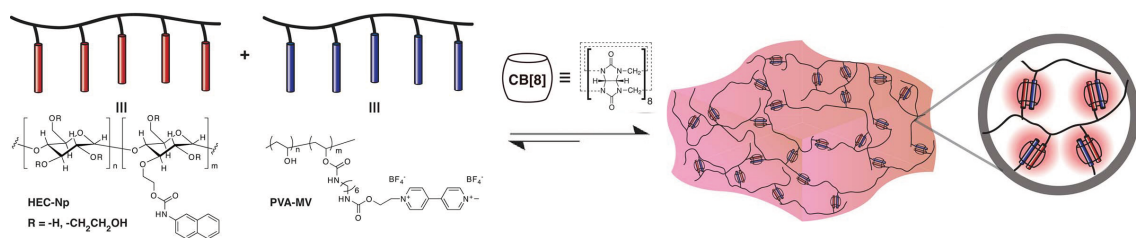


Figure 1.11: Schematic representation of a supramolecular hydrogel prepared through addition of CB[8] to a mixture of multivalent first- and second-guest-functionalised polymers in water.<sup>79</sup>

A wide variety of polymeric materials have been prepared through taking advant-



age of the CB[8] 'hand-cuff'. The first CB[8]-based supramolecular hydrogel has been prepared by Appel *et al.*, where CB[8] is employed to induce the crosslinking formation between a guest-functionalised hydroxyethyl cellulose and a poly(vinyl alcohol) polymer (Figure 1.11). Based on this discovery, a wide variety of hydrogels have been prepared by the Scherman group, including light-tunable networks,<sup>80</sup> hybrid nanocomposites<sup>81</sup> and cargo-loading systems.<sup>82</sup> In addition, through the incorporation of covalent interactions with CB[8] host-guest chemistry, a range of composite supramolecular networks have been prepared, exhibiting attractive properties, such as extreme stretchability, toughness and self-recovery.<sup>19,20,83</sup>

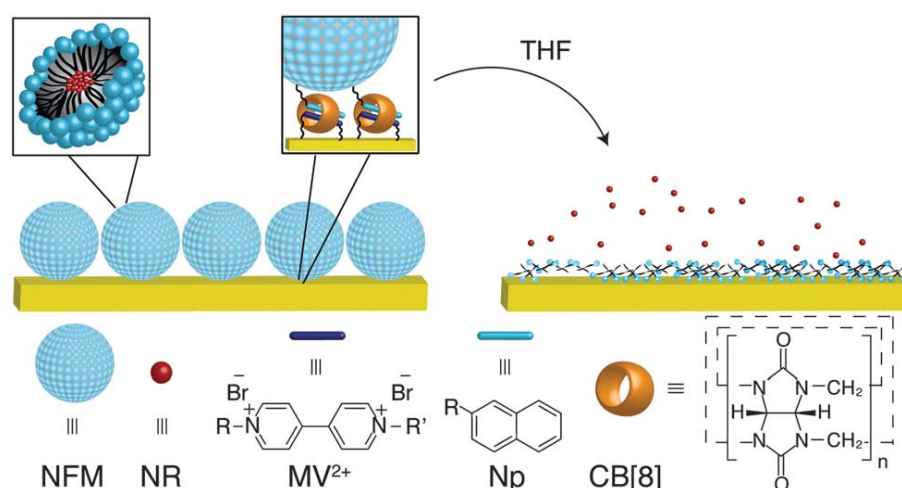


Figure 1.12: Schematic illustration of the surface immobilisation of naphthol-functionalised micelles *via* CB[8]-rotaxanes and the solvent-induced burst release of the loaded guest molecules.<sup>78</sup>

Furthermore, CB[8] has great potential in the fabrication of cargo delivery systems. For example, through conjugating the first guest-functionalised hydrophobic segment and the second guest-functionalised hydrophilic part together *via* host-guest interactions, amphiphilic block co-polymers can be prepared. The supramolecular polymer is assembled to produce functional micelles<sup>84</sup> and vesicles,<sup>85,86</sup> displaying outstanding responsive drug-release properties on account of the dynamic nature of CB[8] 'hand-cuff'. Another example has been reported by Hu *et al.*, a naphthol-functionalised micelle is prepared and subsequently immobilised onto MV@CB[8]-functionalised Au substrate *via* CB[8] host-guest complexation in the aqueous phase.<sup>78</sup> As shown in Figure 1.12, the

drugs encapsulated inside the micelle can be fully released upon the stimuli of organic solvents. Additionally, using a microfluidic set-up, well-defined, monodispersed microcapsules have been prepared by Scherman and co-workers.<sup>21</sup> These microcapsules are capable of orthogonally storing both hydrophilic and hydrophobic cargoes, possessing great potential in drug delivery and magnetic materials.

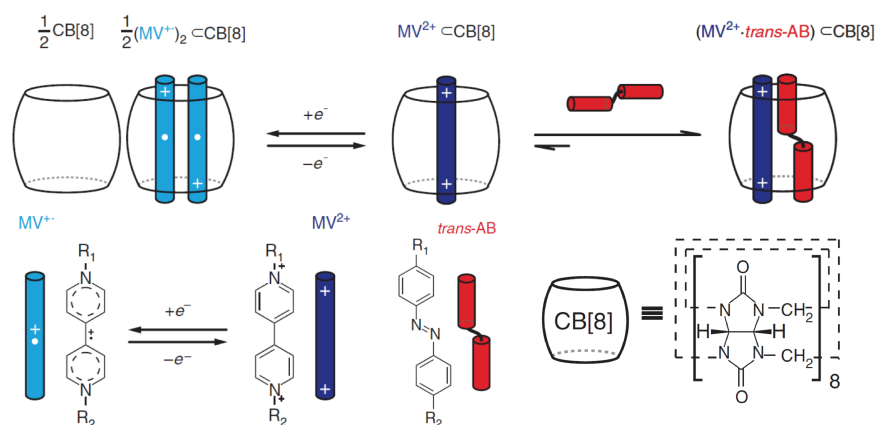


Figure 1.13: Stepwise formation of CB[8]-mediated heteroternary complex (first guest:  $\text{MV}^{2+}$ , second guest: azobenzene derivative) and one-electron reduction of  $\text{MV}^{2+} @ \text{CB}[8]$ .<sup>76</sup>

More importantly, owing to the versatile responsive properties of the guest molecules, a range of  $\text{CB}[n]$ -based stimuli-responsive systems have been developed. As shown in Figure 1.13, the transition from  $\text{MV}^{2+}$  to  $\text{MV}^+$  drives the formation of  $2\text{MV}^+ @ \text{CB}[8]$  homoternary complexes, while the electron-rich second guest is released from the  $\text{CB}[8]$  cavity.<sup>76</sup> In order to avoid the formation of  $2\text{MV}^+ @ \text{CB}[8]$  complexes, an interlocked surface-immobilised rotaxane with redox-responsive behaviours has been prepared by Hu *et al.* (Figure 1.14),<sup>77</sup> which had been further developed to a controlled release system (Figure 1.12).<sup>78</sup>

Inspired by the surface-immobilised rotaxane system, surface-bound  $\text{CB}[8]$  catenanes have been prepared by Scherman and co-workers, where  $\text{MV} @ \text{CB}[8]$  are immobilised onto magnetic silica NPs (Figure 1.15a, 1.15b).<sup>24</sup> As shown in Figure 1.15c, the  $\text{CB}[8]$  catenane structure are employed as a nanoscale molecular receptor to capture and release certain aromatic molecules on account of the redox-responsive behaviours of  $\text{MV}$ . Moreover, through utilising its molecular recognition property towards aromatic pep-

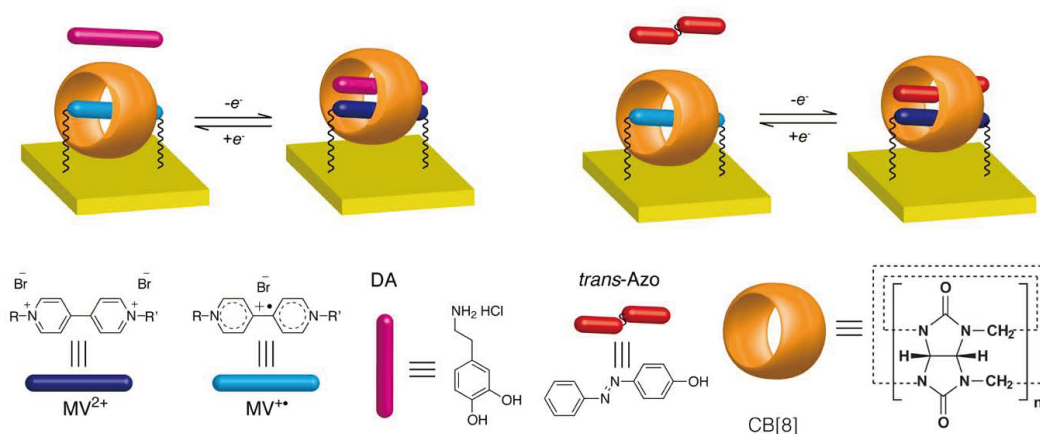


Figure 1.14: Redox-controlled ternary complexations of  $MV^{2+}/DA@CB[8]$  and  $MV^{2+}/Azo@CB[8]$  on the Au surface.<sup>77</sup>

tides, the CB[8] catenane-functionalised  $SiO_2$  NP has been developed to a nano-platform for peptide separation.

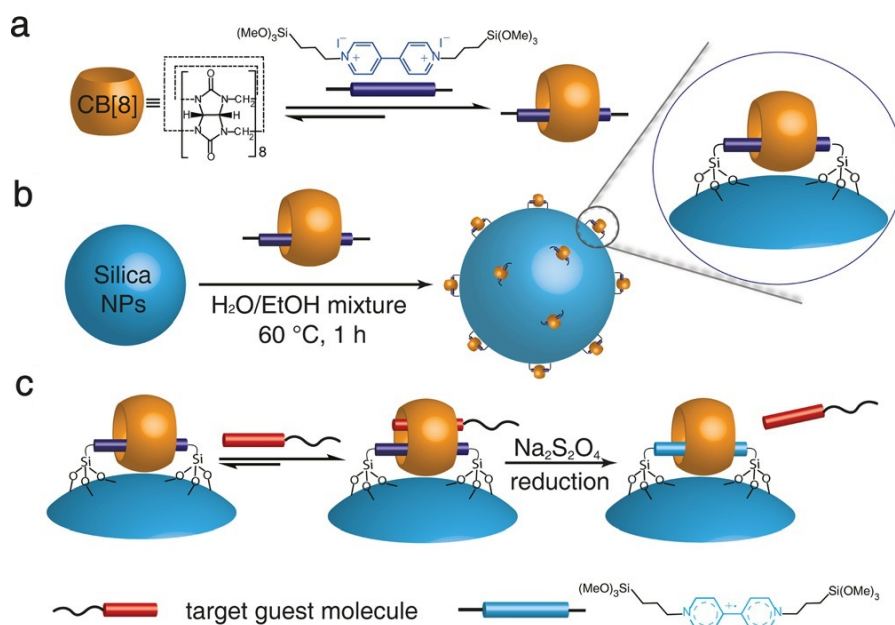


Figure 1.15: **a**, Complexation between CB[8] and MV-silane. **b**, Surface-bound CB[8] catenanes on silica NPs (CBC-NPs) obtained by immobilising MV-silane@CB[8] inclusion complexes onto silica NPs. **c**, Capture and release of a target guest by CBC-NPs.<sup>24</sup>

## 1.2 Azobenzene in host-guest chemistry

Azobenzenes (Azo) are a class of diazene (HN=NH) derivatives with both hydrogens being replaced by phenyl groups. The  $sp^2$  hybridised nitrogen atoms can exist in either the *trans* (also denoted as E state) or *cis* (the Z state) conformation (Figure 1.16a). Azo compounds were discovered as important synthetic colouring agents in the mid 1800s, and have since been widely utilised in the dye industry.<sup>87</sup> In 1937, *cis*-Azo was discovered and isolated through a solvent extraction method by Hartley, where the *trans* isomer was found to be capable of partly converting into *cis*-Azo when exposed to light.<sup>88</sup> The optical properties of the Azo chromophore have now been studied for over 80 years.

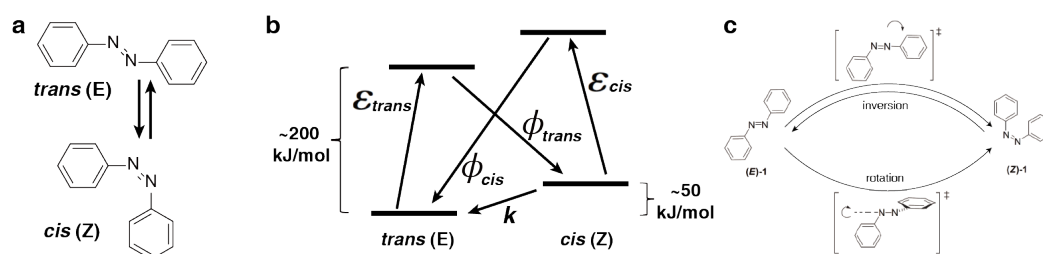


Figure 1.16: **a**, Chemical structures of *trans* and *cis* isomers of azobenzene. **b**, Simplified state model for azobenzene chromophores. The extinction coefficients are denoted  $\epsilon$ , whereas the quantum yields for the photo-isomerisations are labelled  $\phi$ . The rate of thermal relaxation is denoted by  $k$ . Competition between these pathways determines the composition of the photo-stationary state. **c**, Isomerisation pathways from E- to Z-azobenzene and vice versa.<sup>87,89–91</sup>

As shown in Figure 1.16b, the *trans* isomer is approximately 50 kJ/mol more stable than its *cis* counterpart. Hence, the *trans*-Azo is dominant (>99.99 %) in dark environments at equilibrium.<sup>92,93</sup> The *trans* to *cis* isomerisation of Azo occurs upon external stimuli, such as UV irradiation,<sup>88,94</sup> electrostatic stimulation<sup>95,96</sup> and mechanical stress.<sup>97</sup> For example, the absorption of a photon (340 nm irradiation) will result in the movement of aromatic rings, leading to an efficient *trans* to *cis* conversion. The timescale of this photo-isomerisation process is on the order of picoseconds.<sup>98,99</sup> Furthermore, a back-isomerisation (*cis* to *trans*) can be achieved when the *cis* isomer is elicited upon visible light irradiation at 450 nm. As shown in Figure 1.16c, two pathways of the isomerisation mechanism have been proposed.<sup>90,91</sup> The photo-isomerisation step from *trans* to *cis*

is carried out through a rotational or an inversion pathway, while the *cis* to *trans* isomerisation occurs *via* an inversion pathway only. However, since the isomerisation process is affected by various factors, such as the irradiation wavelength,<sup>100,101</sup> substituents<sup>94</sup> and solvent properties,<sup>100,102,103</sup> it cannot be satisfactorily explained by a single mechanism, even for the unsubstituted Azo.<sup>104</sup>

Azo can be synthesised through three typical strategies: the creation of the Azo bond by (i) the coupling of two aromatic compounds;<sup>91</sup> and (ii) the reduction of azoxybenzene compounds<sup>105,106</sup> or (iii) the oxidation of hydrazo derivatives.<sup>107,108</sup> On account of the cleanness of the photoreaction without generating side-products,<sup>89</sup> Azo has been exploited to produce a class of functional materials, such as protein probes,<sup>109,110</sup> surface modified materials,<sup>111,112</sup> molecular machines<sup>113,114</sup> and polymeric materials.<sup>115,116</sup> In addition, Azo derivatives have been employed as chromophores in industrial dyes<sup>117</sup> and pH<sup>118</sup>/metal ion indicators.<sup>119</sup>

### 1.2.1 Photo-responsive host-guest complexes

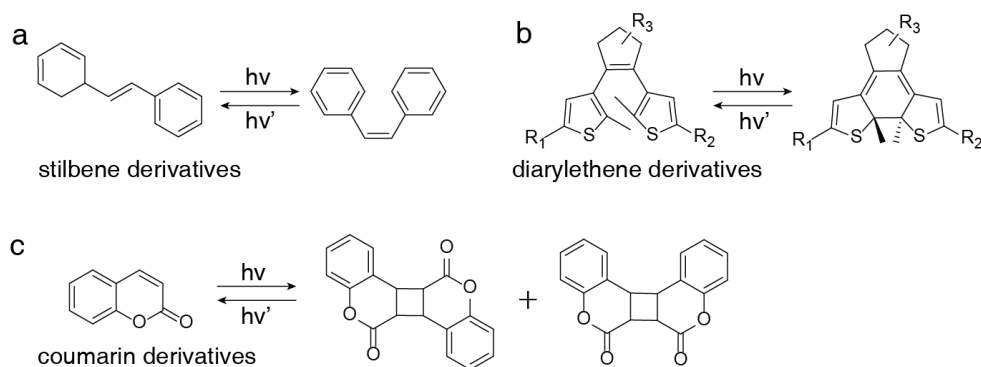


Figure 1.17: The photo-responsive behaviours of **a**, stilbene derivatives; **b**, diarylethene derivatives and **c**, coumarin derivatives.<sup>90,91</sup>

Stimuli-responsive host-guest complexes have attracted a tremendous interest in supramolecular chemistry. The special feature of those complexes includes the encapsulation and release of a guest in a controllable manner upon the stimuli by chemical reagents, light and redox potential changes.<sup>120</sup> Light is an outstanding control element on account of several advantages: (i) it exhibits good cleanness with high efficiency; (ii) it can be eas-

ily switched on and off with precise irradiated wavelengths, intensities and time; (iii) the light-induced transition can happen in a confined space.

Three examples of the commonly used photoswitchers are shown in Figure 1.17: (a) molecules that switch between *trans* and *cis* isomers (such as Azo, fumaramide and stilbene derivatives, Figure 1.17a); (b) molecules with interconverting properties between closed and open rings (such as diarylethene and spiropyran derivatives, Figure 1.17b); (c) molecules with reversible dimerisation properties (such as coumarin and anthracene derivatives, Figure 1.17c).<sup>120</sup>

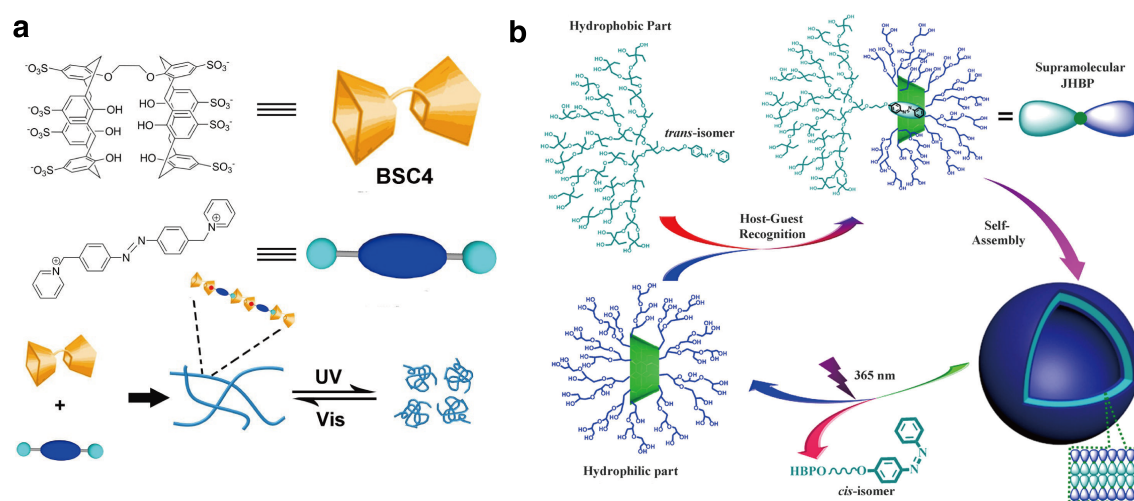


Figure 1.18: **a**, A light-responsive bis(p-sulfonatocalix[4]arene)-based supramolecular polymer.<sup>121</sup> **b**, Preparation, self-assembly and disassembly of the supramolecular Janus hyperbranched polymer (JHBP).<sup>122</sup>

The combination of photo-responsiveness and host-guest chemistry has given birth to a wide range of interesting light-responsive systems, such as supramolecular polymers, vesicles and nano-materials.<sup>121,123,124</sup> Since the binding affinity between *trans*-Azo and macrocyclic hosts is generally much higher than its *cis* counterpart, the *trans* to *cis* transition would likely induce disassembly of the host-guest complex. For example, by using the host-guest recognition between bis(p-sulfonatocalix[4]arene) (BSC4) and Azo, Liu and co-workers have reported a linear supramolecular polymer with light-induced morphology transformations.<sup>121</sup> As shown in Figure 1.18a, upon UV irradiation, the supramolecular polymer transforms from linear chains to spherical nanoparticles, while the reversible *cis* to *trans* isomerisation can be achieved under the irradiation of visible light.

Then a novel Janus hyperbranched amphiphilic polymer has been prepared through the host-guest complexation between Azo and cyclodextrin (CD). The polymer can be further assembled to unilamellar bilayer vesicles (Figure 1.18b),<sup>124</sup> which are able to disassemble under UV irradiation. Furthermore, Azo host-guest complexes have been exploited to fabricate controlled release systems. For example, Ferris *et al.* have reported an Azo-functionalised mesoporous silica nanoparticle with nanovalves, where fluorescent dyes are captured and released in a controllable manner.<sup>123</sup> The operation of the nanovalve is shown in Figure 1.19, where the formation of *trans*-Azo@CD complexes blocks the surface of mesoporous silica nanoparticles, and therefore cargoes are entrapped inside the cavity. Moreover, the pseudorotaxane structure dissociates upon UV irradiation on account of the disassembly of host-guest complexes. As a result, the dye molecules are released, and therefore the cargo loading, blocking and light-controlled releasing procedures have been successfully achieved.

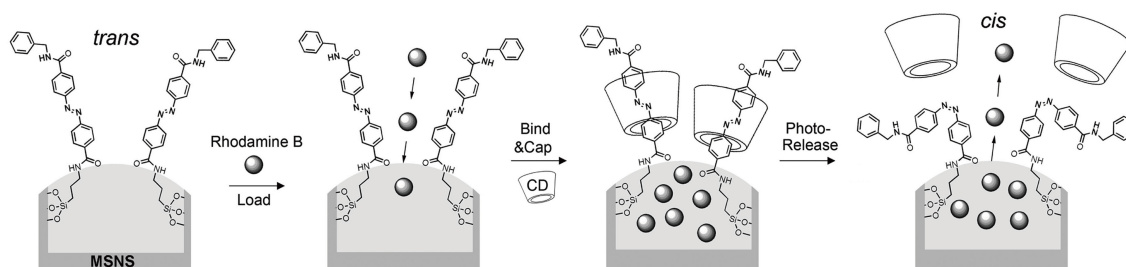


Figure 1.19: Schematic representation of a photocontrollable nanovalve.<sup>123</sup>

### 1.2.2 Azobenzene-CB[*n*] complexation

The first investigation of host-guest chemistry between Azo and CB[*n*] has been carried out by Isaacs and co-workers, where Azo@CB[7] is successfully prepared.<sup>125</sup> However, the photo-induced Azo isomerisation has not been exploited to light-responsive host-guest systems since both *trans* and *cis* Azo isomers are able to bind with CB[7] in a 1:1 fashion. Recently the Scherman group has reported that *trans*-Azo could be employed as the second guest to bind with methylviologen-containing (MV<sup>2+</sup> or MV, the first guest) CB[8], forming an MV@*trans*-Azo@CB[8] ternary complex.<sup>126</sup> In comparison to the MV/*trans*-Azo@CB[8] heteroternary complex, *cis*-Azo is geometrically unfavourable

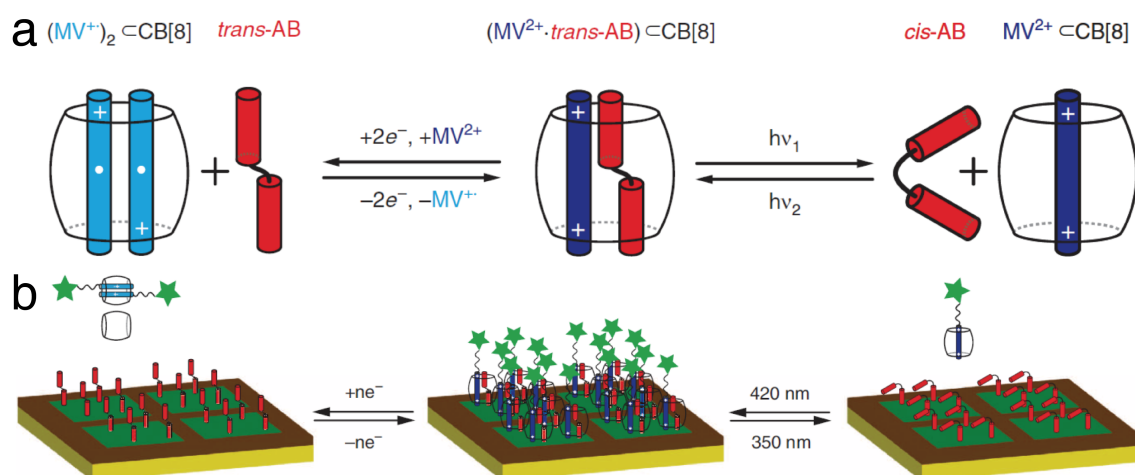


Figure 1.20: **a**, Schematic illustration of the design, formation and orthogonal switching of the heteroternary complex. **b**, Schematic illustration of dimerisation-driven electrochemical switching (left) and isomerisation-driven photoswitching (right) on a surface.<sup>76</sup>

to be encapsulated by CB[8] cavity in the presence of MV, leading to either disassembly or a 1:1 binary inclusion complex.<sup>76</sup> As shown in Figure 1.20a, through incorporating both redox- and light-responsive components, CB[8] mediated host-guest heteroternary complexes are responsive to orthogonal stimuli in a reversible manner, which has been applied to a patterned substrate (Figure 1.20b), resulting in visualised changes of water contact angle measurements and fluorescent microscopic images.

Based on the photo-responsive complexation, MV/*trans*-Azo@CB[8] system has been further exploited to a variety of functional materials, such as supramolecular hydrogels,<sup>80</sup> colloids<sup>23</sup> and rotaxanes.<sup>77</sup> As shown in Figure 1.21, a novel photo-responsive hybrid raspberry-like colloid (HRC) structure has been reported by Scherman and co-workers.<sup>23</sup> Azo is initially immobilised onto the surface of silica nanoparticles (NPs), while MV-functionalised polymeric NPs are employed as the corona. The HRC structure can be readily prepared by mixing the solutions of Azo-silica core and CB[8]-precomplexed MV-NP corona. The reversible assembly and disassembly of HRCs is achieved upon irradiation of visible (420 nm) or UV (350 nm) light respectively, providing potential applications in catalysis and drug delivery. Similarly, a hollow mesoporous raspberry-like colloid has been prepared by Hu *et al.*,<sup>127</sup> where the Azo-modified hollow mesoporous



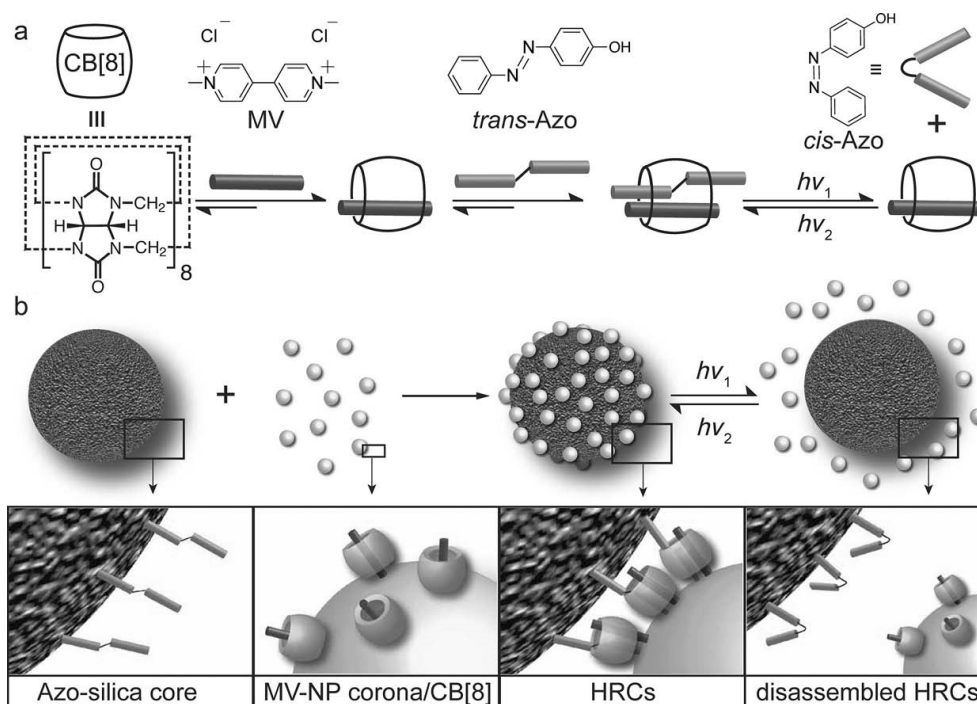


Figure 1.21: **a**, Stepwise formation of MV/*trans*-Azo@CB[8] ternary complex and light-driven reversible disassembly of the complex. **b**, Hybrid raspberry-like colloids obtained by MV/*trans*-Azo@CB[8] complexation and their light-driven reversible disassembly.<sup>23</sup>

silica core is assembled with MV-contained  $\text{Fe}_3\text{O}_4$  NPs *via* CB[8]. The cargoes loaded inside the cavity of mesoporous colloids can be released in a light-controlled manner due to the removal of  $\text{Fe}_3\text{O}_4$  NP ‘caps’.

The crystalline structures of Azo-CB[8] complexes have also been investigated. As shown in Figure 1.22, a CB[8]-mediated supramolecular polymer has been prepared *via* MV/*trans*-Azo@CB[8] complexation, which can be reversibly disassembled upon UV irradiation.<sup>128</sup> More importantly, the solid state structures of both the Azo@CB[8] monomer and the supramolecular polymer have been successfully characterised in this study. Inspired by this, Azo-CB[8] complex has been exploited to impart photo-responsive properties to other photo-inactive phenomena. For example, the thermal phase transition of poly(N-isopropylacrylamide) (PNIPAM) can be regulated in a light-controlled manner through introducing CB[8] and Azo-contained monomers.<sup>129</sup>

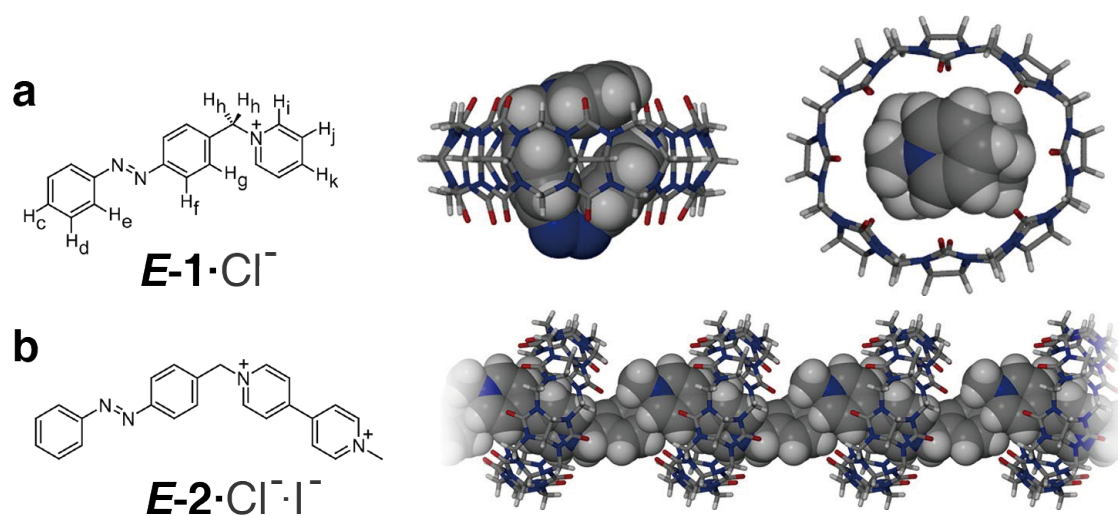


Figure 1.22: **a**, Chemical structure of *E-1*. Side and top view of CB[8]-Z-1. Only the largest component of Z-1 disorder is shown. **b**, Chemical structure of *E-2*. Side view of the supramolecular polymer CB[8]<sub>*n*</sub>·*E-2*<sub>*n*</sub>. C, gray; N, blue; O, red; H, white.<sup>128</sup>

### 1.3 Shape-controlled crystals

Shape-controlled crystals have attracted much attention over the past several decades because the crystalline morphologies have remarkable effects on the optical,<sup>130</sup> electronic<sup>131</sup> and chemical<sup>132,133</sup> properties of the materials. The size and shape distribution of crystals also have a significant importance in chemical industries.<sup>134–136</sup> For example, needle-shaped crystals with high aspect ratio are difficult to process, limiting their pharmaceutical applications.<sup>137</sup> In contrast, needle-like ZnO nanowires show excellent performance in solar cell materials.<sup>138</sup> Unfortunately, morphology-control is still a main challenge in crystallography,<sup>139</sup> since the crystallisation process is fast and kinetically controlled rather than thermodynamically controlled.<sup>140</sup> Therefore, the process is difficult to predict on account of the complicated interactions over multiple levels.

Inorganic semiconducting and metallic materials exhibit size-dependent electrical, optical and chemical properties, contributing to the birth and development of nanoscience and nanotechnology.<sup>142</sup> Thus, a wide variety of nanomaterials with specific shapes have been investigated, such as nanowires,<sup>138</sup> nanotubes,<sup>143</sup> nanosheets,<sup>144</sup> nanoribbons,<sup>145</sup> nanorods<sup>146</sup> and nanospheres etc.<sup>147</sup> For instance, the morphology-control of hydro-

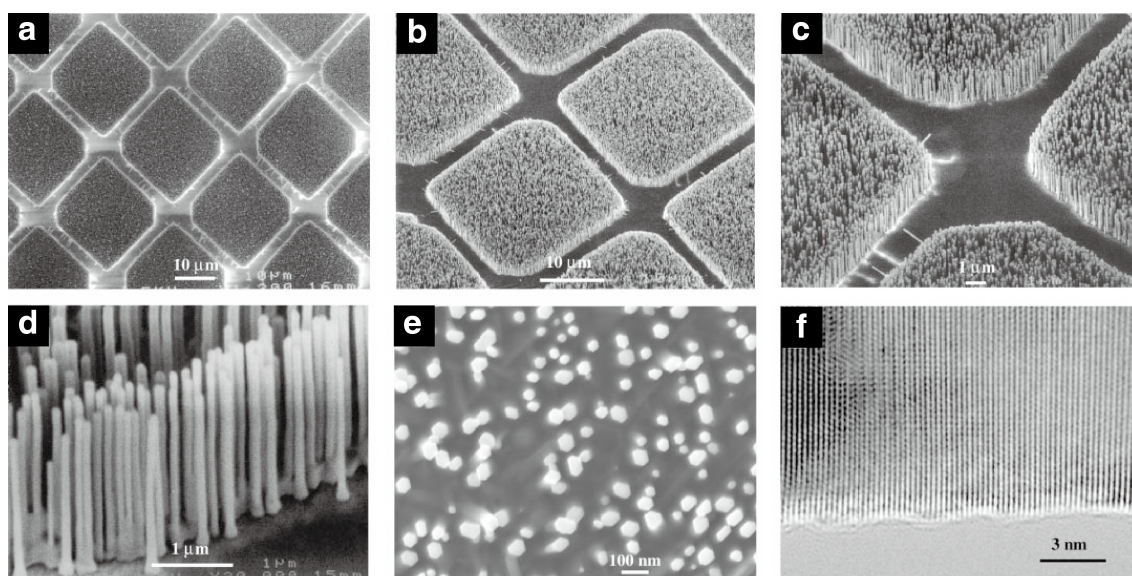


Figure 1.23: **a-e**, SEM images of ZnO nanowire arrays grown on sapphire substrates. A top view of the well-faceted hexagonal nanowire tips is shown in **e**. **f**, High-resolution TEM images of individual ZnO nanowires.<sup>141</sup>

thermally grown ZnO nanowires has been reported,<sup>148</sup> with tunable aspect ratio between 0.1 and 100, while the crystalline shape changes from platelet-like to needle-like. Moreover, as shown in Figure 1.23, Yang's group has introduced the further fabrication of ZnO nano-crystals onto surfaces, resulting in a wide range of oriented vertical nanostructures with fascinating optical properties.<sup>141,149,150</sup>

Organic crystals frequently display size-dependent properties upon the size increase. This phenomenon is called crystallisation-induced effect (CIE).<sup>142</sup> The CIE suggests new electrical, optical and chemical properties of large organic crystals which do not exist in the corresponding molecules. Therefore, organic crystals are likely to exhibit property changes upon the alternation of crystalline geometries.<sup>142</sup> To achieve this goal, through using molecules such as polyacene,<sup>151-153</sup> fullerene<sup>154-156</sup> and phthalocyanine,<sup>157,158</sup> a wide variety of organic crystals with controlled morphologies at nano- or micrometre levels have been designed, prepared and characterised.

Physical vapor transport (PVT) and solution phase crystallisation techniques have been employed as traditional crystallisation methods in preparing various organic and inorganic crystals.<sup>142</sup> Therefore, several modified methods have been recently developed to

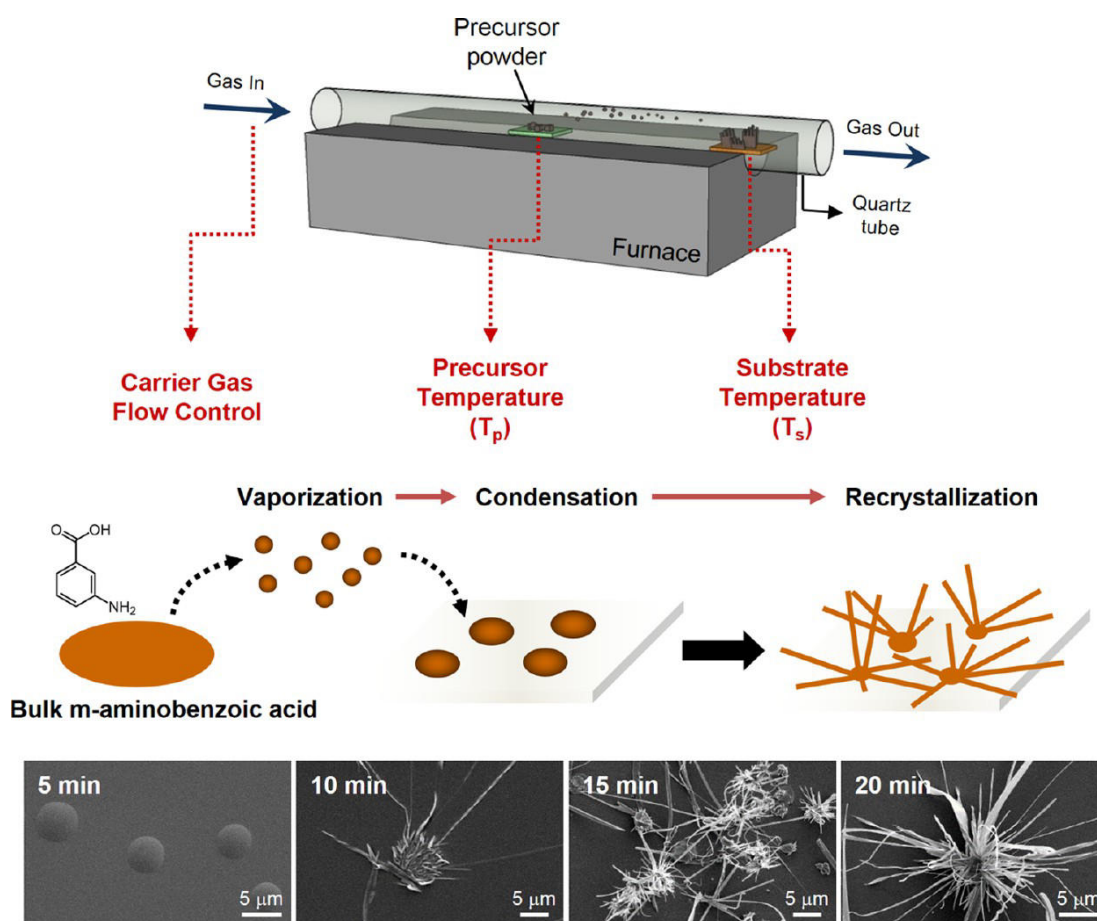


Figure 1.24: Schematic view of f-PVT setup and the mechanism of nanobelt formation during f-PVT process.<sup>159,160</sup>

prepare morphology-controlled crystals, such as flow-type PVT (f-PVT), drop-drying and solvent vapor annealing.<sup>142</sup> Most of these methods regulate the crystal shape through altering the physical factors during crystallisation process, including the pressure, temperature and solvent type. For instance, the process of f-PVT is shown in Figure 1.24, including three main steps: vaporisation, condensation and recrystallisation.<sup>159,160</sup> Firstly, the precursor powder is vaporised from the centre region and transported to the end region by a carrier gas. Secondly, the transported vapors are condensed onto the collecting substrate on account of the lower temperature of the sample-collecting region. Finally, when the collected condensates are populated, the transported vapors are likely to be saturated and resulted in crystals with specific shapes. More importantly, the crystal morphology can be adjusted through altering recrystallisation conditions, such as the

precursor temperature, collecting substrate temperature and gas carrier flow rate. For example, the crystalline shape of pentacene can be tuned between 1D wire-like and 2D disk-like through changing the precursor temperature (Figure 1.25).<sup>152</sup>

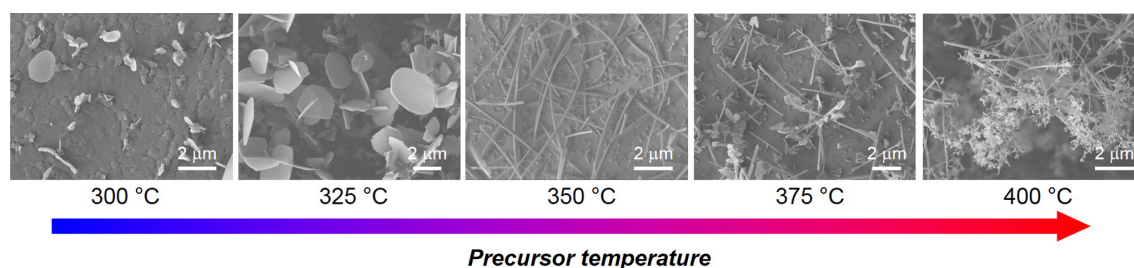


Figure 1.25: SEM images representing the influence of precursor temperature on the morphology of pentacene crystals.<sup>152</sup>

### Shape-controlled crystals *via* supramolecular interactions

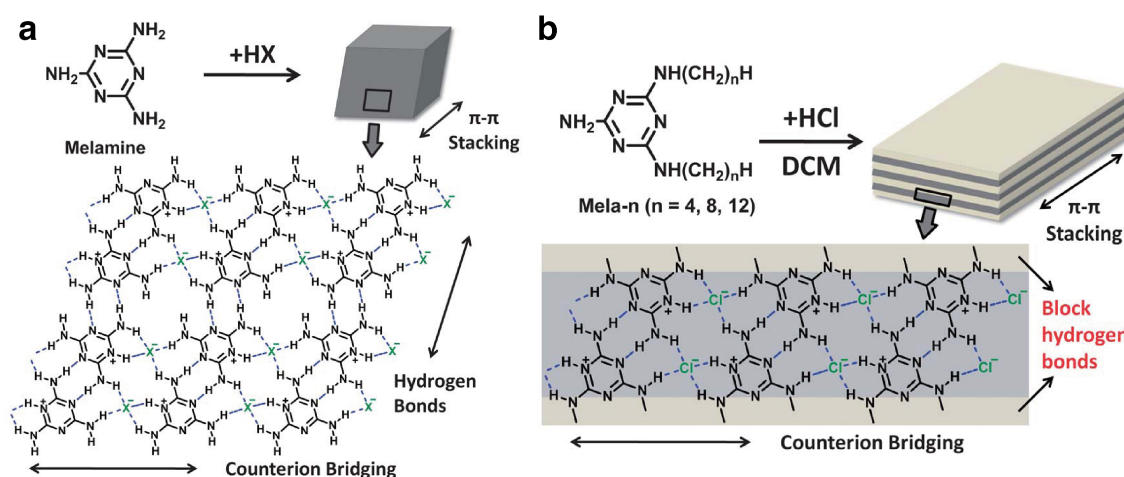


Figure 1.26: Schematic illustration of **a**, the 3D network produced from protonated melamine through multiple hydrogen bonds, counterion bridging and  $\pi$ - $\pi$  stacking and **b**, 2D microsheets produced from dialkylated melaminium derivatives through chloride ion bridged hydrogen bonds as well as electrostatic interaction and  $\pi$ - $\pi$  stacking, while alkyl chains are introduced to eliminate the interaction of multiple hydrogen bonds in the previous 3D network.<sup>161</sup>

Over the past 50 years, with the development of crystal engineering,<sup>162,163</sup> a wide range of intermolecular interactions have been well investigated, such as van der Waals interactions,<sup>164</sup> hydrogen bonds,<sup>165</sup> dipole-dipole interactions<sup>166</sup> and halogen bonds etc.<sup>167</sup> These supramolecular interactions have also been employed in the preparation of shape-

controlled crystals. Zhang and co-workers have reported a 2D organic microsheet through the assembly between dialkylated melamine derivatives and halogen acids. As shown in Figure 1.26, the crystal shape is determined by various supramolecular interactions, and the aspect ratio of microsheets can be modulated by utilising an acid to adjust the counterion-bridged hydrogen bonds,  $\pi$ - $\pi$  stacking and electrostatic interactions.<sup>161</sup> Based on this study, a one-pot method of preparing 1D core/shell microrods has been reported, where the length and width of microrods can be adjusted by simply varying the molar ratio of different compositions.<sup>168</sup>

On the other hand, CB[*n*] also exhibits great potential in the fabrication of shape-controlled crystals. The crystallisation process of the complex between CB[6] and protonated adrenaline guest is shown in Figure 1.27. Upon the transformation of a kinetic 1:1 complex to a thermodynamic 1:2 complex, both needle-like and sheet-like crystals are observed at different times.<sup>56</sup>

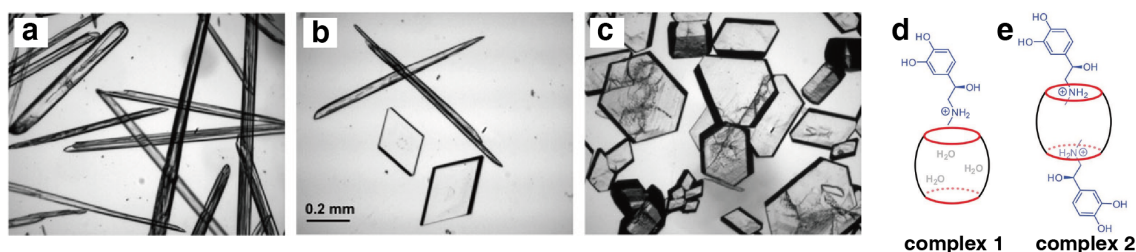


Figure 1.27: Photographs of the crystals of adrenaline-CB[6] complexes at different times: **a**, after 1 hour: needles of complex 1; **b**, after 2 days: both needles of 1 and prisms of complex 2; **c**, after 1 week: only prisms of complex 2. Schematic view of **d**, complex 1 and **e**, complex 2 between CB[6] and protonated adrenaline.<sup>56</sup>

## 1.4 Project aim and thesis overview

The aim of this thesis is exploiting CB[8]-based ternary complexes, especially the complexation with Azo derivatives, to prepare crystalline and composite materials with properties, such as ultra-fast or shape-controlled crystallisation, and potential applications in detergent recycling as well as hydrogel reinforcement. To this end, a series of functional CB[8]-based supramolecular assemblies (crystals, micelle-nanoparticle complex and hy-

drogels) have been produced through hierarchically coordinating materials at molecular or nanometre level. In addition, the obtained structures can be reversibly disassembled by utilising the non-covalent nature of CB[8]-assisted host-guest complexation.

Chapter 2 introduces the interactions between CB[8] and the common dye methyl orange (MO) guest, which, to the best of our knowledge, makes 2MO@CB[8] to be the fastest CB[*n*] ternary complex crystallisation reported to date. Moreover, the host-guest chemistry between CB[8] and a series of MO derivatives with different functional groups is discussed, illustrating the relationship between different guest structures and their crystalline behaviours.

In chapter 3, a series of experimental and computational methods have been carried out to understand the crystallisation mechanism of 2MO@CB[8]. Consequently, control over the crystal shape, length and growth rate can be achieved in a straightforward manner whilst maintaining the same (internal) unit cell. Our understanding of oriented electrostatics provided by the homoternary complex is then exploited to prepare vertical macroscopic free-standing crystalline pillars grown from a glass surface at room temperature.

Chapter 4 introduces the application of Azo-CB[8] complex in a composite system, where Azo-functionalised micelles have been prepared and attached onto the surface of CB[8] catenane-functionalised silica NPs, forming a novel micelle-nanoparticle complex (MNC). Using responsive CB[8] host-guest complexation, a dual recycling system has been proposed, where MNCs are exploited to recycle surfactants (micelles) in aqueous solution, and the hydrophobic molecules (*i.e.* lipophilic cargoes) inside the micelle can be released in a controllable manner. In this process, both the micelles and NPs can be recycled with high efficiency.

In chapter 5, as the last example, a hybrid hydrogel based on CB[8] ternary complex is introduced. The organic supramolecular hydrogel (soft materials) is reinforced through the introduction of extremely small quantities of inorganic CePO<sub>4</sub> nanowires (hard materials). The mechanical properties of the hydrogels have been enhanced through hydrogen bonding interactions and the supporting effects derived from the hybrid construction.

Finally, a concluding and perspective chapter summarises the present work and highlights the great potential of exploiting CB[8]-based ternary complexes as outstanding tools in fabricating crystalline and composite constructions, which will lead to versatile functional materials in the future.



## Chapter 2

# Complexation between CB[8] and methyl orange derivatives

The computational results in this chapter were carried out in collaboration with Hongbin Liu under the supervision of Prof. Xiaosong Li from Department of Chemistry, University of Washington. The Single crystal X-ray diffraction characterisation (data collection and structure solution) was carried out in collaboration with Dr. Perter N. Horton from EPSRC National Crystallography Service, University of Southampton. The data collection of MS was carried out by Dr. Dijana Matak-Vinkovic, Department of Chemistry, University of Cambridge.

This work has been included in the following peer-reviewed article:

**Liu, C.<sup>‡</sup>**; Liu, H.; Wu, Y.; Wu, G.; Horton, P. N.; Xiang, G.; Matak-Vinkovic, D.; Li, X.; Scherman, O. A. 'Formation of shape-controlled crystals through rapid assembly of host-guest tectons'. (submitted)

Among various supramolecular stimuli-responsive materials, photo-sensitive systems are of particular interest, since light can be precisely controlled over specific wavelength and employed as an external stimulus in a remote manner.<sup>76</sup> The first Azo@CB[8] complex was reported by Tian and co-workers in 2014,<sup>76</sup> since then Azo derivatives have attracted great attention in CB[8] host-guest chemistry owing to their fascinating photo-responsive behaviours, leading to a variety of applications (e.g. photo-controlled supramolecular polymers,<sup>128</sup> photo-sensitive hybrid raspberry-like colloids<sup>23</sup> and materials

with photo-responsive solution-phase transitions).<sup>129</sup> However, most of these materials are based on the photo-induced isomerisation of Azo derivatives. The crystalline properties of Azo@CB[8] complexes have not been fully investigated and should be of great significance in the design of CB[8]-based functional materials.

Therefore, in this chapter, a commonly used Azo dye molecule, methyl orange (MO), has been complexed with CB[8], exhibiting fast crystallisation behaviours on account of its particular molecular geometry. To the best of our knowledge, 2MO@CB[8] crystal is the fastest crystallisation of CB[*n*] complexes to date, which can be observed by the naked eye within 10 min. Preliminary characterisations have been carried out to understand the composition of the MO-CB[8] solution. Next, using X-ray diffraction technique, the crystalline structure of 2MO@CB[8] has been investigated, where versatile intermolecular and intercomplex interactions have been discussed. The results of which suggest that the fast crystal growth is driven by strong electrostatic interactions. Finally, in order to understand the relationship between molecular structures and crystalline properties, the complexation of CB[8] and a series of Azo derivatives has been studied. The fundamental study of 2MO@CB[8] in this chapter paves the way for the further fabrication of more sophisticated structures in chapter 3.

## 2.1 Introduction

Cucurbit[8]uril (CB[8]) has been utilised to prepare various self-assembled materials, such as hydrogels,<sup>169</sup> microcapsules<sup>21</sup> and nanocavities<sup>170</sup> owing to their dynamic and reversible binding nature. Several aspects enable the high-affinity binding of CB[*n*]-based host-guest complexes, including ion-dipole interactions,<sup>29</sup> size complementarity<sup>27,30</sup> and the release of high-energy water.<sup>32-34</sup> Due to their strong ion-dipole interactions, various cationic guests for CB[8] have been widely studied.<sup>29,126,171</sup> In contrast, there is very little research about the binding effects of anion-containing guests since they have repulsive interactions with CB[*n*] portals. Recently, a 'back interaction' theory has been proposed by Tao *et al.*,<sup>172,173</sup> which focuses on the secondary interactions between anionic moieties and the outside of the CB[*n*] macrocycle in crystalline solids. As shown in Figure 2.1, the

negatively-charged groups of the guest extend beyond the CB[ $n$ ] cavity and can form ion-dipole, hydrogen bonding or other strong interactions with the neighbouring complex to stabilise the crystalline structure.

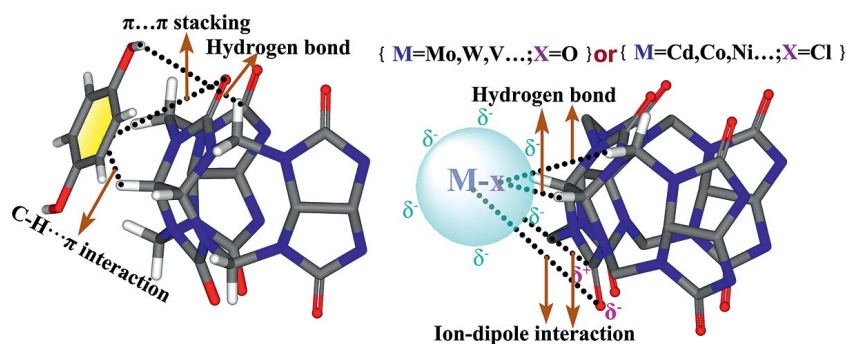


Figure 2.1: Illustration of the secondary interactions outside of the CB[ $n$ ] macrocycle.<sup>172,173</sup>

Crystalline guest@CB[ $n$ ] complexes are of great significance in understanding the binding nature of the system. They are also helpful in the rational design of new complexes and structures.<sup>27,30,46</sup> However, despite the attractive properties of CB[ $n$ ]-based crystals, the time required for the crystal growth (typically on the order of months) has limited their further applications.<sup>40,47,128</sup> As such, ultrafast crystallisation of CB[8]-based complexes is of great interest and might lead to a wide variety of functional materials and potential applications.

Since the first Azo@CB[7] complex reported in 2009,<sup>125</sup> Azo derivatives have played an important role in CB[ $n$ ] host-guest chemistry on account of their *trans-cis* isomerisation. In 2012, the first Azo@CB[8] complex was reported by Tian and co-workers,<sup>76</sup> where MV/Azo@CB[8] formed a 1:1:1 heteroternary complex. In comparison to *trans*-Azo, which can coexist with methyl viologen (MV) guest inside CB[8] cavity, *cis*-Azo is geometrically unfavourable to be encapsulated by CB[8] in the presence of MV, resulting in photo-controlled host-guest complexes. In the following five years, many photo-responsive materials have been prepared based on Azo@CB[8] complexes, including supramolecular polymers,<sup>128</sup> hybrid raspberry-like colloids<sup>23</sup> and functionalised-solid surfaces.<sup>77</sup> However, the crystalline structures of 2Azo@CB[8] homoternary complexes still have not been extensively studied. Although an Azo-CB[8] complex crystal structure

was reported in 2014,<sup>128</sup> only a small part of the Azo guest was encapsulated by CB[8]. Methyl orange (MO) is selected in this thesis to investigate the crystallisation property of Azo@CB[8] complexes on account of its particular molecular structure, where the Azo moiety is functionalised with both a positively charged dimethylamino group and an anionic sulfonate group (Figure 2.2a).

## 2.2 Structural characterisation of the 2MO@CB[8] complex

The MO-CB[8] solution was prepared in an acid condition to investigate their binding behaviours. When a solution of CB[8] and MO (Figure 2.2a) was adjusted to pH 3 with HCl, red needle-like crystals could be observed within 10 min (Figure 2.2b and 2.2c). As shown in Figure 2.2d, the longest crystal observed is more than 1 cm in length and up to 8  $\mu\text{m}$  in width. To the best of our knowledge, this is the fastest crystallisation of a CB[*n*] complex to date, especially compared with the traditional solvent evaporating methods, which generally require several months for crystallisation. In this section, a series of characterisations have been carried out to investigate the composition of both the aqueous solution (NMR spectroscopy and Mass Spectrometry tests) and the crystalline structure (X-ray diffraction technique). Furthermore, various intermolecular and intercomplex interactions in the crystalline construct will be discussed in order to understand the driving force underlying the unique crystalline properties.

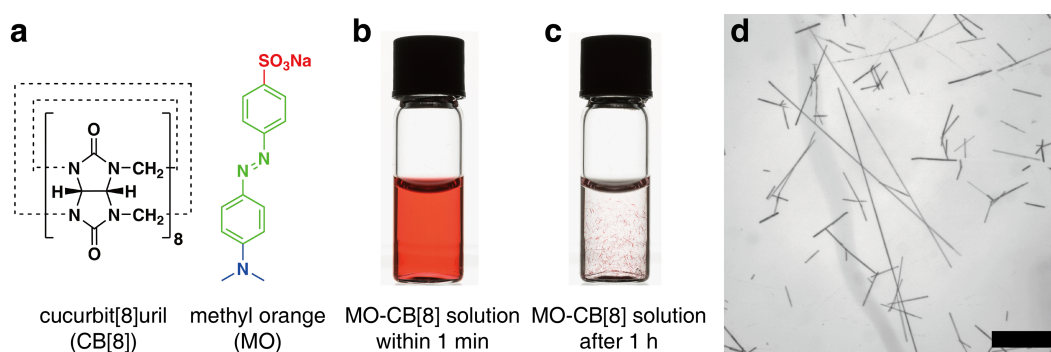


Figure 2.2: **a**, Chemical structure of CB[8] and MO. **b**, MO-CB[8] solution within 1 min after HCl addition. **c**, MO-CB[8] solution after 1 h of HCl addition, indicating crystal formation. **d**, The optical micrograph of the needle-shaped crystals. The longest crystal is over 1 cm (scale bar: 3 mm).

### 2.2.1 Characterisation of the 2MO@CB[8] solution

The composition of aqueous solutions containing both CB[8] and MO was studied through  $^1\text{H}$  NMR titration experiments at pH = 3. The ratio of MO was increased while the concentration of CB[8] was held constant.

Data in Figure 2.3a-2.3e was collected within 10 min to avoid crystal formation, while the samples of Figure 2.3f-2.3i were tested after 12 h to ensure complete crystallisation.  $^1\text{H}$  NMR spectroscopy of pure MO molecules is shown in Figure 2.3a, with sharp peaks ranging from 3.0-8.0 ppm. The peaks have been identified by HMBC, HSQC and COSY NMR spectroscopy (Experimental Section). In Figure 2.3b and 2.3c, the absence of protons:  $\text{H}_a$ ,  $\text{H}_b$ ,  $\text{H}_c$ ,  $\text{H}_d$  and  $\text{H}_e$  illustrates that all of the MO molecules are encapsulated. Specifically,  $\text{H}_c$ ,  $\text{H}_d$  and  $\text{H}_e$  are shifted upfield and broadened ( $\text{H}_{c'}$ ,  $\text{H}_{d'}$  and  $\text{H}_{e'}$ ,  $\text{H}_{e''}$ ), which indicates that  $\text{H}_c$  and  $\text{H}_d$  are inside the CB[8] cavity, resulting in fast exchange on the NMR time scale. However,  $\text{H}_a$  and  $\text{H}_b$  are located outside of the host molecule, demonstrated by the downfield-shifted  $\text{H}_{a'}$  and  $\text{H}_{b'}$  peaks. The reappearance of  $\text{H}_a$ ,  $\text{H}_b$ ,  $\text{H}_c$ ,  $\text{H}_d$  and  $\text{H}_e$  in Figure 2.3d and 2.3e suggests that compared with CB[8], MO is excessive (if the binding ratio of CB[8]:MO is 1:2). Moreover, in comparison to the two proton types of CB[8] ( $\text{H}_f$ ,  $\text{H}_g$ ,  $\text{H}_h$  and  $\text{H}_{f'}$ ,  $\text{H}_{g'}$ ,  $\text{H}_{h'}$ ) in Figure 2.3b and 2.3c, only one type of CB[8] has been observed in Figure 2.3d and 2.3e, indicating the CB[8] with different chemical environments changes to be fully occupied. In addition, the division of  $\text{H}_{e'}$  and  $\text{H}_{e''}$  illustrates that the methyl groups are not able to freely rotate in the complex.

The  $^1\text{H}$  NMR spectroscopy results of the samples after 12 h are shown in Figure 2.3f-2.3i. Signals of the protons from unoccupied CB[8] can only be found in Figure 2.3f and 2.3g, suggesting CB[8] is involved in the crystal growth. Moreover, the sharp peaks of  $\text{H}_a$ ,  $\text{H}_b$ ,  $\text{H}_c$ ,  $\text{H}_d$  and  $\text{H}_e$  in Figure 2.3h and 2.3i suggest that there is no unoccupied CB[8] in the solution, which also proves the 1:2 ternary composition. Therefore,  $^1\text{H}$  NMR titration results suggest that MO and CB[8] are complexed in a 2:1 fashion in acidic conditions.

Mass Spectrometry (MS) of the CB[8]-MO solution at pH = 3 is shown in Figure 2.15 (Experimental Section), where 2MO@CB[8] complex is suggested ( $m/z=967.5$ ). Hence, both NMR spectroscopy and MS confirm the formation of 2MO@CB[8] homoternary

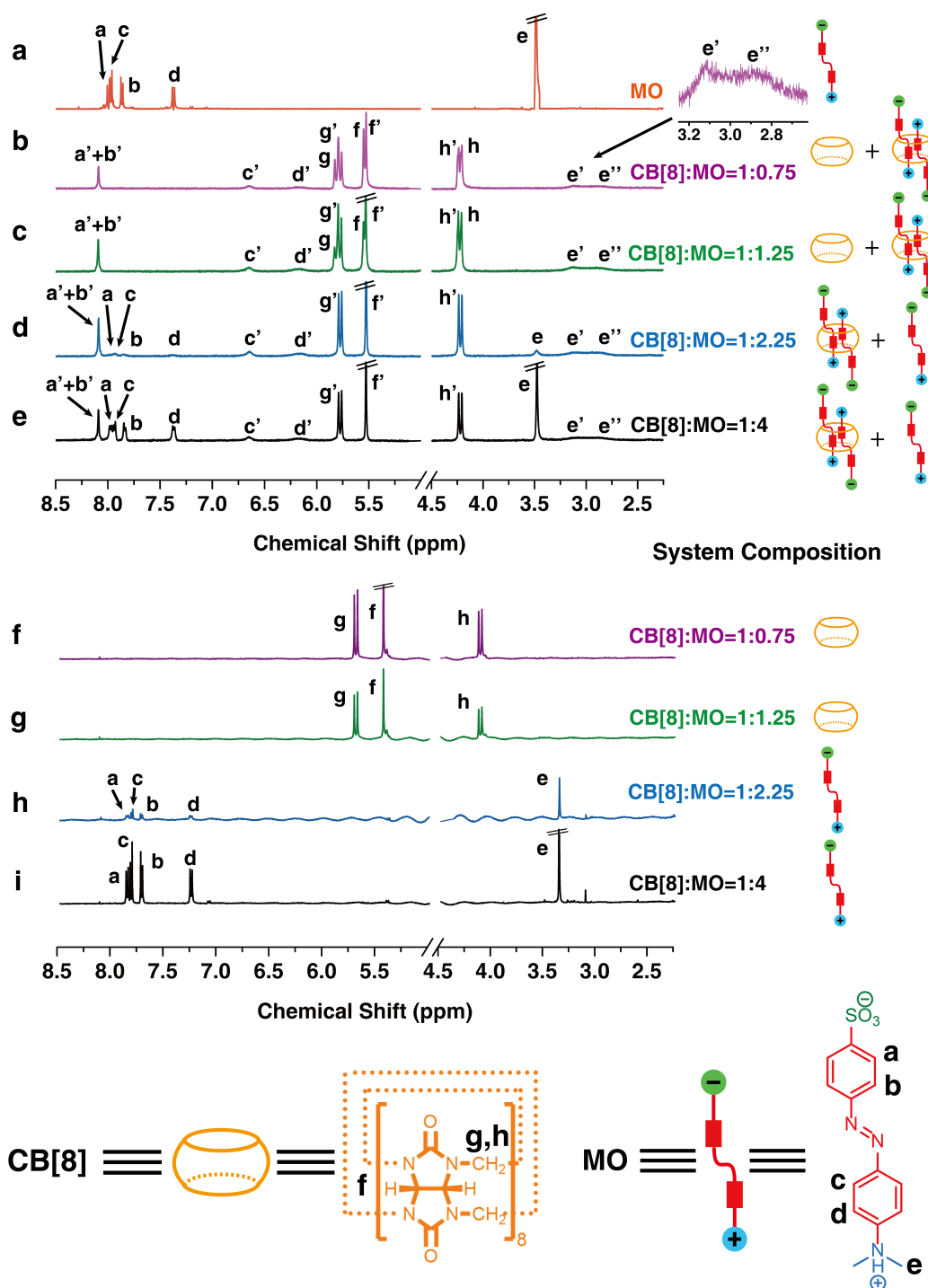


Figure 2.3:  $^1\text{H}$  NMR spectra (500 MHz,  $\text{D}_2\text{O}$ , 298 K) of **a**, pure MO and CB[8]/MO mixture at different ratio: **b**, **f**, 1:0.75; **c**, **g**, 1:1.25; **d**, **h**, 1:2.25 and **e**, **i**, 1:4. Data of **a-e** were collected within 10 min after addition of acid (pH = 3). **f-i** were tested after 12 h to ensure complete crystallisation. The reappearance of  $\text{H}_a$ ,  $\text{H}_b$ ,  $\text{H}_c$ ,  $\text{H}_d$ ,  $\text{H}_e$  suggests the excess MO in **d** and **e**, indicating CB[8]/MO has a 1:2 binding model in solution.

complex in solution. Characterisation details can be found in the Experimental Section.

## 2.2.2 Characterisation of the 2MO@CB[8] crystal

Next, X-ray diffraction was used to investigate the composition of crystals. As shown in Figure 2.4a and 2.4b, each unit cell contains two types of 2MO@CB[8] complex with a nearly orthogonal orientation, implying that MO and CB[8] bind in a 2:1 fashion both in the solution and in the crystals.

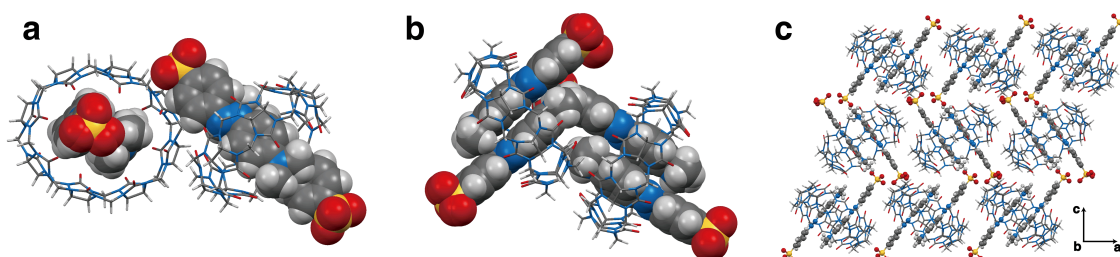


Figure 2.4: The X-ray crystal structures of 2MO@CB[8] complex. **a**, Top view and **b**, side view of the single crystal cell of the 2MO@CB[8] ternary complex. **c**, The herringbone arrangement of the 2MO@CB[8] complex viewed through the b axis. C, gray; N, blue; O, red; S, yellow; H, white.

### Packing coefficient

Compared with the ideal symmetric CB[8] molecule,<sup>46</sup> the occupied CB[8] is distorted to a larger ellipse with the major axis (portal distance = 10.88 Å) ~24% longer than the minor axis (8.79 Å). Figure 2.5a demonstrates that the convex of the van der Waals (vdw) surfaces of two MO guests nicely complements the concave of CB[8] cavity. In order to further understand the host-guest binding, the packing coefficient of 2MO@CB[8] complex was calculated to be 53.0%, which agrees with Rebek's rule ('For the molecular recognition systems, the encapsulation process with a packing coefficient of ~55% generally associated with highest binding affinity'),<sup>27,30,174</sup> demonstrating the perfect size complementarity. Theoretical calculation details can be seen in **s2.5.1**. In addition, from the theory of 'high energy water' (chapter 1), this fully occupied structure also indicates the release of all high energy water inside the CB[8] cavity, which favours the formation of the homoternary complex.<sup>32-34</sup>

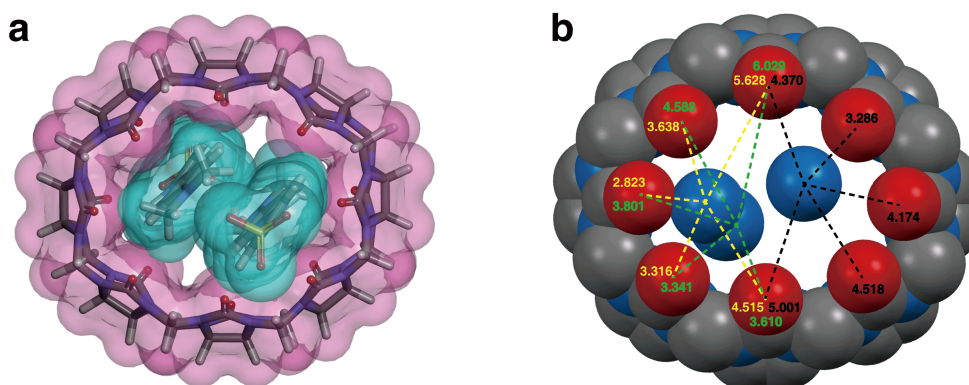


Figure 2.5: Structural analysis for 2MO@CB[8] crystals. **a**, Top view of the van der Waals surfaces of CB[8] (pink) and MO (green) from the crystal structure. **b**, The distances of N<sup>+</sup>...O=C ion-dipole interactions in 2MO@CB[8], only the related atoms have been shown for clarity. C, gray; N, blue; O, red.

### Intermolecular interactions

The 2MO@CB[8] complexes can be employed as building blocks (tectons or ‘tectonic tiles’) for the further assembly of crystalline structure on account of several stabilising interactions inside the complex. In acidic conditions, the cationic charge is delocalised across the dimethylamine and azobenzene groups, which are located proximate to the CB[8] portals (Figure 2.6a and 2.6c). Thus, the short N<sup>+</sup>...O=C distance generates the maximum ion-dipole interactions between the protonated nitrogen atoms and the δ<sup>-</sup> CB[8] portals. From Figure 2.5b, each positively-charged nitrogen has five N<sup>+</sup>...O=C interactions with an average N<sup>+</sup>...O=C distance of 4.18 Å, suggesting 30 ion-dipole interactions in total per complex. This explains the important role of protonated amino groups and the acid-induced crystal formation. In contrast, the average <sup>-</sup>O<sub>3</sub>S...O=C distance is > 6.91 Å, avoiding electrostatic repulsion. Furthermore, the two encapsulated aromatic units have a parallel face-to-face π-π stacking interaction with an average distance of 3.85 Å.

### Intercomplex interactions

Next, the stable tectonic units can assemble into a solid-state herringbone structure on account of several intercomplex interactions, including the enhanced Coulombic force and a variety of secondary interactions. Firstly, as shown in optimised geometry and electrostatic potential maps (Figure 2.6, the calculation is done in gas phase), there is



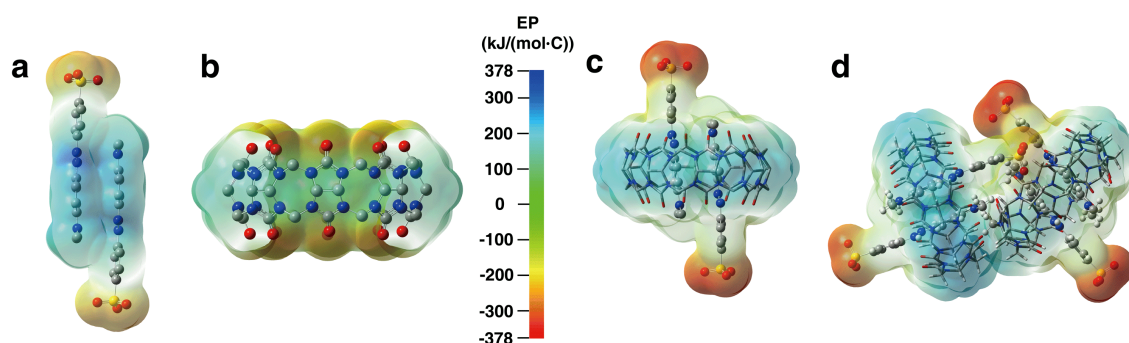


Figure 2.6: The optimised geometry and electrostatic potential map (gas phase) of **a**, MO pairs, **b**, CB[8], **c**, 2MO@CB[8] complex and **d**, the single crystal cell. Density functional theory (DFT) was employed in the calculation.

an electrostatic potential redistribution of the overall structure upon 2MO@CB[8] formation. In comparison to the original MO pairs (Figure 2.6a), an increased (from -200 to -350 kJ/(mol·C))  $\delta^-$   $-\text{SO}_3^-$  group can be achieved by the formation of 2MO@CB[8] complex (Figure 2.6c). Therefore, in the crystal cell, the sulfonate is oriented towards the protonated dimethylamine on the adjacent complex, in order to maximise the Coulombic interactions (Figure 2.6d). Secondly, there are a range of secondary interactions between the neighbouring 2MO@CB[8] complexes.<sup>172,173</sup> Figure 2.6b and 2.6c demonstrate that the  $\delta^+$  methine and methylene groups of CB[8] are enhanced from 100 to 200 kJ/(mol·C) upon complex formation, which are more favourable for the intercomplex secondary interactions. In the solid state (Figure 2.4c), each  $-\text{SO}_3^-$  group has three neighbouring CB[8] molecules with short distances between  $-\text{SO}_3^- \cdots \text{H-C}$  (observed  $\text{O} \cdots \text{C}$  3.47(2) Å, implying an  $\text{O} \cdots \text{H}$  distance of ca. 2.48 Å) and  $-\text{SO}_3^- \cdots \text{H}_2\text{C}$  (observed  $\text{O} \cdots \text{C}$  3.45(4) Å, implying an  $\text{O} \cdots \text{H}$  distance of ca. 2.44 Å) for non-traditional hydrogen bonds, and between  $-\text{SO}_3^- \cdots \text{C=O}$  (3.28(5) Å) for ion-dipole interactions (Figure 2.7a). Additionally, as shown in Figure 2.7b, the unencapsulated aromatic ring of one tecton is stacked on top of a neighbouring methylene group, providing a  $\text{CH}_2 \cdots \pi$  interaction (observed  $\text{C} \cdots \text{C}$  3.85(4) Å, implying an  $\text{H} \cdots \pi$  distance of ca. 2.87 Å).

On account of these intercomplex interactions, the solid state 2MO@CB[8] is likely more stable than the solvated complex, resulting in a decreased solubility. Subsequently, during the host-guest complexation, the solution will change to an unstable supersatur-

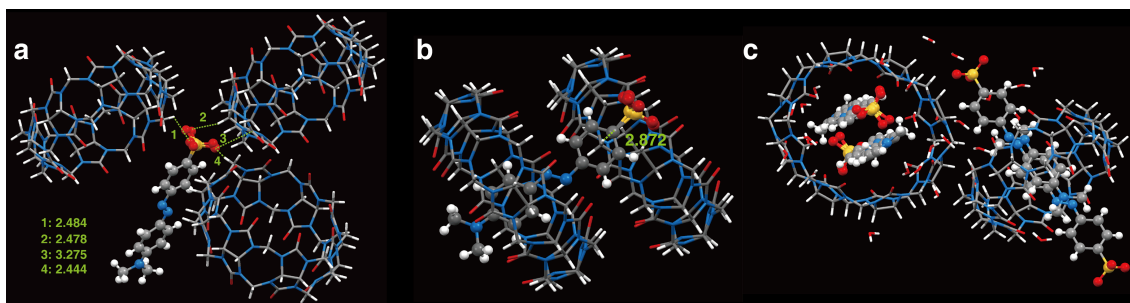
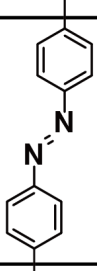
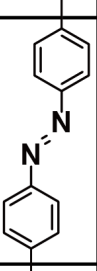
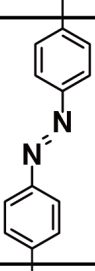
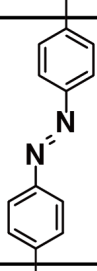
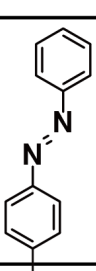
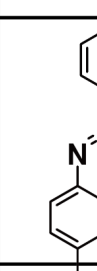
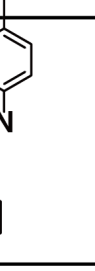
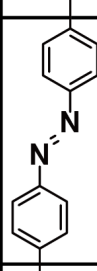
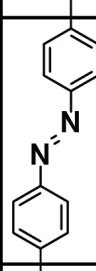


Figure 2.7: **a**, The distances between  $-\text{SO}_3^-$  and neighboring CB[8] molecules (unit: Å). **b**, The shortest distance between the uncapsulated benzene group and the methylene group of neighboring CB[8] molecules (unit: Å). **c**, The  $\text{H}_2\text{O}$  molecules in the crystalline structure.

ated condition. In order to reach a lower energy state, crystallisation will happen by the generation of crystal nucleus under small external perturbations. Therefore, the various intercomplex interactions arising from the  $2\text{MO}@\text{CB}[8]$  complexes accounts for the unusual, fast crystallisation. However, on account of the short timescale of the crystalline nucleus formation, it is difficult to monitor the kinetic process of the crystal growth. The further investigation about the detailed mechanism for the ultra-rapid crystallisation is still in progress (see chapter 6). In addition, the crystal structure is filled with numerous water molecules (Figure 2.7c), which provide ‘water bridges’ and enable the formation of extended hydrogen-bonded networks, further stabilising the crystalline structure. A control experiment was performed with CB[7], where rapid crystallisation was not observed within 24 hours (Experimental Section).

### 2.3 Host-guest chemistry between CB[8] and methyl orange derivatives

To further understand the relationship between molecular structures and their crystalline properties, the host-guest chemistry between CB[8] and a series of MO derivatives with different functional groups was investigated. Their labels, chemical structures and characterisation results are shown in Figure 2.8. Among these guests, MN, ME, MP and MH all bind in a 2:1 fashion with CB[8] under acidic conditions. However, likely due to the steric hindrance arising from amino groups with larger substituents, only MN ex-

label	MO	MN	ME	MP	MH	MC		MI	MD
anionic groups	SO <sub>3</sub> Na	SO <sub>3</sub> Na	SO <sub>3</sub> Na	SO <sub>3</sub> Na		COONa		NO <sub>2</sub>	NH <sub>2</sub>
azobenzene structure									
cationic groups	NMe <sub>2</sub>	NH <sub>2</sub>	NEt <sub>2</sub>	NHPh	NH <sub>2</sub>	NMe <sub>2</sub>		NMe <sub>2</sub>	NMe <sub>2</sub>
binding fashion	2:1	2:1	2:1	2:1	2:1	1:1	2:1		1:1
crystallisation results	within 10 min	within 6 h	no crystals	no crystals	no crystals	no crystals	within <sup>a</sup> 5 d	no <sup>b</sup> crystals	no crystals

<sup>a</sup> Crystals were observed at a pH between 9 to 11 for MC.

<sup>b</sup> No crystals were observed due to the low water solubility of MI.

Figure 2.8: Chemical structures, labels and crystallisation results (pH = 3) of a wide range of azobenzene derivatives with different terminal groups.

hibits rapid crystallisation properties. The characterisation details can be found in the Experimental Section.

As shown in Figure 2.9, 2MN@CB[8] and 2MO@CB[8] have similar unit cells and arrangements, suggesting the generality of this crystalline system. No crystals were formed for MH and MD, indicating the important role of negatively-charged groups in the rapid crystallisation process. Crystallisation of the MO derivative bearing a nitro group (MI) was also attempted, however, its poor water solubility limited the investigation. In addition, the MN derivative is currently being investigated in order to introduce defects into the crystal of 2MO@CB[8], yielding MN/MO@CB[8] ternary complex crystals. The MS results for MO-MN-CB[8] system at pH=3 suggest the formation of MN/MO@CB[8] ternary complex in the solution (Figure 2.17, Experimental Section).

Particularly, unlike the MO-CB[8] system crystallised in acid conditions, the weaker carboxylic acid group on the MC derivative is deprotonated under alkaline conditions, leading to a substantially slower crystalline growth rate. The growth of 2MC@CB[8] tectons requires at least 5 days at a pH between 9 to 11. Furthermore, as shown in Fig-

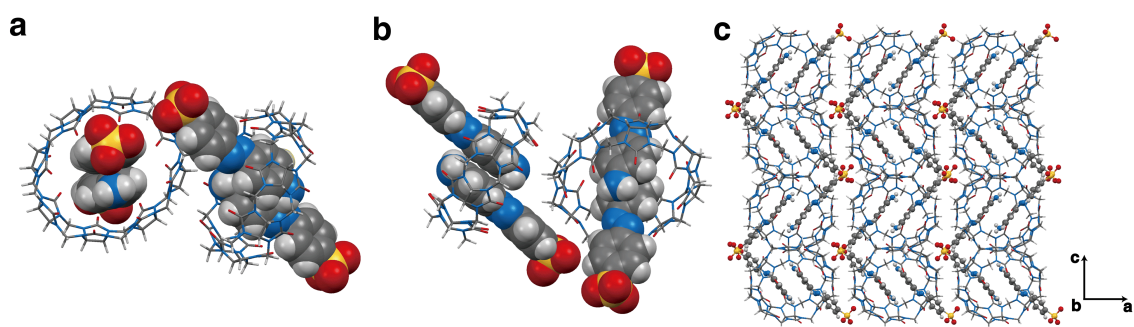


Figure 2.9: The X-ray crystal structures of 2MN@CB[8] complex. **a**, Top view and **b**, side view of the single crystal cell of 2MN@CB[8] ternary complex. **c**, The herringbone arrangement of the 2MN@CB[8] complex viewed through the b axis. C, gray; N, blue; O, red; S, yellow; H, white.

ure 2.10a and 2.10b, the unit cell of the 2MC@CB[8] crystals is substantially different from that observed from 2MO@CB[8]. 2MC@CB[8] crystals consist of two CB[8] molecules, one filled with two MC guests and the other remained unoccupied, leading to a 1:1 stoichiometry of the host and guest. In such a staggered arrangement, the unoccupied CB[8] forms a 1D channel, with potential applications in gas storage and proton conductivity (Figure 2.10c).<sup>36,50,51</sup>

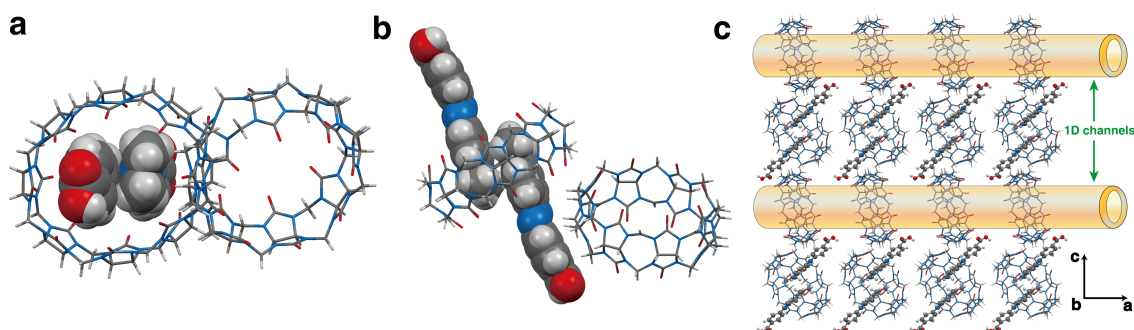


Figure 2.10: The X-ray crystal structures of 2MC@CB[8] complex. **a**, Top view and **b**, side view of the single crystal cell of 2MC@CB[8] ternary complex. In each single crystal cell, one CB[8] is occupied by two MC guests while the other one unoccupied. **c**, Arrangement of the 2MC@CB[8] crystal and its hollow 1D channels (viewed through the b axis). C, gray; N, blue; O, red; H, white.

## 2.4 Conclusions

In conclusion, for the MO-CB[8] system, investigations of both the solution and the crystalline structure suggest a 2:1 binding fashion. More importantly, owing to the strong Coulombic force (between  $\text{-SO}_3^-$  and protonated amino groups) as well as the secondary interactions arising from the negatively-charged sulfonic groups with surrounding CB[8] host molecules, the rapidly-formed 2MO@CB[8] crystals can be observed by the naked eye within 10 min. This crystallisation is, to the best of our knowledge, the fastest crystallisation process of a CB[*n*] complex to date.

Moreover, the negatively charged anionic group of the guest molecule has been further investigated in this work for its significant role in the crystallisation of CB[8] complexes, providing new opportunities in the design of rapid-grown crystals of host-guest complexes. The binding model as well as crystalline property of MO derivatives have been studied, suggesting the generality of rapid crystallisation. In this process, a novel 2MC@CB[8] crystal with 1D hollow channels in the crystalline structure has been prepared, possessing great potential in gas storage and proton conductivity. Additionally, on account of the similar chemical structure and binding model, some derivatives could be used to introduce defects to the crystalline structure and build more advanced constructs in the future.

## 2.5 Experimental

### 2.5.1 Theoretical calculation

The packing coefficient is calculated using the method introduced by Nau and his colleagues.<sup>30</sup> Two identical cyclic graphene-like sheets are utilised as the hypothetical 'lids' to artificially seal the cavity of CB[8]. The inner cavity is then defined as the vdW surface of the blocking group, which penetrates to the plane defined by the portal oxygen nuclei (Figure 2.11). The vdW volume of the stacking MO molecules is calculated only counting the part inside the cavity (*i.e.* the two stacked benzene ring). The volumes of these vdW surfaces are given by the DeepView/Swiss-Pdb Viewer software.<sup>175,176</sup> The packing

coefficient is then given by the equation:

$$C = \frac{V_{molecule}}{V_{cavity}} = \frac{182}{343} = 53.0\% \quad (2.1)$$

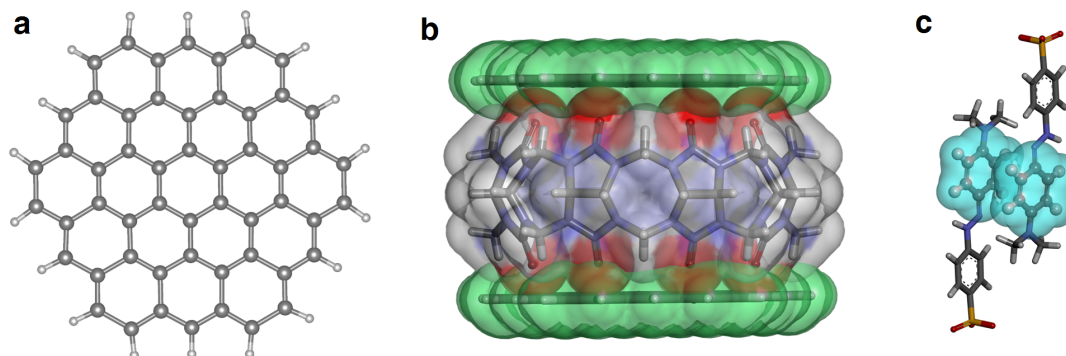


Figure 2.11: **a**, The graphene-like sheet is used as the hypothetical lid to seal the cavity. **b**, The illustration figure of the definition of inner cavity. **c**, The vdW surface of the stacking MO molecules counted in the cavity calculation.

## 2.5.2 Materials and general methods

All starting chemicals were purchased from Sigma Aldrich and used as received unless stated otherwise. CB[7] and CB[8] were prepared according to previously published protocols.<sup>16,177</sup>

<sup>1</sup>H NMR (500 MHz), HMBC, HSQC and COSY spectra were recorded by using a Bruker Avance QNP 500 Cryo Ultrashield. Chemical shifts were measured in ppm ( $\delta$ ) in D<sub>2</sub>O with the internal reference set to 4.79 ppm.

Microscopic images were obtained by using an Olympus IX81 inverted optical microscope coupled with a camera of Andor Technology EMCCD iXonEM DU 897.

Mass Spectra were recorded on a Synapt HD mass spectrometer (Waters UK). 2.5  $\mu$ L of the sample solution was nanoelectrosprayed from a borosilicate emitter (Thermo Scientific) for sampling. Typical instrument tuning conditions were capillary voltage 1.8-2.5 kV, cone voltage 60-120 V, collision voltage 10-30 V, with backing pressure 3-4 mbar and source temperature of 20 °C. Only positive ions were detected in this work. Solution was directly intruded into source without chromatography. Spectra were calibrated

externally using sodium iodide. Data acquisition and processing were performed using MassLynx 4.1 (Waters UK).

Single crystal X-ray diffraction characterisation: the single crystals were obtained by crystallisation from water (acidified to pH = 4 by HCl for 2MO@CB[8] and 2MN@CB[8]; made slightly alkaline to pH = 11 by NaOH for 2MC@CB[8]). A suitable crystal was selected and mounted on a MITIGEN holder in oil on a Rigaku FRE+ equipped with HF Varimax confocal mirrors and an AFC10 goniometer and HG Saturn 724+ detector diffractometer. The crystal was kept at T = 100 (2) K during data collection. Using Olex2,<sup>178</sup> the structure was solved with the Superflip<sup>179</sup> structure solution program, using the Charge Flipping solution method. The model was refined with version 2014/7 of ShelXL<sup>180</sup> using Least Squares minimisation.

### 2.5.3 Preparation and characterisation of the 2MO@CB[8] complex

**Preparation of 2MO@CB[8] crystals.** 120  $\mu$ L of MO solution (5 mM) was added to 5 mL of a 0.06 mM CB[8] solution. The system was then adjusted to pH = 3 through the addition of 0.2 M HCl, resulting in a transparent solution with the colour changing from orange to red. Needle-like crystals were obtained within 10 min. Control experiments without CB[8] and with CB[7] can be seen in Figure 2.12.

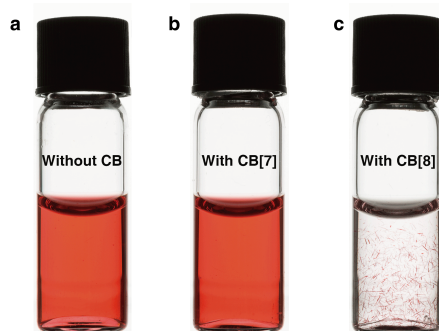
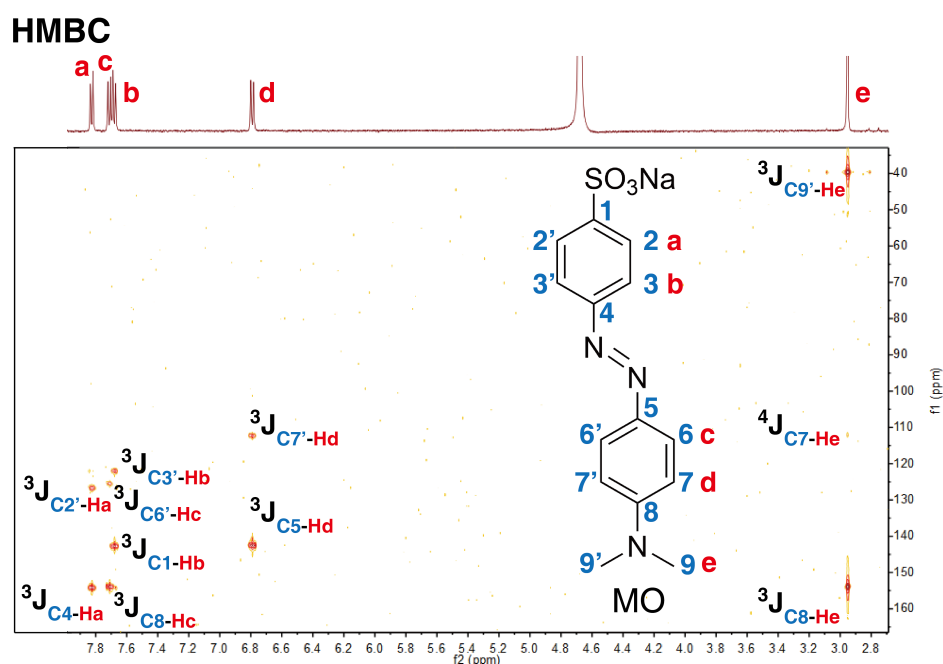
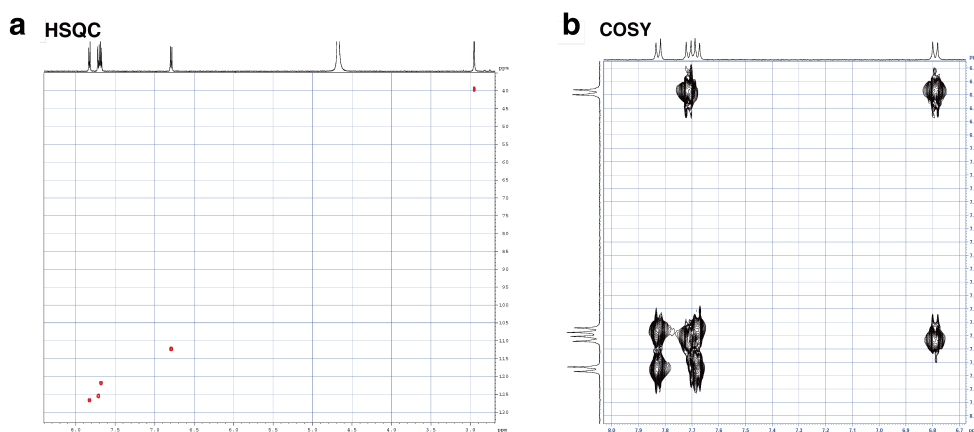


Figure 2.12: The crystallisation results for the samples of MO **a**, without CB[8], **b**, with CB[7] and **c**, with CB[8] at pH = 3.

HMBC, HSQC and COSY NMR spectroscopy (Figure 2.13-2.14) were carried out at pH = 7 to identify the peaks of MO.

Figure 2.13: HMBC (500 MHz, D<sub>2</sub>O) of MO at pH = 7.Figure 2.14: **a**, HSQC (500 MHz, D<sub>2</sub>O) and **b**, COSY (500 MHz, D<sub>2</sub>O) of MO at pH = 7.

**Crystal Data for 2MO@CB[8]:** C<sub>76</sub>H<sub>132</sub>N<sub>38</sub>O<sub>49</sub>S<sub>2</sub>;  $M = 2426.31 \text{ g mol}^{-1}$ ;  $T = 100(2) \text{ K}$ ;  $\lambda = 0.71073 \text{ \AA}$ ; Triclinic, space group  $P - 1$ ;  $a = 15.0843(3)$ ,  $b = 18.1006(5)$ ,  $c = 19.6688(6) \text{ \AA}$ ;  $V = 5271.3(2) \text{ \AA}^3$ ;  $Z = 2$ ;  $\rho_{\text{calc}} = 1.529 \text{ Mg m}^{-3}$ ;  $\mu(\text{CuK}\alpha) = 0.165 \text{ mm}^{-1}$ ;  $F(000) = 2556$ ; crystal size =  $0.260 \times 0.030 \times 0.020 \text{ mm}^3$ .  $2.205 \leq \theta \leq 27.485^\circ$ , 1501 parameters, 2232 restraints,  $GoF = 1.028$ ,  $R_1[I > 2\sigma(I_0)] = 0.0883$ ,  $wR_2[I > 2\sigma(I_0)] = 0.2282$ ;  $R_1$  (all reflections) = 0.1520,  $wR_2$  (all reflections) = 0.2710;  $-0.551 < \Delta\rho < 1.123 \text{ e\AA}^{-3}$ . CCDC 1504660.

**Crystal Data for 2MN@CB[8]:** C<sub>72</sub>H<sub>116</sub>N<sub>38</sub>O<sub>45.5</sub>S<sub>2</sub>;  $M = 2306.14 \text{ g mol}^{-1}$ ;  $T = 100(2) \text{ K}$ ;



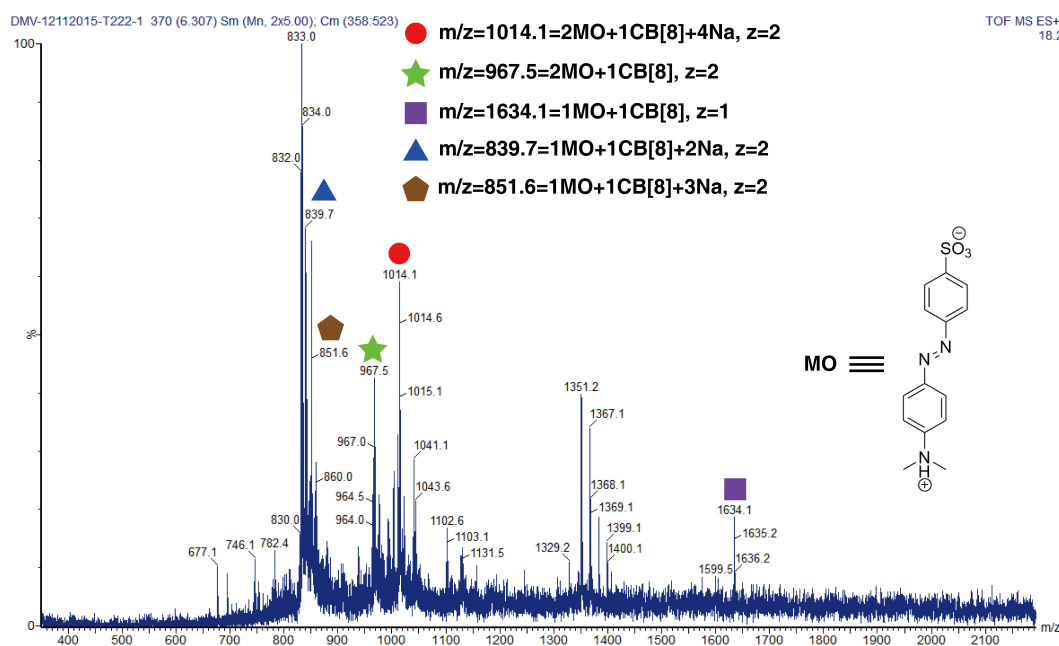


Figure 2.15: MS of 2MO@CB[8] complex at pH = 3.

$\lambda = 0.71073 \text{ \AA}$ ; Triclinic, space group  $P-1$ ;  $a = 15.0634(4)$ ,  $b = 15.8688(3)$ ,  $c = 20.4754(5) \text{ \AA}$ ;  $V = 4892.3(2) \text{ \AA}^3$ ;  $Z = 2$ ;  $\rho_{\text{calc}} = 1.566 \text{ Mg m}^{-3}$ ;  $\mu(\text{CuK}\alpha) = 0.171 \text{ mm}^{-1}$ ; crystal size =  $0.220 \times 0.100 \times 0.090 \text{ mm}^3$ .  $1.634 \leq \theta \leq 27.484^\circ$ , 1433 parameters, 2457 restraints,  $GoF = 1.615$ ,  $R_1[I > 2\sigma(I_0)] = 0.1290$ ,  $wR_2[I > 2\sigma(I_0)] = 0.3732$ ;  $R_1$  (all reflections) = 0.1546,  $wR_2$  (all reflections) = 0.3971;  $-1.308 < \Delta\rho < 1.431 \text{ e}\text{\AA}^{-3}$ . CCDC 1504659.

**Crystal Data for 2MC@CB[8]:**  $\text{C}_{63}\text{H}_{62}\text{N}_{35}\text{O}_{18}$ ;  $M = 1597.47 \text{ g mol}^{-1}$ ;  $T = 100(2) \text{ K}$ ;  $\lambda = 0.71073 \text{ \AA}$ ; Monoclinic, space group  $P21/c$ ;  $a = 27.9493(7)$ ,  $b = 14.9587(3)$ ,  $c = 25.1405(7) \text{ \AA}$ ;  $V = 10362.4(4) \text{ \AA}^3$ ;  $Z = 4$ ;  $\rho_{\text{calc}} = 1.024 \text{ Mg m}^{-3}$ ;  $\mu(\text{CuK}\alpha) = 0.079 \text{ mm}^{-1}$ ; crystal size =  $0.270 \times 0.035 \times 0.035 \text{ mm}^3$ .  $1.549 \leq \theta \leq 25.027^\circ$ , 1117 parameters, 2237 restraints,  $GoF = 0.961$ ,  $R_1[I > 2\sigma(I_0)] = 0.0878$ ,  $wR_2[I > 2\sigma(I_0)] = 0.2625$ ;  $R_1$  (all reflections) = 0.1216,  $wR_2$  (all reflections) = 0.2911;  $-0.423 < \Delta\rho < 0.407 \text{ e}\text{\AA}^{-3}$ . CCDC 1504658.

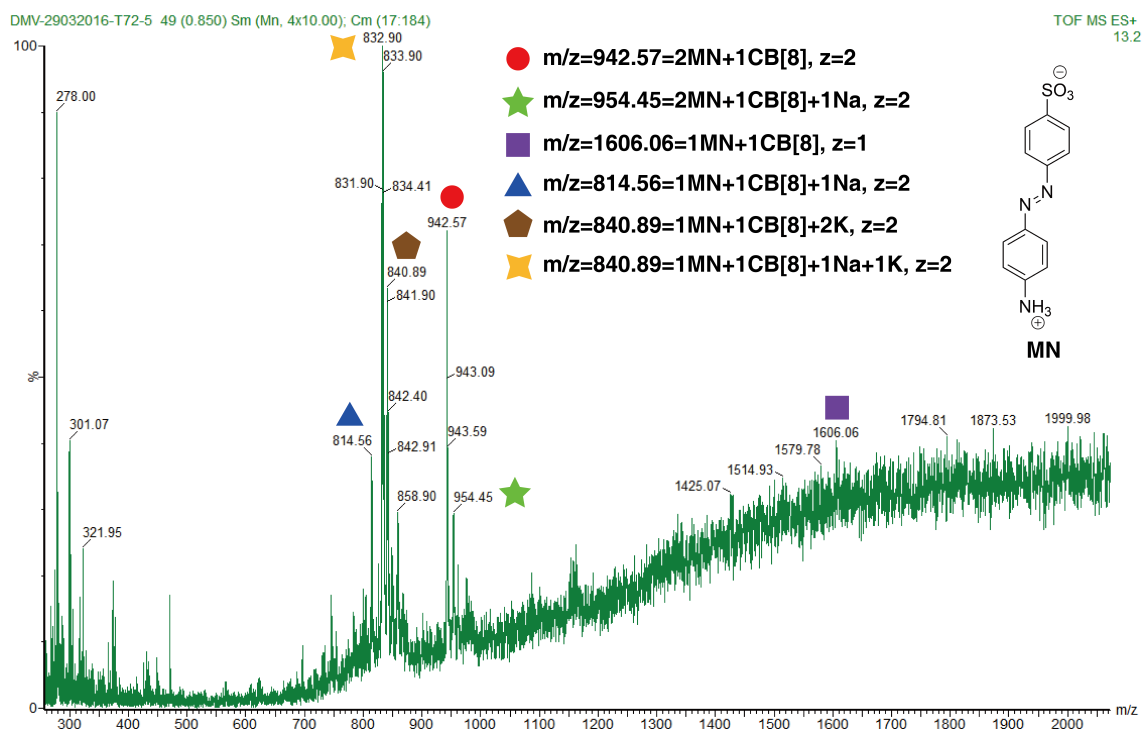


Figure 2.16: MS of MN-CB[8] system at pH = 3, suggesting the 2:1 binding fashion.

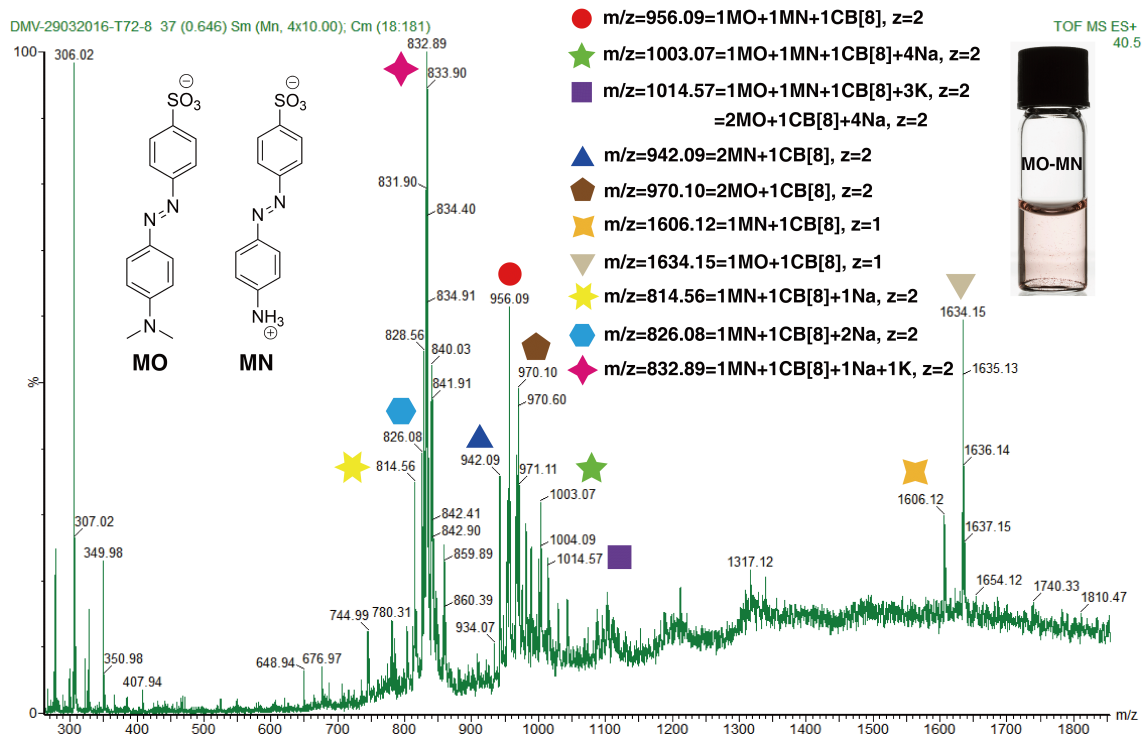


Figure 2.17: MS of MO-MN-CB[8] system at pH = 3, suggesting the formation of MN/MO@CB[8] in the solution.

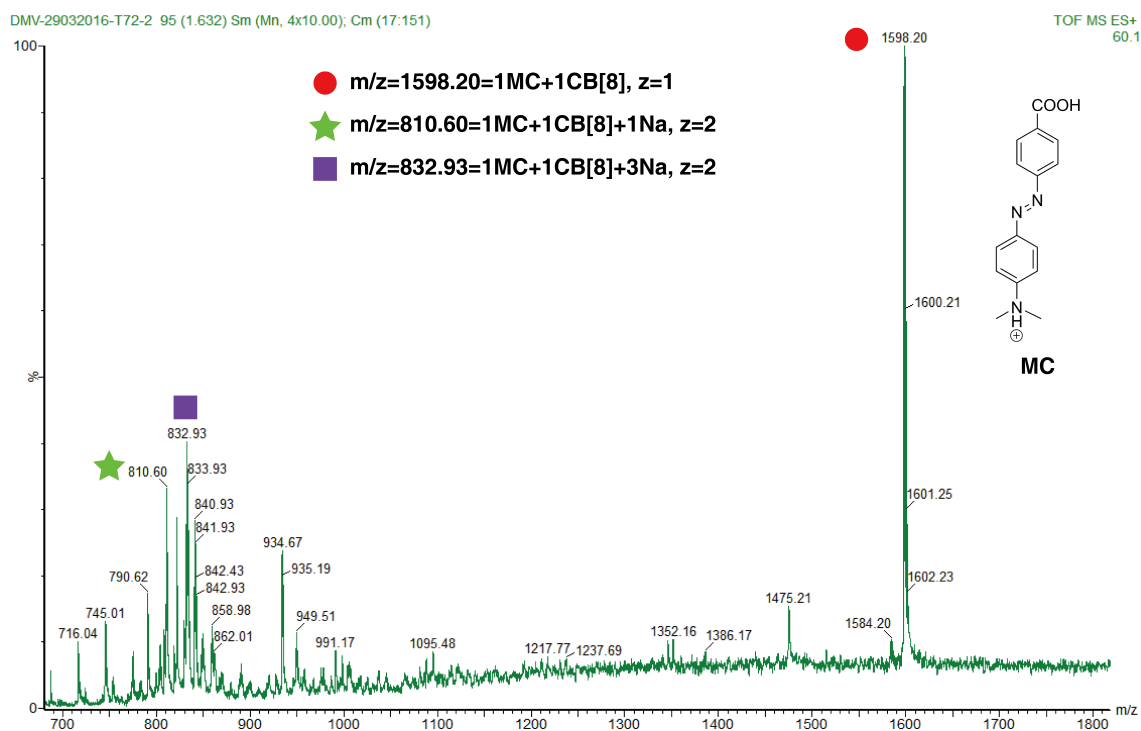


Figure 2.18: MS of MC-CB[8] system at pH = 3, suggesting the 1:1 binding fashion.

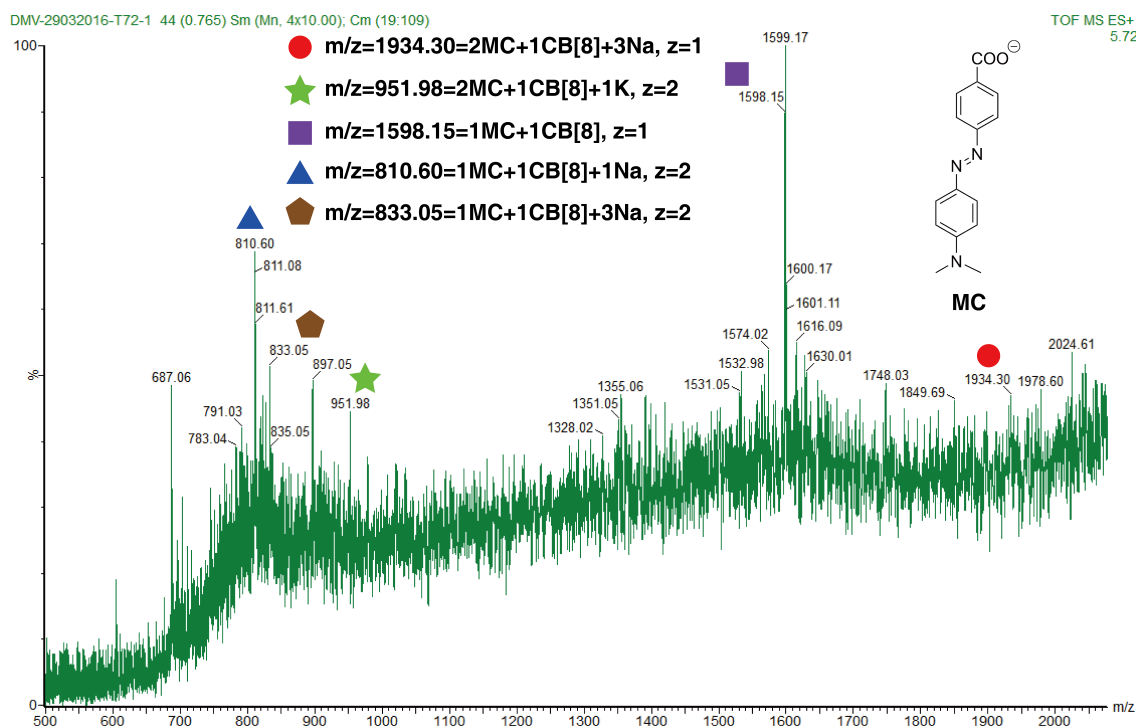


Figure 2.19: MS of MC-CB[8] system at pH = 10, suggesting the 2:1 binding fashion.

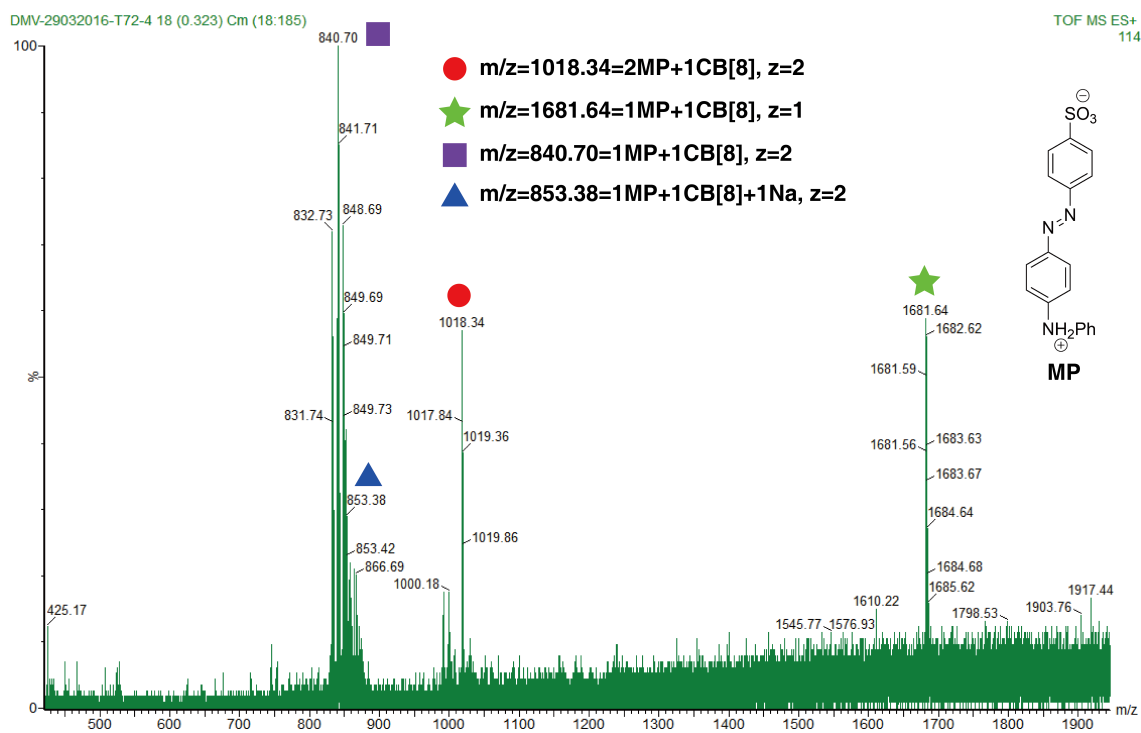


Figure 2.20: MS of MP-CB[8] system at pH = 3, suggesting the 2:1 binding fashion.

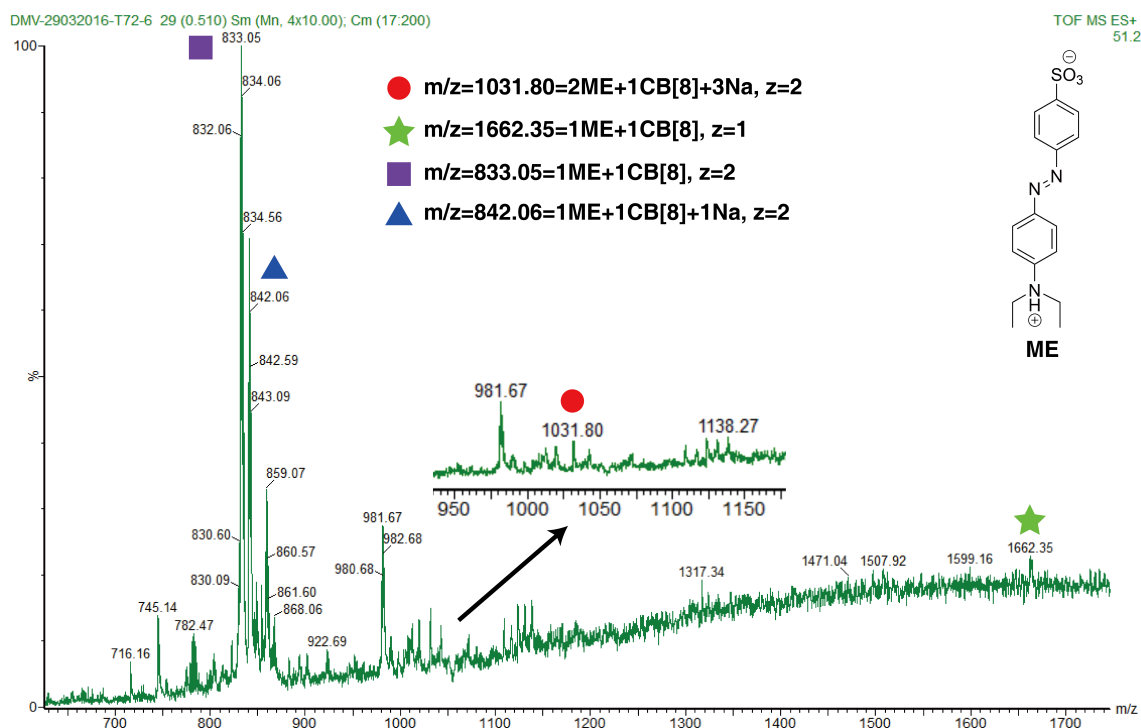


Figure 2.21: MS of ME-CB[8] system at pH = 3, suggesting the 2:1 binding fashion.

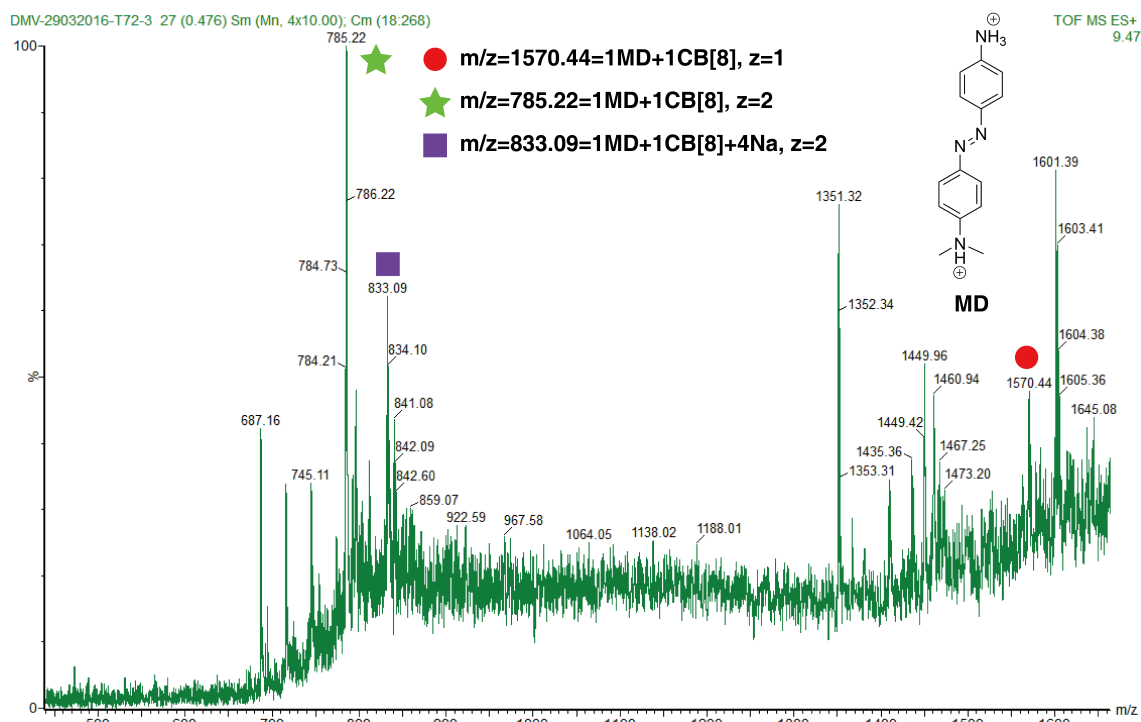


Figure 2.22: MS of MD-CB[8] system at pH = 3, suggesting the 1:1 binding fashion.

## 2.5.4 Characterisation of complexes between CB[8] and MO derivatives

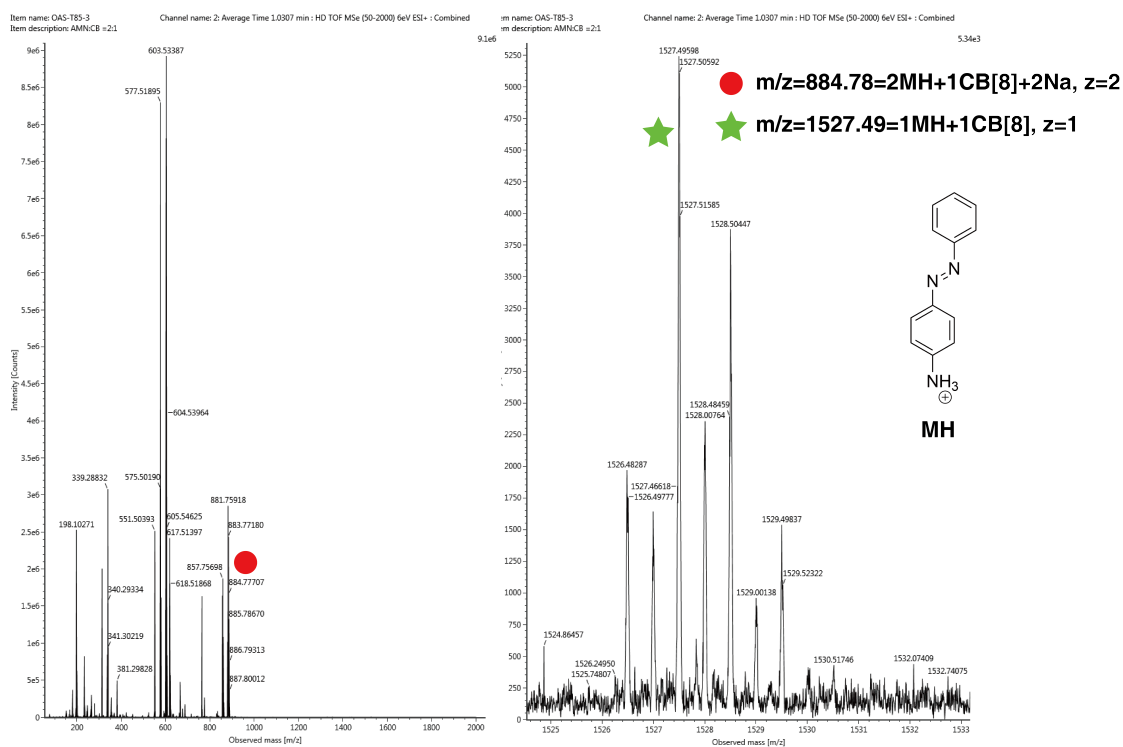


Figure 2.23: MS of MH-CB[8] system at pH = 3, suggesting the 2:1 binding fashion.

## Chapter 3

# Formation of shape-controlled crystals through rapid assembly of host-guest tectons

The computational results in this chapter were carried out in collaboration with Hongbin Liu under the supervision of Prof. Xiaosong Li from Department of Chemistry, University of Washington.

This work has been included in the following peer-reviewed article:

**Liu, C.<sup>‡</sup>**; Liu, H.; Wu, Y.; Wu, G.; Horton, P. N.; Xiang, G.; Matak-Vinkovic, D.; Li, X.; Scherman, O. A. 'Formation of shape-controlled crystals through rapid assembly of host-guest tectons'. (submitted)

The preparation of shape-controlled crystals of organic molecules is a challenging topic in crystallography on account of the intricate interactions present in 3D spatial structures. The high binding affinity associated with host-guest complexation allows for the confinement of organic guest molecules inside the cavity of the macrocyclic host, resulting in surface electrostatic potential redistribution of the guest. Therefore, host-guest chemistry presents opportunities for the intercomplex interactions to be assembled together into a designed morphology. Herein, based on the study of 2MO@CB[8] complex in chapter 2, we present a simple approach to assemble macroscale crystals which can be tuned at the molecular level using CB[8] and MO. Through host-guest chemistry, we are able to con-

control the growth properties of the crystal, including shape, size, rate of formation as well as direction of growth. Specifically, the homoternary 2MO@CB[8] complex serves as a 'tectonic' building block, which stacks into a herringbone arrangement. 2MO@CB[8] crystals can be readily engineered into different macroscopic structures such as 1D needles, 2D sheets and more complex shapes by readily changing the ionic strength of the solution whilst maintaining the same unit cell. Moreover, free standing crystalline pillars have been prepared from a modified glass surface, providing a promising approach to organic crystalline patterns.

### **3.1 Introduction**

Morphology-controlled organic crystals have given rise to a new generation of functional materials. This is mainly because the optical, electrical and chemical properties of organic molecules can be amplified through the formation of large structures.<sup>142,155</sup> In the past two decades, a range of nanoscale shape-controlled inorganic crystals have been reported,<sup>148,181–184</sup> which can be further fabricated onto inorganic substrates, resulting in oriented nanostructures.<sup>141,150,185</sup> Morphologically-controlled crystals of organic molecules, however, remain challenging, with few reports demonstrating shape-control at a nano- or micrometer level and often utilising time-consuming procedures.<sup>151,186,187</sup> Little is known about the general approaches towards macroscopic organic crystals with controlled morphologies. This is due to the difficulty in predicting assembly behaviours of molecules into large-sized crystalline networks arising from myriad complex interactions.<sup>152</sup> Therefore, designing organic building blocks with concepts of particular ordered packing potential might provide an ideal approach to organise and control the morphology of crystalline constructs through hierarchical self-assemblies.<sup>188,189</sup>

Recently various non-covalent interactions has been investigated in the field of crystal engineering, such as hydrogen bonds, halogen bonds, ion-dipole, and van der Waals forces.<sup>162,163</sup> As a typical macrocyclic host, CB[*n*]s have been employed in the preparation of shape-controlled crystals. For example, Li's group has reported that through the self-assembly of CB[8] and small organic molecules (quinoline, naphthalene, styrene,

carbazole and tetrahydronaphthalene), a variety of micro- and nanostructures can be prepared with multiple morphologies (octahedron, truncated octahedron and square sheet).<sup>190,191</sup> However, the crystal formation mechanism has not been fully understood on account of having incomplete single-crystal structures. Additionally, while investigating the self-assembly between CB[6] and adrenaline, Danylyuk and co-workers have discovered that the crystalline shape can be adjusted from needle-like to sheet-like, on account of the binding fashion changing from a kinetic 1:1 complex to a thermodynamic 2:1 complex.<sup>56</sup> However, to the best of our knowledge, the redistribution of surface electrostatic potential during CB[*n*] host-guest complexation has not been employed in fabricating morphology-controlled macroscopic crystalline materials.

Herein, we report a rapid formation of shape-controlled organic crystals assisted by CB[8] host-guest chemistry, as shown in Figure 3.1. As discussed in chapter 2, MO binds with CB[8] in a 2:1 fashion in acidic conditions, yielding stable building blocks (tectons or 'tectonic tiles') for further assembly into a herringbone arrangement (Figure 3.1a-3.1c). Furthermore, taking advantage of the ability of CB[8] to encapsulate two guests in a specific orientation, the crystal morphology can be engineered into needle-like, sheet-like and more advanced architectures by changing the ionic strength of the solution, while the crystalline unit cell remains the same (Figure 3.1d). This provides a simple approach to assemble tectons under mild conditions, which hierarchically forms macroscopic shape-controlled organic single crystals. In addition, the crystalline size, rate of formation and deformation can be readily controlled by altering the conditions of crystal growth, such as pH, ionic strength and the inclusion of competitive guests. More significantly, an oriented organic needle-like construct has been fabricated from a glass surface at ambient pressure and temperature, providing a promising method for the preparation of unique organic crystalline patterns with potential optical and electronic properties of interest.



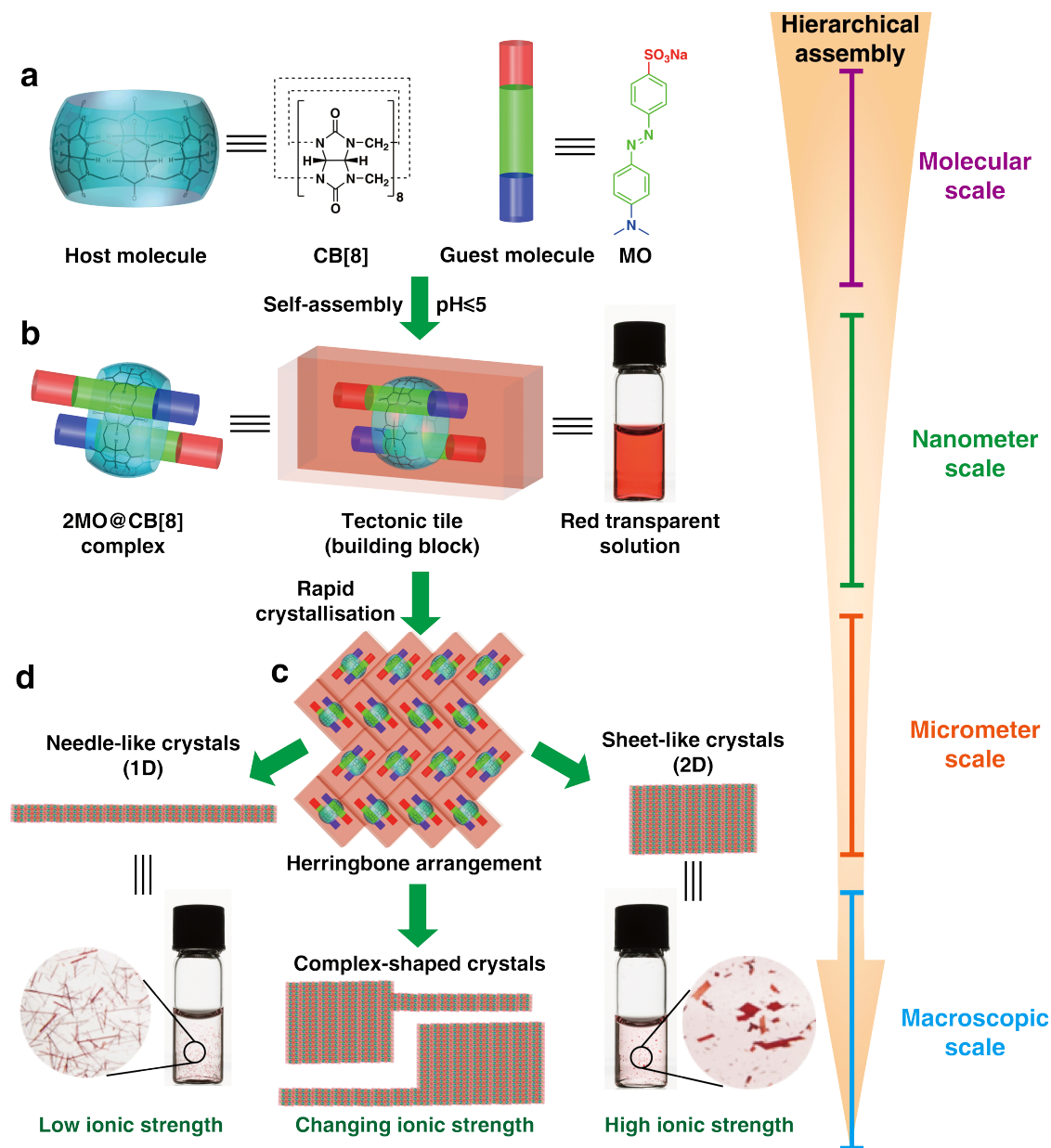


Figure 3.1: The rapid formation of hierarchical tectons for growth of shape-controlled crystals based on host-guest chemistry. **a**, Chemical structures of CB[8] host and MO guest. **b**, Self-assembly of CB[8] and MO in acidic conditions ( $\text{pH} \leq 5$ ) led to 2MO@CB[8] complex formation, then tectonic 'tiles' rapidly assembled, forming crystals. **c**, The 2MO@CB[8] building blocks display a herringbone arrangement during the rapid crystallisation process. **d**, Needle-like, sheet-like and needle-sheet complex-shaped crystals are obtained at low ( $\leq 10^{-3}$  M), high (0.1 - 0.4 M) and dynamic ionic strength respectively.

## 3.2 Shape-controlled 2MO@CB[8] crystals

### 3.2.1 Computational results

Theoretical calculations were utilised to simulate the crystalline growth process, and aid the design of shape-controlled crystals. The interplanar spacing along the [100], [010] and [001] planes were calculated with the value of 14.82, 17.77 and 19.67 Å, respectively, suggesting the growth rate is higher along the **a**-axis when applying the Bravais, Friedel, Donnay, Harker (BFDH) model,<sup>192</sup> due to the small spacing along the [100] plane. Molecular mechanics calculations and the attachment energy model<sup>193</sup> were also employed to gain further insight into the origin of the crystalline morphology of 2MO@CB[8] crystals. By using the DREIDING force field (QEq formalism is adopted to compute the electrostatic force),<sup>194,195</sup> the attachment energy of crystal growth along the **a**, **b** and **c** axes was calculated with the following results:  $E_a = -94.7$ ,  $E_b = -61.4$ ,  $E_c = -58.1$  kcal/mol. Both the BFDH and attachment energy models suggest that the **a**-axis should be the most energetically favourable direction of crystal growth, yielding 1D needle-like crystals.

More comprehensive calculations were carried out at the Density Functional Theory (DFT) level. In a solution with high ionic strength, the cations will have a competitive effect to the crystallisation through binding with the  $\delta^-$  CB[8] portals and  $-\text{SO}_3^-$  groups of MO, which will slow down the crystal growth. The Coulombic contribution, polarisability and the vector decomposition of the sulfonic groups are discussed in this chapter to investigate the anisotropic effects (along different directions) of the ionic strength to the crystal growth. Firstly, the Coulombic contributions to the total attachment energies along the **a**, **b** and **c** directions were calculated as 29.9%, 25.9% and 35.5%, respectively. Next, the polarisability can be calculated with quantum mechanics. The calculated polarisabilities of the 2MO@CB[8] tecton along the **a**, **b** and **c** axes are 328.34 Å<sup>3</sup>, 284.60 Å<sup>3</sup> and 386.91 Å<sup>3</sup>, respectively. Finally, as the electrostatic potential map suggests that the most negative partial charge density is localised on the  $-\text{SO}_3^-$  moieties, a vector decomposition of the  $-\text{SO}_3^-$  groups (see S3.6.1.4) was carried out, indicating the sulfonic groups contribute more Coulombic interaction in the **a** and **c** directions. Therefore, the Coulombic contribution, polarisability and the vector decomposition analysis are all in agreement,

suggesting the high ionic strength likely slow down the crystallisation rate more along the **a** and **c** axes than in the **b** direction. This will lead to a similar growth rate along **a** and **b** directions, resulting in sheet-like crystals. Theoretical calculation details are provided in the S3.6.1.

### 3.2.2 Shape-controlled crystallisation mechanism

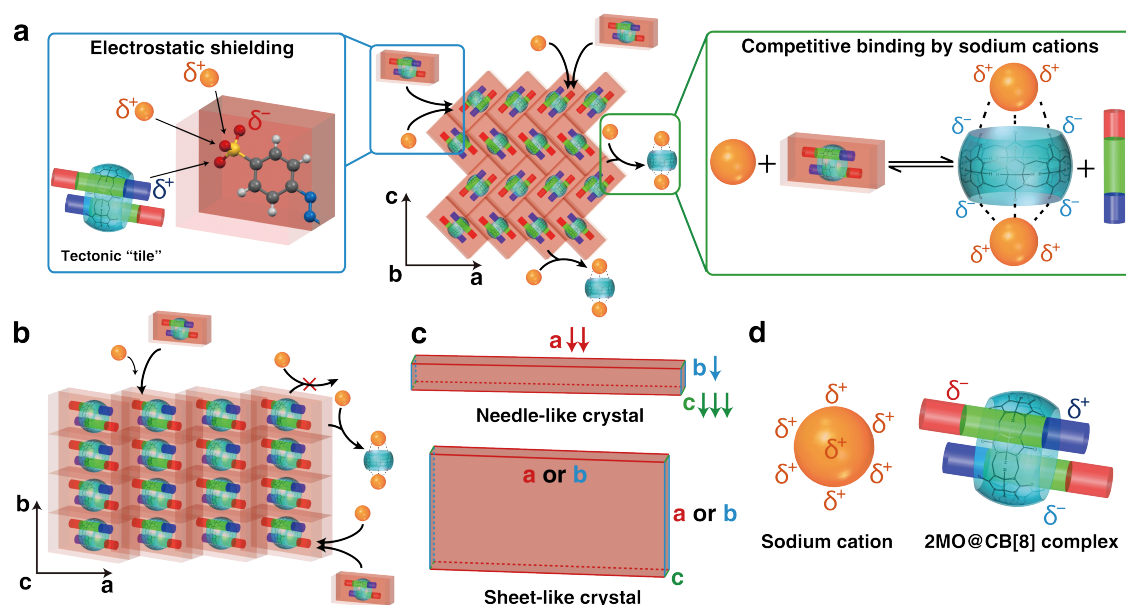


Figure 3.2: Ionic strength effects on 2MO@CB[8] crystal growth along **a**, **b** and **c** directions. **a**, Two synergetic effects of the ionic strength along the **a** and **c** axes. Left: electrostatic shielding of the  $-\text{SO}_3^-$  groups arises from an increased ionic strength, which weakens the Coulombic interactions. Right: interactions of the sodium cations with the 2MO@CB[8] complex dissociation. **b**, Only a minor effect of ionic strength exists along the **b** direction due to stacking between electroneutral CB[8] macrocycles. **c**, Up: the formation of 1D needle-like crystals. Down: in the presence of an increased ionic strength, 2D sheet-like crystals have been formed. Letters **a**, **b** and **c** represent the growth directions. The arrows represent the magnitude of the decrease in growth rates, where  $c > a > b$ , resulting in similar growth rates along **a** and **b** directions. **d**, Representation of positively-charged sodium cation and the charge distribution of the 2MO@CB[8] complex. In the latter, the different colour of  $\delta^-$  represents the electronegative part of the CB[8] portals and  $-\text{SO}_3^-$  groups of the guest.

Based on the theoretical calculations, a schematic illustration in Figure 3.2 helps to understand the mechanism of shape-controlled crystal growth. NaCl can be employed to increase the ionic strength of the solution. Since the concentrations of HCl and MO

are far less than NaCl (or other salts), the ionic strength of the solution in this chapter is approximately equal to the concentration of NaCl (or other salts). In the absence of NaCl, the CB[8] macrocycle orients the charges of the MO guests and shields repulsive interactions, yielding fast electrostatically-driven 1D crystal growth. However, under high ionic strength conditions, CB[8] macrocycles exhibit a 'confining effect' to provide anisotropic Coulombic interactions, restricting the effect of ions to the [100] and [001] planes and protecting the [010] plane from a reduced growth rate.

Specifically, the Coulombic interactions along **a** and **c** directions are weakened on account of two synergetic effects from salt ions. The effects of both electrostatic shielding (Figure 3.2a, left box) and competitive binding (Figure 3.2a, right box) decrease the growth rate in the **a** and **c** directions. By comparison, the increased ionic strength affects the **b** axis least. The stacking between electroneutral CB[8] macrocycles along the **b** direction protects the tectons from the influence of sodium cations (Figure 3.2b). Consequently, as shown in Figure 3.2c, as increasing the ionic strength decreases the overall crystalline growth rate, and minimises the influence along **b** direction, allowing a similar growth rate along **a** and **b** axes. The slowest direction of growth is along **c** axis, resulting in a 2D sheet-like crystalline morphology. However, on account of competitive cation binding with the CB[8] portals (Figure 3.2a), extremely high ionic strength would likely hinder crystal formation in all directions.

### **3.2.3 Preparation of shape-controlled crystals**

Based on the theoretical calculations, several experiments were designed to prepare shape-controlled crystals by adjusting the ionic strength of the system. Crystals were first prepared in a pH 3 solution at low ionic strength conditions (without any additional salt). As shown in Figure 3.4a and 3.4b, 2MO@CB[8] displays needle-like crystals and the XRD face-index (Figure 3.12a, Experimental Section) suggests rapid growth along the [100] plane. Crystals prepared under these conditions may be a favourable model for the investigation of needle-like crystal growth in real time, as the growth time scale is suitable for the direct observation through an optical microscope. Optical micrographs of

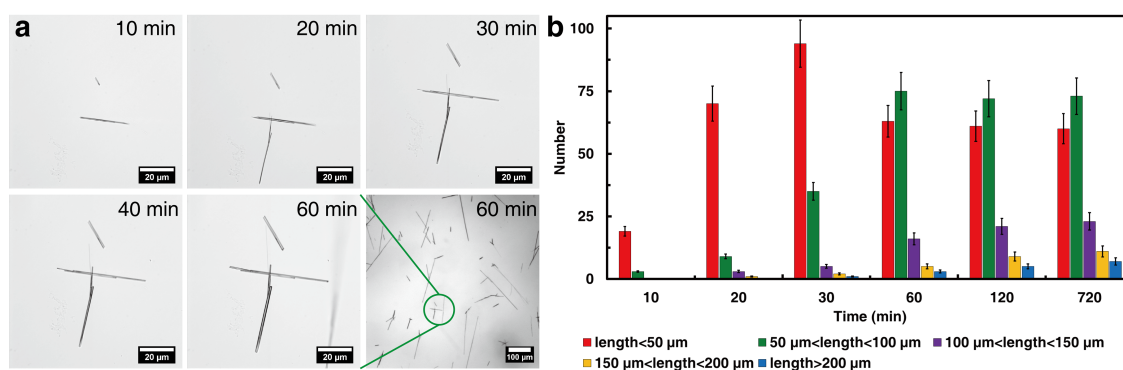


Figure 3.3: **a**, Optical micrographs at different time of the crystal growth within 1 h (pH = 3, scale bar: 20  $\mu\text{m}$ ). **b**, Length distribution of needle-shaped crystals at different time (pH = 3).

the samples taken every 10 min during the first hour of growth demonstrate that one-dimensional crystal formation happened rapidly upon the addition of HCl (Figure 3.3a). The calculated length distributions are shown in Figure 3.3b, where the number of small-sized crystals (length < 50  $\mu\text{m}$ ) increased in the first 30 min, and subsequently decreased as they grew into larger needles. After 1 h, no obvious changes were observed in the system.

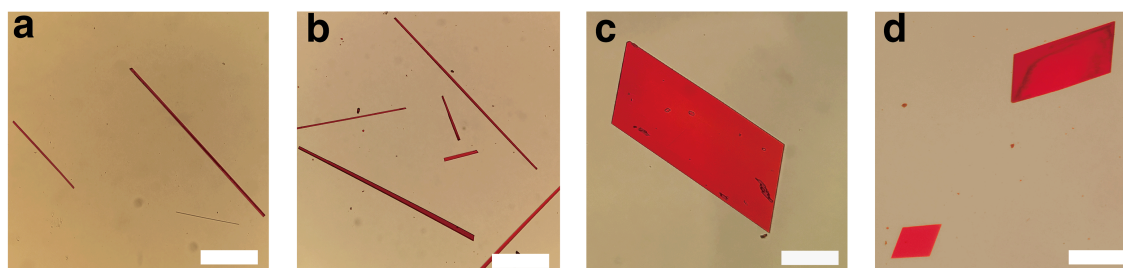


Figure 3.4: Microscopic images of shape-controlled 2MO@CB[8] crystals. **a-b**, Needle-like crystals. Scale bar of a: 50  $\mu\text{m}$ ; b: 40  $\mu\text{m}$ . **c-d**, Sheet-like crystals. Scale bar of c: 10  $\mu\text{m}$ ; d: 15  $\mu\text{m}$ .

Next, a crystal sample was prepared in 0.1 M ionic conditions (pH = 3) through the addition of NaCl. As shown in Figure 3.4c and 3.4d, rectangular sheet-like crystals have been observed, with a long side of 35  $\mu\text{m}$  and a short side of 15  $\mu\text{m}$ . Importantly, the X-ray single crystal analysis suggests that the sheet-like crystals have an identical composition as their needle-like counterpart, indicating that NaCl is not presented in their structure. Additionally, the XRD face-index (Figure 3.12b, Experimental Section) illus-

trates the height of the sheet-like crystals is along the *c* axis. Therefore, the experimental observations correlate well with both the attachment energy analysis and the quantum mechanically calculated polarisabilities. This strongly supports our hypothesis that the ionic strength of the solution during crystal growth will affect the shape of the resultant crystals.

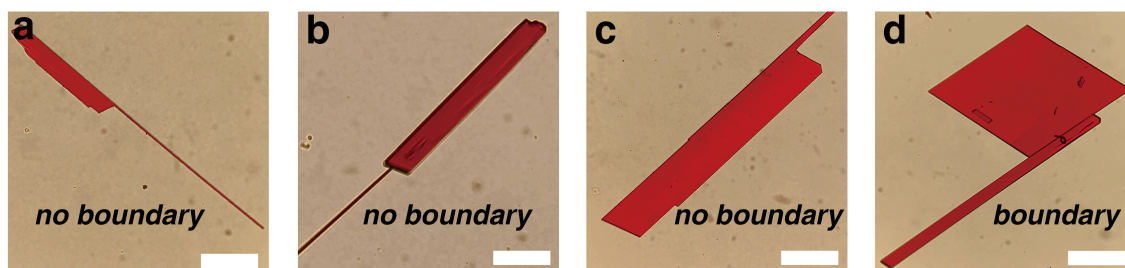


Figure 3.5: Microscopic images of **a-c**, needle-sheet complex-shaped crystals; **d**, physically attached crystals with a clear boundary (scale bar: 15  $\mu\text{m}$ ).

Understanding the effect of ionic strength on crystal formation could lead to the formation of interesting crystal structures through alteration of the NaCl concentration during crystal growth. Crystals were first prepared with a needle shape in the absence of NaCl, then an increase of the ionic strength to 0.1 M resulted in the formation of novel complex-shaped crystals (Figure 3.5 a-c). To ensure that the complex-shaped crystals did not arise from simple physical contact between needle-like and sheet-like crystals, a control experiment was carried out. Needle-like and sheet-like crystals were prepared independently and then mixed together (Figure 3.5d), where a clear boundary can be seen in the obtained structures.

### 3.3 Influencing factors of 2MO@CB[8] crystal growth

The mechanism of rapid crystal growth and the anisotropic effects of ionic strength on the crystallisation process have been discussed. Through adjusting the self-assemblies of 2MO@CB[8] building blocks, multi-control over crystal shape, size and growth rate can be readily achieved by the alternation of crystallisation conditions. This section will discuss the three factors (ionic strength, pH and competitive guests) influencing the crystallisation.

### 3.3.1 Ionic strength effect

The previous discussion has demonstrated that changing ionic strength would lead to crystals with different morphologies. Particularly, for the needle-sheet complex-shaped crystals, NaCl was introduced during the crystal formation process. Therefore, the addition of NaCl at different times during crystal formation would result in varying compositions of complex crystals. As shown in Figure 3.6a, introducing NaCl at 20 min after crystallisation started would yield the highest percentage of complex-shaped crystals. Almost no complex-shaped crystals were observed with the NaCl addition after 40 min, suggesting most of the free 2MO@CB[8] tectons in the solution were used up and unable to continue forming crystalline structures.

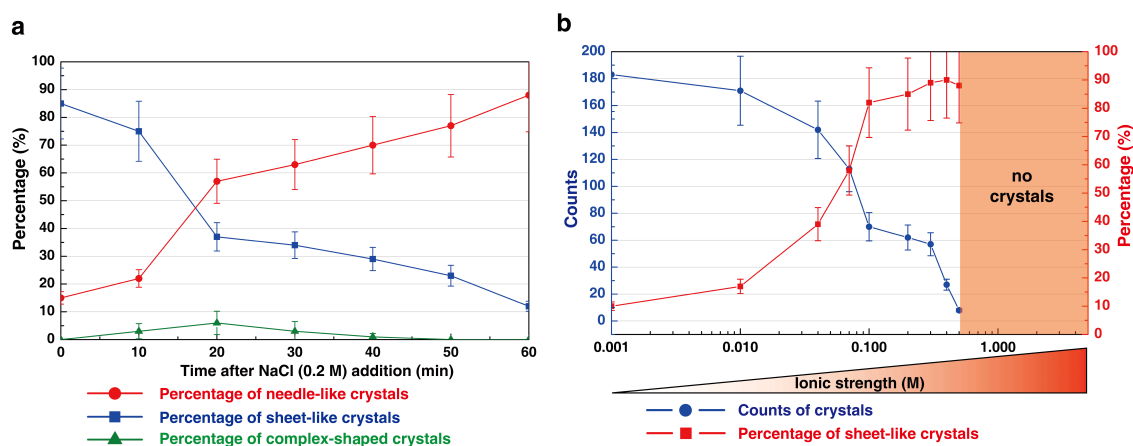


Figure 3.6: Ionic strength effects on crystal growth. **a**, Change of the composition as a function of time (pH = 3) after introduction of 0.2 M NaCl. **b**, The influence of NaCl ionic strength on 2MO@CB[8] crystal formation (pH = 3). As NaCl concentration increased, the percentage of sheet-like (length/width < 6:1) crystals also increased, however, the overall quantity of crystals declined. No crystals were observed with NaCl concentration above 0.5 M.

More importantly, Figure 3.6d illustrates that the total number of crystals decreased with a gradual increase in NaCl concentration, however, the percentage of sheet-like crystals increased. No crystals were observed at salt concentrations > 0.5 M, as excess NaCl significantly inhibits 2MO@CB[8] complex formation (Figure 3.2a). This also suggests that introducing a high concentration of NaCl post crystallisation would result in the crystal structure collapse. As shown in Figure 3.13a-3.13d (Experimental Section), both

needle-like and sheet-like crystals deformed immediately (within 10 s) after excess NaCl addition. This effect is much faster than crystal deformation from the introduction of a competitive guest, which requires more than 24 h for 1-adamantylamine (Figure 3.15a, Experimental Section). The reappearance of the unencapsulated MO in  $^1\text{H}$  NMR spectroscopy of the collapsed crystal sample suggests the complex dissociation (Figure 3.13e, Experimental Section). In addition, control experiments (Table 3.1) illustrate that the sheet-like crystals can also be prepared with other salts, such as LiCl, KCl, RbCl, CsCl,  $\text{Na}_2\text{SO}_4$ ,  $\text{CaCl}_2$  and TBACl.

Salt type (ionic strength=0.2 M)	LiCl	NaCl	KCl	RbCl	CsCl	$\text{CaCl}_2$	$\text{Na}_2\text{SO}_4$	$\text{NMe}_4\text{Cl}$
Counts of crystals	59	62	52	56	53	59	53	49
Percentage of sheet-like crystals	84%	85%	89%	84%	77%	83%	88%	80%

Table 3.1: The crystallisation results with different salts (ionic strength = 0.2 M).

A dynamic experiment was designed to investigate the influence of high ionic strength on the deformation of crystalline structures.  $2\text{MO}@\text{CB}[8]$  crystals in a small amount of NaCl solution (0.3 M) were observed through optical microscope. The solvent was evaporated in the open air environment. The microscopic images in Figure 3.14 (Experimental Section) were taken within the last 12 seconds before the evaporation finished. With the evaporation of  $\text{H}_2\text{O}$ , the local concentration of NaCl around the crystals rapidly increased, leading to the fast collapse of the crystalline construct.

### 3.3.2 pH effect

As the rapid crystal growth was observed only in acid condition, it is predicted that the crystal formation should be a partially pH-driven process. In highly acidic conditions, the increase in protonated amino groups provides stronger intermolecular and inter-tecton interactions, resulting in a short crystallisation time. However, for  $\text{pH} \geq 6$ , the increased proportion of unprotonated amino groups reduces the electrostatic interactions, removing the benefit of rapid crystallisation.<sup>196</sup> This is clearly illustrated through a graph of crystal formation time vs. pH (Figure 3.7a), where a longer time is required for crystal



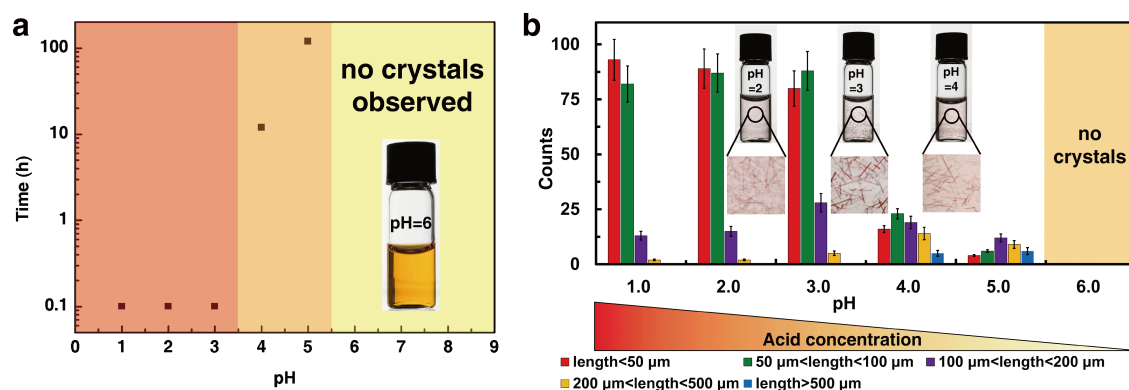


Figure 3.7: The pH effects on the crystal growth. **a**, The crystal formation time-pH graph. **b**, Histogram showing the length distribution of needle-like crystals at different pH values.

formation as pH increased, and without any rapid crystallisation observed with  $\text{pH} \geq 6$ . Figure 3.7b shows the length distribution of needle-like crystals with different pH values. At  $\text{pH} \leq 3$ , short crystals are most prominent, as the system tends to nucleate and crystallise rapidly without sufficient time to form larger crystals. However, at  $\text{pH} = 4$  and 5, the tiny crystals would grow to larger sizes, resulting in a decrease in the number of short crystals. Additionally, 2MO@CB[8] crystals can also be prepared through employing other acids (e.g.  $\text{CH}_3\text{COOH}$  and  $\text{HNO}_3$ ) to adjust the pH.

### 3.3.3 Competitive guests effect

Since the crystalline structure is based on 2MO@CB[8] tectons, introducing competitive guests to the system might affect the formation of the building block, resulting in crystal deformation or decreased crystallisation rate. For example, the strong competitive guest, 1-adamantylamine is able to deform the crystalline construct of both needle-like and sheet-like crystals within 24 h (Figure 3.15a, Experimental Section).

In chapter 2, the binding behaviours between CB[8] and a series of MO derivatives have been discussed. Therefore, the similar chemical structure and binding properties of MO and its derivatives enable simple mixing of the guests in solution to slow down the rate of crystal formation (Figure 3.15b, Experimental Section). As shown in Figure 3.8, MN was utilised to adjust the crystallisation rate of 2MO@CB[8]. In a MN+MO:CB[8]=2:1 system after 60 min, the total number of crystals decreases with the increase of the mole

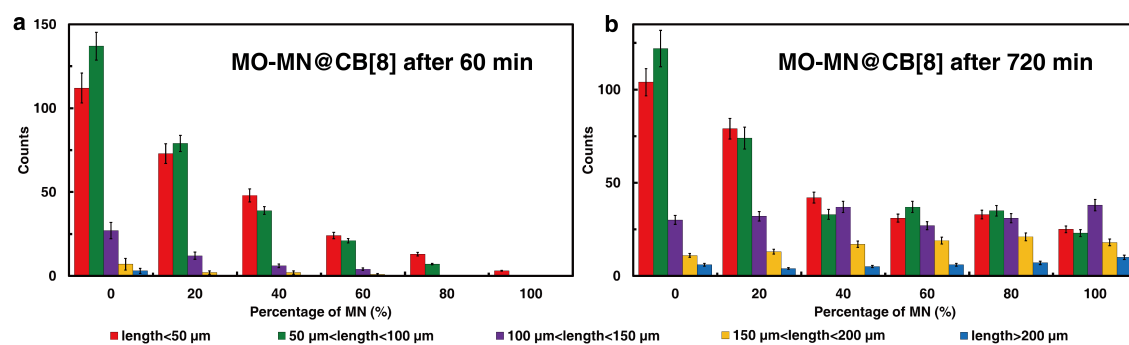


Figure 3.8: Total number of crystals in the MN-MO@CB[8] (2:1) solution as a function of the mole percentage of MN after **a**, 60 min and **b**, 720 min.

percentage of MN (Figure 3.8a). Interestingly, from the test after 720 min, the introduction of MN is likely to result in longer crystals (Figure 3.8b). This further demonstrates that MO derivatives would affect the crystalline properties of 2MO@CB[8].

### 3.4 Oriented organic crystals

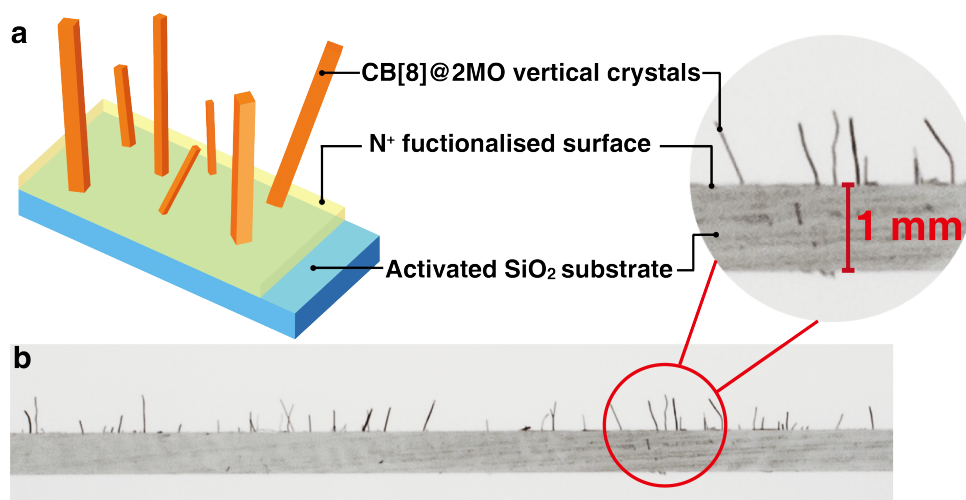


Figure 3.9: Preparation of vertically-oriented crystals. **a**, Schematic of vertical crystalline pillars grown from a glass surface. **b**, Optical image of pillars on a glass substrate.

As the rapid crystal growth in the 2MO@CB[8] system is an electrostatically-driven process, it is possible to fabricate oriented organic crystals onto surfaces. From the theoretical model, the **a**-axis is most favourable in terms of attachment energy and electrostatic interactions. Therefore, the negatively-charged sulfonate moieties ( $-\text{SO}_3^-$ ) aligned along

the **a** direction likely have a strong interaction with the positively-charged glass surface. Growth can be initiated from such a glass surface to generate vertical structures. As shown in Figure 3.9, under mild conditions, 2MO@CB[8] crystals grew vertically from a -NH<sub>2</sub> functionalised SiO<sub>2</sub> surface reaching heights of up to ~1 mm. In contrast, previous attempts to grow vertically-oriented inorganic crystals from a surface required higher temperature and lengthy crystallisation times, only yielding nanoscale objects.<sup>150</sup> An elevated side view of the surface as well as the control experiment without surface modification are shown in the Experimental Section.

### 3.5 Conclusions

This chapter has introduced a novel strategy to construct shape-controlled organic crystals through rapid assembly of host-guest tectonic building blocks. The CB[8] macrocycle orients the charge of MO guests and shields repulsive interactions, leading to fast electronically-driven 1D crystal growth. Control over crystal shape, length and growth rate can be achieved by simple methods. For example, tuning the ionic strength enables a second growth dimension, yielding crystals with sheet-like and more complex structures.

Furthermore, through utilising this system, a macroscopic oriented crystalline structure has been grown from glass surface at room temperature. In addition, on account of the *cis-trans* isomerisation of the azobenzene structures, investigation into novel light-responsive and light-controlled crystals are in progress. As MO derivative dyes are commercially available, we believe 2Azo@CB[8] host-guest tectons possess great potential in preparing optical and electrical devices, and will open a new branch for both supramolecular chemistry and hierarchical crystal growth.

### 3.6 Experimental

#### 3.6.1 Theoretical calculation

The crystal growth rate was analysed using both the BFDH model<sup>192</sup> and the attachment energy model.<sup>193</sup>

### 3.6.1.1 Interplanar spacing

In the BFDH model, the growth rate is inversely proportional to interplanar spacing. The interplanar spacing along the **a**, **b** and **c**-axes is obtained using their corresponding Miller indices [100], [010] and [001]. The equations used to calculate the interplanar spacing are:

$$d = \frac{V}{\sqrt{S_{11}h^2 + S_{22}k^2 + S_{33}l^2 + 2S_{12}hk + 2S_{23}kl + 2S_{13}hl}}$$

$$S_{11} = b^2c^2 \sin^2(\alpha)$$

$$S_{22} = a^2c^2 \sin^2(\beta)$$

$$S_{33} = a^2b^2 \sin^2(\gamma)$$

$$S_{12} = abc^2(\cos(\alpha)\cos(\beta) - \cos(\gamma))$$

$$S_{23} = a^2bc(\cos(\beta)\cos(\gamma) - \cos(\alpha))$$

$$S_{13} = ab^2c(\cos(\gamma)\cos(\alpha) - \cos(\beta))$$

$$V = abc\sqrt{(1 - \cos^2(\alpha) - \cos^2(\beta) - \cos^2(\gamma) + 2\cos(\alpha)\cos(\beta)\cos(\gamma))}$$
(3.1)

where  $d$  is the interplanar spacing.  $h, k, l$  are the Miller indices of the plane.  $a, b, c$  and  $\alpha, \beta, \gamma$  are the lattice parameters. In our case,  $a = 15.09430 \text{ \AA}$ ,  $b = 18.10060 \text{ \AA}$ ,  $c = 19.66880 \text{ \AA}$ ,  $\alpha = 90.2700^\circ$ ,  $\beta = 90.0980^\circ$ ,  $\gamma = 101.0100^\circ$ . The spacing of the [100], [010], [001] planes are calculated as  $d_a = 14.82 \text{ \AA}$ ,  $d_b = 17.77 \text{ \AA}$ ,  $d_c = 19.67 \text{ \AA}$ , respectively.

### 3.6.1.2 Attachment energy model

In the attachment energy model, the crystal growth rate is proportional to the attachment energy along different planes, where the attachment energy can be defined as the energy released on attaching a growth slice of molecules to a growing crystal face.

$$E_{att} = E_{lattice} - E_{slice}$$
(3.2)

Molecular mechanics calculations have been carried out by using the DREIDING force field,<sup>194</sup> which is a generic all-atom force field especially suitable for organic molecules,

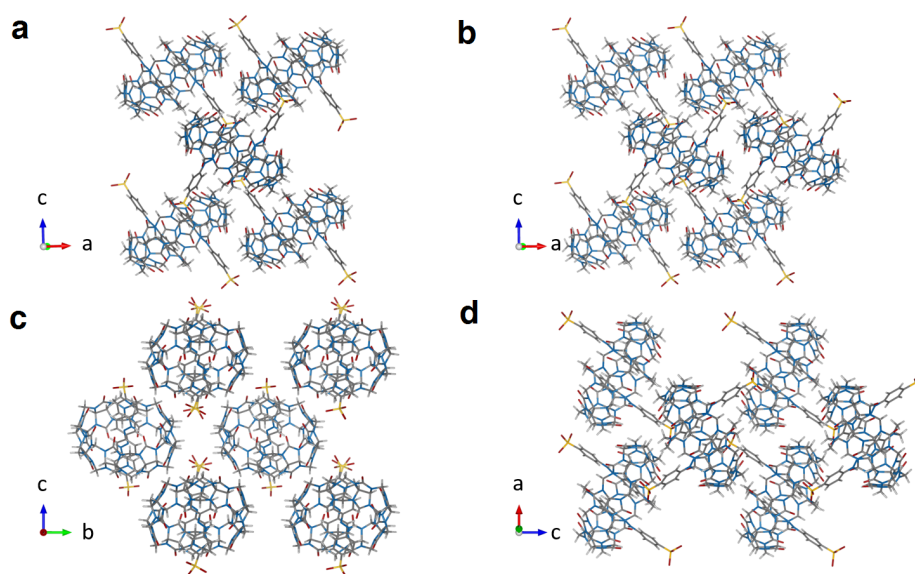


Figure 3.10: **a**, The original lattice used in the attachment energy model. **b**, The growth slice used in the attachment energy model along the a-axis direction. **c**, The growth slice used in the attachment energy model along the b-axis direction. **d**, The growth slice used in the attachment energy model along the c-axis direction.

to study the attachment energy to a growth slice of lattice along the **a**, **b**, **c**-axis (Figure 3.10), due to its acceptable performance through recent benchmarks calibrations.<sup>197</sup> The QEq (charge equilibration) formalism<sup>195</sup> is also adopted to compute the electrostatic force. The Coulombic contribution in the attachment energy is evaluated through the equation:

$$\frac{E_{Dreiding+QEq} - E_{Dreiding}}{E_{Dreiding+QEq}} \quad (3.3)$$

The results of the calculations are listed in Table 3.2

Absorption Energy (kcal/mol)	a	b	c
DREIDING	-66.4	-45.5	-37.5
DREIDING+QEq	-94.7	-61.4	-58.1
Electrostatic Interaction	-28.3	-15.9	-20.6
Coulomb contribution	29.9%	25.9%	35.5%

Table 3.2: The absorption energy of attaching a growth slice of molecule to the lattice using DREIDING force field and DREIDING force field with QEq formalism.

### 3.6.1.3 Quantum mechanics calculation

Quantum mechanics calculations have been applied to study the electronic structure properties in 2MO@CB[8] complexes. All the quantum mechanics calculations are done in gas phase using Gaussian 09 program.<sup>198</sup> We use the CAM-B3LYP<sup>199</sup> long-range corrected hybrid exchange-correlation functional with the 6-31g(d)<sup>200,201</sup> basis set to optimise the hydrogen positions of 2MO@CB[8] molecule and calculate its partial charge density. The Grimme's DFT-D3<sup>202</sup> correction is also adopted to count for the dispersion interaction between host and guest. In the polarisability calculation, due to the non-orthogonality of the triclinic crystal. The molecule cluster has been re-oriented to ensure the  $x,y,z$  axes of molecule cluster are aligned with the  $\mathbf{a}, \mathbf{b}, \mathbf{c}$  axes of lattice. The polarisabilities along the  $\mathbf{a}, \mathbf{b}, \mathbf{c}$  axes, which are corresponding to  $\alpha_{xx}, \alpha_{yy}, \alpha_{zz}$  respectively, are obtained from calculations of corresponding molecule cluster orientation. The same treatment has been employed in the field-involved calculations. We sampled several electric field strengths starting from the value close to the electric field of water, which is 70 MV/cm, in equivalent to 0.013 Hartree.<sup>203</sup> The results are listed in the Table.3.3. The changes of anisotropic dipole moment when  $\mathbf{a}_{x,y,z}$ -traversed static electric field is applied and consistent with the polarisability results.

Field Strength (Hartree)	0.01	0.02	0.04
a(x)-traversed	$ \Delta\mu_a  = -5.64$	$ \Delta\mu_a  = -11.29$	$ \Delta\mu_a  = -22.61$
b(y)-traversed	$ \Delta\mu_b  = -4.89$	$ \Delta\mu_b  = -9.77$	$ \Delta\mu_b  = -19.55$
c(z)-traversed	$ \Delta\mu_c  = -6.65$	$ \Delta\mu_c  = -13.31$	$ \Delta\mu_c  = -26.73$

Table 3.3: The change of dipole moment with respect to the introducing static electric field in different directions. The results show that the dipole moment change along the  $\mathbf{c}$  direction is more than that along the  $\mathbf{a}$  direction. The dipole moment along the  $\mathbf{b}$  direction has the least response to the electric field. The results match with the Coulomb contribution and the polarisability interpretation and the experimental phenomenon.

### 3.6.1.4 $-\text{SO}_3^-$ direction

According to the symmetry of the complex, there are only two kinds of  $\text{SO}_3^-$  group in the primitive cell. The fraction coordinates subtraction of sulfur and connecting carbon atoms gives the direction vector of the  $\text{SO}_3^-$  group, (Table 3.4, Figure 3.11).

	S atom coordinates	C atom coordinates	Orientation Vector
1st $\text{SO}_3^-$ group	(0.4449, 0.4968, -0.3196)	(0.3849, 0.5087, 0.2411)	(-0.060, 0.012, 0.078)
2nd $\text{SO}_3^-$ group	(0.0572, 1.0141, 0.1829)	(0.1133, 0.9997, 0.2579)	(0.056, -0.014, 0.075)

Table 3.4: The fractional coordinates of S and connecting C atoms in the two kinds of  $\text{SO}_3^-$  groups. The subtraction of the S and connecting C coordinates give the orientation vector of the  $\text{SO}_3^-$  group.

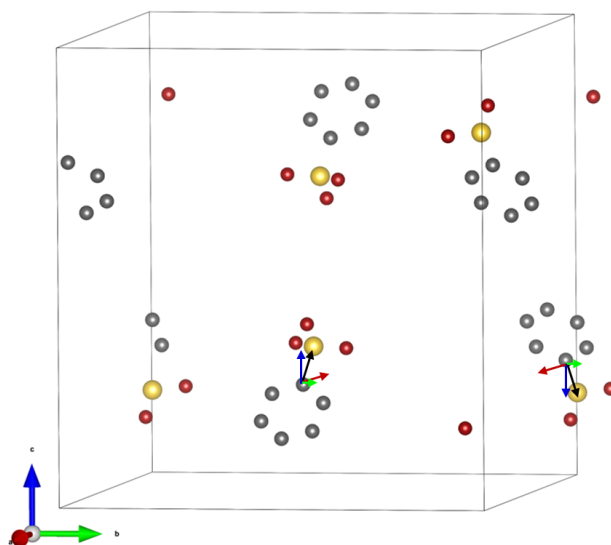


Figure 3.11: The vector of  $-\text{SO}_3^-$  groups and its decomposition to the a,b and c axes.

## 3.6.2 Materials and general methods

All starting chemicals were purchased from Sigma Aldrich and used as received unless stated otherwise. CB[7] and CB[8] were prepared according to previously published protocols.<sup>16,177</sup>

Microscopic images were obtained by using an Olympus IX81 inverted optical microscope coupled with a camera of Andor Technology EMCCD iXonEM DU 897.

Statistical data was obtained by counting the number of crystals in  $1.6 \times 1.6 \text{ cm}^2$  microscopic images. Each test was repeated five times.

### 3.6.3 Preparation and characterisation of shape-controlled 2MO@CB[8] crystals

120  $\mu\text{L}$  of MO (5 mM) solution was added to 5 mL of a 0.06 mM CB[8] solution. Then the system was adjusted to  $\text{pH} = 3$  through the addition of 0.2 M HCl, resulting in a transparent solution with the colour changing from orange to red. Needle-like crystals were obtained within 10 min. Sheet-like crystals were prepared through a similar method where the ionic strength of the solution was increased to 0.2 M before HCl addition by introducing NaCl. For needle-sheet complex-shaped crystals, NaCl was introduced after 20 min of HCl addition.

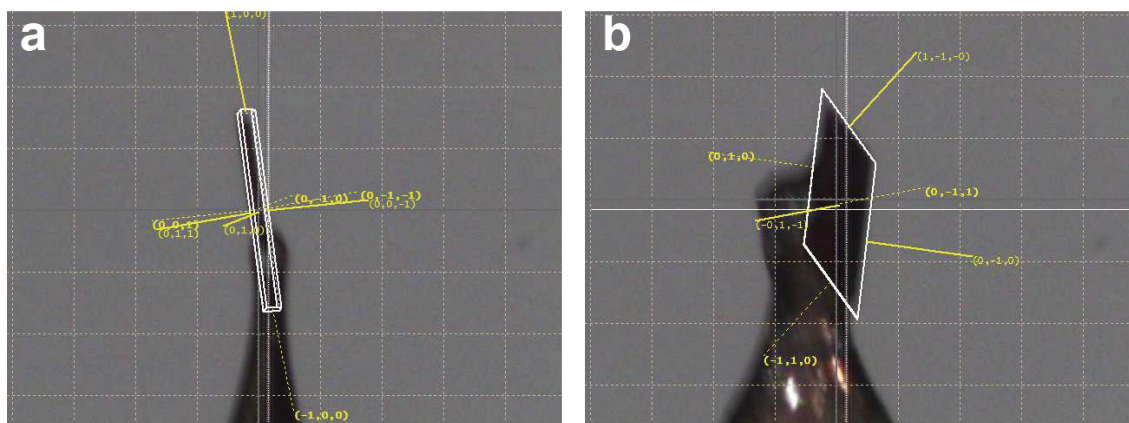


Figure 3.12: The face-index results of **a**, needle-like and **b**, sheet-like crystals.

### 3.6.4 Preparation and characterisation of oriented 2MO@CB[8] crystals

A glass surface was cleaned with a FEMTO plasma cleaner, then immersed into 5% ( $v/v$ ) (3-aminopropyl) triethoxysilane (APTES) anhydrous ethanol solution. After rinsing with ethanol, acetone and deionised (DI) water, the amino functionalised surface was immersed into a mixed solution of 0.06 mM CB[8] and 0.12 mM MO. Then the solution



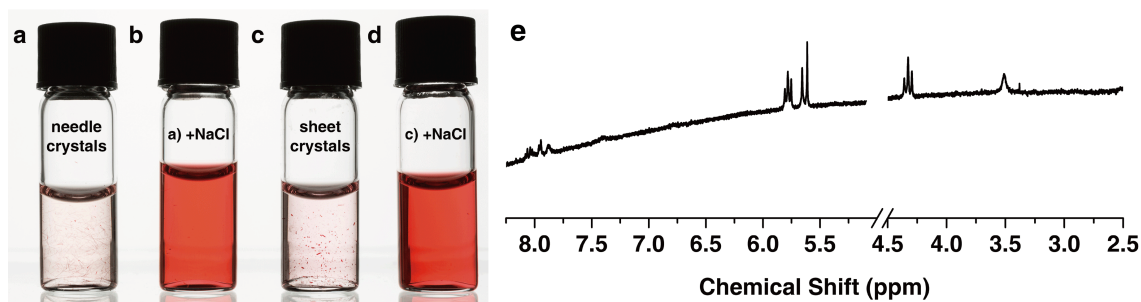


Figure 3.13: The samples of **a-b**, needle-like and **c-d**, sheet-like crystals before and after adding excess NaCl addition (after 10 s, final NaCl concentration = 1 M). **e**, <sup>1</sup>H NMR spectrum of deformed crystal sample by the addition of excess NaCl (final NaCl concentration = 1 M).

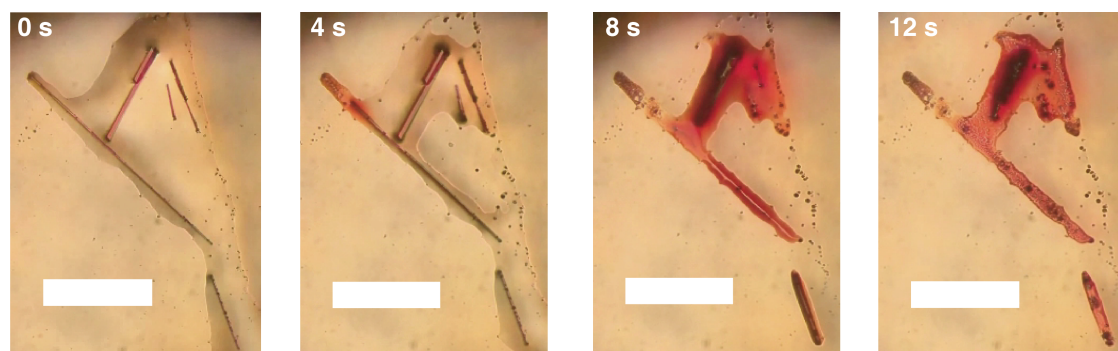


Figure 3.14: Microscopic images of 2MO@CB[8] crystal samples in a small amount of NaCl solution (0.3 M) at different time (0, 4, 8, 12 s) of solvent evaporation process (scale bar: 100  $\mu$ m). The images were taken within the last 12 seconds before the evaporation finished. The crystalline structure collapsed instantly due to the increased local ionic strength during H<sub>2</sub>O evaporation.

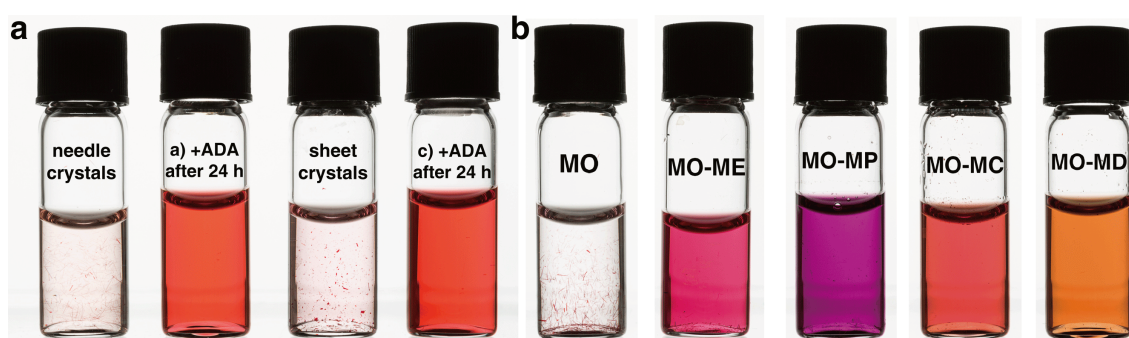


Figure 3.15: **a**, The samples of needle-like and sheet-like crystals before and after adding competitive guest 1-adamantylamine (after 24 h). **b**, Samples of Azo-MO-CB[8] systems with different Azo derivatives at pH = 3 after 24 h.

was adjusted to pH = 3 through the addition of HCl. Oriented crystals were obtained within 12 h, and washed with DI water to remove any physically attached crystals. The top view of the vertical crystals and the control sample without surface modification are shown in Figure 3.16a and 3.16b respectively.

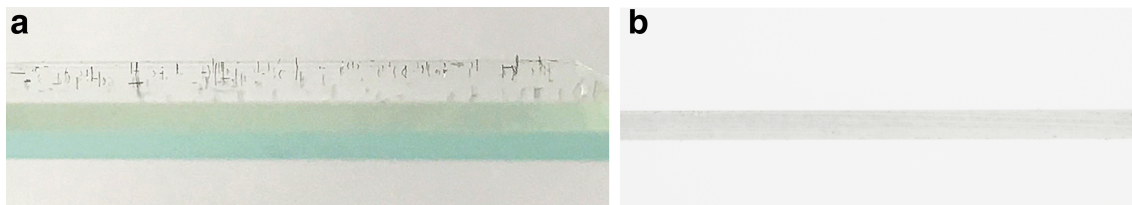


Figure 3.16: **a**, Pictures of the top view of vertical crystals on glass surface. **b**, Pictures of the control sample without surface modification.

## Chapter 4

# Conjugation of micelles and nanoparticles *via* CB[8] host-guest chemistry

The preparation and TEM characterisation of the nanoparticles in this chapter were carried out in collaboration with Xiaohe Ren from Department of Chemistry, University of Cambridge.

This work has been included in the following peer-reviewed article:

Liu, C.<sup>‡</sup>; Ren, X.<sup>‡</sup>; Wu, Y.; Scherman, O. A. 'A novel surfactant recycling system based on cucurbit[8]uril-mediated host-guest chemistry'. (submitted)

Previous chapters have introduced the application of Azo-CB[8] complexes in crystalline constructs. In this chapter, CB[8] and Azo derivatives are exploited to build composite materials, where a novel cucurbit[8]uril (CB[8])-mediated micelle-nanoparticle complex (MNC) has been proposed in order to recycle surfactant micelles in aqueous phase. Firstly, azobenzene (Azo)-functionalised amphiphilic diblock co-polymers have been prepared and self-assembled into micelles. The hydrophobic molecule, Nile Red, is chosen as a model cargo, which can be trapped within the micelles. Secondly, through the adsorption of micelles onto the surface of CB[8] catenane-functionalised SiO<sub>2</sub> nanoparticles (NPs) *via* MV/*trans*-Azo@CB[8] complexation, MNC structure has been fabricated. The obtained MNCs can be collected in proximity to a magnet on account of the iron NPs loaded inside the SiO<sub>2</sub> NPs. Owing to the photo-isomerisation of the Azo moiety, the micelles can be re-dispersed in water upon UV irradiation. Finally, the hydrophobic mo-

lecules trapped in the micelle cavity have been released in a controllable manner *via* pH or thermal stimuli. Interestingly, both the micelles and NPs can be recycled after their use.

## 4.1 Introduction

Surfactants play an important role in both fundamental science and our daily life. For example, soap and detergents, the typical amphiphilic surfactants, are composed of both hydrophobic and hydrophilic segments. During the cleaning process in aqueous environment, the hydrophobic tails pack together into the core, surrounded by hydrophilic headgroups. The hydrophobic molecules (*i.e.* oils, waxes and lipophilic dirt) can be encapsulated in the micelle cavity and removed from the aqueous system. Among various surfactants, polymeric micelles have sparked a great interest on account of their applications in detergents,<sup>204,205</sup> drug delivery and controlled release.<sup>206–208</sup> Micelles offer several advantages over other nanocarriers.<sup>209–211</sup> The core-shell structure of micelles allows the loading of water insoluble drugs into the hydrophobic core, increasing water solubility and *in vivo* compatibility.<sup>212,213</sup> Their small size also provides excellent drug delivery capabilities. Some typical structures of block co-polymers are shown in Figure 4.1a. After tuning the polymer chain arrangements, the amphiphilic block co-polymers are able to assemble themselves to spherical micelles, cylindrical micelles, vesicles, lamellae and bicontinuous structures, depending the ratio of each block (Figure 4.1b).<sup>214,215</sup>

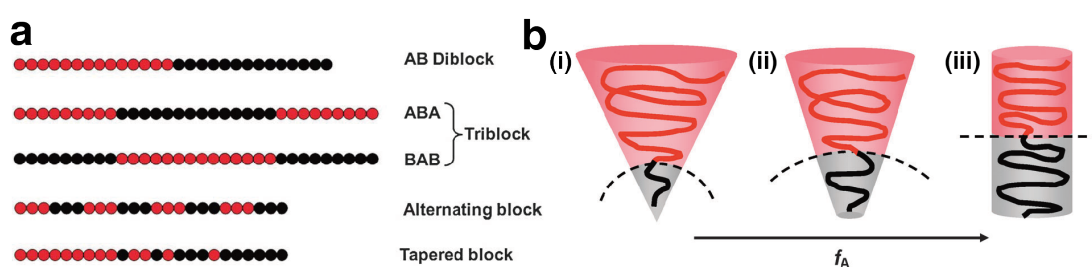


Figure 4.1: **a**, Typical structures of block co-polymers containing A and B blocks. **b**, Schematic illustration of the possible polymer chain arrangements in different morphologies of AB diblocks changing from **i**, sphere to **ii**, cylinder and to **iii**, lamella, as the volume fraction of the A block (black) increases to  $\sim 0.5$ . The dash curve in each morphology represents a part of the interface between A and B domains.<sup>214</sup>

With the development of living/controlled polymerisations, such as Atom Transfer Radical Polymerisation (ATRP),<sup>216,217</sup> Nitroxide-Mediated Polymerisation (NMP)<sup>218</sup> and Reversible Addition Fragmentation Transfer (RAFT),<sup>219,220</sup> a variety of stimuli-responsive amphiphilic co-polymers have been synthesised. These 'smart' co-polymers have given birth to micellar systems that responsive to various external stimuli,<sup>212,221</sup> such as temperature,<sup>222</sup> pH<sup>223</sup> and UV light.<sup>224</sup> As a typical pH-responsive polymer, poly[2-(N,N-dimethylamino) ethyl methacrylate] (PDMAEMA) displays changing water solubility with varying pH, depending on the degree of protonation of dimethylamino moieties ( $pK_a=7.6$ ).<sup>225</sup> Over the past two decades, a series of PDMAEMA-based amphiphilic block co-polymers have been synthesised through ATRP<sup>216</sup> and RAFT<sup>219,220</sup> techniques, which has led to the synthesis of a variety of pH-responsive systems.<sup>226</sup> Another example, poly(*N*-isopropyl acrylamide) (PNIPAM) is known for its outstanding thermal-responsive property. The hydrophilic polymer chain of PNIPAM displays a phase transition to a hydrophobic structure during the temperature increase from below to above the lower critical solution temperature (LCST, 32 °C for PNIPAM).<sup>227</sup> A block co-polymer with dual responsiveness, PNIPAM-*b*-PDMAEMA can be synthesised *via* RAFT polymerisation, where the first polymerised PDMAEMA is employed as the macro-CTA (chain transfer agent) to mediate further polymerisation of NIPAM monomers.<sup>228,229</sup>

Most polymeric micelles are prepared through tedious synthetic procedures,<sup>209,230,231</sup> but unfortunately few of them can be recycled. Therefore, in order to overcome these challenges, it is worthwhile to design an efficient recycling system for micelle-based surfactants and drug carriers. Host-guest chemistry has been widely applied to design various reversible systems due to the dynamic nature of non-covalent binding.<sup>35,232,233</sup> As an important member of macrocyclic hosts, CB[8] is capable of exploiting as a dynamic linker to build supramolecular architectures among different systems, including silica nanoparticles,<sup>23</sup> gold nanorods<sup>75</sup> and solid substrates, due to its ability to accommodate two guests.<sup>78</sup> Therefore, CB[8] possesses a great potential in the design of micelle-based recycling systems, in which it will act as a molecular 'hand-cuff' to build substructures.

Catenanes, with special mechanically-interlocked molecular architectures,<sup>234-239</sup> have

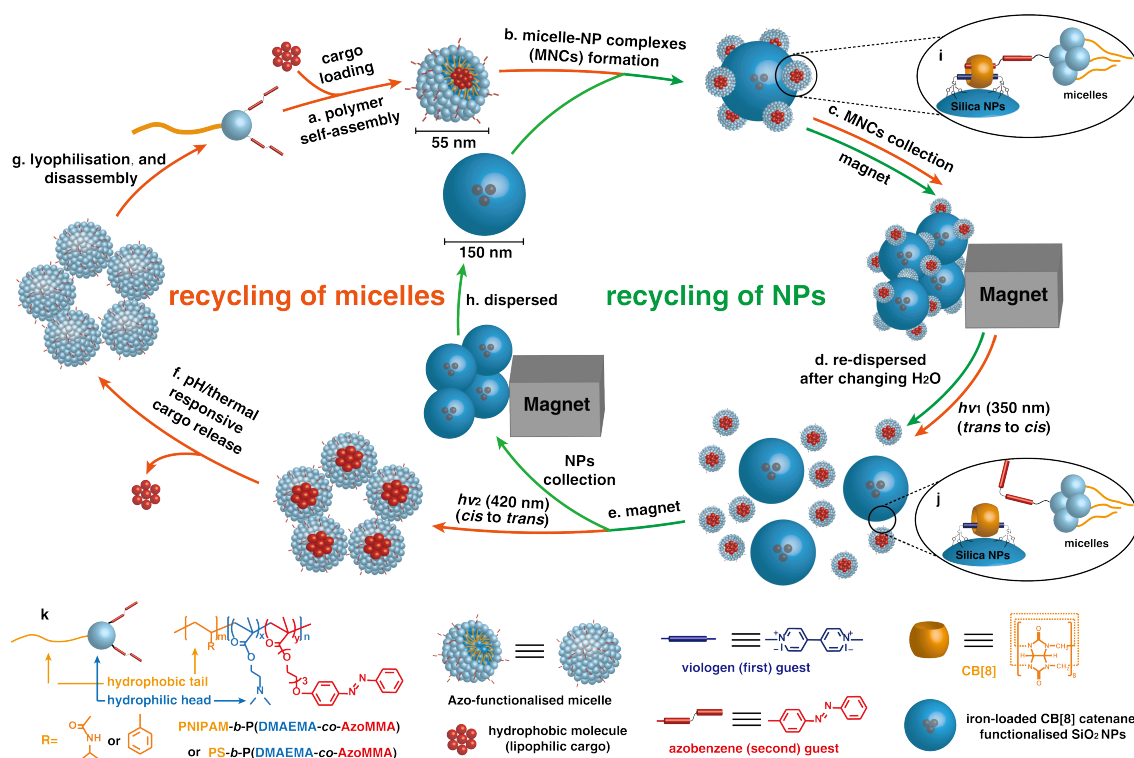


Figure 4.2: Schematic illustration of the dual recycling system through MNCs. During the micelle recycling process, the hydrophobic molecules can be **a**, collected and **f**, controlled-released, while both the micelles (orange cycle) and NPs (green cycle) can be recycled and re-utilised through the reversible assembly of MNCs. **i**, The MNC structure formed by the MV/*trans*-Azo@CB[8] ternary complex. **j**, The disassembly of MNC due to *trans* to *cis* isomerisation of the Azo guest. **k**, The hydrophilic head and hydrophobic tail of Azo-functionalised amphiphilic diblock co-polymers.

been exploited as molecular machines,<sup>240,241</sup> sensors,<sup>242,243</sup> and switches.<sup>244–247</sup> Recently, a surface-bound CB[8] catenane has been reported by our group, where MV@CB[8] has been immobilised onto magnetic silica NPs.<sup>24</sup> By taking advantage of the redox-responsive behaviours of MV, CB[8] catenanes have been used as a nano-platform for peptide separation (Figure 1.15, chapter 1). Inspired by this, a novel micelle-nanoparticle complex (MNC) system constructed *via* the host-guest complexation of CB[8] catenanes is proposed.

In this chapter, a dual recycling system has been designed in order to collect surfactant micelles from aqueous solution (Figure 4.2). Firstly, Azo-functionalised amphiphilic block co-polymers have been prepared and assembled into cargo-loaded micelles, with

the hydrophobic molecules (Nile Red as a lipophilic cargo) encapsulated in the core (Figure 4.2a and 4.2k). Secondly, with the introduction of iron-loaded CB[8] catenane-functionalised SiO<sub>2</sub> nanoparticles (NPs), the loaded micelles are assembled onto the surface of NPs, forming micelle-nanoparticle complexes (MNCs) (Figure 4.2b and 4.2i). Those complexes are collected in proximity to a magnet (Figure 4.2c). Next, the MNCs are re-dispersed in water under UV irradiation (*trans-cis* isomerisation), resulting in separated micelles and NPs (Figure 4.2d and 4.2j). The micelles can be further isolated after the removal of NPs with a magnet (Figure 4.2e). Finally, the hydrophobic cargoes can be released in a controllable manner on account of the stimuli-responsive properties of the polymer backbone (Figure 4.2f). In conclusion, both the micelles (Figure 4.2, orange cycle) and NPs (Figure 4.2, green cycle) have been recycled and re-utilised (Figure 4.2g-4.2h). The experimental details can be found in the Experimental Section.

## 4.2 Azo-functionalised micelles

Azo methyl methacrylate (Azo-MMA) monomer (Figure 4.3a) has been used to synthesise two Azo-functionalised amphiphilic diblock co-polymers: PS-*b*-P(DMAEMA-*co*-AzoMMA) and PNIPAM-*b*-P(DMAEMA-*co*-AzoMMA), dubbed as PS-based and PNIPAM-based polymer respectively. Subsequently, these polymers have been self-assembled to micelles in an aqueous media (Figure 4.2a). Finally, their cargo loading and thermal/pH stimuli-responsive cargo release behaviours have been investigated (Figure 4.2a and 4.2f).

### Azo-functionalised amphiphilic block co-polymers

Azo-MMA has been utilised in this project on account of its structural similarity to DMAEMA. The chemical structure and synthetic procedure of Azo-MMA is shown in Figure 4.3a. The ethylene glycol unit between MMA and Azo is designed to enhance the flexibility and water solubility of the monomer. Azo-functionalised amphiphilic diblock co-polymers were synthesised through a stepwise manner *via* RAFT polymerisation. The first block of P(DMAEMA-*co*-AzoMMA) was synthesised through a one-pot RAFT polymerisation of DMAEMA and AzoMMA monomers (Figure 4.3b). <sup>1</sup>H NMR spectroscopy suggests that the block length of PDMAEMA is around 77 with an Azo/DMAEMA

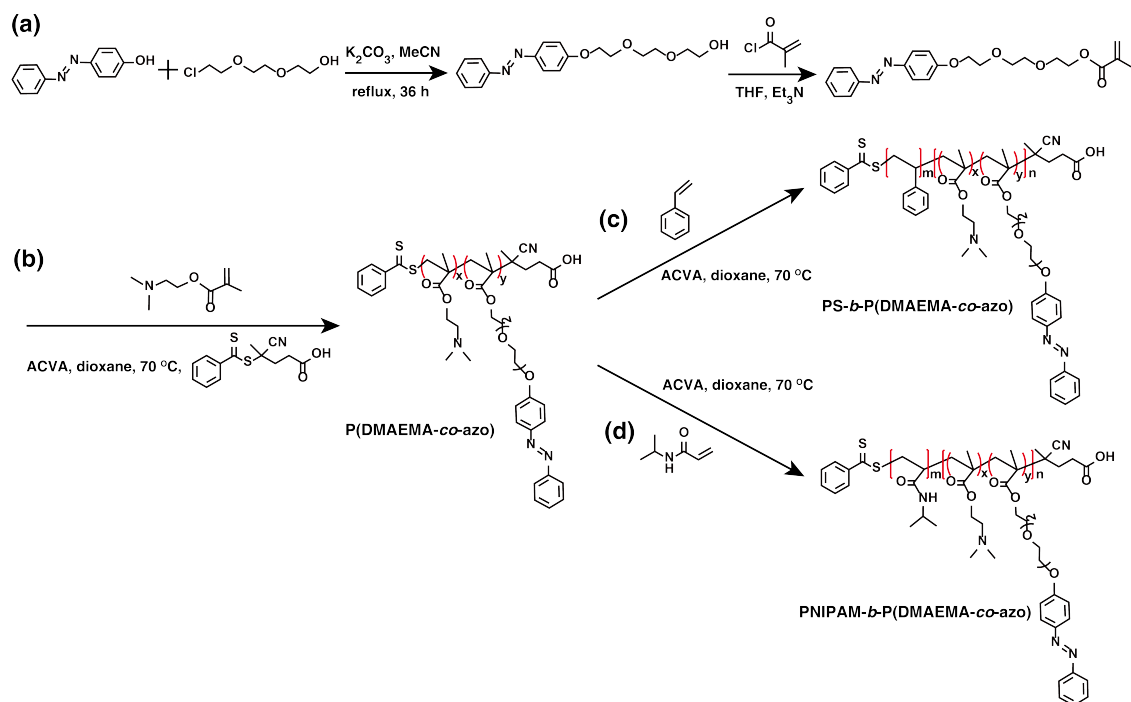


Figure 4.3: Synthetic procedures forming Azo-functionalised amphiphilic block co-polymers.

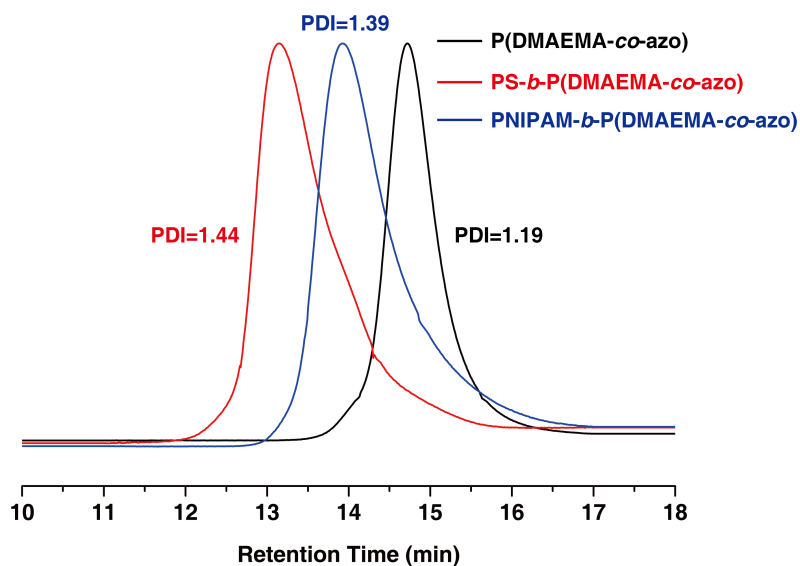


Figure 4.4: GPC curves of P(DMAEMA-co-AzoMMA), PS-*b*-P(DMAEMA-co-AzoMMA) and PNIPAM-*b*-P(DMAEMA-co-AzoMMA).



ratio of 3 %. Details can be found in the Experimental Section. Next, P(DMAEMA-co-AzoMMA) acted as macro-CTA (chain transfer agent) to mediate the following extension of the second PS/PNIPAM segments (Figure 4.3c, 4.3d). As shown in Figure 4.4, gel permeation chromatography (GPC) analysis confirmed an increase of  $M_n$  from 10 kDa to 35 kDa (for PS-based co-polymer) and to 32 kDa (for PNIPAM-based co-polymer) when the polymer chain extended from P(DMAEMA-co-AzoMMA) to diblock co-polymers.

#### Characterisation of Azo-functionalised micelles

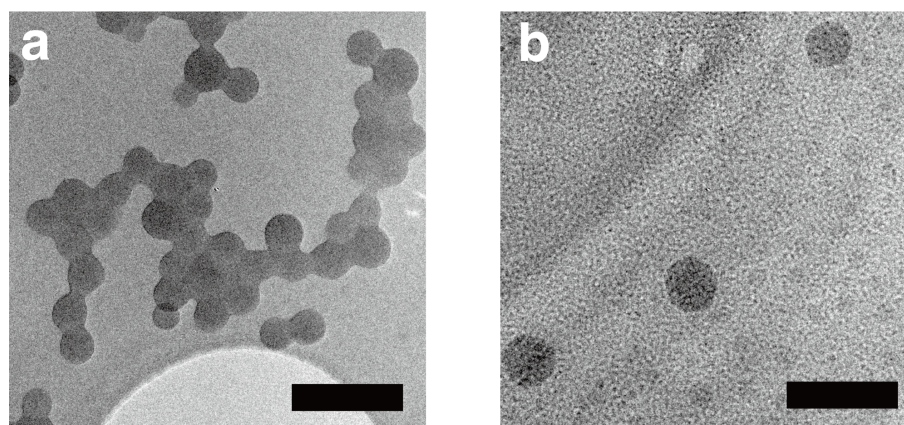


Figure 4.5: **a**, TEM image of PS-based micelles at pH=7 (Scale bar: 180 nm). **b**, TEM image of PNIPAM-based micelles prepared at 40 °C (Scale bar: 150 nm).

During the self-assembly in water, the Azo-functionalised hydrophilic head is stretched into water while shielding the hydrophobic PS/PNIPAM tail in the core. TEM images (Figure 4.5) show spherical micelles with diameters of around  $55 \pm 5$  nm and  $60 \pm 5$  nm of PS-based and PNIPAM-based micelles respectively. The statistical data (based on 50 micelles) of the micellar size can be found in Figure 4.17a (Experimental Section). The size dispersion is probably due to the broad polymer length distribution. The TEM sample of PNIPAM-based micelle was prepared at 40 °C. Some air bubbles were formed due to the quick solvent evaporation under high temperature, which were surrounded by some polymers, likely resulting in the light-colour spherical objects in the background of Figure 4.5b. However, those small grey objects were not included in the size distribution in Figure 4.17a. The  $\zeta$  potential curves in Figure 4.17b (Experimental Section) suggests that both the PS-based (39.6 mV) and PNIPAM-based micelles (23.1 mV) are electronically positive. As shown in Figure 4.2a, the hydrophobic molecules can be encapsulated

inside the micelle. Nile Red, the commonly used lipophilic stain, has been utilised in this thesis as a model of hydrophobic cargoes. The critical micelle concentrations (CMC) have been recorded as 0.028 and 0.053 mg/mL for PS-based and PNIPAM-based micelles respectively (Figure 4.18, Experimental Section).

### The stimuli-responsive properties of Azo-functionalised micelles

The stimuli-responsive behaviours of these micelles were investigated by the dynamic light scattering (DLS) measurement. For PS-based micelles, a series of samples were prepared at different pH conditions (in Britton-Robinson buffer). As shown in Figure 4.6a, the diameter of PS-based micelles decreased up to 35% when the pH of the system increased from 2 to 12, on account of the deprotonation of the dimethylamino moieties. Hence, the corona of the micelle would shrink into the hydrophobic core, leading to a decrease in micellar size. In addition, compared with TEM results, the larger size of the micelle, measured by DLS is likely due to the water shell surrounding the micelles, since the hydrodynamic diameter is typically larger than the dehydrated samples determined by TEM.

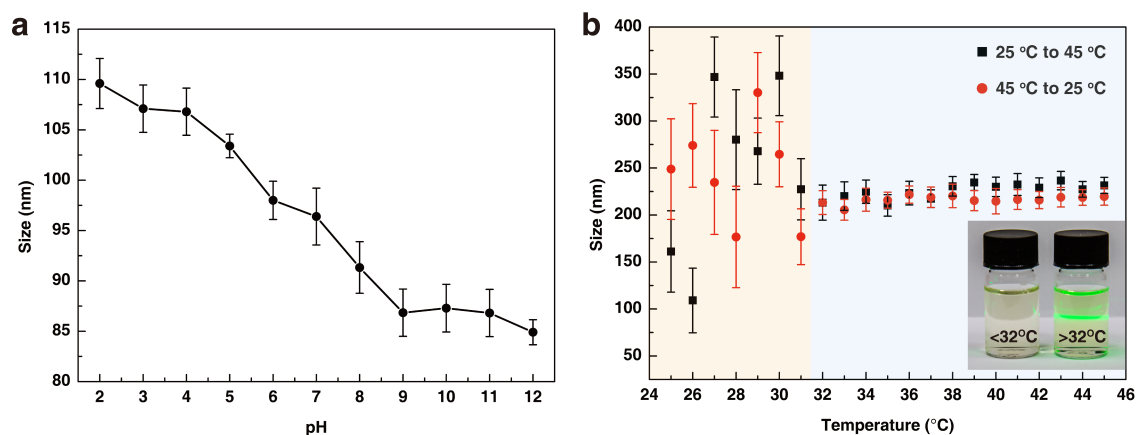


Figure 4.6: **a**, Size of PS-based micelles as a function of pH, showing a 35% size decrease with pH changing from 2 to 12. **b**, Size of PNIPAM-based micelles as a function of temperature from 25 °C to 45 °C (black plots) and back (red plots). A constant size can be collected from above 32 °C. Insert image: solutions of PNIPAM-based micelles with green laser, showing the tyndall effect above 32 °C.

DLS test of PNIPAM-based micelles was carried out at different temperatures. The stable data could only be collected when the temperature is above the LCST (32 °C, Fig-

ure 4.6b), suggesting the formation of micelles. Indeed, with the temperature increase, the hydrogen bonds between NIPAM moieties and water molecules broken, resulting in a more hydrophobic PNIPAM segment. Above the LCST, the polymer was transformed from hydrophilic to amphiphilic form, which further displayed self-assembling properties.

### The responsive cargo release of micelles

Furthermore, based on this stimuli-responsive self-assembly, the loaded-micelles should possess controlled cargo release behaviours. This process can be monitored by fluorescent spectroscopy through employing Nile Red as a model cargo. As shown in Figure 4.7a, PS-based micelles demonstrated an enhanced release rate while pH decreased. After 24 h, the cargo release percentage of the sample at pH=3 increased to 34%. This value is much higher when compared with its counterpart at pH=11 (5%). This is because the protonated amino groups of PDMAEMA segment at lower pH would lead to micelle swelling and accelerate the cargo release. For PNIPAM-based micelles, more than 50% cargoes were released within 5 hours at 25 °C, which is even higher than its counterpart at 40 °C after 72 h (Figure 4.6b), due to the micelle deformation under LCST. Therefore, the hydrophobic cargoes loaded by these novel Azo-functionalised micelles can be released in a controlled manner upon different stimuli, which is demonstrated in Figure 4.2f.

## 4.3 Self-assembly of Azo-functionalised micelles and silica nanoparticles

In this section, a new **MNC** structure has been prepared after using MV/*trans*-Azo@CB[8] ternary complex. PS-based micelles have been used as an example to test the feasibility of this method. The experimental data for PNIPAM-based **MNCs** are presented in the Experimental Section. MV-functionalised silica NPs have been first used to test the possibility of bridging micelles and NPs through CB[8] host-guest interactions. Then more advanced **MNC** structures have been obtained through employing CB[8] catenane-

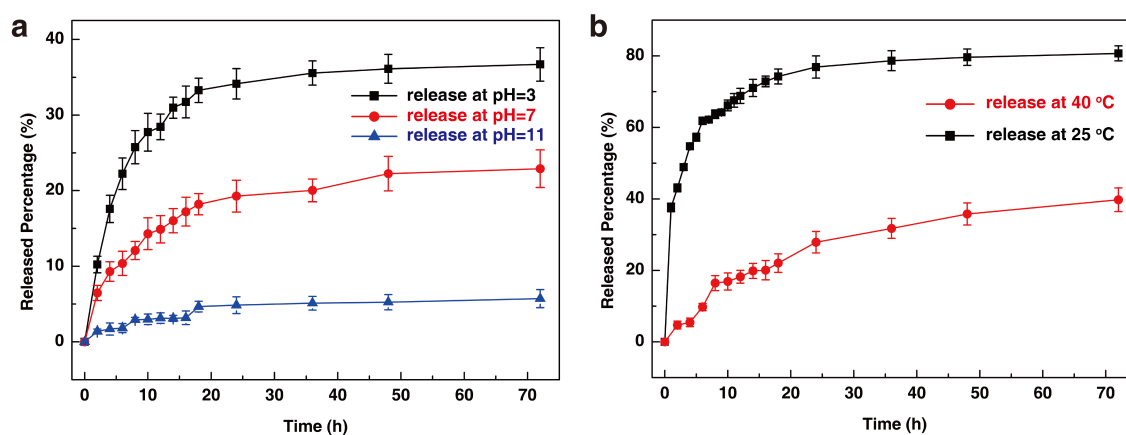


Figure 4.7: **a**, Release percentage of Nile Red molecules from PS-based micelles as a function of time for three different pH values in Britton-Robinson buffer at 25 °C. **b**, Release percentage of Nile Red molecules from PNIPAM-based micelles as a function of time at 25 and 40 °C.

contained magnetic SiO<sub>2</sub> NPs. At last, this approach has been further exploited to an efficient micelle recycling system.

#### Self-assembly between Azo-functionalised micelles and MV-functionalised SiO<sub>2</sub> NPs

In order to investigate the self-assembly between the micelles and SiO<sub>2</sub> NPs, MV-functionalised silica NPs were employed as the preliminary attempt. MV-functionalised SiO<sub>2</sub> NPs were first mixed with CB[8] to yield inclusion complexes (MV@CB[8]) on the NP surface (Figure 4.8a and 4.8b), then PS-based Azo-functionalised micelles were introduced to the mixture (Figure 4.8c). As shown in the TEM images (Figure 4.9), complex structures have been formed *via* CB[8] complexation, where the micelles act as ‘linkers’ to conjugate silica NPs. Therefore, the non-covalent CB[8] host-guest interactions are capable of connecting micelles and NPs. The detailed synthetic procedures and characterisations can be found in the Experimental Section.

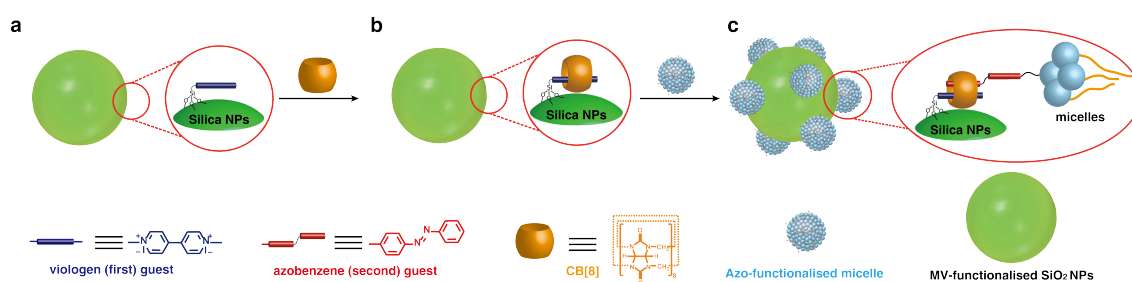


Figure 4.8: Schematic illustration of **a**, MV-functionalised SiO<sub>2</sub> NP; **b**, MV@CB[8]-functionalised SiO<sub>2</sub> NP and **c**, the complex structure between Azo-functionalised micelles and MV-functionalised SiO<sub>2</sub> NP *via* CB[8].

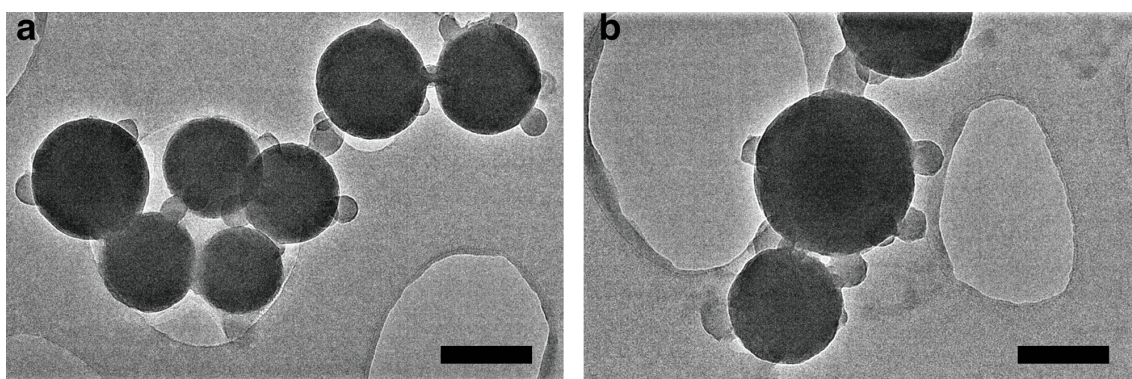


Figure 4.9: TEM images of the self-assembly of Azo-functionalised micelles and MV-functionalised SiO<sub>2</sub> NPs. Scale bar: **a**, 180 nm, **b**, 200 nm.

#### Self-assembly between Azo-functionalised micelles and CB[8] catenane-functionalised magnetic SiO<sub>2</sub> NPs

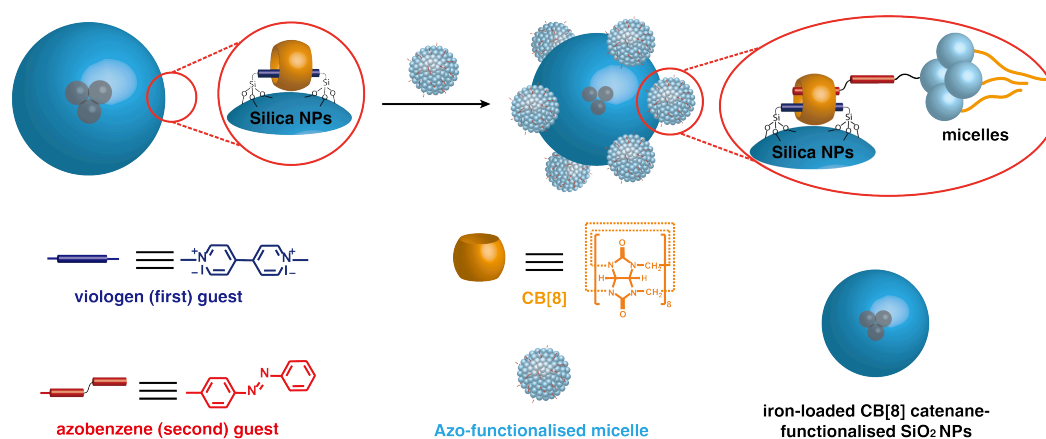


Figure 4.10: Schematic illustration of the formation of MNC structure through employing Azo-functionalised micelles and CB[8] catenane-functionalised magnetic SiO<sub>2</sub> NPs.

As shown in Figure 4.10, CB[8] catenane-functionalised NPs have been employed to assemble **MNCs**. CB[8] catenane-contained magnetic SiO<sub>2</sub> NPs were prepared according to our previous work.<sup>24</sup> **MNCs** were prepared through the addition of micelle solution to the aqueous dispersion of SiO<sub>2</sub> NPs. A new peak with a larger average hydrodynamic diameter (around 369 nm) can be observed from the DLS measurement (Figure 4.11a), suggesting the formation of **MNCs**. Furthermore, TEM images in Figure 4.11b-4.11d demonstrate that each SiO<sub>2</sub> NP (dark colour with a diameter of around 150 nm) is assembled with 3-4 micelles (light color with a diameter of around 55 nm). The multiple linking between micelles and NPs in Figure 4.11b and 4.11c is due to the drying effect in the TEM grid, since from DLS data, no aggregation has been observed in aqueous phase. Moreover,  $\zeta$  potential values (Experimental Section) suggest that both catenane-functionalised SiO<sub>2</sub> NPs ( $\sim$ 35.5 mV) and micelles ( $\sim$ 39.6 mV) are positively charged, confirming that the **MNC** is not formed by electrostatic forces. Additionally, the iron NPs can be observed inside the SiO<sub>2</sub> NPs.

#### 4.4 Applications of micelle-nanoparticle complexes

Utilising the iron NPs inside SiO<sub>2</sub> NPs, the **MNCs** can be collected in proximity to a magnet (Figure 4.2c). Moreover, owing to the photo-responsive property of the Azo moiety, **MNCs** can be disassembled into the original micelles and NPs (Figure 4.2d and 4.2j). In this way, we have demonstrated that **MNCs** can be used to recycle micelles in aqueous solution. During the dual recycling cycle in Figure 4.2, both the micelles and NPs can be recycled and re-utilised. In order to test the recycling efficiency during the assembly and disassembly of **MNCs**, two separate experiments have been designed for micelles and NPs respectively, where Nile Red-loaded micelles are employed to monitor the recycling process through fluorescent spectroscopy.

The recycling efficiency test of the micelles is shown in Figure 4.12a. The fluorescent intensity of Nile Red-loaded PS-based micelles was recorded. After the assembly of **MNCs** (stage 1), a magnet was utilised to collect the **MNCs** (stage 2). Next, the **MNCs** were disassembled and re-dispersed under UV irradiation (stage 3). The TEM image of the

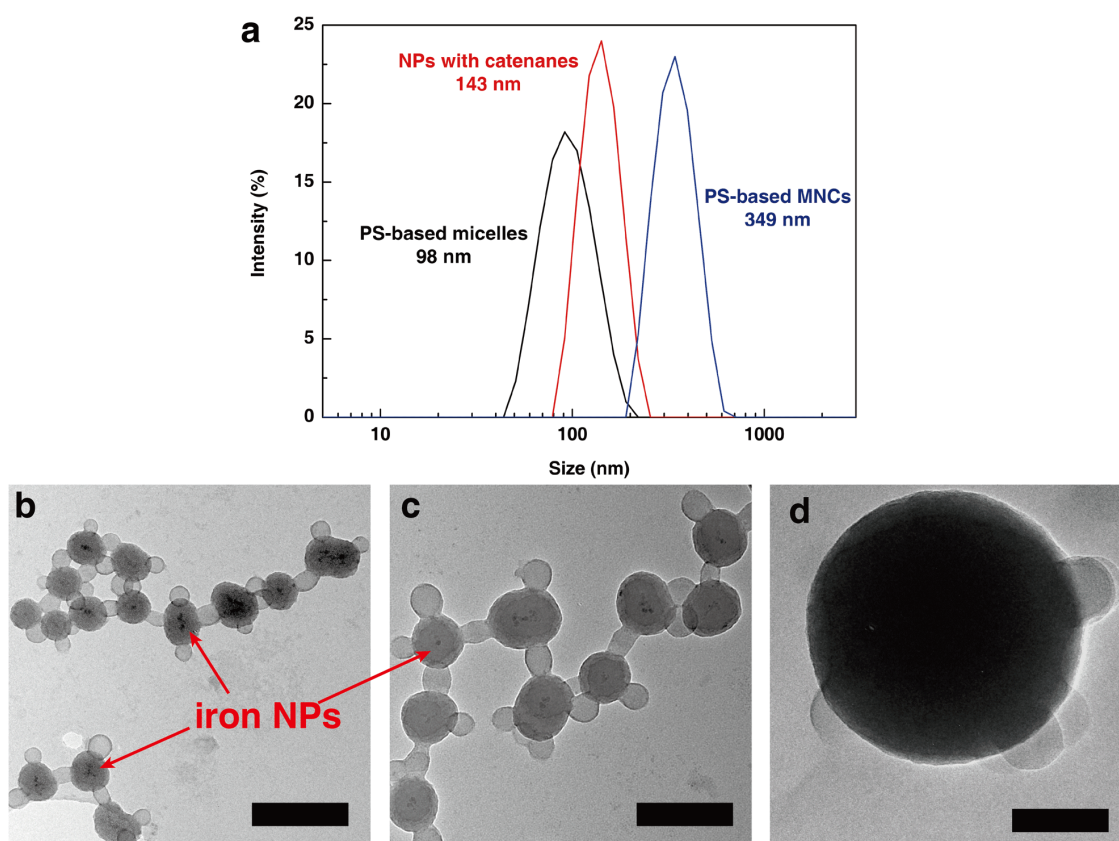


Figure 4.11: Characterisation of the PS-based MNC. **a**, DLS results of CB[8] catenane-functionalised magnetic  $\text{SiO}_2$  NPs, PS-based micelles and MNCs. **b-c**, TEM images of PS-based MNCs. Scale bar of **b**: 200 nm, **c**: 150 nm. The dark spherical iron NPs can be seen inside  $\text{SiO}_2$  NPs. **d**, TEM image of a single PS-based MNC (scale bar: 70 nm).

separated micelles and NPs at stage 3 is shown in Figure 4.12c. Finally, the number of the recycled micelles were recorded after removing the NPs (stage 4). Pictures of samples at different stages in the cycle are shown in Figure 4.12b. The solution at stage 2 exhibited the least fluorescent intensity, as the most cargo-loaded micelles were collected by the magnet. As shown in Figure 4.12d,  $\sim 90\%$  micelles were recycled (each single cycle), with an overall  $\sim 60\%$  efficiency after five cycles.

Another experiment was designed to test the recycling efficiency of NPs. As shown in Figure 4.13a, after the formation (stage 1) and disassembly (stage 3) of MNCs, the original NPs were collected (stage 4) and re-utilised to assemble with new micelles. Through testing the fluorescent intensity at stage 3, the retained NPs could be calculated. After five cycles, more than 80% ( $\sim 96\%$  of each cycle) NPs were retained (Figure 4.13b), suggesting

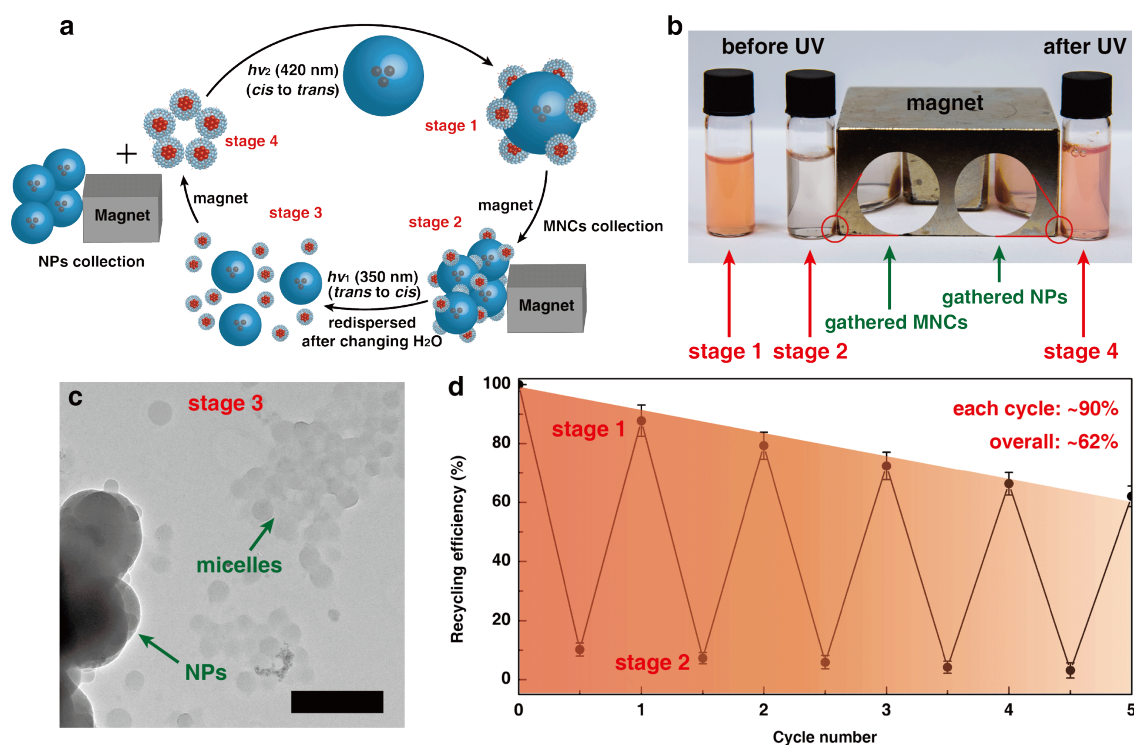


Figure 4.12: **a**, Schematic illustration of the recycling efficiency test of PS-based micelles. **b**, Pictures of the samples at different stages. **c**, TEM image of the solution after UV irradiation, where separated PS-based micelles and NPs can be observed (scale bar: 140 nm). **d**, Recycling efficiency of the sample after each single cycle (~90%) and after five cycles (~60%).

the outstanding efficiency of the MNC method. Therefore, the MNCs can be employed as an efficient tool for micellar recycling, while most of the micelles as well as NPs can be re-collected after the recycling process.

## 4.5 Conclusions

In conclusion, a composite system of MNC has been fabricated *via* MV/Azo@CB[8] heteroternary complexation. Firstly, Azo-functionalised amphiphilic block co-polymers have been prepared *via* RAFT polymerisation, which could subsequently assemble to micelles and act as pre-designed 'detergents' to encapsulate hydrophobic molecules (*i.e.* lipophilic cargoes) in aqueous solution. Next, a well designed MNC structure has been prepared *via* CB[8] mediated host-guest chemistry. Through the assembly and disassembly of MNCs, both the NPs and cargo-loaded micelles can be collected and isolated with a high ef-



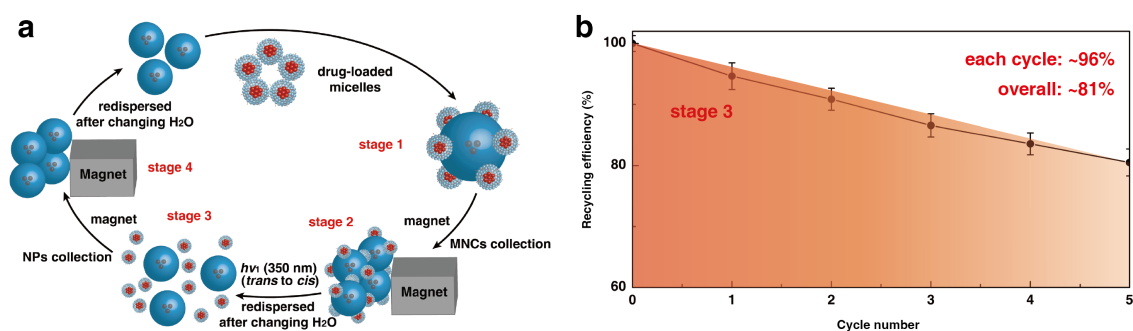


Figure 4.13: **a**, Schematic illustration of the recycling efficiency test of NPs. **b**, Recycling efficiency of the NPs. After five cycles, more than 80% (~96% of each cycle) NPs were retained.

efficiency. Finally, the cargoes inside the micelle cavity can be released in a controlled manner and the block co-polymers have been re-utilised. Therefore, MNCs provide a promising platform for the recycle of versatile drug carriers through host-guest chemistry.

## 4.6 Experimental

### 4.6.1 Materials and general methods

All starting chemicals were purchased from Sigma Aldrich and used as received unless stated otherwise. CB[8]<sup>16,177</sup> and iron-loaded CB[8] catenane-functionalised SiO<sub>2</sub> NPs<sup>24</sup> were prepared according to previously published protocols. Britton-Robinson buffer was used to adjust the pH for PS-based micelles. The N-isopropylacrylamide (NIPAM) and 4,4'-azobis(4-cyanovaleric acid) (ACVA) were recrystallised before use.

<sup>1</sup>H NMR (400 MHz) spectra were recorded using a Bruker Avance QNP 400. <sup>1</sup>H NMR (500 MHz) spectra were recorded using Bruker Avance QNP 500 Cryo Ultrashield. Chemical shifts were measured in ppm ( $\delta$ ) in D<sub>2</sub>O and CDCl<sub>3</sub> with the internal reference set to 4.79 ppm and 7.26 ppm respectively.

Number average molecular weight ( $M_n$ ), Weight average molecular weight ( $M_w$ ) and polydispersity ( $M_w/M_n$ ) were obtained by THF GPC. The THF GPC setup consisted of two 30 cm PLgel Mixed-C columns in series, eluted using THF and calibrated against a series of 12 near-monodisperse PMMA standards ( $M_p$  from 690 to 1,944,000 g/mol). The

polymers were analysed in THF at a concentration of 5.0 mg/mL. All calibrations and analysis were performed at 35 °C at a flow rate of 1 mL/min.

Fluorescent spectra were performed on an Eclipse fluorescence spectrophotometre at 25 and 45 °C. The excitation wavelength of the fluorescent measurements was 540 nm, with the monitored emission from 550 to 800 nm. The excitation and emission slit widths were 5.0 nm and the scan rate was 600 nm/min.

ATR FT-IR spectroscopy was conducted using a Perkin-Elmer Spectrum 100 series FT-IR spectrometre equipped with a universal ATR sampling accessory.

DLS and  $\zeta$ -potential measurements were performed on a Malvern Zeta-sizer NS90 equipment under different temperatures.

TEM characterisations were carried out on a FEI Philips Tecnai 20 TEM under an accelerating voltage of 80 kV. Samples were prepared by applying one drop of the as-synthesised microspheres onto a Holey R carbon coated copper TEM grid (400 mesh) and dried overnight at room temperature or 45 °C.

#### 4.6.2 Preparation and characterisation of Azo-functionalised micelles

**Azo-MMA.** Azo-MMA was synthesised by a two-step reaction (Figure 4.3a). For the first step, triethylene glycol monochlorohydrin (14.00 g, 84.00 mmol), potassium carbonate (22.96 g, 168.0 mmol) and 4-(phenyldiazenyl)phenol (33.31 g, 168.0 mmol) were placed in a 1000 mL flask with the addition of acetonitrile (420 mL). Then the system was stirred and refluxed under N<sub>2</sub> (g) for 36 h. After cooling to room temperature, excess K<sub>2</sub>CO<sub>3</sub> was removed by filtration, followed by the removal of acetonitrile. The crude product was dissolved in 50 mL DCM and washed (extraction) by HCl solution (0.1 M) three times and then washed with water. Then the product was concentrated by removing the volatiles, after which the solution was passed through a silica column by using ethyl acetate as the eluent. Finally, the relevant fractions were collected, combined and condensed *in vacuo* to give a red powder (19.40 g, 70%). <sup>1</sup>H NMR (400 MHz, CDCl<sub>3</sub>), 7.96 (d, 2H), 7.92 (d, 2H), 7.54 (t, 2H), 7.46 (d, 1H), 7.07 (d, 2H), 4.26 (t, 2H), 3.78 (t, 2H), 3.73 (m, 6H), 3.66 (t, 2H).<sup>21</sup>

Next, a solution of triethylene glycol azobenzene (6.00 g, 18.16 mmol) and triethylamine (3.78 mL, 27.24 mmol) in THF (100 mL) was cooled to  $-20\text{ }^{\circ}\text{C}$ . To this solution, methacryloyl chloride (2.64 mL, 27.24 mmol) in THF (25 mL) was added dropwise over 30 min. The mixture was stirred at room temperature for 24 h. Then the triethylammonium chloride salt and THF were removed by filtration and evaporation respectively. The crude product was washed with sodium bicarbonate solution (0.5 M) three times. After being purified by flash chromatography ( $\text{SiO}_2$ , 2:1 *v/v* ethyl acetate/hexane), the product Azo-MMA monomer was obtained as an orange oil (6.20 g, 85%).  $^1\text{H}$  NMR (400 MHz,  $\text{CDCl}_3$ ), 7.95 (d, 2H), 7.90 (d, 2H), 7.54 (t, 2H), 7.44 (d, 1H), 7.04 (d, 2H), 6.16 (s, 1H), 5.59 (s, 1H), 4.34 (t, 2H), 4.24 (t, 2H), 3.93 (t, 2H), 3.76 (m, 6H), 2.07 (s, 3H).<sup>21</sup>

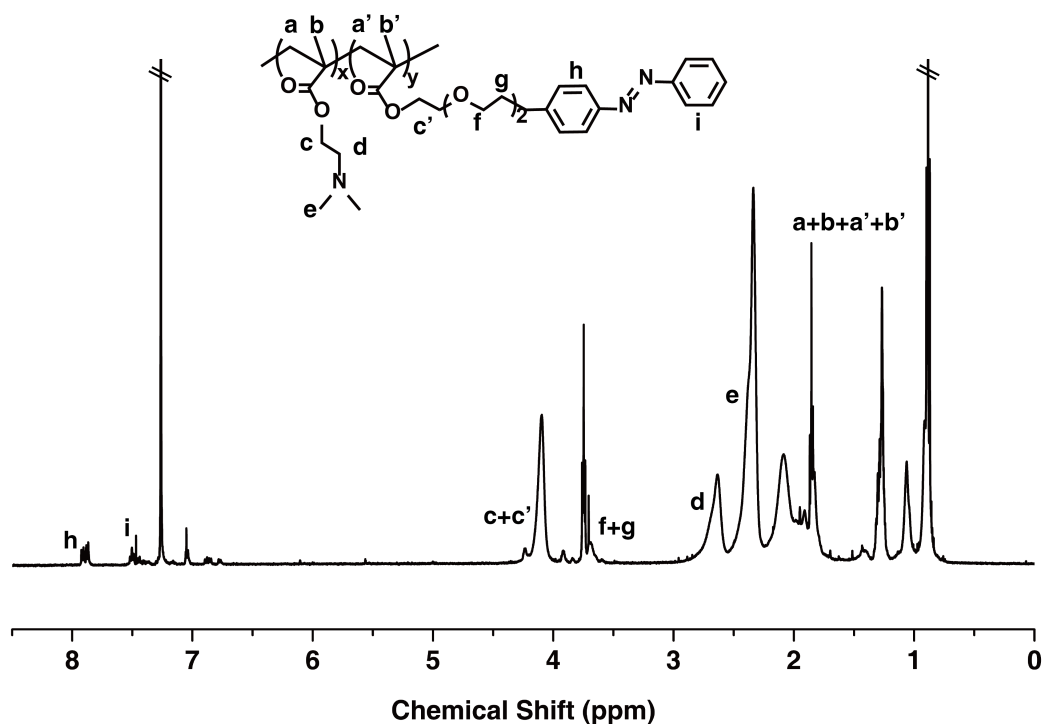


Figure 4.14:  $^1\text{H}$  NMR spectrum (500 MHz) of P(DMAEMA-co-AzoMMA).

**P(DMAEMA-co-AzoMMA).** P(DMAEMA-co-AzoMMA) was prepared *via* a RAFT polymerisation (Figure 4.3b). The mixture of 2-(dimethylamino)ethyl methacrylate (DMAEMA, 5.00 g, 31.80 mmol, 100 eq), Azo-MMA (886.95 mg, 2.226 mmol, 7 eq) and 4-cyano-4-(phenylcarbonothioylthio)pentanoic acid (88.84 mg, 0.318 mmol, 1 eq) were dissolved in 10.6 mL dioxane (3 M). The reaction mixture was degassed by three freeze-pump-thaw

cycles and left under nitrogen. Then ACVA (17.83 mg, 0.0636 mmol, 0.2 eq) was added and the flask was immersed in an oil bath at 70 °C.  $^1\text{H}$  NMR spectroscopy was used to monitor the conversion during the reaction. Finally, the reaction was stopped by quenching in liquid nitrogen and the mixture was precipitated by dropping the dioxane solution into cold hexane. The crude polymer was collected and re-dissolved in THF. The precipitation procedure was repeated for three times. After filtration and desiccation, P(DMAEMA-*co*-Azo) was obtained as an orange powder.  $M_w/M_n=1.19$  (GPC),  $DP_{(PDMAEMA)}=77$  ( $^1\text{H}$  NMR),  $M_n=12,000$  g/mol ( $^1\text{H}$  NMR) and  $\alpha_{Azo/DMAEMA}=3\%$ .  $^1\text{H}$  NMR spectroscopy and GPC results are shown in Figure 4.14 and Figure 4.4 respectively.

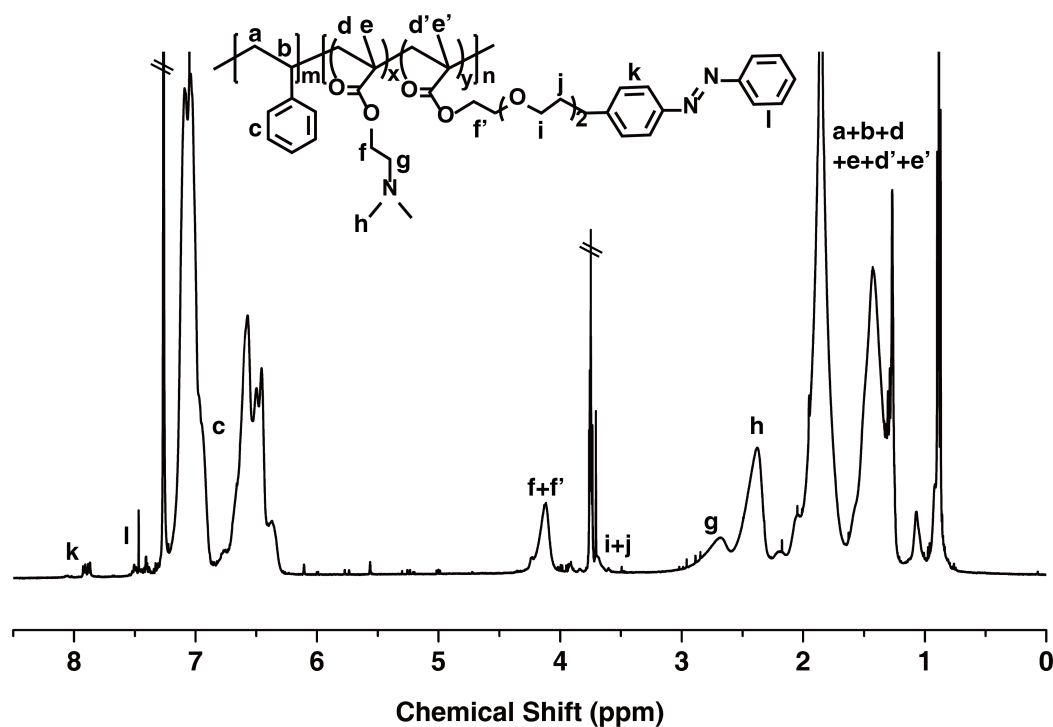


Figure 4.15:  $^1\text{H}$  NMR spectrum (500 MHz) of PS-*b*-P(DMAEMA-*co*-AzoMMA).

**PS-*b*-P(DMAEMA-*co*-AzoMMA).** Styrene (17.4 g, 167 mmol, 2000 eq) and P(DMAEMA-*co*-Azo) (macro-CTA,  $M=12,000$  g/mol, 1000 mg, 0.083 mmol, 1 eq) were dissolved in THF (55.5 mL, 3 M). After being degassed by three freeze-pump-thaw cycles and purged with nitrogen, AIBN (3.4 mg, 0.02 mmol, 0.25 eq) was added and the flask was immersed in an oil bath at 70 °C under stirring. The conversion was monitored by  $^1\text{H}$  NMR. The

reaction was stopped by quenching in liquid nitrogen. Then the crude products were precipitated by dropping the dioxane solution into cold hexane. The polymer was collected and re-dissolved in THF. The precipitation procedure was repeated for three times. After being filtered and dried in a vacuum oven at 30 °C for 24 h, PS-*b*-P(DMAEMA-*co*-Azo) was collected as an orange powder.  $M_w/M_n=1.44$  (GPC),  $DP_{(PS)}=550$  ( $^1\text{H NMR}$ ) and  $DP_{(PDMAEMA)}=77$  ( $^1\text{H NMR}$ ).  $^1\text{H NMR}$  spectroscopy and GPC results are shown in Figure 4.15 and Figure 4.4 respectively.

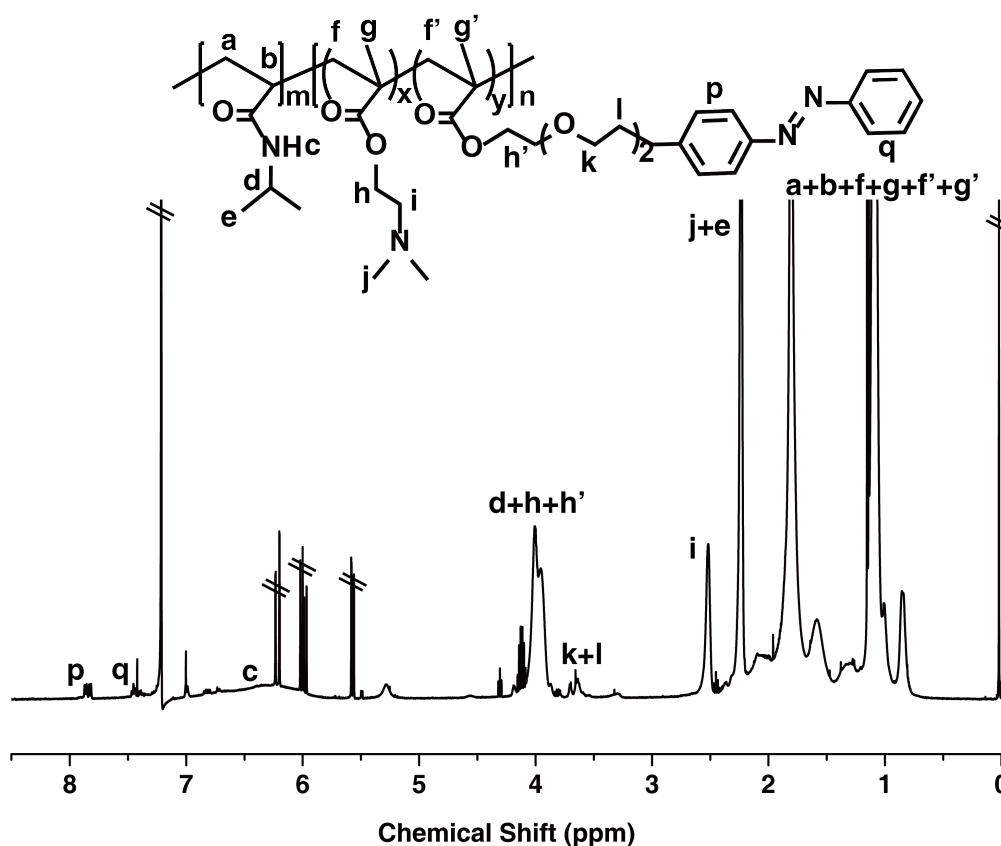


Figure 4.16:  $^1\text{H NMR}$  spectrum (500 MHz) of PNIPAM-*b*-P(DMAEMA-*co*-AzoMMA).

**PNIPAM-*b*-P(DMAEMA-*co*-AzoMMA).** NIPAM (2.62 g, 23.2 mmol, 400 eq) and P(DMAEMA-*co*-Azo) (macro-CTA,  $M=12,000$  g/mol, 696 mg, 0.058 mmol, 1 eq) were dissolved in dioxane (9.28 mL, 2.5 M). After being degassed by three freeze-pump-thaw cycles and purged with nitrogen, AIBN (3.36 mg, 0.012 mmol, 0.20 eq) was added and the flask was immersed in an oil bath at 70 °C under stirring. The conversion was monitored by  $^1\text{H NMR}$  spectroscopy. The reaction was stopped by quenching in liquid nitrogen.

Then the crude products were precipitated by dropping the dioxane solution into cold hexane. The polymer was collected and re-dissolved in THF. The precipitation procedure was repeated for three times. After being filtered and dried in a vacuum oven at 30 °C for 24 h, PNIPAM-*b*-P(DMAEMA-*co*-Azo) was collected as an orange powder.  $M_w/M_n=1.39$  (GPC),  $DP_{(PNIPAM)}=340$  ( $^1\text{H NMR}$ ) and  $DP_{(PDMAEMA)}=77$  ( $^1\text{H NMR}$ ).  $^1\text{H NMR}$  spectroscopy and GPC results are shown in Figure 4.16 and Figure 4.4 respectively.

**Preparation of PS-based micelle solution (0.5 mg/mL).** 5.0 mg of PS-*b*-P(DMAEMA-*co*-AzoMMA) block co-polymer was dissolved in 5 mL THF. Then 10 mL DI water was added dropwise under vigorous stirring (400 rpm). After the addition was finished, the micelle solution was further stirred for another 24 h until the THF was completely evaporated (the smell of THF disappeared).

**Preparation of PNIPAM-based micelle solution (0.5 mg/mL).** 5.0 mg of PNIPAM-*b*-P(DMAEMA-*co*-AzoMMA) block co-polymer was dissolved in 10 mL DI water at room temperature under vigorous stirring (400 rpm). After the addition was finished, the solution was heated to 45 °C under stirring, resulting in micelle formation.

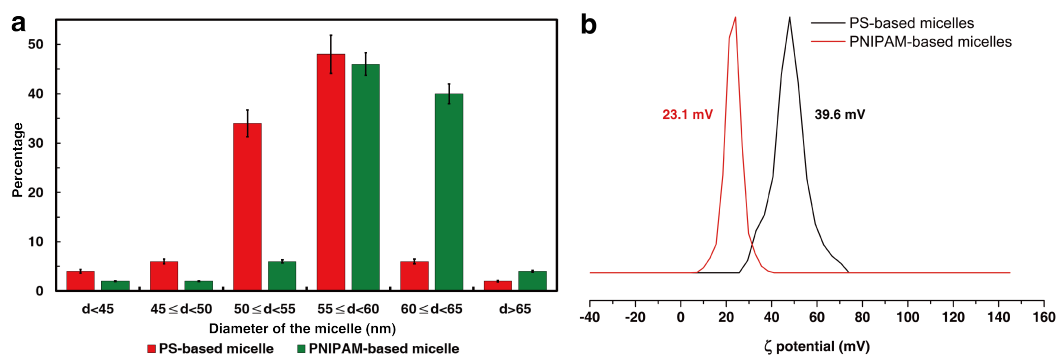


Figure 4.17: **a**, statistical analysis of the size distributions of PS-based and PNIPAM-based micelles from TEM results. The data was based on 50 micelles. **b**, The  $\zeta$  potential curves for cargo-loaded PS-based (black) and PNIPAM-based (red) micelles.

**Preparation of cargo-loaded PS-based micelle solution.** 5.0 mg PS-based block co-polymers were dissolved in 5 mL THF, where 150  $\mu\text{L}$  Nile Red solution (0.02 mg/mL, THF) was added as hydrophobic drugs. Then 10 mL DI water was added dropwise under vigorous stirring (400 rpm). After the addition process was finished, the drug-loaded micelle solution was further stirred for another 24 h until the THF was completely

evaporated (the smell of THF disappeared). The final concentration of polymers and Nile Red were 0.5 and  $3 \times 10^{-4}$  mg/mL respectively.

**Preparation of cargo-loaded PNIPAM-based micelle solution.** 5.0 mg PNIPAM-based block co-polymers were dissolved in 10 mL DI water at room temperature, where 150  $\mu$ L Nile Red solution (0.02 mg/mL, THF) was added as hydrophobic drugs. Then the temperature was increased to 45 °C under vigorous stirring (400 rpm). The drug-loaded micelle solution was further stirred for another 24 h until the THF was completely evaporated (the smell of THF disappeared). The final concentration of polymers and Nile Red were 0.5 and  $3 \times 10^{-4}$  mg/mL respectively.

**Determination of the critical micelle concentration (CMC).** CMC was tested through a fluorescent method, where Nile Red was used as a fluorescent probe. The block copolymer concentrations varied from  $10^{-3}$  mg/mL to 1 mg/mL. Next, Nile Red (THF solution, 0.02 mg/mL) was added to get the final concentration of  $3 \times 10^{-4}$  mg/mL in each solution. The fluorescent results of the solution with different micelle concentration were monitored *via* fluorimetre. The PNIPAM-based micelle was tested at 45 °C.

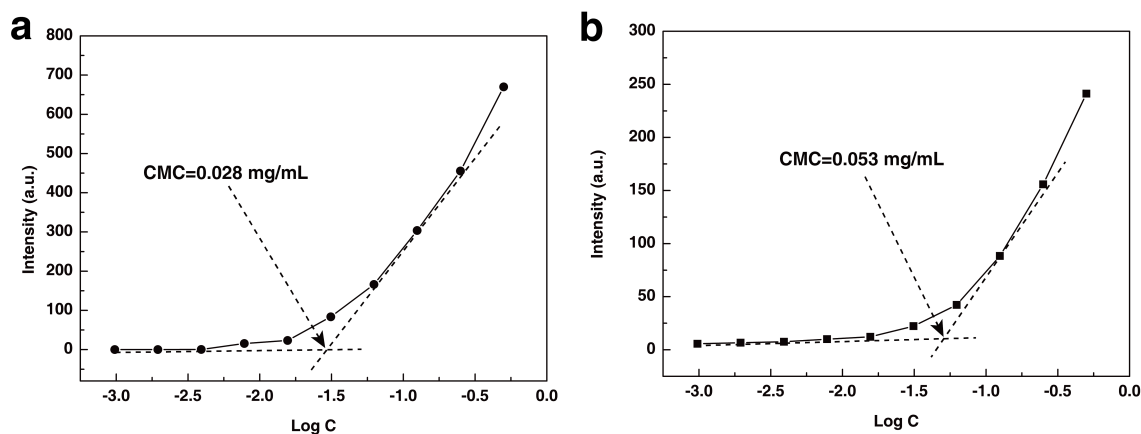


Figure 4.18: The CMC of **a**, PS-based and **b**, PNIPAM-based micelles.

**Responsive cargo release of PS-based micelles.** 10.0 mg PS-based block co-polymers were dissolved in 10 mL THF, where 300  $\mu$ L Nile Red solution (0.02 mg/mL, THF) was added as hydrophobic cargoes. Then 20 mL Britton-Robinson buffer (pH=3, 7 and 11) was added dropwise under vigorous stirring (400 rpm). After the addition process was finished, the drug-loaded micelle solution was further stirred for another 24 h until the

THF was completely evaporated (the smell of THF disappeared). The final concentration of polymers and Nile Red were 0.5 mg/mL and  $3 \times 10^{-4}$  mg/mL respectively. Then the micelle solution was dialysed against the corresponding buffer solution. The fluorescent results of the micelle solution were monitored at different times.

**Responsive cargo release of PNIPAM-based micelles.** 10.0 mg PNIPAM-based block co-polymers were dissolved in 20 mL DI water at room temperature, where 300  $\mu$ L Nile Red solution (0.02 mg/mL, THF) was added as hydrophobic cargoes. Then the temperature was increased to 45 °C under vigorous stirring (400 rpm). The drug-loaded micelle solution was further stirred for another 24 h until the THF was completely evaporated (the smell of THF disappeared). The final concentration of polymers and Nile Red were 0.5 mg/mL and  $3 \times 10^{-4}$  mg/mL respectively. Then the micelle solution was dialysed against water at 25 °C and 45 °C respectively. The fluorescent results of the micelle solution were monitored at different times.

### 4.6.3 Preparation of micelle-nanoparticle complexes

**Preparation of MV-functionlised SiO<sub>2</sub> NPs.** The preparation of MV-functionlised SiO<sub>2</sub> NPs is shown in Figure 4.19. Bare SiO<sub>2</sub> NPs and MV-silane were prepared first.

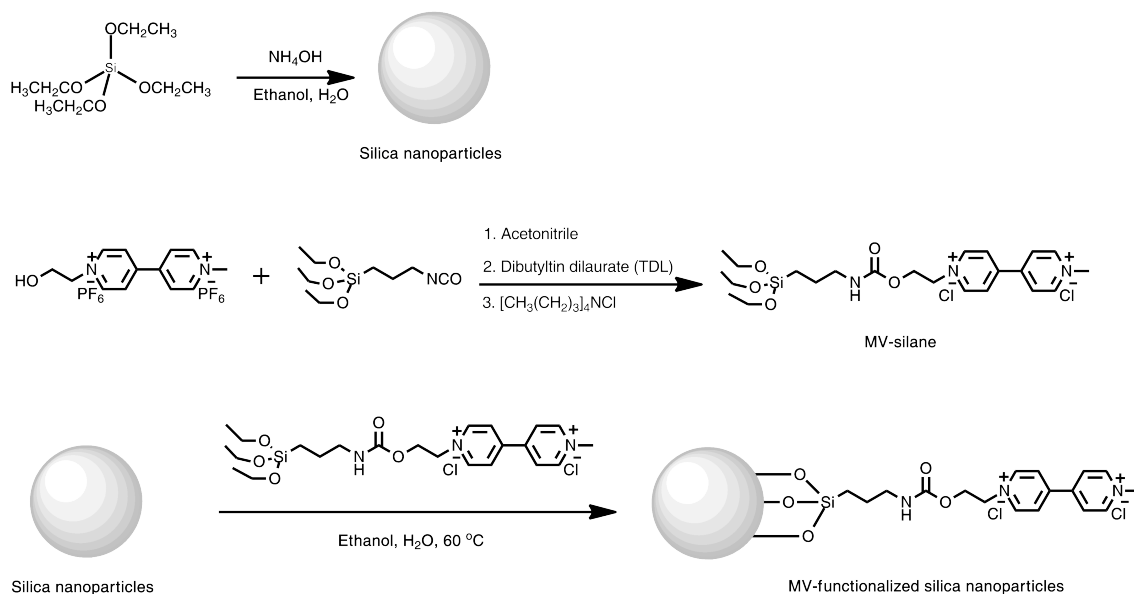


Figure 4.19: The scheme of the preparation of MV-functionalised silica NP.



**Preparation of SiO<sub>2</sub> NP.** To a 250 mL flask, 3 mL of ammonium hydroxide solution (25 %), 20 mL of water and 70 mL of ethanol were added. Subsequently 2.08 g (10 mmol) of tetraethyl orthosilicate (TEOS) was dissolved in 10 mL ethanol, and the mixture was added to the previous solution with vigorous mechanical stirring at 500 rpm for 12 h. Finally, the product was washed by three cycles of centrifuge/redispersion using ethanol (100 mL) and once with DI water (100 mL).

**Preparation of MV-silane.** MV-OH (1.51 g, 3.0 mmol) and Silane-NCO (7.41 g, 30 mmol) were dissolved in 30 mL of dry acetonitrile in a 100 mL pre-dried round bottom flask. Subsequently, one drop of dibutyltin dilaurate (TDL) was added under stirring (500 rpm), and the mixture was stirred for 48 h at room temperature. Then tetrabutylammonium chloride (5.00 g, 18 mmol) was added and the crude product was precipitated. After filtration, washed with diethyl ether and dried in a vacuum oven for 24 h, the pure product was collected as a brown powder. <sup>1</sup>H NMR (400 MHz, D<sub>2</sub>O), 9.05 (dd, 4H), 8.49 (dd, 4H), 4.94 (s, 2H), 4.57 (d, 2H), 4.44 (s, 3H), 3.76 (q, 6H), 2.94 (t, 2H), 1.44 (t, 2H), 1.13 (t, 9H). <sup>13</sup>C NMR (100 MHz, D<sub>2</sub>O), 192.1, 146.2, 127.0, 126.7, 62.8, 61.1, 59.2, 48.4, 43.0, 22.0, 17.3, 6.1. FTIR, 3372 cm<sup>-1</sup>(N-H), 2975 cm<sup>-1</sup>(C-H), 1705 cm<sup>-1</sup>(-NH(CO)O-). MS spectra, m/z=463.2 g/mol.

**Preparation of MV-functionalised SiO<sub>2</sub> NP.** To a 100 mL flask, 50 mg of bare silica NPs were dispersed in the mixture of 40 mL ethanol/water (ethanol/water=1/9). Then 15 mg of MV-silane was added to the solution under vigorous mechanical stirring at 500 rpm, and the mixture was heated to 60 °C for 1 h. Subsequently, the resultant product was washed by three cycles of centrifuge/redispersion using ethanol (100 mL) and once with DI water (100 mL). At last, the final product MV-functionalised silica NPs were dispersed in 500 mL water. According to the characterisation results, during modification process, both the ζ potential increase (from -56.0 mV to +8.48 mV) and the appearance of N-H stretching vibration peak (3343 cm<sup>-1</sup>) in FT-IR (Figure 4.20) suggest that the MV moiety was functionalised onto the surface of SiO<sub>2</sub> NPs.

**Self-assembly between PS-based micelles and MV-functionalised SiO<sub>2</sub> NPs.** MV-functionalised SiO<sub>2</sub> NPs were dispersed in DI water to yield a solution of 0.05 mg/mL

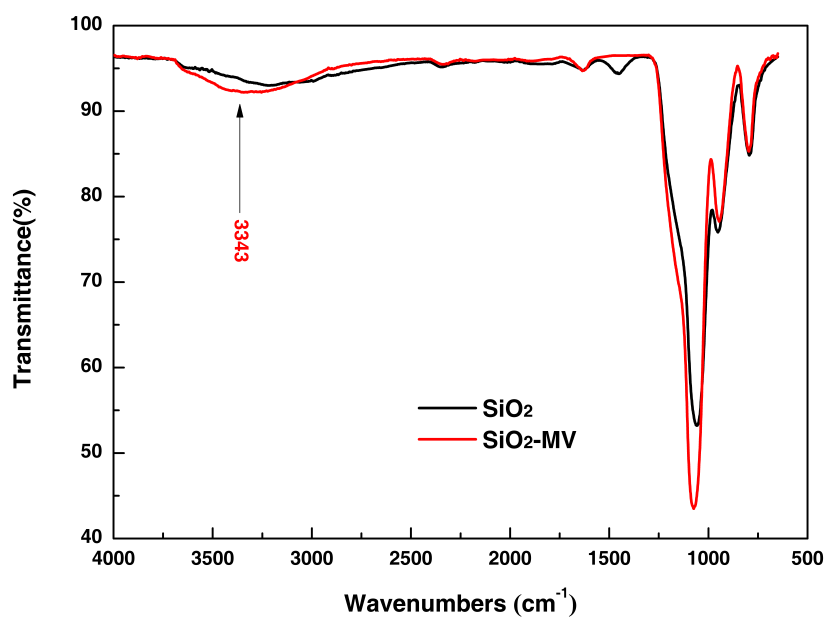


Figure 4.20: FTIR of SiO<sub>2</sub> particles before and after functionalisation.

(A). CB[8] was dissolved in water to get a 0.04 mg/mL solution (B). Then 16 mL of A and 4 mL of B was mixed under vigorous stirring (500 rpm), resulting in MV@CB[8]-functionalised SiO<sub>2</sub> NPs. Next, 1 mL micelle solution (0.1 mg/mL) was mixed with 1 mL MV@CB[8]-functionalised silica NPs solution under stirring, after which MV/*trans*-Azo@CB[8] ternary complex was obtained.

**Self-assembly between PS-based micelles and CB[8] catenane-functionalised magnetic SiO<sub>2</sub> NPs.** CB[8] catenane-functionalised magnetic SiO<sub>2</sub> NPs were dispersed in DI water to yield a 1 mL solution of 0.04 mg/mL, where 250  $\mu$ L micelle solution (0.5 mg/mL) was then introduced under stirring, resulting in MNCs.

**Self-assembly between PNIPAM-based micelles and CB[8] catenane-functionalised magnetic SiO<sub>2</sub> NPs.** CB[8] catenane-functionalised magnetic SiO<sub>2</sub> NPs were dispersed in DI water to yield a 1 mL solution of 0.04 mg/mL at 45 °C, where 250  $\mu$ L micelle solution (0.5 mg/mL, 45 °C) was then introduced under stirring, resulting in MNCs. The characterisations of PNIPAM-based MNCs are shown in Figure 4.21.

**Experimental procedures for the recycling cycle of Figure 4.2.** 5 mL cargo-loaded (Nile Red,  $3 \times 10^{-4}$  mg/mL) micelle solution (0.5 mg/mL) was added to 20 mL of the CB[8] catenane-functionalised magnetic SiO<sub>2</sub> NPs (0.04 mg/mL) solution under stirring,

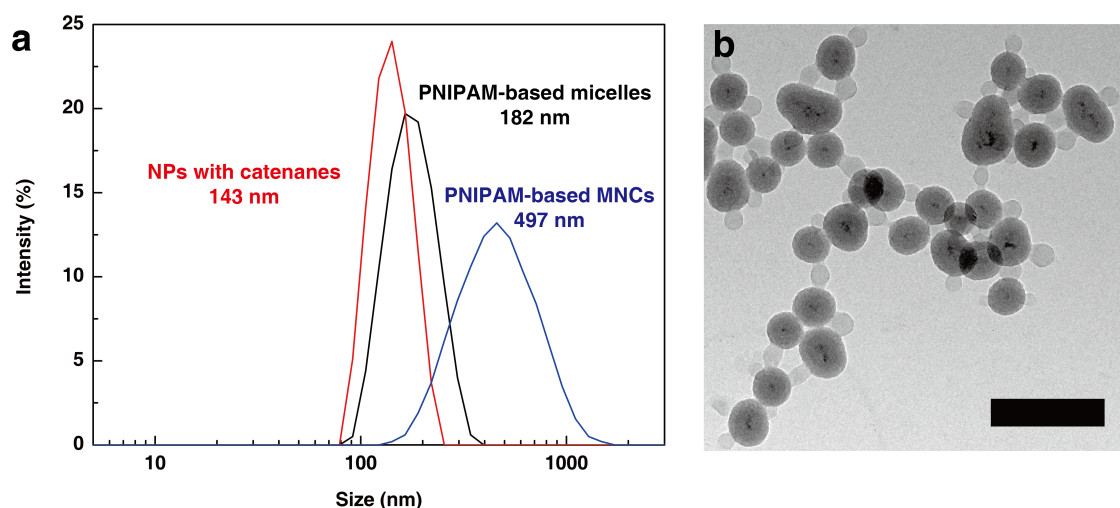


Figure 4.21: Characterisation of PNIPAM-based MNC. **a**, DLS results of CB[8] catenane-contained magnetic SiO<sub>2</sub> NPs, PNIPAM-based micelles and PNIPAM-based MNCs. **b**, TEM image of PNIPAM-based MNCs. (scale bar: 450 nm).

forming MNCs. Next the MNCs were concentrated in proximity to a magnet. The solution was replaced by 5 mL water, where the MNCs were re-dispersed under UV irradiation at 350 nm (*trans* to *cis*). The TEM image for the dispersed solution is shown in Figure 4.12c, suggesting separated micelles and NPs. NPs were further removed by a magnet and can be re-utilised for the next cycle. The micelle solution was irradiated by visible light at 420 nm to achieve *trans*-Azo, followed by the dialysis against Britton-Robinson buffer (pH=3) for 36 h to release most of the Nile Red. After lyophilisation, the polymer were recycled and the extra Nile red can be further removed by the precipitation into cold hexane for three times. The efficiency tests for both micelles and NPs have similar procedures.

## Chapter 5

# Hybrid organic-inorganic supramolecular hydrogel reinforced with CePO<sub>4</sub> nanowires

The preparation and characterisation (TEM, TGA and SEM) of the nanowires in this chapter were carried out in collaboration with Dr. Guolei Xiang from Department of Chemistry, University of Cambridge.

This work has been published in the following peer-reviewed article:

Liu, C.<sup>‡</sup>; Xiang, G.<sup>‡</sup>; Wu, Y.; Barrow, S. J.; Rowland, M. J.; Clarke, D. E.; Wu, G.; Scherman, O. A. 'Hybrid organic–inorganic supramolecular hydrogel reinforced with CePO<sub>4</sub> nanowires', *Polym. Chem.* **2016**, *7*, 6485-6489.

In this chapter, another composite material based on cucurbit[8]uril (CB[8]) ternary complexes is introduced. As an important class of soft materials, supramolecular hydrogels have attracted a tremendous interest on account of their shear-thinning, self-healing and stimuli-responsive properties.<sup>17,79,248</sup> However, the scope of their applications is typically limited to the soft properties (*i.e.* shear-thinning and self-healing).<sup>249</sup> To the best of our knowledge, there is little discussion of utilising non-covalent interactions to enhance mechanical properties of CB[8]-based hydrogels, as the host-guest interactions are very sensitive to external stimuli.<sup>250</sup> Herein, we report a method to enhance the stiffness in the rheological yield strain of CB[8]-based hydrogels by introducing inorganic nanowires (NWs) into the supramolecular networks. The supramolecular hydrogel is comprised of methyl viologen-functionalised poly(vinyl alcohol) (PVA-MV), hydroxyethyl cellulose

with naphthyl moieties (HEC-Np) and CB[8] macrocyclic hosts. The gel structure can be effectively enhanced by the framework supporting effects of cerous phosphate NWs and additional hydrogen bonding interactions between the NWs and the PVA-MV/HEC-Np polymers. The high aspect ratio NWs there serve as a 'skeleton' for the network providing extra physical crosslinks, resulting in a single continuous phase hybrid supramolecular network with improved strength. This advanced structure based on supramolecular interactions, including CB[8] host-guest chemistry and hydrogen bonding, presents a general approach to reinforce soft materials.

## **5.1 Introduction**

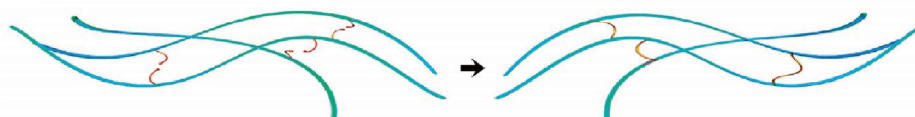
Hybrid materials composed of organic molecules (small molecules or polymers) and inorganic nanostructures typically exhibit enhanced mechanical properties and display multi-functionality on account of their molecular scale interactions and synergistic effects.<sup>251–253</sup> In such materials the inorganic components can act as a rigid skeleton while the organic constituent parts serve as a flexible entangled mesh to generate an extended network of interactions.<sup>254</sup> In the past two decades, one-dimensional (1D) nanostructures, such as inorganic nanowires (NWs), carbon nanotubes and nanobelts have been extensively explored due to their importance in both intriguing mesoscopic physical properties and technological applications.<sup>255,256</sup> They are expected to be used as next-generation building blocks for energy harvesting/storage/conversion devices, chemical/bio sensors and nanoscale photoelectronic/electronic devices owing to their unique geometric characteristics.<sup>255–258</sup>

Among different 1D nanostructures, NWs are of particular interest and have been widely used in preparing various hybrid materials, such as superconductor/ semiconductor devices,<sup>259</sup> magnetic nanomaterials<sup>260</sup> and nanophotonic devices,<sup>261</sup> on account of their relatively high carrier mobility, optical and electrical properties. More importantly, NWs constitute an interesting class of 1D nanostructures in the fabrication of reinforced hybrid materials, as they can link multiple binding sites along their extended dimension, which induces the formation of 3D networks.<sup>262,263</sup> The ductility of NWs

arising from their unique 1D geometric characteristics drives them to form 3D networks, and therefore reinforcing the hybrid materials.<sup>264–266</sup> The intrinsic mechanical strength of inorganic NWs, however, has not been extensively studied for the reinforcement of organic soft materials.

As an important class of soft materials, polymeric hydrogels are formed through the 3D crosslinking of hydrophilic polymer chains, resulting in high water content and outstanding biocompatibility.<sup>248,267,268</sup> Polymeric hydrogels can be classified as either covalent (Figure 5.1a) or non-covalent networks (Figure 5.1b), depending on the type of employed crosslinking.<sup>268,269</sup> Owing to the development of synthetic chemistry, a wide range of chemically cross-linked hydrogels have been prepared through various methods, such as click chemistry,<sup>270</sup> thiol conjugate addition,<sup>271</sup> Schiff base formation,<sup>272</sup> enzymatic cross-linking<sup>273</sup> and disulfide bond formation etc.<sup>274</sup> However, due to the irreversible nature of covalent crosslinkings, most covalent hydrogels are brittle, poorly transparent and non-injectable. Therefore, their applications are restricted to robust, tough and elastic materials.<sup>275</sup> Physically cross-linked hydrogels have been developed to overcome these deficits.

**a** Chemical crosslinking



**b** Self-assembly

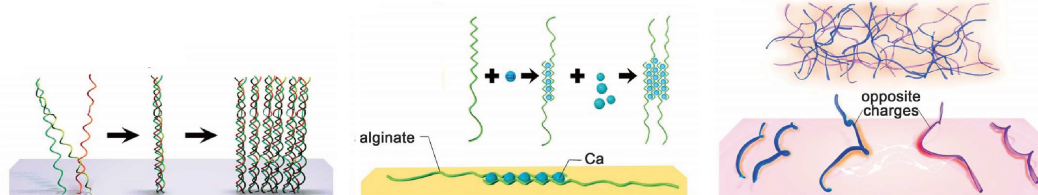


Figure 5.1: The crosslinking of hydrogels. **a**, Chemical crosslinkings. **b**, Physical crosslinkings.<sup>268</sup>

With the development of supramolecular chemistry,<sup>35,232,233</sup> dynamic non-covalent interactions have been exploited as structural crosslinkers between polymer chains, resulting in mouldable 3D networks, named supramolecular hydrogels.<sup>248</sup> Thus supramolecu-

lar hydrogels can be served as attractive alternatives to covalent hydrogels on account of the special properties arising from their dynamic physical crosslinks, such as stimuli-responsiveness, shear-thinning and self-healing behaviours.<sup>17,209,248,267,276</sup> Over the past several decades, a wide variety of supramolecular motifs have been applied in fabricating supramolecular hydrogels, (Figure 5.1b),<sup>248,268,277,278</sup> including self-assemblies (host-guest complexation,<sup>279,280</sup> hydrophobic interactions,<sup>169</sup> hydrogen bonds<sup>281–283</sup>), metal-ligand interactions<sup>284–286</sup> and electrostatic interactions.<sup>287</sup> Particularly, through utilising host-guest chemistry, a range of supramolecular hydrogels have been prepared by employing macrocyclic hosts, such as cyclodextrins (CDs),<sup>288,289</sup> CB[*n*]s,<sup>28,79,290</sup> calixarenes<sup>291–294</sup> and crown ethers.<sup>279,295–298</sup> Among these host molecules, CB[*n*]s are of great interest as they are nontoxic, biocompatible and exhibiting much higher  $K_{eq}$  values,<sup>57</sup> providing great potential in biological applications.<sup>248</sup>

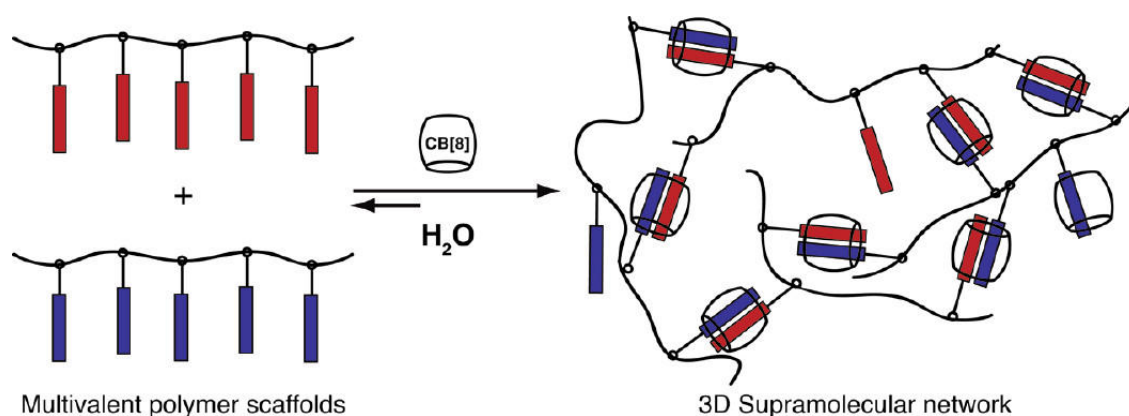


Figure 5.2: Supramolecular hydrogel formation *via* CB[8].<sup>17</sup>

CB[8] has been firstly utilised in the fabrication of supramolecular cross-linked networks by Scherman and co-workers (Figure 5.2).<sup>17</sup> Through free radical polymerisation techniques, multivalent copolymers with either pendant MV (first guest) or Np derivatives (second guests) have been prepared and served as network backbones, after which CB[8] is introduced to initiate 3D crosslinkings and form gel-like viscoelastic materials with injectable potential. Scherman *et al.* have continued their exploration and reported a high water content (up to 99.7%) hydrogel with a minimal polymer content of 0.5 wt.%.<sup>79</sup> Upon the addition of Np-functionalised hydroxyethyl cellulose (HEC-Np,

$M_w = 1.3$  MDa) to the solution of CB[8] and poly(vinyl alcohol) functionalised with MV moieties (PVA-MV,  $M_w = 1.5$  MDa), the viscoelastic hydrogel can be formed. Exemplified through rheology experiments, these materials display excellent shear-thinning, self-healing properties and responsive to a series of stimuli, such as temperature, chemical potential and competitive guests. Then the cargo release behaviours of the hydrogel have been investigated.<sup>82</sup> Next, in the following five years, a range of CB[8]-based hydrogels have been introduced through employing versatile guest molecules. For example, hydrogels with impressive viscoelastic behaviours have been prepared through the strong 1:2 ‘homoternary’ complexation between CB[8] and two Phe peptides.<sup>290</sup> Additionally, through utilising photo-isomerisable azobenzene derivatives, a CB[8]-mediated supramolecular polymer network with light-tunable rheological properties has been prepared.<sup>80</sup> Recently, a library of CB[8] hydrogel networks have been reported *via in situ* polymerisation of the solution with a range of vinyl monomers.<sup>299</sup>

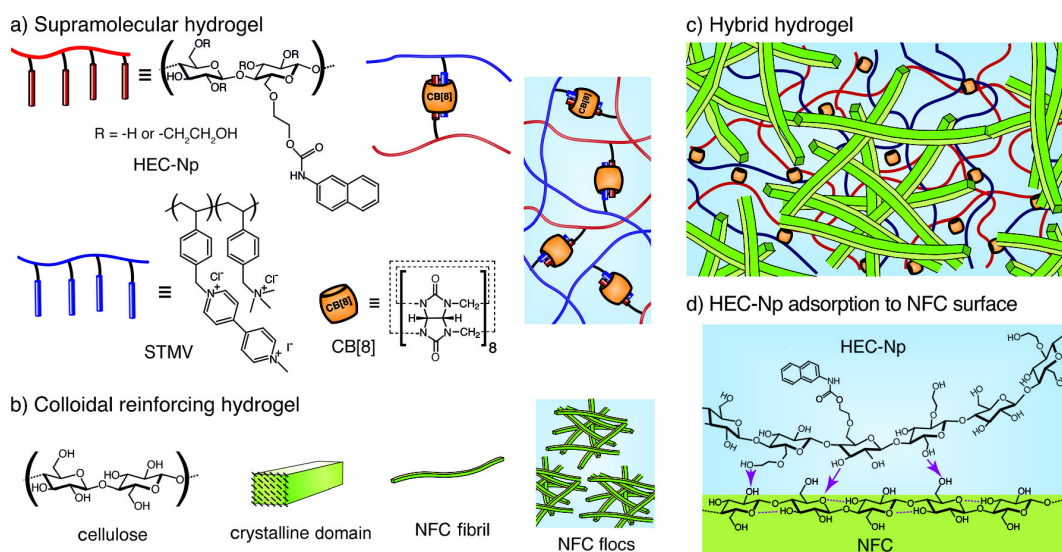


Figure 5.3: **a**, Supramolecular hydrogel consisting of HEC-Np, STMV, and the CB[8] host motif capable of binding the first guest naphthyl and the second guest viologen highly dynamically. **b**, Colloidal reinforcing nanofibrillated cellulose, also showing the denser and less dense network regimes. **c**, Interpenetrating hybrid hydrogel consisting of the molecular-level supramolecular and colloidal-level nanofibrillated cellulose hydrogel. Because of its rigid nanofibres and short aspect ratio, network aggregates are formed (flocs). **d**, Surface adsorption of HEC-Np onto the nanofibrillated cellulose surface. Possible hydrogen bonding is schematically shown.<sup>81</sup>



More importantly, CB[8]-based hydrogels can be exploited in the fabrication of composite materials, endowing the resulting double networks with supramolecular characteristics (*i.e.* shear-thinning, self-healing and stimuli-responsive properties). In 2015, a supramolecular double network hydrogel was reported by Li *et al.*,<sup>83</sup> exhibiting excellent ductility, shear-thinning and stimuli-responsive properties, on account of the cooperation of DNA hybridisation and host-guest chemistry. Similarly, through the combination of CB[8]-based supramolecular hydrogels and colloidal nanofibrillar hydrogels, a novel hybrid nanocomposite has been successfully prepared by Scherman and co-workers,<sup>81</sup> displaying an enhanced rheological storage modulus and a synergistic improvement in elastic yield values in comparison to the original nanofibrillated cellulose colloidal hydrogels. As shown in Figure 5.3, the enhancement is achieved on account of the fast dissociation/association dynamics arising from the CB[8]-mediated cross-links and the adsorption of hydroxyethyl cellulose component to the nanofibrillated cellulose nanofibres.

However, due to the weak non-covalent bonding nature of host-guest interaction, the scope of supramolecular hydrogel applications is typically limited to materials requiring soft properties.<sup>249</sup> Compared with covalently crosslinked hydrogels,<sup>169,300,301</sup> supramolecular hydrogels based on host-guest interactions are difficult to reinforce through the introduction of metal NPs, as the host molecule can preferentially bind to the NP. For example, the macrocyclic host, CB[8], forms strong subnanometre junctions with gold nanoparticles, due to the relative high binding constant compared with small guest molecules.<sup>250</sup> Therefore, few samples have been reported to date of utilising extended 1D inorganic structures to reinforce CB[8]-based supramolecular hydrogels.<sup>81,83,302</sup> Inspired by the geometric structure of NWs, this chapter will present a method to enhance the mechanical properties of CB[8]-mediated hydrogels by taking advantage of the supramolecular interactions between NWs and the polymer networks.

## 5.2 Design and preparation of nanowire-reinforced hydrogels

As shown in Figure 5.4a, the polymer backbone of the hydrogel is based on PVA-MV and HEC-Np, where the guests (MV and Np) can form ternary complex with CB[8]. CePO<sub>4</sub>

NWs have been utilised in this study on account of its highly hydrated surface and chemical inertness with CB[8] (Figure 5.4b). By employing inorganic NWs as skeletal constructs, CB[8]-based supramolecular hydrogels exhibit a 50 % increase in storage modulus. This prominent reinforcement is achieved from two simultaneous components (Figure 5.4c and 5.4d), firstly,  $\text{CePO}_4$  NWs provide extra crosslinks through the hydrogen bonds between the polymer chain and the hydroxy-rich NW surface. Secondly, the polymer networks replicate the 'soft' tissue, holding a high content of water through CB[8]-mediated supramolecular crosslinks, while the NWs serve as an extended scaffold for the polymeric network.

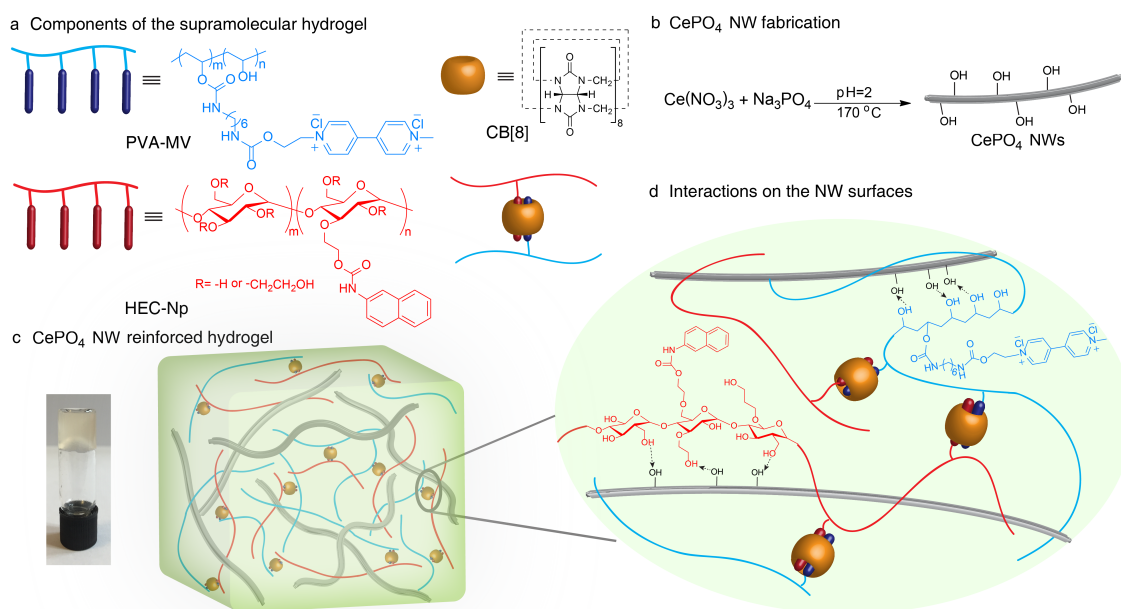


Figure 5.4: **a**, The chemical structure of PVA-MV, HEC-Np, CB[8] and the highly dynamical 1:1:1 ternary complex formed by CB[8] host-guest chemistry between MV and Np. **b**, Schematic representation of cerous phosphate NWs prepared by a hydrothermal method, with hydroxyl groups on the surface. **c**, The structure of the NW-reinforced organic-inorganic hybrid supramolecular hydrogel based on CB[8] host-guest interactions. **d**, NWs were employed as a 'skeleton' to bridge polymers through hydrogen bonds between NWs and PVA-MV/HEC-Np polymers.

### Preparation and characterisation of $\text{CePO}_4$ nanowires

$\text{CePO}_4$  NWs were synthesised by a hydrothermal reaction at 170 °C from  $\text{Na}_3\text{PO}_4$  and  $\text{CeNO}_3$  precursors, under acidic conditions (pH = 2, HCl aq, 1M) (Figure 5.4b).<sup>303</sup> A

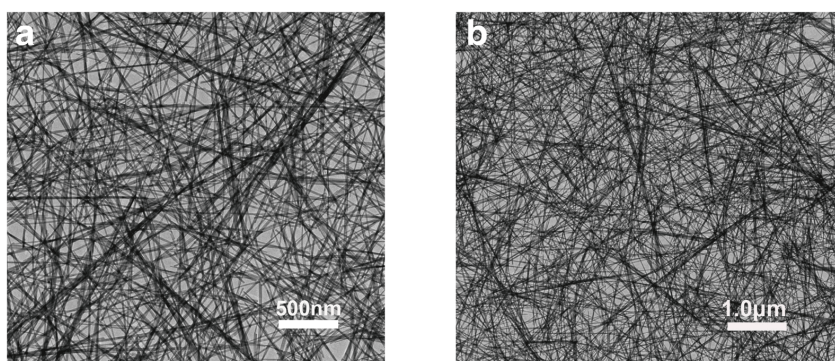


Figure 5.5: TEM images of CePO<sub>4</sub> nanowires. Scale bar: **a**, 500 nm, **b**, 1 μm.

clear colloidal suspension was obtained after a 10 h reaction without the appearance of any large aggregates. The morphology of the product was characterised by TEM, which indicated the pure nanowires were successfully fabricated (Figure 5.5). The average diameter of the NWs was 15 nm with an average length of 3 μm. Since the nanowires were prepared in the absence of any capping ligands, their surfaces were highly hydrated in water and thus, were covered with hydroxyl groups, resulting in a highly hydrophilic surface.

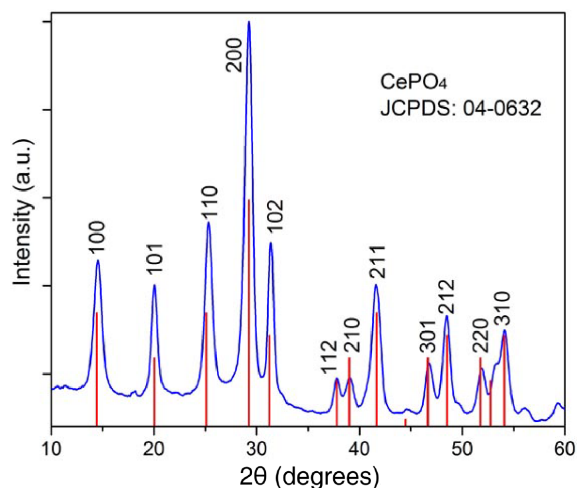


Figure 5.6: Powder X-ray diffraction results of CePO<sub>4</sub> nanowires.

The hydroxyl groups on the NW surface were confirmed by FT-IR spectroscopy (Figure 5.17a, Experimental Section). The density of OH groups was estimated by TGA (Figure 5.17b, Experimental Section) due to hydroxyl condensation at high temperature, and found to be around 24 nm<sup>-2</sup>. This result reflects the maximal OH density, since the at-

tached water molecules are not necessarily removed during the preheating process. The hydrophilicity of the NWs enable them to be dispersed in aqueous solutions. Furthermore, crystallinity of the nanowires were characterised through powder X-ray diffraction (Figure 5.6). The pattern indicates the high purity of CePO<sub>4</sub>, which can be indexed to a JCPDS card of 04-0632.

#### **Preparation and characterisation of HEC-Np and PVA-MV**

PVA-MV (205 KDa, 5 mol% MV loading) was synthesised through a post functionalisation.<sup>79</sup> As shown in the <sup>1</sup>H NMR spectroscopy (Figure 5.15a, Experimental Section), the signals from 9.17-8.96 ppm and 8.52-8.42 ppm illustrate the viologen group of PVA-MV. Furthermore, the absorption of 1711 cm<sup>-1</sup> from FT-IR results (Figure 5.15b, Experimental Section) also demonstrates the functionalisation.

HEC-Np (1.3 MDa, 5 mol% Np loading) was synthesised according to previous literature.<sup>79</sup> The chemical shift at 7.91-7.35 ppm of Figure 5.16a (Experimental Section) indicates the naphthyl group of the HEC-Np product. Moreover, the characteristic absorption of the FT-IR spectrum (Figure 5.16b, Experimental Section) at 1645 cm<sup>-1</sup> is attributed to the C=O group of HEC-Np, confirming the successful post reaction.

#### **Hydrogel formation**

According to our previous work,<sup>79</sup> HEC-Np and PVA-MV are able to form a dynamic hydrogel *via* CB[8] host-guest interactions (Figure 5.4a). The composition of the hydrogel can be varied from 0.25 wt% HEC-Np, 0.05 wt% PVA-MV@CB[8] to 1.5 wt% HEC-Np, 0.3 wt% PVA-MV@CB[8], with the storage modulus increased from 10 Pa to 500 Pa (10 rad/s frequency and 1% oscillation strain).<sup>79</sup> Here the supramolecular hydrogels composed of HEC-Np (0.5 wt%), PVA-MV (0.05 wt%) and CB[8] (0.05 wt%) have been used in this study, which can be readily enhanced through the addition of an extremely small amount of CePO<sub>4</sub> NWs (0.001-0.030 wt%). The preparation details can be seen in the Experimental Section.

### 5.3 Characterisation of nanowire-reinforced hydrogels

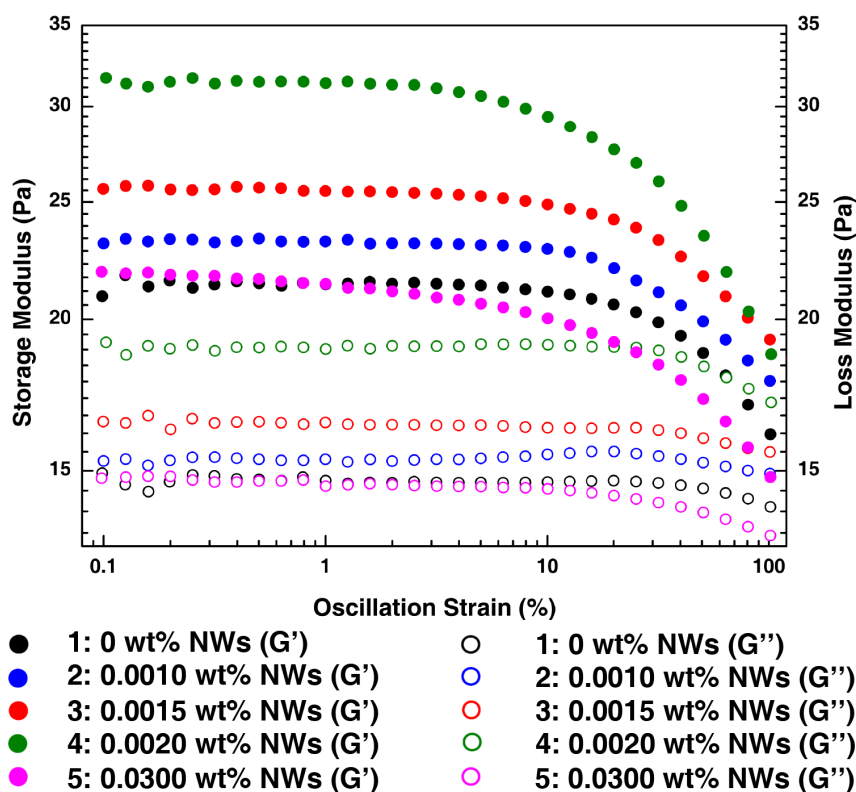


Figure 5.7: Storage ( $G'$ ) and loss ( $G''$ ) moduli from amplitude dependent oscillatory rheology of CePO<sub>4</sub> NWs enhanced hybrid supramolecular hydrogels at 0.5 wt% HEC-Np, 0.05 wt% PVA-MV and 0.05 wt% CB[8] with NW concentration ranges from 0 to 0.0300 wt% (labelled as sample 1-5).

Amplitude dependent oscillatory rheology of the hydrogel has been investigated to understand the dependence of the material strength (Figure 5.7) on increasing amounts of CePO<sub>4</sub> NWs from 0.0010 wt% to 0.0020 wt%. Hydrogel samples with 0, 0.0010, 0.0015, 0.0020 and 0.0300 wt% CePO<sub>4</sub> NWs are labelled as 1-5, respectively. All samples display broad elastic properties before the critical strain point, where  $G'$  (storage moduli)  $>$   $G''$  (loss moduli), indicating the elastic hydrogel behaviour of the hybrid materials. The material strength can be investigated by the value of  $G'$ , the moduli difference ( $G' - G''$ ) and  $\tan \delta$  (the ratio of  $G''/G'$ ).<sup>290</sup> The  $G'$  values display a 48% increase (from  $21.3 \pm 0.3$  Pa to  $31.5 \pm 0.3$  Pa) upon addition of the NWs. Moreover,  $\tan \delta$  in the broad viscoelastic region of sample 1 is 0.69, and decreases to 0.59 with the addition of NWs (sample 4), high-

lighting that hydrogel strength is enhanced upon the addition of NWs. Additionally, the complete amplitude dependent oscillatory rheology results of samples with different NW concentrations of 0 wt%, 0.0010 wt%, 0.0015 wt%, 0.0020 wt%, 0.0025 wt%, 0.0030 wt%, 0.0035 wt% and 0.0300 wt% can be seen in Figure 5.19 (Experimental Section), where the gel with 0.0020 wt% CePO<sub>4</sub> NWs have the highest  $G'$  value.

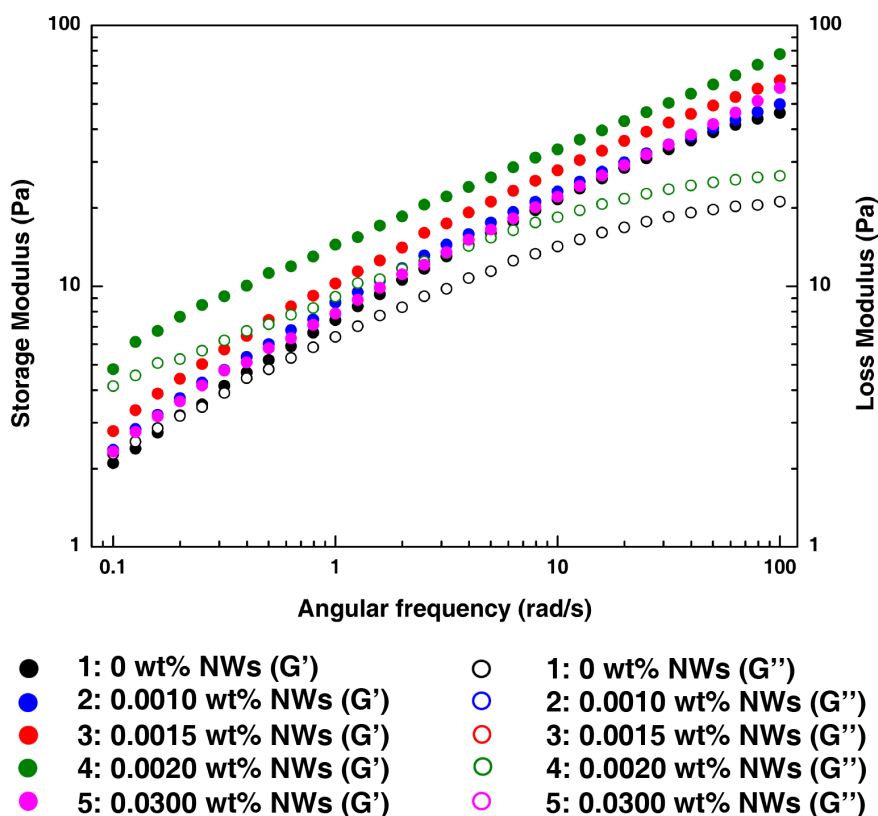


Figure 5.8: Storage ( $G'$ ) and loss ( $G''$ ) moduli from frequency dependent oscillatory rheology of CePO<sub>4</sub> NWs enhanced hybrid supramolecular hydrogels at 0.5 wt% HEC-Np, 0.05 wt% PVA-MV and 0.05 wt% CB[8] with NW concentration ranges from 0 to 0.0300 wt% (labelled as sample 1-5).

Hydrogels fabricated by non-covalent interactions typically exhibit frequency dependence on account of finite crosslink lifetimes.<sup>304</sup> The frequency sweep results (Figure 5.18, Experimental Section) illustrate that for all samples,  $G'$  is dominant over  $G''$  at higher angular frequencies, indicating that all samples have gel-like structures with short crosslink lifetimes. As shown in Figure 5.8, at frequencies below 0.2 rad/s,  $G''$  is slightly dominant over  $G'$  in sample 1. This is likely due to its bulk relaxation being longer than that in the

other samples, resulting in viscous flow behaviours.<sup>290</sup> However, for sample 4, across the range of frequencies tested,  $G'$  exceeds  $G''$ , implying an enhanced crosslinked structure. Even at lower frequencies when the crosslink off rate is faster than the oscillation periods, the sample 4 still retains a gel structure. This is likely due to the supporting effect from the NW network. Moreover, as shown in Figure 5.18 (Experimental Section), the complete frequency dependent oscillatory rheology results of sample with different NW concentrations of 0 wt%, 0.0010 wt%, 0.0015 wt%, 0.0020 wt%, 0.0025 wt% and 0.0300 wt% indicate that 0.0020 wt% CePO<sub>4</sub> NWs is the optimal concentration for this system on account of the highest  $G'$  value.

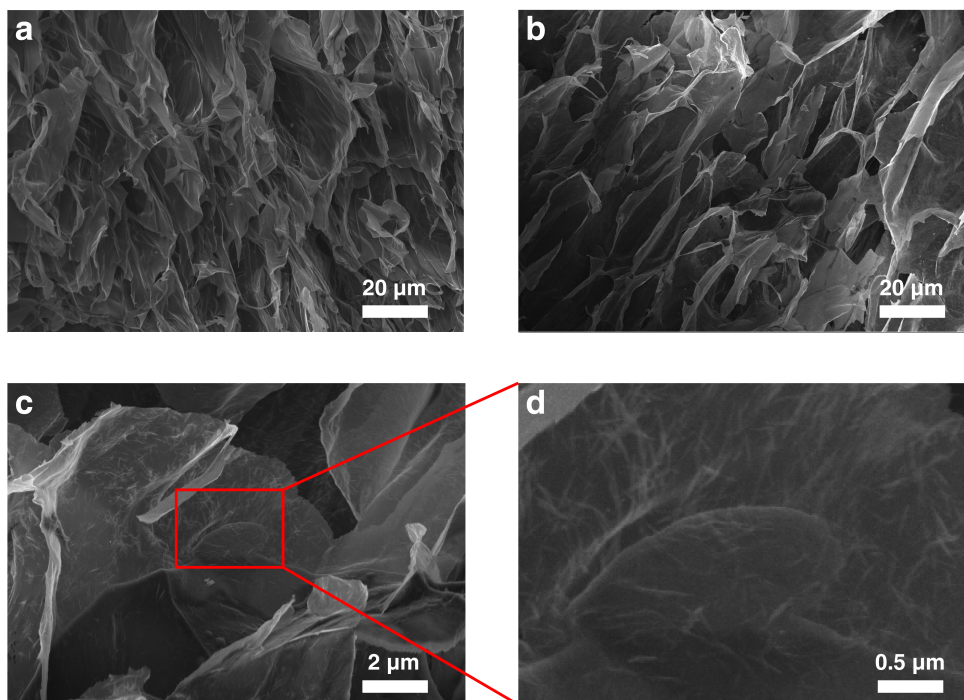


Figure 5.9: SEM images of cryo-dried and lyophilised hydrogel samples **a**, in absence of NWs (scale bar: 20  $\mu\text{m}$ ); **b-d**, with 0.0020 wt% NWs (scale bar of **b**: 20  $\mu\text{m}$ , scale bar of **c**: 2  $\mu\text{m}$ , scale bar of **d**: 0.5  $\mu\text{m}$ ); while NWs in the hybrid gel can clearly be seen in **c** and **d**.

The microstructure of cryo-dried and lyophilised hydrogel samples was observed by scanning electron microscopy (SEM). Figure 5.9a and 5.9b reveal that the hybrid hydrogel retains a similar gel structure to that of a pure supramolecular hydrogel after the addition of NWs. At higher magnification, the NW structures are clearly dispersed and embed-

ded within the polymer network, as shown in Figure 5.9c and 5.9d. The location of NWs might be further investigated through the energy-dispersive X-ray spectroscopy (EDX) in the future. The strength-reinforced behaviours of CePO<sub>4</sub> NW hydrogels may be attributed to two mutually occurring interactions. Compared with the soft polymer chains, the inorganic CePO<sub>4</sub> NWs have a larger aspect ratio and remain in an extended conformation with excellent ductility. This enables the polymer chains to complex with the NWs through hydrogen bonding and the NWs can serve as a supporting skeleton to reinforce the 3D network. The hydrogen bonding interactions between the hydroxyl groups on the polymer chains and the surface of the cerous phosphate NWs provide more physical crosslinks in addition to the CB[8] mediated 3D network.

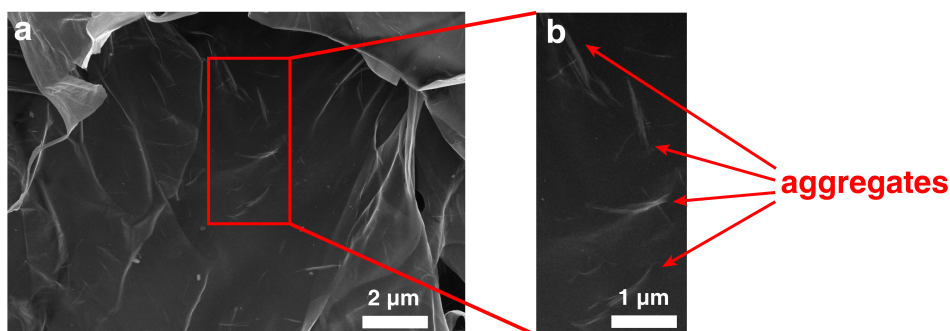


Figure 5.10: SEM image of cryo-dried and lyophilised samples of hydrogels with 0.0025 wt% NWs, which confirms the NWs aggregates. Scale bar of **a**: 2 μm. Scale bar of **b**: 1 μm.

When the amount of NWs exceeded 0.0020 wt%, the strength of hydrogels decreased (Figure 5.7, 5.8, 5.19, 5.18). We hypothesise that excess NWs over a critical value would lead to aggregation. As a consequence, the polymer-NW interactions decrease and result in a weaker internal network. Aggregates of the NWs were indeed observed by SEM (Figure 5.10). In addition, control experiment was carried out, demonstrating the 'excess' NWs drive weaker interactions with the polymer chain (Figure 5.13).



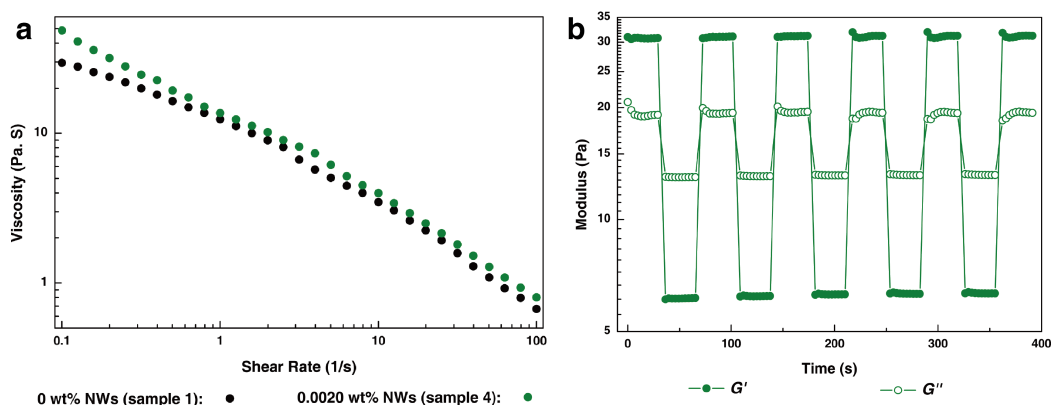


Figure 5.11: **a**, Shear dependent rheology of CePO<sub>4</sub> NW-enhanced hybrid supramolecular hydrogels at 0.5 wt% HEC-Np, 0.05 wt% PVA-MV and 0.05 wt% CB[8] without CePO<sub>4</sub> NWs (sample 1) and with 0.0020 wt% NWs (sample 4). **b**, Alternating strain experiment on NW-enhanced hybrid hydrogel. The oscillatory strain alternated between 1 and 1000% every 30 s.  $G''$  dominates at high strain whilst  $G'$  recovers rapidly when the applied strain reverts back to 1% and the original viscoelastic property is recovered. This process was repeated five times, demonstrating good recyclability.

Dynamic viscosity rheology with different shear rates indicates the hybrid hydrogels exhibit shear-thinning, viscoelasticity and non-Newtonian behaviours on the account of various non-covalent interactions within the materials. As shown in Figure 5.11a, the viscosity of both sample 1 and 4 decreases to a low level around 0.6–0.8 Pa·s with the shear rate rising to 100 s<sup>-1</sup>, since the high shear rate breaks most CB[8]-facilitated crosslinks and the materials tend to express liquid behaviours with a much lower viscosity.<sup>290</sup> Moreover, at a low shear rate (0.1 s<sup>-1</sup>), sample 4 has the highest viscosity value of 48.6 Pa·s, while a value of only 29.6 Pa·s is obtained for sample 1, which further confirms that hydrogel 4 has a deformation resistant structure.

Furthermore, the hybrid gel shows its self-healing nature as a supramolecular network (Figure 5.11b). In addition, as shown in Figure 5.12, the rheological and inverted vial tests demonstrate that the introduction of competitive guest 1-adamantylamine (ADA) will lead to the deformation of the gel structure, suggesting excellent stimulus-responsive properties. Therefore, the NW-reinforced hybrid hydrogels have retained the shear-thinning, self-healing and stimulus-responsive properties of supramolecular networks, allowing for potential applications in injectable delivery systems.

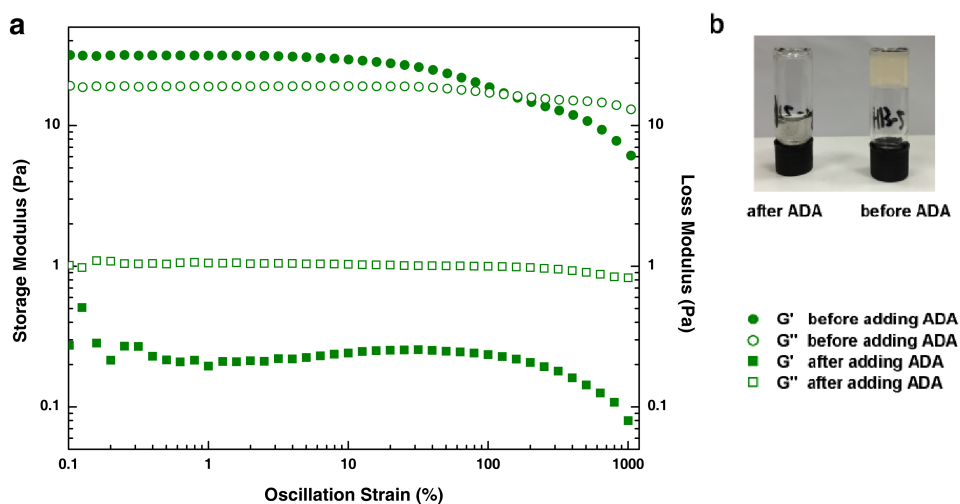


Figure 5.12: **a**, Storage ( $G'$ ) and loss ( $G''$ ) moduli from amplitude dependent oscillatory rheology for the control experiment with and without ADA. **b**, The inverted vial test results. The gels was composed of 0.5 wt% HEC-Np, 0.05 wt% PVA-MV, 0.05 wt% CB[8] and 0.0020 wt% CePO<sub>4</sub> NWs before and after adding ADA.

### Control experiments

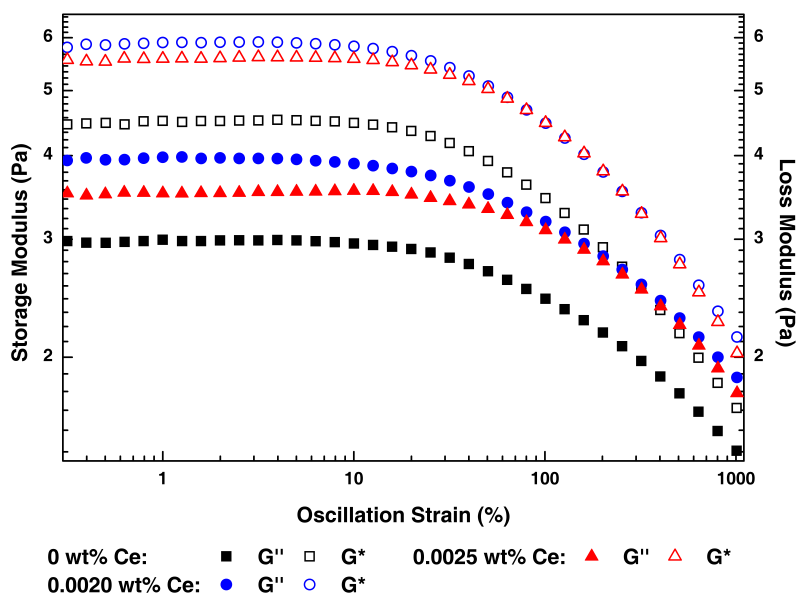


Figure 5.13: Loss ( $G''$ ) and complex ( $|G^*|=[G'^2+G''^2]^{1/2}$ ) moduli from amplitude dependent oscillatory rheology of the solution of 0.5 wt% HEC-Np, 0.05 wt% PVA-MV (without CB[8]) with different concentration of CePO<sub>4</sub> NWs.

To prove that the stiffening effect of NWs on the hydrogel is derived from the in-

interactions between the NWs and the polymer networks, the first control experiment was designed, where the samples with the same composition of HEC-Np and PVA-MV polymers but without any CB[8], containing nanowire concentrations of 0, 0.0020 and 0.0025 wt% were tested. As the samples display liquid behaviours without CB[8]-based crosslinkings, the amplitude dependent oscillatory rheology of the control samples is  $G''$ -dominant. Thus  $G^*$  (complex moduli,  $|G^*|=[G'^2+G''^2]^{1/2}$ ) and  $G''$  are discussed in Figure 5.13. Both  $G^*$  and  $G''$  increased with the introduction of 0.0020 wt% NWs, confirming the stiffening effect of NWs on the polymer networks. However,  $G^*$  and  $G''$  then undergo a decrease with 'excess' NWs addition (0.0025 wt%) due to the hindering effects of excess NWs on the NW-polymer interactions.

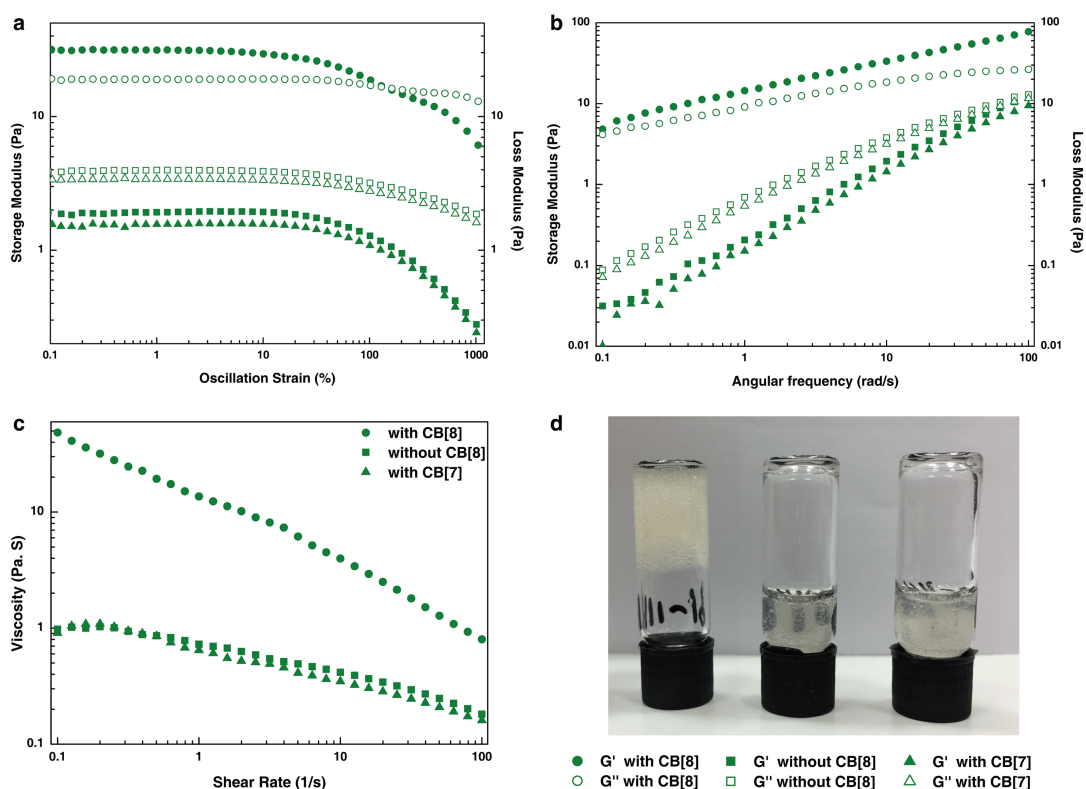


Figure 5.14: Storage ( $G'$ ) and loss ( $G''$ ) moduli from **a**, amplitude dependent oscillatory rheology, **b**, frequency dependent oscillatory rheology and **c**, shear dependent rheology for the control experiment. **d**, The inverted vial test results for the hydrogels with CB[8] (left), without CB[8] (middle) and with CB[7] (right). The gels was composed of 0.5 wt% HEC-Np, 0.05 wt% PVA-MV and 0.0020 wt% CePO<sub>4</sub> nanowires with CB[8], without CB[8] and with CB[7].

Next control experiment was designed to demonstrate that the hydrogel structure is

based on CB[8] complexation crosslinkings instead of the hydrogen bonding between NWs and polymer networks. A series of hydrogels consist of 0.5 wt% HEC-Np, 0.05 wt% PVA-MV and 0.0020 wt% CePO<sub>4</sub> nanowires with CB[8], without CB[8] and with CB[7] were prepared. Both the rheology test (Figure 5.14a-c) and the inverted vial test (Figure 5.14d) suggest that without host-guest ternary complexations (samples without CB[8] and with CB[7]), gel-like properties would not exist. Therefore, the simply supporting effects from the NWs are not able to maintain the gel structure. The reinforced hybrid hydrogel is based on the crosslinkings arised from CB[8] host-guest interactions.

## **5.4 Conclusions**

In conclusion, the mechanical properties of CB[8]-based supramolecular hydrogels have been significantly enhanced by the formation of hybrid hydrogels with extremely small quantities of CePO<sub>4</sub> NWs. The addition of CePO<sub>4</sub> NWs generates physical interactions resulting from the hydrogen bonding between the NW surface and the polymer network. The NWs have been found to act as a 'skeleton', leading to an enhanced continuous phase hybrid network and allowed for the supramolecular hydrogels to retain their attractive properties, including stimuli-responsivity, shear-thinning and self-healing.

This work outlines a general approach for the use of inorganic NWs as frameworks to enhance the mechanical properties of organic soft materials through the formation of organic-inorganic hybrid networks based on supramolecular interactions (CB[8] host-guest chemistry and hydrogen bonding). In addition, this work suggests that the introduction of inorganic materials to CB[8]-based supramoleuclar hydrogels might drive versatile properties. For example, inspired by this work, a supramolecular polymer-colloidal hydrogel has been successfully prepared by readily introducing functional polymer-grafted silica nanoparticles to CB[8]-based hydrogels, which can be drawn into novel biocompatible 'supramolecular fibres' at room temperature.<sup>305</sup>

## 5.5 Experimental

### 5.5.1 Materials and general methods

All starting chemicals were purchased from Sigma Aldrich and used as received unless stated otherwise. Poly(vinyl alcohol)(PVA,  $M_n = 205$  KDa) first dissolved in water at 5 wt%, then precipitated from a solution of acetone and methanol (1:1) and dried overnight at 60 °C. Hydroxyethyl cellulose (HEC), with a number-average molecular weight ( $M_n$ ) of 1.3 MDa, dried overnight in a vacuum oven at 105 °C before use. CB[7], CB[8]<sup>16,177</sup> and MV-NCO<sup>306</sup> were prepared according to previously published protocols.

<sup>1</sup>H NMR (400 MHz) spectra were recorded using a Bruker Avance QNP 400. <sup>1</sup>H NMR (500 MHz) spectra were recorded using Bruker Avance QNP 500 Cryo Ultrashield. Chemical shifts were measured in ppm ( $\delta$ ) in D<sub>2</sub>O and CDCl<sub>3</sub> with the internal reference set to  $\delta$  4.79 ppm and 7.26 ppm respectively.

Rheological characterisation was performed using a TA Instruments Discovery Hybrid Rheometer (DHR)-2 controlled stress rheometer fitted with a Peltier Plate set to 20 °C. All measurements were performed using a 40 mm parallel plate geometry (500  $\mu$ m gap size) and analysed using TA Instruments TRIOS software. Dynamic oscillatory strain amplitude sweep measurements were conducted at a frequency of 10 rad/s between 0.1 % and 1000 % oscillation strains. Dynamic oscillatory frequency sweep measurements were performed at a 1% strain amplitude, between 0.01 to 100 rad/s. The flow sweep tests were conducted between 0.01 and 100 S<sup>-1</sup>.

ATR FT-IR spectroscopy was conducted using a Perkin-Elmer Spectrum 100 series FT-IR spectrometer equipped with a universal ATR sampling accessory.

TEM characterisation was carried out on a FEI Philips Tecnai 20 TEM under an accelerating voltage of 80 kV. Samples were prepared by applying one drop of the as-synthesised microspheres onto a Holey R carbon coated copper TEM grid (400 mesh) and dried overnight.

SEM images were obtained using a Zeiss (Jena, Germany) FE-SEM with variable pressure at 1.5 keV. SEM samples were prepared by freezing of the supramolecular hydrogels in liquid nitrogen followed by lyophilisation. The resulting materials were imaged after

sputtering.

### 5.5.2 General procedure for hydrogel preparation

**PVA-MV.** PVA ( $M_n=205$  KDa, 1.00 g) and MV-NCO were first dissolved in NMP (60 mL). After addition of dibutyltin dilaurate (3 drops), the mixture was stirred overnight at room temperature. Then the mixture was dialysed against NaCl solution (0.1 M, 24 h) and water (48 h) to exchange counter-ions before freeze drying to yield a yellowish solid (1.56 g, 96 %). <sup>1</sup>H NMR (500 MHz, D<sub>2</sub>O)  $\delta$ (ppm=) 9.17-8.96 (br, MV aryl-H), 8.52-8.42 (br, MV aryl-H), 4.56-4.51 (br, MV-CH<sub>2</sub>), 4.42 (s, MV-CH<sub>3</sub>), 4.00-3.89 (br, MV-CH<sub>2</sub>-CH<sub>2</sub>-OCN- and -NCO-CH from the backbone), 2.95-2.83 (br, -CH<sub>2</sub>-NCO), 2.05-1.25 (br, polymer backbone and hexamethylene linker).<sup>79</sup>

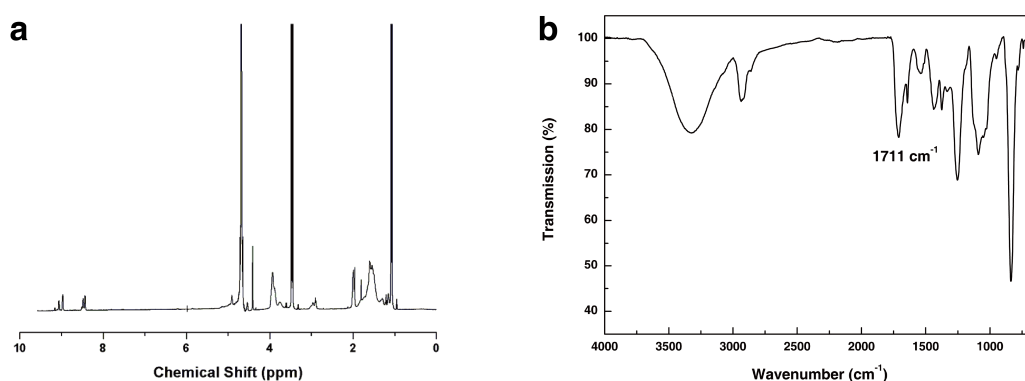


Figure 5.15: **a**, <sup>1</sup>H NMR spectrum (500 MHz) and **b**, FT-IR characterisation of PVA-MV.

**HEC-Np.** HEC ( $M_n=1.3$  MDa, 2.00 g) was dissolved in NMP (300 ml). The mixture was heated to 110 °C under nitrogen to yield a pale yellow clear solution. The solution was then cooled to room temperature and Np-NCO (60.2 mg, 3.55 mmol) as well as dibutyltin dilaurate (6 drops) were added. After stirring overnight, the solution was precipitated from cooled acetone. The solid was collected by filtration, which was dissolved in DI H<sub>2</sub>O before dialysed against H<sub>2</sub>O for three days. After freeze drying, the product was obtained as a white solid (2.02 g, 98 %). <sup>1</sup>H NMR (500 MHz, D<sub>2</sub>O)  $\delta$ (ppm=) 7.91-7.35 (m, naphthyl), 4.28-2.93 (br, polymer backbone).<sup>79</sup>

**CePO<sub>4</sub> nanowires.** The CePO<sub>4</sub> nanowires were prepared using a hydrothermal method. In the synthesis, Ce(NO<sub>3</sub>)<sub>3</sub> (0.40 g) and Na<sub>3</sub>PO<sub>4</sub> (0.30 g) were dissolved in 30 mL of DI

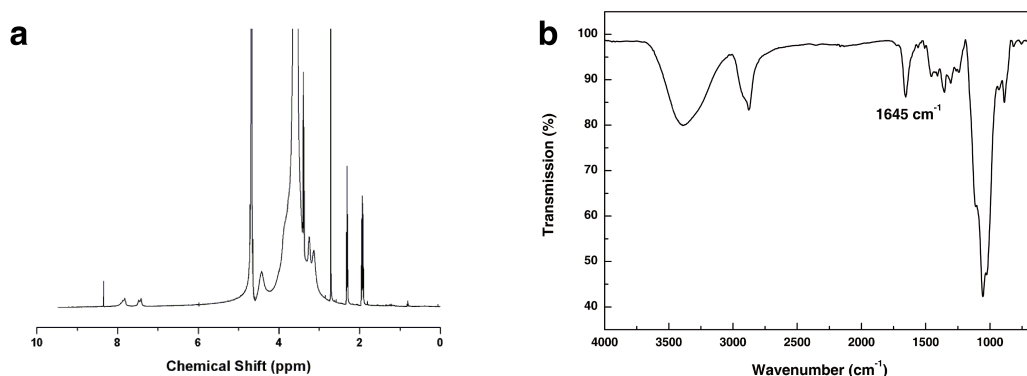


Figure 5.16: **a**, <sup>1</sup>H NMR spectrum (500 MHz) and **b**, FT-IR characterisation of HEC-Np.

water in a Teflon autoclave reactor, the pH of the solution was adjusted to 2 using HCl (aq, 1M). After being sealed, the solution was heated at 170 °C for 10 h in an electric oven, which yielded a clear colloid. The products were then separated by centrifugation at 10,000 rpm and washed with DI water.

The phase of the products was characterised *via* powder X-ray diffraction (XRD) on Bruker D8 Advance with the energy of 40 kV and 40 mA. Their morphology was verified by TEM.

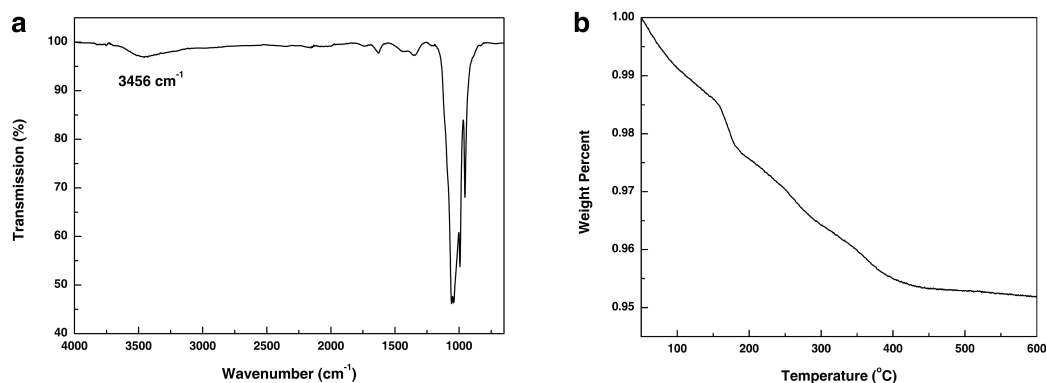


Figure 5.17: **a**, FT-IR characterisation of CePO<sub>4</sub> nanowires. **b**, TGA results of CePO<sub>4</sub> nanowires.

**Hydrogel preparation.** An example of the general hydrogel preparation is described here for a HEC-Np/PVA-MV/CB[8]/NW 0.5/0.05/0.05/0.001 wt% gel. Firstly, HEC-Np (7.5 mg) was dissolved in DI water (0.5 mL) with stirring and mild heating. Secondly, a mixture of PVA-MV (0.75 mg) and CB[8] (0.75 mg) was dissolved in water (0.5 mL) and sonicated <5 min). Similarly, CePO<sub>4</sub> nanowires (0.015 mg) were first dispersed in

DI water (0.5 mL) and sonicated. Finally, the solutions were mixed and vortexed for approximately 1 s to achieve a combined hydrogel and any bubbles were removed by centrifuge at 10000 rpm for 3 minutes.

### 5.5.3 Hydrogel characterisation

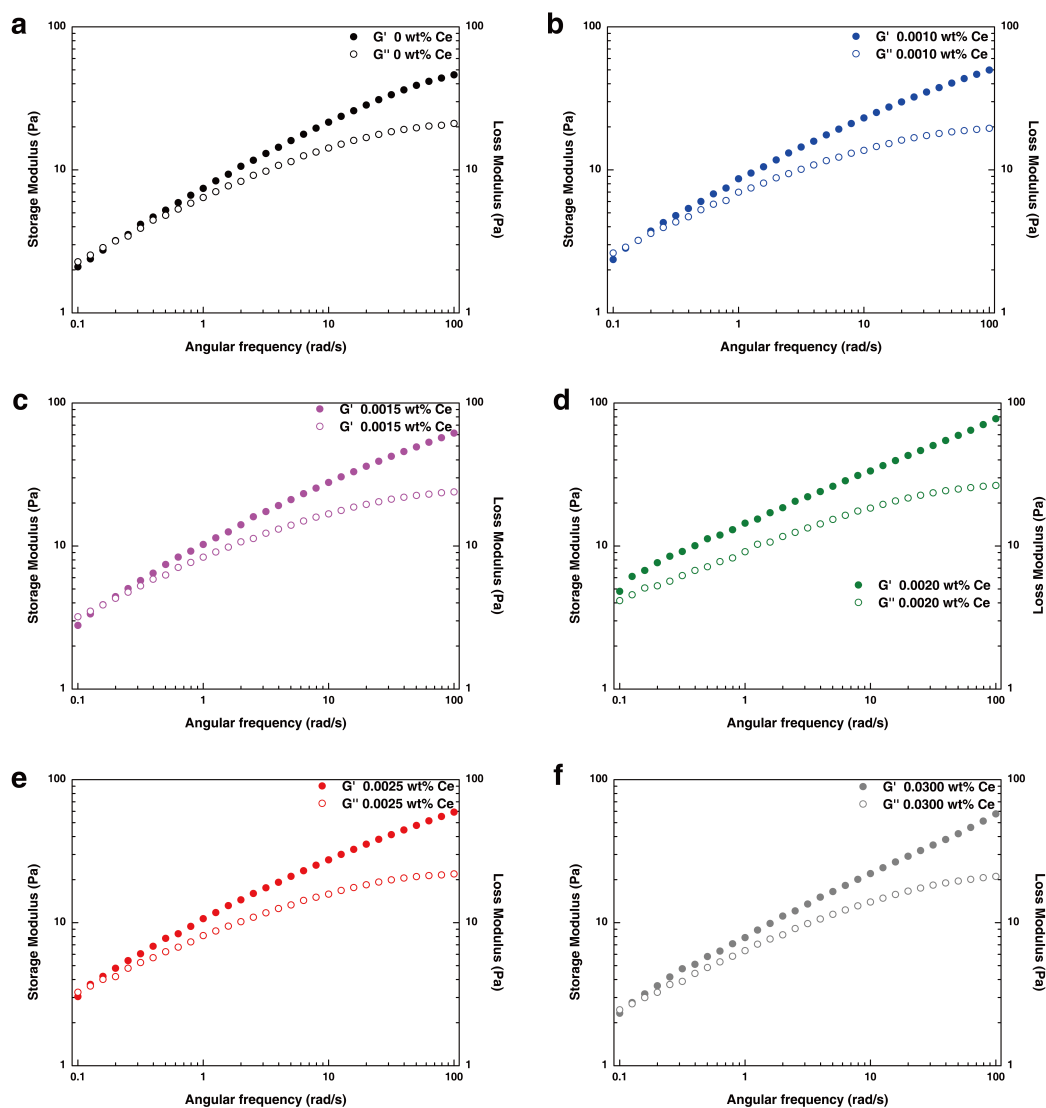


Figure 5.18: Storage ( $G'$ ) and loss ( $G''$ ) moduli from frequency dependent oscillatory rheology of  $\text{CePO}_4$  enhanced hybrid supramolecular hydrogels at 0.5 wt% HEC-Np, 0.05 wt% PVA-MV and 0.05 wt% CB[8] with different concentration of  $\text{CePO}_4$  NWs: **a**, 0 wt%; **b**, 0.0010 wt%; **c**, 0.0015 wt%; **d**, 0.0020 wt%; **e**, 0.0025 wt%; **f**, 0.0300 wt%. The data indicates that 0.0020 wt%  $\text{CePO}_4$  NWs is the optimal concentration for this system.



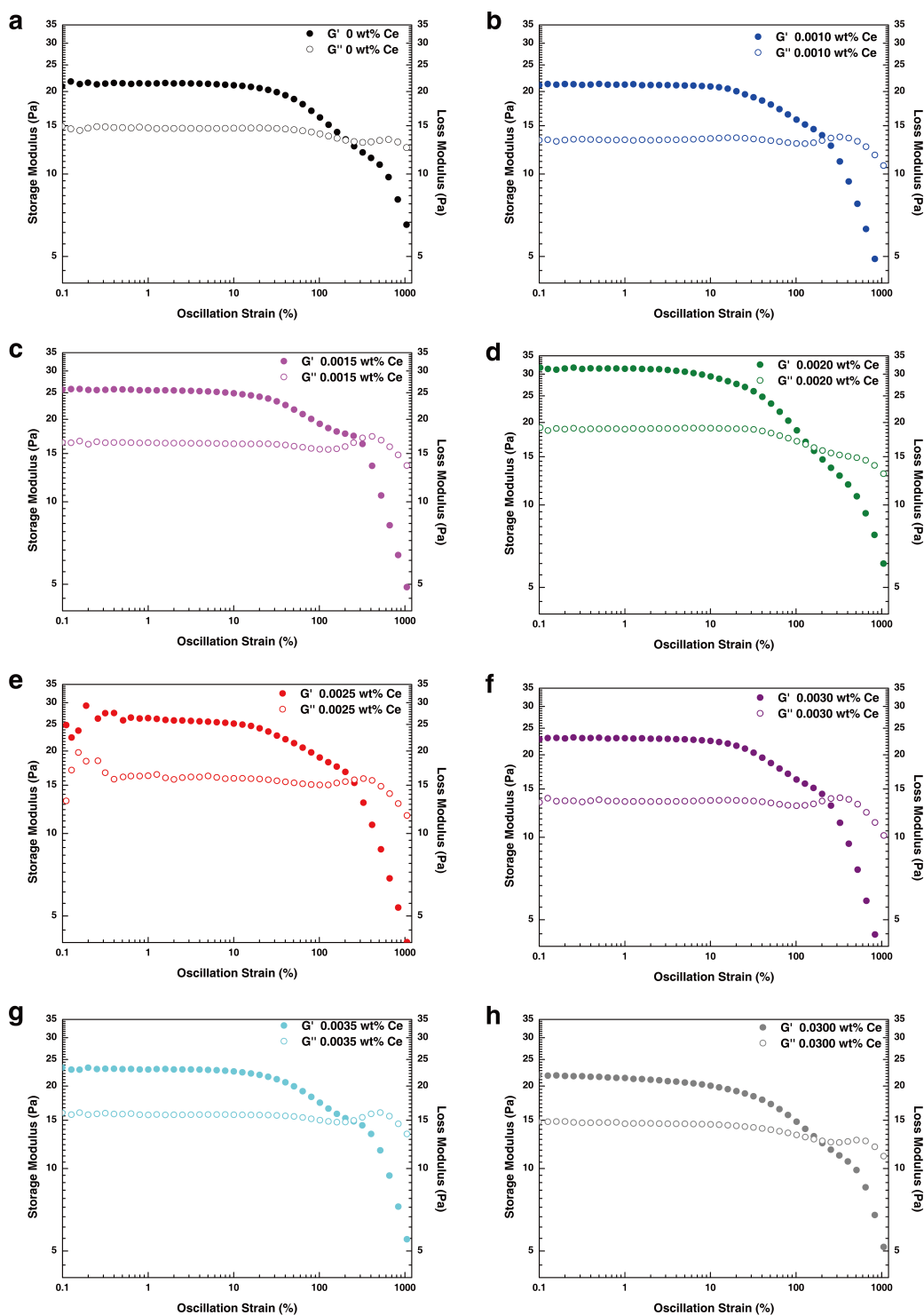


Figure 5.19: Storage ( $G'$ ) and loss ( $G''$ ) moduli from amplitude dependent oscillatory rheology of CePO<sub>4</sub> enhanced hybrid supramolecular hydrogels at 0.5 wt% HEC-Np, 0.05 wt% PVA-MV and 0.05 wt% CB[8] with different concentration of CePO<sub>4</sub> NWs: **a**, 0 wt%; **b**, 0.0010 wt%; **c**, 0.0015 wt%; **d**, 0.0020 wt%; **e**, 0.0025 wt%; **f**, 0.0030 wt%; **g**, 0.0035 wt%; **h**, 0.0300 wt%. The results demonstrate that the gel with 0.0020 wt% CePO<sub>4</sub> NWs have stronger and more ordered networks than others.

## Chapter 6

### Summary and outlook

CB[8] has become an important member in supramolecular host-guest chemistry due to its capability to form strong yet dynamic 1:2 ternary complexes with versatile guest molecules. Owing to the non-covalent binding, CB[8] has provided an outstanding platform to achieve macroscopic properties through the modification of molecular-level supramolecular interactions. Therefore, throughout this thesis, CB[8] ternary complexes, especially the complexation between CB[8] and Azo derivatives, have been exploited to fabricate novel crystalline and composite architectures through hierarchically self-assembled processes. More importantly, by taking advantage of the various supramolecular interactions in the structure, CB[8]-based materials have been endowed with interesting properties and applications, such as morphology-control crystallisation, micelle recycling and reinforced mechanical strength.

The thesis starts with the crystalline system based on the binding between CB[8] and an intriguing Azo-dye molecule: methyl orange (chapter 2), which possesses electronically-positive and negative terminal groups simultaneously. The intermolecular and inter-complex supramolecular interactions (strong Coulombic forces, secondary interactions) furnish the 2MO@CB[8] complex with fast crystallisation properties, making it the fastest CB[*n*] complex crystallisation to date. This study provides a promising host-guest strategy for the preparation of crystals from molecules that are difficult to crystallise by traditional methods. As there will be a colour fading process of the 2MO@CB[8] solution during the crystal growth (formation of the crystalline nucleus and large crystals),

the crystallisation can be monitored through the UV/Vis technique. The simulation and calculation of this kinetic process might be achieved based on the changes of the absorption spectra. Therefore, the investigation of the detailed mechanism is still under way. Furthermore, the binding study has been extended to a series of MO derivatives, where a novel 2MC@CB[8] crystal with 1D channels in the crystalline structure have been reported. The investigation of its potential applications in gas storage and proton conductivity is in progress. In addition, with the aim of introducing defects to 2MO@CB[8] crystals and building more complex structures, an MO/MN@CB[8] crystal is currently being studied.

Inspired by the electrostatically-driven 1D crystal growth of 2MO@CB[8] complex, CB[8] can be utilised to orientate the electrostatic charges of the guests, resulting in anisotropic Coulombic interactions. Therefore, 2MO@CB[8] complex can be further explored as tectonic 'tiles' to hierarchically build crystalline constructs with different morphologies (chapter 3). The three main factors (ionic strength, pH and competitive guests) affecting the crystal growth process have been discussed. For instance, our understanding of the anisotropic effects from ionic strength variations can be exploited to prepare 2D sheet-like and more complex-shaped crystals, which might provide an ideal tool to deal with the challenging topic: preparing shape-controlled crystals at a macroscopic level. To the best of our knowledge, this is the first report of utilising ionic strength to adjust the shape of CB[n]-based complex crystals. Moreover, the oriented electrostatic properties have been exploited to fabricate macroscopic free-standing crystalline pillars grown from a modified glass surface through simple procedures at room temperature. This might provide a promising approach to fabricate organic crystalline patterns in the near future. On account of the photo-responsive property of Azo moiety, 2Azo@CB[8] crystals possess great potential in preparing optical and electrical functional materials, which will open a new window for the fields of both supramolecular chemistry and crystallography.

Next, CB[8] 'hand-cuffs' have been employed in the fabrication of organic-inorganic composite materials. In chapter 4, Azo-functionalised micelles with cargo-loading capabilities have been prepared and attached onto the surface of CB[8] catenane-functionalised

magnetic SiO<sub>2</sub> NPs *via* CB[8] host-guest chemistry, forming a novel MNC structure. By taking advantage of its magnetic and photo-responsive properties, the micelles are concentrated and collected through the assembly and disassembly of MNCs. In the last step, the hydrophobic cargoes inside the micelle can be released in a controllable manner, on account of the pH and thermal responsive properties of PDMAEMA and PNIPAM blocks respectively. More importantly, both the micelles and NPs can be recycled with nice efficiency through this method. Therefore, MNCs provide a novel strategy for the recycling of versatile drug carriers in the future.

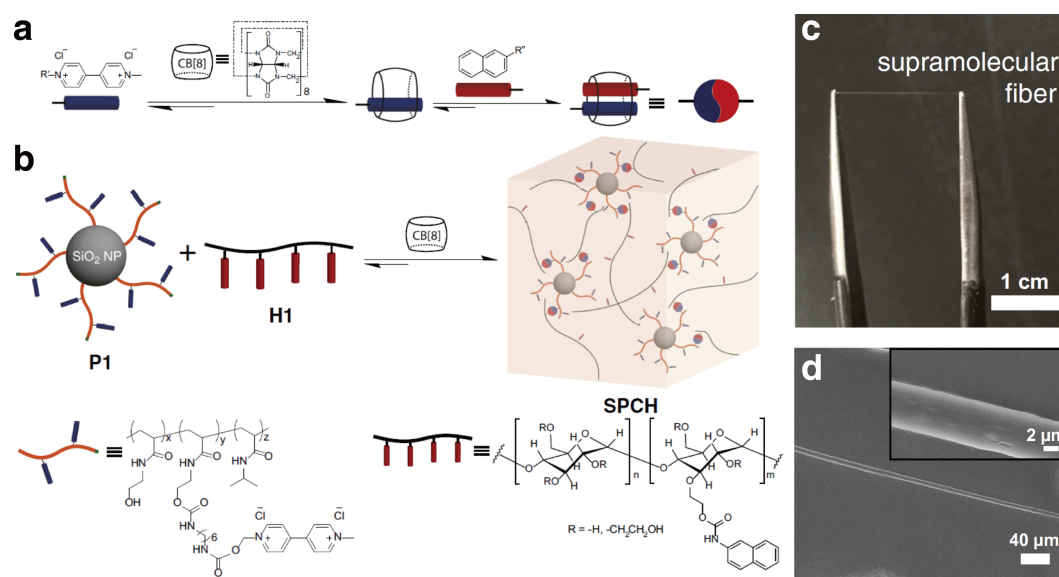


Figure 6.1: **a**, Schematic of the two-step, three-component binding of CB[8] in water. **b**, Schematic representation of a hierarchical supramolecular polymer-colloidal hydrogel (SPCH) prepared through addition of CB[8] to a mixture of polymer-grafted silica P1 (functionalised with MV) and a linear HEC-NP H1 in water. **c**, Photograph of the supramolecular fiber after the hydrogel filament undergoes fast dehydration. **d**, SEM image of the supramolecular fiber (Inset, zoomed-in view of fiber).<sup>305</sup>

Finally CB[8] ternary complexes have been exploited in the preparation of composite hydrogels (chapter 5), where the mechanical property of the organic hydrogel has been reinforced through the addition of extremely small amounts of inorganic NWs. By employing the high aspect ratio CePO<sub>4</sub> NWs as skeletal constructs, the resulted continuous phase hybrid network exhibits a 50 % increase in storage modulus. This is a result of the hydrogen bonds between the polymer chains and the hydroxy-rich NW surfaces.

The location of NWs inside the gel structure might be further investigated through EDX technique in the future. The fascinating properties of supramolecular networks, including stimuli-responsivity, shear-thinning and self-healing, have been retained in the reinforced hybrid hydrogel. This work highlights a general approach of incorporating CB[8]-based hydrogels with inorganic nano-materials to tailor their macroscopic properties. Inspired by this work, a supramolecular polymer–colloidal hydrogel has been reported by our group (Figure 6.1), where functional polymer-grafted silica nanoparticles have been introduced to CB[8]-mediated networks.<sup>305</sup> The resulted hydrogel can be drawn into novel biocompatible ‘supramolecular fibres’, exhibiting a unique combination of stiffness and remarkable damping performance.

Through the investigation of the host-guest chemistry between CB[8] and Azo derivatives, a series of supramolecular assemblies have been fabricated in a hierarchical manner, resulting in a variety of properties and potential applications in the fields of crystalline and composite materials. In conclusion, this thesis shows that CB[8]-based ternary complexes could significantly contribute to the fields of both supramolecular chemistry and materials science. This trend is expected to continue in the future.

## Bibliography

- [1] Lehn, J.-M. *Angew. Chem. Int. Ed.* **1992**, *27*, 89–112.
- [2] Koshland, D. E. *Angew. Chem. Int. Ed.* **1995**, *33*, 2375–2378.
- [3] Kollman, P. A.; Allen, L. C. *Chem. Rev.* **1972**, *72*, 283–303.
- [4] Stupp, S. I.; LeBonheur, V.; Walker, K.; Li, L.-S.; Huggins, K. E.; Keser, M.; Amstutz, A. *Science* **1997**, *276*, 384–389.
- [5] Ikkala, O.; ten Brinke, G. *Chem. Commun.* **2004**, 2131.
- [6] Webber, M. J.; Appel, E. A.; Meijer, E. W.; Langer, R. *Nat. Mater.* **2016**, *15*, 13–26.
- [7] Amabilino, D. B.; Smith, D. K.; Steed, J. W. *Chem. Soc. Rev.* **2017**, *46*, 2404–2420.
- [8] Tsuda, M.; Shigemoto-Mogami, Y.; Koizumi, S.; Mizokoshi, A.; Kohsaka, S.; Salter, M. W.; Inoue, K. *Nature* **2003**, *424*, 778–783.
- [9] Smith, D. K. *J. Chem. Educ.* **2005**, *82*, 393.
- [10] Hastings, C. J.; Pluth, M. D.; Bergman, R. G.; Raymond, K. N. *J. Am. Chem. Soc.* **2010**, *132*, 6938–6940.
- [11] Lagona, J.; Mukhopadhyay, P.; Chakrabarti, S.; Isaacs, L. *Angew. Chem. Int. Ed.* **2005**, *44*, 4844–70.
- [12] Szejtli, J. *Cyclodextrin Technology*; New York: Springer, 1988.
- [13] Gutsche, C. D. *Calixarenes*; Cambridge: Royal Society of Chemistry, 1989.
- [14] Behrend, R.; Meyer, E.; Rusche, F. *Justus Liebigs Ann. Chem.* **1905**, *339*, 1–37.

- [15] Day, A. I.; Arnold, A. P.; Blanch, R. J.; Snushall, B. *J. Org. Chem.* **2001**, *66*, 8094–100.
- [16] Kim, J.; Jung, I.-S.; Kim, S.-Y.; Lee, E.; Kang, J.-K.; Sakamoto, S.; Yamaguchi, K.; Kim, K. *J. Am. Chem. Soc.* **2000**, *122*, 540–541.
- [17] Appel, E. A.; Biedermann, F.; Rauwald, U.; Jones, S. T.; Zayed, J. M.; Scherman, O. A. *J. Am. Chem. Soc.* **2010**, *132*, 14251–14260.
- [18] Liu, C.; Xiang, G.; Wu, Y.; Barrow, S. J.; Rowland, M. J.; Clarke, D. E.; Wu, G.; Scherman, O. A. *Polym. Chem.* **2016**, *7*, 6485–6489.
- [19] Liu, J.; Tan, C. S. Y.; Yu, Z.; Li, N.; Abell, C.; Scherman, O. A. *Adv. Mater.* **2017**, 1605325.
- [20] Liu, J.; Tan, C. S. Y.; Yu, Z.; Lan, Y.; Abell, C.; Scherman, O. A. *Adv. Mater.* **2017**, *29*, 1604951.
- [21] Zheng, Y.; Yu, Z.; Parker, R. M.; Wu, Y.; Abell, C.; Scherman, O. A. *Nat. Commun.* **2014**, *5*, 5772.
- [22] Liu, J.; Lan, Y.; Yu, Z.; Tan, C. S.; Parker, R. M.; Abell, C.; Scherman, O. A. *Acc. Chem. Res.* **2017**, *50*, 208–217.
- [23] Lan, Y.; Wu, Y.; Karas, A.; Scherman, O. A. *Angew. Chem. Int. Ed.* **2014**, *53*, 2166–2169.
- [24] Ren, X.; Wu, Y.; Clarke, D. E.; Liu, J.; Wu, G.; Scherman, O. A. *Chem. Asian J.* **2016**, *11*, 2382–2386.
- [25] Freeman, W. A.; Mock, W. L.; Shih, N. Y. *J. Am. Chem. Soc.* **1981**, *103*, 7367–7368.
- [26] Lee, J. W.; Samal, S.; Selvapalam, N.; Kim, H.-J.; Kim, K. *Acc. Chem. Res.* **2003**, *36*, 621–30.
- [27] Assaf, K. I.; Nau, W. M. *Chem. Soc. Rev.* **2014**, *44*, 394–418.
- [28] Barrow, S. J.; Kasera, S.; Rowland, M. J.; del Barrio, J.; Scherman, O. A. *Chem. Rev.* **2015**, *115*, 12320–12406.

- [29] Marquez, C.; Hudgins, R. R.; Nau, W. M. *J. Am. Chem. Soc.* **2004**, *126*, 5806–5816.
- [30] Nau, W. M.; Florea, M.; Assaf, K. I. *Isr. J. Chem.* **2011**, *51*, 1869–5868.
- [31] Masson, E.; Ling, X.; Joseph, R.; Kyeremeh-Mensah, L.; Lu, X. *RSC Adv.* **2012**, *2*, 1213–1247.
- [32] Biedermann, F.; Uzunova, V. D.; Scherman, O. A.; Nau, W. M.; De Simone, A. *J. Am. Chem. Soc.* **2012**, *134*, 15318–15323.
- [33] Biedermann, F.; Vendruscolo, M.; Scherman, O. A.; De Simone, A.; Nau, W. M. *J. Am. Chem. Soc.* **2013**, *135*, 14879–14888.
- [34] Biedermann, F.; Nau, W. M.; Schneider, H.-J. *Angew. Chem. Int. Ed.* **2014**, *53*, 11158–11171.
- [35] Yu, G.; Jie, K.; Huang, F. *Chem. Rev.* **2015**, *115*, 7240–7303.
- [36] Kim, H.; Kim, Y.; Yoon, M.; Lim, S.; Park, S. M.; Seo, G.; Kim, K. *J. Am. Chem. Soc.* **2010**, *132*, 12200–12202.
- [37] Zhang, H.; Paulsen, E. S.; Walker, K. A.; Krakowiak, K. E.; Dearden, D. V. *J. Am. Chem. Soc.* **2003**, *125*, 9284–9285.
- [38] Buschmann, H.-J.; Jansen, K.; Schollmeyer, E. *Inorg. Chem. Commun.* **2003**, *6*, 531–534.
- [39] Jeon, W. S.; Moon, K.; Park, S. H.; Chun, H.; Ko, Y. H.; Lee, J. Y.; Lee, E. S.; Samal, S.; Selvapalam, N.; Rekharsky, M. V.; Sindelar, V.; Sobransingh, D.; Inoue, Y.; Kaifer, A. E.; Kim, K. *J. Am. Chem. Soc.* **2005**, *127*, 12984–12989.
- [40] Cao, L.; Sekutor, M.; Zavalij, P. Y.; Mlinaric-Majerski, K.; Glaser, R.; Isaacs, L. *Angew. Chem. Int. Ed.* **2014**, *53*, 988–993.
- [41] Ko, Y. H.; Kim, E.; Hwang, I.; Kim, K. *Chem. Commun.* **2007**, 1305–15.
- [42] Lan, Y.; Loh, X. J.; Geng, J.; Walsh, Z.; Scherman, O. A. *Chem. Commun.* **2012**, *48*, 8757–8759.



- [43] Day, A. I.; Arnold, A. P.; Blanch, R. J.; Snushall, B. *J. Org. Chem.* **2001**, *66*, 8094–8100.
- [44] Day, A. I.; Blanch, R. J.; Arnold, A. P.; Lorenzo, S.; Lewis, G. R.; Dance, I. *Angew. Chem. Int. Ed.* **2002**, *41*, 275–277.
- [45] Kim, S.-Y.; Jung, I.-S.; Lee, E.; Kim, J.; Sakamoto, S.; Yamaguchi, K.; Kim, K. *Angew. Chem. Int. Ed.* **2001**, *40*, 2119–2121.
- [46] Kim, J.; Jung, I.-S.; Kim, S.-Y.; Lee, E.; Kang, J.-K.; Sakamoto, S.; Yamaguchi, K.; Kim, K. *J. Am. Chem. Soc.* **2000**, *122*, 540–541.
- [47] Heitmann, L. M.; Taylor, A. B.; Hart, P. J.; Urbach, A. R. *J. Am. Chem. Soc.* **2006**, *128*, 12574–12581.
- [48] Kim, K.; Selvapalam, N.; Ko, Y. H.; Park, K. M.; Kim, D.; Kim, J. *Chem. Soc. Rev.* **2007**, *36*, 267–279.
- [49] Ayhan, M. M.; Karoui, H.; Hardy, M.; Rockenbauer, A.; Charles, L.; Rosas, R.; Udachin, K.; Tordo, P.; Bardelang, D.; Ouari, O. *J. Am. Chem. Soc.* **2015**, *137*, 10238–10245.
- [50] Lim, S.; Kim, H.; Selvapalam, N.; Kim, K.-J.; Cho, S.; Seo, G.; Kim, K. *Angew. Chem. Int. Ed.* **2008**, *47*, 3352–3355.
- [51] Yoon, M.; Suh, K.; Kim, H.; Kim, Y.; Selvapalam, N.; Kim, K. *Angew. Chem. Int. Ed.* **2011**, *50*, 7870–7873.
- [52] Freeman, W. A. *Acta Crystallogr. B* **1984**, *40*, 382–387.
- [53] Mock, W. L.; Shih, N. Y. *J. Org. Chem.* **1986**, *51*, 4440–4446.
- [54] Mock, W. L.; Shih, N. Y. *J. Am. Chem. Soc.* **1988**, *110*, 4706–4710.
- [55] El-Sheshtawy, H. S.; Bassil, B. S.; Assaf, K. I.; Kortz, U.; Nau, W. M. *J. Am. Chem. Soc.* **2012**, *134*, 19935–19941.
- [56] Danylyuk, O.; Fedin, V. P.; Sashuk, V. *Chem. Commun.* **2013**, *49*, 1859.

- [57] Liu, S.; Ruspic, C.; Mukhopadhyay, P.; Chakrabarti, S.; Zavalij, P. Y.; Isaacs, L. *J. Am. Chem. Soc.* **2005**, *127*, 15959–15967.
- [58] Lee, J. W.; Samal, S.; Selvapalam, N.; Kim, H.-J.; Kim, K. *Acc. Chem. Res.* **2003**, *36*, 621–630.
- [59] Hwang, I.; Baek, K.; Jung, M.; Kim, Y.; Park, K. M.; Lee, D.-W.; Selvapalam, N.; Kim, K. *J. Am. Chem. Soc.* **2007**, *129*, 4170–4171.
- [60] Šekutor, M.; Molčanov, K.; Cao, L.; Isaacs, L.; Glaser, R.; Mlinarić-Majerski, K. *Eur. J. Org. Chem.* **2014**, *2014*, 2533–2542.
- [61] Ling, Y.; Mague, J.; Kaifer, A. *Chem. Eur. J.* **2007**, *13*, 7908–7914.
- [62] Wu, X.; Meng, X.; Cheng, G. *J. Inclusion Phenom. Macrocyclic Chem.* **2009**, *64*, 325–329.
- [63] Mitkina, T. V.; Naumov, D. Y.; Gerasko, O. A.; Fedin, V. P. *Inorg. Chim. Acta* **2010**, *363*, 4387–4391.
- [64] Sigwalt, D.; Šekutor, M.; Cao, L.; Zavalij, P. Y.; Hostaš, J.; Ajani, H.; Hobza, P.; Mlinarić-Majerski, K.; Glaser, R.; Isaacs, L. *J. Am. Chem. Soc.* **2017**, *139*, 3249–3258, PMID: 28182422.
- [65] Liu, S.; Zavalij, P. Y.; Isaacs, L. *J. Am. Chem. Soc.* **2005**, *127*, 16798–16799.
- [66] Liu, S.; Shukla, A.; Gadde, S.; Wagner, B.; Kaifer, A.; Isaacs, L. *Angew. Chem. Int. Ed.* **2008**, *47*, 2657–2660.
- [67] Wittenberg, J. B.; Costales, M. G.; Zavalij, P. Y.; Isaacs, L. *Chem. Commun.* **2011**, *47*, 9420.
- [68] Huang, W.-H.; Liu, S.; Zavalij, P. Y.; Isaacs, L. *J. Am. Chem. Soc.* **2006**, *128*, 14744–14745.
- [69] Appel, E. A.; Barrio, J. d.; Dyson, J.; Isaacs, L.; Scherman, O. A. *Chem. Sci.* **2012**, *3*, 2278.

- [70] Mecozzi, S.; Rebek, J., *Julius Chem. Eur. J.* **1998**, *4*, 1016–1022.
- [71] Lin, R.; Long, L.; Huang, R.; Zheng, L. *Cryst. Growth Des.* **2008**, *8*, 791–794.
- [72] Thuery, P.; Masci, B. *Cryst. Growth Des.* **2010**, *10*, 716–725.
- [73] Thuery, P. *Cryst. Growth Des.* **2011**, *11*, 5702–5711.
- [74] Ji, N.; Cheng, X.; Liang, L.; Xiao, X.; Zhang, Y.; Xue, S.; Tao, Z.; Zhu, Q. *CrystEngComm* **2013**, *15*, 7709–7717.
- [75] Jones, S. T.; Zayed, J. M.; Scherman, O. A. *Nanoscale* **2013**, *5*, 5299–5302.
- [76] Tian, F.; Jiao, D.; Biedermann, F.; Scherman, O. A. *Nat. Commun.* **2012**, *3*, 1207.
- [77] Hu, C.; Lan, Y.; Tian, F.; West, K. R.; Scherman, O. A. *Langmuir* **2014**, *30*, 10926–10932.
- [78] Hu, C.; Zheng, Y.; Yu, Z.; Abell, C.; Scherman, O. A. *Chem. Commun.* **2015**, *51*, 4858–4860.
- [79] Appel, E. A.; Loh, X. J.; Jones, S. T.; Biedermann, F.; Dreiss, C. A.; Scherman, O. A. *J. Am. Chem. Soc.* **2012**, *134*, 11767–11773.
- [80] Tan, C. S. Y.; del Barrio, J.; Liu, J.; Scherman, O. A. *Polym. Chem.* **2015**, *6*, 7652–7657.
- [81] Janeček, E.-R.; McKee, J. R.; Tan, C. S. Y.; Nykänen, A.; Kettunen, M.; Laine, J.; Ikkala, O.; Scherman, O. A. *Angew. Chem. Int. Ed.* **2015**, *54*, 5383–5388.
- [82] Appel, E. A.; Forster, R. A.; Rowland, M. J.; Scherman, O. A. *Biomaterials* **2014**, *35*, 9897–9903.
- [83] Li, C.; Rowland, M. J.; Shao, Y.; Cao, T.; Chen, C.; Jia, H.; Zhou, X.; Yang, Z.; Scherman, O. A.; Liu, D. *Adv. Mater.* **2015**, *27*, 3298–3304.
- [84] Loh, X. J.; del Barrio, J.; Toh, P. P. C.; Lee, T.-C.; Jiao, D.; Rauwald, U.; Appel, E. A.; Scherman, O. A. *Biomacromolecules* **2012**, *13*, 84–91.

- 
- [85] Jiao, D.; Geng, J.; Loh, X. J.; Das, D.; Lee, T.-C.; Scherman, O. A. *Angew. Chem. Int. Ed.* **2012**, *51*, 9633–9637.
- [86] Loh, X. J.; Barrio, J. d.; Lee, T.-C.; Scherman, O. A. *Chem. Commun.* **2014**, *50*, 3033–3035.
- [87] Beharry, A. A.; Woolley, G. A. *Chem. Soc. Rev.* **2011**, *40*, 4422–4437.
- [88] Hartley, G. S. *Nature* **1937**, *140*, 281.
- [89] Yager, K. G.; Barrett, C. J. *J. Photochem. Photobiol., A* **2006**, *182*, 250–261.
- [90] Crecca, C. R.; Roitberg, A. E. *J. Phys. Chem. A* **2006**, *110*, 8188–8203.
- [91] Hamon, F.; Djedaini-Pilard, F.; Barbot, F.; Len, C. *Tetrahedron* **2009**, *65*, 10105–10123.
- [92] Rau, H. *Angew. Chem. Int. Ed.* **1973**, *12*, 224–235.
- [93] Dias, A. R.; Da Piedade, M. M.; Simoes, J. M.; Simoni, J. A.; Teixeira, C.; Diogo, H. P.; Meng-Yan, Y.; Pilcher, G. J. *Chem. Thermodyn.* **1992**, *24*, 439–447.
- [94] Rau, H.; Lueddecke, E. *J. Am. Chem. Soc.* **1982**, *104*, 1616–1620.
- [95] Henzl, J.; Mehlhorn, M.; Gawronski, H.; Rieder, K.-H.; Morgenstern, K. *Angew. Chem. Int. Ed.* **2006**, *45*, 603–606.
- [96] Tong, X.; Pelletier, M.; Lasia, A.; Zhao, Y. *Angew. Chem. Int. Ed.* **2008**, *47*, 3596–3599.
- [97] Turanský, R.; Konôpka, M.; Doltsinis, N. L.; Štich, I.; Marx, D. *Phys. Chem. Chem. Phys.* **2010**, *12*, 13922.
- [98] Kobayashi, T.; Degenkolb, E. O.; Rentzepis, P. M. *J. Phys. Chem.* **1979**, *83*, 2431–2434.
- [99] Lednev, I. K.; Ye, T.-Q.; Hester, R. E.; Moore, J. N. *J. Phys. Chem.* **1996**, *100*, 13338–13341.
- [100] Bortolus, P.; Monti, S. *J. Phys. Chem.* **1979**, *83*, 648–652.
- [101] Wang, L.; Xu, W.; Yi, C.; Wang, X. *J. Mol. Graphics Modell.* **2009**, *27*, 792–796.

- [102] Gegiou, D.; Muszkat, K. A.; Fischer, E. J. *Am. Chem. Soc.* **1968**, *90*, 12–18.
- [103] Siampiringue, N.; Guyot, G.; Monti, S.; Bortolus, P. J. *Photochem.* **1987**, *37*, 185–188.
- [104] Bandara, H. M. D.; Burdette, S. C. *Chem. Soc. Rev.* **2012**, *41*, 1809–1825.
- [105] Buncl, E. *Acc. Chem. Res.* **1975**, *8*, 132–139.
- [106] Aly, A. A. *Tetrahedron* **2003**, *59*, 1739–1747.
- [107] Barth, M.; Shah, S. T. A.; Rademann, J. *Tetrahedron* **2004**, *60*, 8703–8709.
- [108] Drug, E.; Gozin, M. J. *Am. Chem. Soc.* **2007**, *129*, 13784–13785.
- [109] Wang, J.; Liu, H.-B.; Ha, C.-S. *Tetrahedron* **2009**, *65*, 9686–9689.
- [110] Kim, Y.; Phillips, J. A.; Liu, H.; Kang, H.; Tan, W. *Proc. Natl. Acad. Sci. U. S. A.* **2009**, *106*, 6489–6494.
- [111] Wen, Y.; Yi, W.; Meng, L.; Feng, M.; Jiang, G.; Yuan, W.; Zhang, Y.; Gao, H.; Jiang, L.; Song, Y. *J. Phys. Chem. B* **2005**, *109*, 14465–14468.
- [112] Ferri, V.; Elbing, M.; Pace, G.; Dickey, M.; Zharnikov, M.; Samorì, P.; Mayor, M.; Rampi, M. *Angew. Chem. Int. Ed.* **2008**, *47*, 3407–3409.
- [113] Murakami, H.; Kawabuchi, A.; Kotoo, K.; Kunitake, M.; Nakashima, N. *J. Am. Chem. Soc.* **1997**, *119*, 7605–7606.
- [114] Muraoka, T.; Kinbara, K.; Aida, T. *Nature* **2006**, *440*, 512–515.
- [115] Puntoriero, F.; Ceroni, P.; Balzani, V.; Bergamini, G.; Vögtle, F. J. *Am. Chem. Soc.* **2007**, *129*, 10714–10719.
- [116] Parker, R. M.; Gates, J. C.; Rogers, H. L.; Smith, P. G. R.; Grossel, M. C. *J. Mater. Chem.* **2010**, *20*, 9118.
- [117] He, T.; Cheng, Y.; Du, Y.; Mo, Y. *Opt. Commun.* **2007**, *275*, 240–244.
- [118] Escudero, D.; Trupp, S.; Bussemer, B.; Mohr, G. J.; González, L. J. *Chem. Theory Comput.* **2011**, *7*, 1062–1072.

- [119] Shi, Y.-W.; Liu, X.-Q.; Shi, P.; Zhang, X.-Y. *Arch. Biochem. Biophys.* **2010**, *494*, 1–6.
- [120] Qu, D.-H.; Wang, Q.-C.; Zhang, Q.-W.; Ma, X.; Tian, H. *Chem. Rev.* **2015**, *115*, 7543–7588.
- [121] Qian, H.; Guo, D.-S.; Liu, Y. *Asian J. Org. Chem.* **2012**, *1*, 155–159.
- [122] Tao, W.; Liu, Y.; Jiang, B.; Yu, S.; Huang, W.; Zhou, Y.; Yan, D. *J. Am. Chem. Soc.* **2012**, *134*, 762–764.
- [123] Ferris, D. P.; Zhao, Y.-L.; Khashab, N. M.; Khatib, H. A.; Stoddart, J. F.; Zink, J. I. *J. Am. Chem. Soc.* **2009**, *131*, 1686–1688.
- [124] Liu, Y.; Yu, C.; Jin, H.; Jiang, B.; Zhu, X.; Zhou, Y.; Lu, Z.; Yan, D. *J. Am. Chem. Soc.* **2013**, *135*, 4765–4770.
- [125] Wu, J.; Isaacs, L. *Chem. Eur. J.* **2009**, *15*, 11675–11680.
- [126] Rauwald, U.; Biedermann, F.; Deroo, S.; Robinson, C. V.; Scherman, O. A. *J. Phys. Chem. B* **2010**, *114*, 8606–8615.
- [127] Hu, C.; West, K. R.; Scherman, O. A. *Nanoscale* **2016**, *8*, 7840–7844.
- [128] del Barrio, J.; Horton, P. N.; Lairez, D.; Lloyd, G. O.; Toprakcioglu, C.; Scherman, O. A. *J. Am. Chem. Soc.* **2013**, *135*, 11760–11763.
- [129] del Barrio, J.; Ryan, S. T. J.; Jambrina, P. G.; Rosta, E.; Scherman, O. A. *J. Am. Chem. Soc.* **2016**, *138*, 5745–5748.
- [130] Andelman, T.; Gong, Y.; Polking, M.; Yin, M.; Kuskovsky, I.; Neumark, G.; O'Brien, S. *J. Phys. Chem. B* **2005**, *109*, 14314–14318.
- [131] Sun, B.; Siringhaus, H. *Nano Lett.* **2005**, *5*, 2408–2413.
- [132] Narayanan, R.; El-Sayed, M. A. *J. Phys. Chem. B* **2005**, *109*, 12663–12676.
- [133] McLaren, A.; Valdes-Solis, T.; Li, G.; Tsang, S. C. *J. Am. Chem. Soc.* **2009**, *131*, 12540–12541.

- [134] Riebel, U.; Kofler, V.; Löffler, F. *Part. Part. Syst. Charact.* **1991**, *8*, 48–54.
- [135] Heng, J. Y. Y.; Bismarck, A.; Lee, A. F.; Wilson, K.; Williams, D. R. *Langmuir* **2006**, *22*, 2760–2769.
- [136] Meagley, K. L.; Garcia, S. P. *Cryst. Growth Des.* **2012**, *12*, 707–713.
- [137] Variankaval, N.; Cote, A. S.; Doherty, M. F. *AIChE J.* **2008**, *54*, 1682–1688.
- [138] Law, M.; Greene, L. E.; Johnson, J. C.; Saykally, R.; Yang, P. *Nat. Mater.* **2005**, *4*, 455–459.
- [139] Adair, J. H.; Suvaci, E. *Curr. Opin. Colloid Interface Sci.* **2000**, *5*, 160–167.
- [140] Meldrum, F. C.; Cölfen, H. *Chem. Rev.* **2008**, *108*, 4332–4432.
- [141] Huang, M. H.; Mao, S.; Feick, H.; Yan, H.; Wu, Y.; Kind, H.; Weber, E.; Russo, R.; Yang, P. *Science* **2001**, *292*, 1897–1899.
- [142] Park, C.; Park, J. E.; Choi, H. C. *Acc. Chem. Res.* **2014**, *47*, 2353–2364.
- [143] Kong, J.; Franklin, N. R.; Zhou, C.; Chapline, M. G.; Peng, S.; Cho, K.; Dai, H. *Science* **2000**, *287*, 622–625.
- [144] Yoo, E.; Kim, J.; Hosono, E.; Zhou, H.-s.; Kudo, T.; Honma, I. *Nano Lett.* **2008**, *8*, 2277–2282.
- [145] Li, X.; Wang, X.; Zhang, L.; Lee, S.; Dai, H. *Science* **2008**, *319*, 1229–1232.
- [146] Huynh, W. U.; Dittmer, J. J.; Alivisatos, A. P. *Science* **2002**, *295*, 2425–2427.
- [147] Haynes, C. L.; Van Duyne, R. P. *J. Phys. Chem. B* **2001**, *105*, 5599–5611.
- [148] Joo, J.; Chow, B. Y.; Prakash, M.; Boyden, E. S.; Jacobson, J. M. *Nat. Mater.* **2011**, *10*, 596–601.
- [149] Yang, P.; Yan, H.; Mao, S.; Russo, R.; Johnson, J.; Saykally, R.; Morris, N.; Pham, J.; He, R.; Choi, H.-J.; others, *Adv. Funct. Mater.* **2002**, *12*, 323.

- [150] Tian, Z. R.; Voigt, J. A.; Liu, J.; Mckenzie, B.; Mcdermott, M. J.; Rodriguez, M. A.; Konishi, H.; Xu, H. *Nat. Mater.* **2003**, *2*, 821–826.
- [151] Liu, H.; Li, Y.; Xiao, S.; Gan, H.; Jiu, T.; Li, H.; Jiang, L.; Zhu, D.; Yu, D.; Xiang, B.; Chen, Y. *J. Am. Chem. Soc.* **2003**, *125*, 10794–10795.
- [152] Park, J. E.; Son, M.; Hong, M.; Lee, G.; Choi, H. C. *Angew. Chem. Int. Ed.* **2012**, *51*, 6383–6388.
- [153] Mei, J.; Diao, Y.; Appleton, A. L.; Fang, L.; Bao, Z. *J. Am. Chem. Soc.* **2013**, *135*, 6724–6746.
- [154] Shin, H.; Yoon, S.; Tang, Q.; Chon, B.; Joo, T.; Choi, H. *Angew. Chem. Int. Ed.* **2008**, *47*, 693–696.
- [155] Babu, S. S.; Möhwald, H.; Nakanishi, T. *Chem. Soc. Rev.* **2010**, *39*, 4021–4035.
- [156] Park, C.; Yoon, E.; Kawano, M.; Joo, T.; Choi, H. C. *Angew. Chem. Int. Ed.* **2010**, *49*, 9670–9675.
- [157] Tang, Q.; Tong, Y.; Li, H.; Ji, Z.; Li, L.; Hu, W.; Liu, Y.; Zhu, D. *Adv. Mater.* **2008**, *20*, 1511–1515.
- [158] Yoon, S. M.; Song, H. J.; Hwang, I.-C.; Kim, K. S.; Choi, H. C. *Chem. Commun.* **2009**, *46*, 231–233.
- [159] Yoon, S. M.; Hwang, I.-C.; Shin, N.; Ahn, D.; Lee, S. J.; Lee, J. Y.; Choi, H. C. *Langmuir* **2007**, *23*, 11875–11882.
- [160] Yoon, S. M.; Song, H. J.; Choi, H. C. *Adv. Mater.* **2010**, *22*, 2164–2167.
- [161] Xu, J.; Wu, G.; Wang, Z.; Zhang, X. *Chem. Sci.* **2012**, *3*, 3227–3230.
- [162] Desiraju, G. R. *Angew. Chem. Int. Ed.* **2007**, *46*, 8342–8356.
- [163] Desiraju, G. R. *J. Am. Chem. Soc.* **2013**, *135*, 9952–9967.
- [164] Paulini, R.; Müller, K.; Diederich, F. *Angew. Chem. Int. Ed.* **2005**, *44*, 1788–1805.



- [165] Nishio, M. *CrystEngComm* **2004**, *6*, 130–158.
- [166] Whitesell, J. K.; Davis, R. E.; Saunders, L. L.; Wilson, R. J.; Feagins, J. P. *J. Am. Chem. Soc.* **1991**, *113*, 3267–3270.
- [167] Metrangolo, P.; Neukirch, H.; Pilati, T.; Resnati, G. *Acc. Chem. Res.* **2005**, *38*, 386–395.
- [168] Xu, J.; Yu, H.; Yang, L.; Wu, G.; Wang, Z.; Wang, D.; Zhang, X. *Chem. Sci.* **2015**, *6*, 4907–4911.
- [169] Appel, E. A.; Tibbitt, M. W.; Webber, M. J.; Mattix, B. A.; Veisoh, O.; Langer, R. *Nat. Commun.* **2015**, *6*, 6295.
- [170] Chikkaraddy, R.; de Nijs, B.; Benz, F.; Barrow, S. J.; Scherman, O. A.; Rosta, E.; Demetriadou, A.; Fox, P.; Hess, O.; Baumberg, J. *Nature* **2016**,
- [171] Lee, T.-C.; Kalenius, E.; Lazar, A. I.; Assaf, K. I.; Kuhnert, N.; Grün, C. H.; Jänis, J.; Scherman, O. A.; Nau, W. M. *Nat. Chem.* **2013**, *5*, 376–382.
- [172] Ni, X.-L.; Xiao, X.; Cong, H.; Liang, L.-L.; Cheng, K.; Cheng, X.-J.; Ji, N.-N.; Zhu, Q.-J.; Xue, S.-F.; Tao, Z. *Chem. Soc. Rev.* **2013**, *42*, 9480–9508.
- [173] Ji, N.; Cheng, X.; Zhao, Y.; Liang, L.; Chen, K.; Xiao, X.; Zhang, Y.; Zhu, Q.; Xue, S.; Tao, Z. *Eur. J. Inorg. Chem.* **2014**, *2014*, 1435–1438.
- [174] Mecozzi, S.; Rebek, J., Jr. *Chem. Eur. J.* **1998**, *4*, 821–828.
- [175] Gues, N.; Peitsch, M. C. *Electrophoresis* **1997**, *18*, 2714–2723.
- [176] Gues, N.; Peitsch, M. C.; Schwede, T.; Diemand, A. *DeepView, Swiss-Pdb Viewer. Ver. 4.1.0.*; Swiss Institute of Bioinformatics, 2012.
- [177] Jiao, D. Z.; Zhao, N.; Scherman, O. A. *Chem. Commun.* **2010**, *46*, 2007–2009.
- [178] Dolomanov, O. V.; Bourhis, L. J.; Gildea, R. J.; Howard, J. A.; Puschmann, H. *J. Appl. Cryst.* **2009**, *42*, 339–341.
- [179] Palatinus, L.; Chapuis, G. *J. Appl. Cryst.* **2007**, *40*, 786–790.

- [180] Sheldrick, G. M. *Acta Cryst.* **2015**, *71*, 3–8.
- [181] Aizenberg, J.; Black, A. J.; Whitesides, G. M. *Nature* **1999**, *398*, 495.
- [182] Kong, X. Y.; Ding, Y.; Yang, R.; Wang, Z. L. *Science* **2004**, *303*, 1348–1351.
- [183] Yang, H. G.; Sun, C. H.; Qiao, S. Z.; Zou, J.; Liu, G.; Smith, S. C.; Cheng, H. M.; Lu, G. Q. *Nature* **2008**, *453*, 638–641.
- [184] Wang, F.; Han, Y.; Lim, C. S.; Lu, Y.; Wang, J.; Xu, J.; Chen, H.; Zhang, C.; Hong, M.; Liu, X. *Nature* **2010**, *463*, 1061–1065.
- [185] Noorduyn, W. L.; Grinthal, A.; Mahadevan, L.; Aizenberg, J. *Science* **2013**, *340*, 832–837.
- [186] Yoon, S.; Hwang, I.-C.; Kim, K.; Choi, H. *Angew. Chem. Int. Ed.* **2009**, *48*, 2506–2509.
- [187] Xu, J.; Yu, H.; Yang, L.; Wu, G.; Wang, Z.; Wang, D.; Zhang, X. *Chem. Sci.* **2015**, *6*, 4907–4911.
- [188] O’Leary, L. E. R.; Fallas, J. A.; Bakota, E. L.; Kang, M. K.; Hartgerink, J. D. *Nat. Chem.* **2011**, *3*, 821–828.
- [189] Lin, N.; Liu, X. Y. *Chem. Soc. Rev.* **2015**, *44*, 7881–7915.
- [190] An, Q.; Chen, Q.; Zhu, W.; Li, Y.; Tao, C.; Yang, H.; Li, Z.; Wan, L.; Tian, H.; Li, G. *Chem. Commun.* **2010**, *46*, 725–727.
- [191] An, Q.; Dong, C.; Zhu, W.; Tao, C.; Yang, H.; Wang, Y.; Li, G. *Small* **2012**, *8*, 562–568.
- [192] Donnay, J. D. H.; Harker, D. *Am. Mineralogist.* **1937**, *22*, 446–467.
- [193] Hartman, P.; Perdok, W. G. *Acta Cryst.* **1955**, *8*, 49–52.
- [194] Mayo, O. B. D., Stephen L.; Goddard, W. A. *J. Phys. Chem.* **1990**, *94*, 8897–8909.
- [195] Rappe, A. K.; Goddard, W. A. *J. Phys. Chem.* **1991**, *95*, 3358–3363.
- [196] He, S.; Sun, X.; Zhang, H. *J. Mol. Struct.* **2016**, *1107*, 182–188.

- [197] Grancic, P.; Bylsma, R.; Meekes, H.; Cuppen, H. M. *Cryst. Growth Des.* **2015**, *15*, 1625–1633.
- [198] Frisch, M. J. *Gaussian 09 Revision D.01*; Gaussian Inc., Wallingford CT, 2013.
- [199] Yanai, T.; Tew, D. P.; Handy, N. C. *Chem. Phys. Lett.* **2004**, *393*, 51–57.
- [200] Hariharan, P. C.; Pople, J. A. *Theoret. Chim. Acta* **1973**, *28*, 213–222.
- [201] Francl, M. M.; Pietro, W. J.; Hehre, W. J.; Binkley, J. S.; Gordon, M. S.; DeFrees, D. J.; Pople, J. A. *J. Chem. Phys.* **1982**, *77*, 3654.
- [202] Grimme, S.; Antony, J.; Ehrlich, S.; Krieg, H. *J. Chem. Phys.* **2010**, *132*, 154104.
- [203] Fried, S. D.; Wang, L.-P.; Boxer, S. G.; Ren, P.; Pande, V. S. *J. Phys. Chem. B* **2013**, *117*, 16236–16248.
- [204] Alexandridis, P. *Curr. Opin. Colloid Interface Sci.* **1996**, *1*, 490–501.
- [205] Smart, T.; Lomas, H.; Massignani, M.; Flores-Merino, M. V.; Perez, L. R.; Battaglia, G. *Nano Today* **2008**, *3*, 38–46.
- [206] Riess, G. *Prog. Polym. Sci.* **2003**, *28*, 1107–1170.
- [207] Lodge, T. P. *Macromol. Chem. Phys.* **2003**, *204*, 265–273.
- [208] Hamley, I. W. *Nanotechnology* **2003**, *14*, 39–54.
- [209] Stuart, M. A. C.; Huck, W. T. S.; Genzer, J.; Müller, M.; Ober, C.; Stamm, M.; Sukhorukov, G. B.; Szleifer, I.; Tsukruk, V. V.; Urban, M.; Winnik, F.; Zauscher, S.; Luzinov, I.; Minko, S. *Nat. Mater.* **2010**, *9*, 101–113.
- [210] Tang, F.; Li, L.; Chen, D. *Adv. Mater.* **2012**, *24*, 1504–1534.
- [211] Tarn, D.; Ashley, C. E.; Xue, M.; Carnes, E. C.; Zink, J. I.; Brinker, C. J. *Acc. Chem. Res.* **2013**, *46*, 792–801.
- [212] Sutton, D.; Nasongkla, N.; Blanco, E.; Gao, J. *Pharm. Res.* **2007**, *24*, 1029–1046.

- [213] Bae, Y.; Kataoka, K. *Adv. Drug. Deliv. Rev.* **2009**, *61*, 768–784.
- [214] Mai, Y.; Eisenberg, A. *Chem. Soc. Rev.* **2012**, *41*, 5969–5985.
- [215] Fong, C.; Le, T.; Drummond, C. J. *Chem. Soc. Rev.* **2012**, *41*, 1297–1322.
- [216] Matyjaszewski, K.; Xia, J. *Chem. Rev.* **2001**, *101*, 2921–2990.
- [217] Ouchi, M.; Terashima, T.; Sawamoto, M. *Chem. Rev.* **2009**, *109*, 4963–5050.
- [218] Hawker, C. J.; Bosman, A. W.; Harth, E. *Chem. Rev.* **2001**, *101*, 3661–3688.
- [219] Chiefari, J.; Chong, Y. K. B.; Ercole, F.; Krstina, J.; Jeffery, J.; Le, T. P. T.; Mayadunne, R. T. A.; Meijs, G. F.; Moad, C. L.; Moad, G.; Rizzardo, E.; Thang, S. H. *Macromolecules* **1998**, *31*, 5559–5562.
- [220] Lowe, A. B.; McCormick, C. L. *Prog. Polym. Sci.* **2007**, *32*, 283–351.
- [221] Tebaldi, M. L.; Leal, D. A.; Montoro, S. R.; Petzhold, C. J. *Mater. Res.* **2014**, *17*, 191–196.
- [222] Fujishige, S.; Kubota, K.; Ando, I. *J. Phys. Chem.* **1989**, *93*, 3311–3313.
- [223] Alexandra Munoz-Bonilla, M. F.-G.; Haddleton, D. M. *Soft Matter* **2007**, *3*, 725–731.
- [224] Liu, F.; Urban, M. W. *Prog. Polym. Sci.* **2010**, *35*, 3–23.
- [225] Chatterjee, U.; Jewrajka, S. K.; Mandal, B. M. *Polymer* **2005**, *46*, 10699–10708.
- [226] Zhu, Y. J. *Express. Polym. Lett.* **2008**, *2*, 214–225.
- [227] Schild, H. G. *Prog. Polym. Sci.* **1992**, *17*, 163–249.
- [228] Li, Y.; Smith, A. E.; Lokitz, B. S.; McCormick, C. L. *Macromolecules* **2007**, *40*, 8524–8526.
- [229] Smith, A. E.; Xu, X.; Abell, T. U.; Kirkland, S. E.; Hensarling, R. M.; McCormick, C. L. *Macromolecules* **2009**, *42*, 2958–2964.
- [230] Ge, Z.; Liu, S. *Chem. Soc. Rev.* **2013**, *42*, 7289.

- [231] Zhuang, J.; Gordon, M. R.; Ventura, J.; Li, L.; Thayumanavan, S. *Chem. Soc. Rev.* **2013**, *42*, 7421.
- [232] Dong, S.; Zheng, B.; Wang, F.; Huang, F. *Acc. Chem. Res.* **2014**, *47*, 1982–1994.
- [233] Yang, L.; Tan, X.; Wang, Z.; Zhang, X. *Chem. Rev.* **2015**, *115*, 7196–7239.
- [234] Lu, T.; Zhang, L.; Gokel, G. W.; Kaifer, A. E. *J. Am. Chem. Soc.* **1993**, *115*, 2542–2543.
- [235] Goldup, S. M.; Leigh, D. A.; Long, T.; McGonigal, P. R.; Symes, M. D.; Wu, J. *J. Am. Chem. Soc.* **2009**, *131*, 15924–15929.
- [236] Coronado, E.; Gaviña, P.; Tatay, S. *Chem. Soc. Rev.* **2009**, *38*, 1674–1689.
- [237] Neal, E. A.; Goldup, S. M. *Chem. Commun.* **2014**, *50*, 5128–5142.
- [238] Gil-Ramírez, G.; Leigh, D. A.; Stephens, A. J. *Angew. Chem. Int. Ed.* **2015**, *54*, 6110–6150.
- [239] Lewis, J. E. M.; Modicom, F.; Goldup, S. M. *J. Am. Chem. Soc.* **2018**, *140*, 4787–4791.
- [240] Sauvage, J.-P. *Acc. Chem. Res.* **1998**, *31*, 611–619.
- [241] Collin, J.-P.; Dietrich-Buchecker, C.; Gaviña, P.; Jimenez-Molero, M. C.; Sauvage, J.-P. *Acc. Chem. Res.* **2001**, *34*, 477–487.
- [242] Nakatani, Y.; Furusho, Y.; Yashima, E. *Angew. Chem. Int. Ed.* **2010**, *49*, 5463–5467.
- [243] Caballero, A.; Zapata, F.; White, N. G.; Costa, P. J.; Félix, V.; Beer, P. D. *Angew. Chem. Int. Ed.* **2012**, *124*, 1912–1916.
- [244] Collier, C. P.; Mattersteig, G.; Wong, E. W.; Luo, Y.; Beverly, K.; Sampaio, J.; Raymo, F. M.; Stoddart, J. F.; Heath, J. R. *Science* **2000**, *289*, 1172–1175.
- [245] Deng, W.-Q.; Flood, A. H.; Stoddart, J. F.; Goddard, W. A. *J. Am. Chem. Soc.* **2005**, *127*, 15994–15995.
- [246] Bonnet, S.; Collin, J.-P.; Koizumi, M.; Mobian, P.; Sauvage, J.-P. *Adv. Mater.* **2006**, *18*, 1239–1250.

- [247] Klajn, R.; Fang, L.; Coskun, A.; Olson, M. A.; Wesson, P. J.; Stoddart, J. F.; Grzybowski, B. A. *J. Am. Chem. Soc.* **2009**, *131*, 4233–4235.
- [248] Appel, E. A.; del Barrio, J.; Loh, X. J.; Scherman, O. A. *Chem. Soc. Rev.* **2012**, *41*, 6195.
- [249] Calvert, P. *Adv. Mater.* **2009**, *21*, 743–756.
- [250] Kasera, S.; Biedermann, F.; Baumberg, J. J.; Scherman, O. A.; Mahajan, S. *Nano Lett.* **2012**, *12*, 5924–5928.
- [251] Li, L.; Beniash, E.; Zubarev, E. R.; Xiang, W.; Rabatic, B. M.; Zhang, G.; Stupp, S. I. *Nat. Mater.* **2003**, *2*, 689–694.
- [252] Balazs, A. C.; Emrick, T.; Russell, T. P. *Science* **2006**, *314*, 1107–1110.
- [253] Munch, E.; Launey, M. E.; Alsem, D. H.; Saiz, E.; Tomsia, A. P.; Ritchie, R. O. *Science* **2008**, *322*, 1516–1520.
- [254] Podsiadlo, P.; Kaushik, A. K.; Arruda, E. M.; Waas, A. M.; Shim, B. S.; Xu, J.; Nandivada, H.; Pumphlin, B. G.; Lahann, J.; Ramamoorthy, A.; Kotov, N. A. *Science* **2007**, *318*, 80–83.
- [255] Xia, Y.; Yang, P.; Sun, Y.; Wu, Y.; Mayers, B.; Gates, B.; Yin, Y.; Kim, F.; Yan, H. *Adv. Mater.* **2003**, *15*, 353–389.
- [256] Zhai, T.; Li, L.; Ma, Y.; Liao, M.; Wang, X.; Fang, X.; Yao, J.; Bando, Y.; Golberg, D. *Chem. Soc. Rev.* **2011**, *40*, 2986–3004.
- [257] Cui, Y.; Lieber, C. M. *Science* **2001**, *291*, 851–853.
- [258] Long, Y.; Yu, M.; Sun, B.; Gu, C.; Fan, Z. *Chem. Soc. Rev.* **2012**, *41*, 4560.
- [259] Mourik, V.; Zuo, K.; Frolov, S. M.; Plissard, S. R.; Bakkers, E. P. a. M.; Kouwenhoven, L. P. *Science* **2012**, *336*, 1003–1007.
- [260] Yuan, J.; Xu, Y.; Muller, A. H. E. *Chem. Soc. Rev.* **2011**, *40*, 640–655.

- [261] Oulton, R. F.; Sorger, V. J.; Genov, D. A.; Pile, D. F. P.; Zhang, X. *Nat. Photonics*. **2008**, *2*, 496–500.
- [262] Liang, H.; Liu, S.; Yu, S. *Adv. Mater.* **2010**, *22*, 3925–3937.
- [263] Long, Y.; Hui, J.; Wang, P.; Hu, S.; Xu, B.; Xiang, G.; Zhuang, J.; Lv, X.; Wang, X. *Chem. Commun.* **2012**, *48*, 5925.
- [264] Vendamme, R.; Onoue, S.-Y.; Nakao, A.; Kunitake, T. *Nat. Mater.* **2006**, *5*, 494–501.
- [265] Hu, S.; Liu, H.; Wang, P.; Wang, X. *J. Am. Chem. Soc.* **2013**, *135*, 11115–11124.
- [266] Patil, A. J.; Kumar, R. K.; Barron, N. J.; Mann, S. *Chem. Commun.* **2012**, *48*, 7934–7936.
- [267] Lee, K. Y.; Mooney, D. J. *Chem. Rev.* **2001**, *101*, 1869–1880.
- [268] Zhang, Y. S.; Khademhosseini, A. *Science* **2017**, *356*, eaaf3627.
- [269] Peppas, N. A.; Bures, P.; Leobandung, W.; Ichikawa, H. *Eur. J. Pharm. Biopharm.* **2000**, *50*, 27–46.
- [270] Malkoch, M.; Vestberg, R.; Gupta, N.; Mespouille, L.; Dubois, P.; F. Mason, A.; L. Hedrick, J.; Liao, Q.; W. Frank, C.; Kingsbury, K.; J. Hawker, C. *Chem. Commun.* **2006**, *0*, 2774–2776.
- [271] Lutolf, M.; Raeber, G.; Zisch, A.; Tirelli, N.; Hubbell, J. *Adv. Mater.* **2003**, *15*, 888–892.
- [272] Tan, H.; Chu, C. R.; Payne, K. A.; Marra, K. G. *Biomaterials* **2009**, *30*, 2499–2506.
- [273] McHale, M. K.; Setton, L. A.; Chilkoti, A. *Tissue engineering* **2005**, *11*, 1768–1779.
- [274] Shu, X. Z.; Liu, Y.; Luo, Y.; Roberts, M. C.; Prestwich, G. D. *Biomacromolecules* **2002**, *3*, 1304–1311.
- [275] Peppas, N. A.; Huang, Y.; Torres-Lugo, M.; Ward, J. H.; Zhang, J. *Annu. Rev. Biomed. Eng.* **2000**, *2*, 9–29.
- [276] Lutolf, M. *Nat. Mater.* **2009**, *8*, 451–453.

- [277] Seiffert, S.; Sprakel, J. *Chem. Soc. Rev.* **2012**, *41*, 909–930.
- [278] Goh, C. Y.; Mocerino, M.; Ogden, M. I. *Supramol. Chem.* **2013**, *25*, 555–566.
- [279] Zhang, M.; Xu, D.; Yan, X.; Chen, J.; Dong, S.; Zheng, B.; Huang, F. *Angew. Chem. Int. Ed.* **2012**, *124*, 7117–7121.
- [280] Tan, S.; Ladewig, K.; Fu, Q.; Blencowe, A.; Qiao, G. G. *Macromol. Rapid Commun.* **2014**, *35*, 1166–1184.
- [281] Bosman, A. W.; Sijbesma, R. P.; Meijer, E. W. *Mater. Today* **2004**, *7*, 34–39.
- [282] Habibi, Y.; Lucia, L. A.; Rojas, O. J. *Chem. Rev.* **2010**, *110*, 3479–3500.
- [283] Rusli, R.; Shanmuganathan, K.; Rowan, S. J.; Weder, C.; Eichhorn, S. J. *Biomacromolecules* **2010**, *11*, 762–768.
- [284] Weng, W.; Beck, J. B.; Jamieson, A. M.; Rowan, S. J. *J. Am. Chem. Soc.* **2006**, *128*, 11663–11672.
- [285] Kumpfer, J. R.; Rowan, S. J. *J. Am. Chem. Soc.* **2011**, *133*, 12866–12874.
- [286] Holten-Andersen, N.; Harrington, M. J.; Birkedal, H.; Lee, B. P.; Messersmith, P. B.; Lee, K. Y. C.; Waite, J. H. *Proc. Natl. Acad. Sci. U. S. A.* **2011**, *108*, 2651–2655.
- [287] Morton, S. W.; Herlihy, K. P.; Shopsowitz, K. E.; Deng, Z. J.; Chu, K. S.; Bowerman, C. J.; DeSimone, J. M.; Hammond, P. T. *Adv. Mater.* **2013**, *25*, 4707–4713.
- [288] Nakahata, M.; Takashima, Y.; Yamaguchi, H.; Harada, A. *Nat. Commun.* **2011**, *2*, 511.
- [289] Rodell, C. B.; Kaminski, A. L.; Burdick, J. A. *Biomacromolecules* **2013**, *14*, 4125–4134.
- [290] Rowland, M. J.; Atgie, M.; Hoogland, D.; Scherman, O. A. *Biomacromolecules* **2015**, *16*, 2436–2443.
- [291] Becker, T.; Goh, C. Y.; Jones, F.; McIldowie, M. J.; Mocerino, M.; Ogden, M. I. *Chem. Commun.* **2008**, *0*, 3900–3902.
- [292] Zhang, J.; Guo, D.; Wang, L.; Wang, Z.; Liu, Y. *Soft Matter* **2011**, *7*, 1756–1762.



- [293] Song, S.; Wang, J.; Feng, H.; Zhu, Z.; Zheng, Y. *RSC Adv.* **2014**, *4*, 24909–24913.
- [294] Wang, K.; Chen, Y.; Liu, Y. *Chem. Commun.* **2015**, *51*, 1647–1649.
- [295] Ge, Z.; Hu, J.; Huang, F.; Liu, S. *Angew. Chem. Int. Ed.* **2009**, *121*, 1830–1834.
- [296] Dong, S.; Luo, Y.; Yan, X.; Zheng, B.; Ding, X.; Yu, Y.; Ma, Z.; Zhao, Q.; Huang, F. *Angew. Chem. Int. Ed.* **2011**, *123*, 1945–1949.
- [297] Dong, S.; Zheng, B.; Xu, D.; Yan, X.; Zhang, M.; Huang, F. *Adv. Mater.* **2012**, *24*, 3191–3195.
- [298] Yan, X.; Xu, D.; Chen, J.; Zhang, M.; Hu, B.; Yu, Y.; Huang, F. *Polym. Chem.* **2013**, *4*, 3312–3322.
- [299] Liu, J.; Soo Yun Tan, C.; Lan, Y.; Scherman, O. A. *J. Polym. Sci., Part A: Polym. Chem.* **2017**, *55*, 3105–3109.
- [300] Sun, J.-Y.; Zhao, X.; Illeperuma, W. R. K.; Chaudhuri, O.; Oh, K. H.; Mooney, D. J.; Vlassak, J. J.; Suo, Z. *Nature* **2012**, *489*, 133–136.
- [301] Rose, S.; Prevoteau, A.; Elzière, P.; Hourdet, D.; Marcellan, A.; Leibler, L. *Nature* **2013**, *505*, 382–385.
- [302] McKee, J. R.; Appel, E. A.; Seitsonen, J.; Kontturi, E.; Scherman, O. A.; Ikkala, O. *Adv. Funct. Mater.* **2014**, *24*, 2706–2713.
- [303] Tang, C.; Bando, Y.; Golberg, D.; Ma, R. *Angew. Chem. Int. Ed.* **2005**, *44*, 576–579.
- [304] Yount, W. C.; Loveless, D. M.; Craig, S. L. *Angew. Chem. Int. Ed.* **2005**, *44*, 2746–2748.
- [305] Wu, Y.; Shah, D. U.; Liu, C.; Yu, Z.; Liu, J.; Ren, X.; Rowland, M. J.; Abell, C.; Ramage, M. H.; Scherman, O. A. *Proc. Natl. Acad. Sci. U. S. A.* **2017**, *114*, 8163–8168.
- [306] Biedermann, F.; Appel, E. A.; del Barrio, J.; Gruending, T.; Barner-Kowollik, C.; Scherman, O. A. *Macromolecules* **2011**, *44*, 4828–4835.